SYNTHETIC, STRUCTURAL, AND SPECTROSCOPIC STUDY OF LUMINESCENT TRANSITION METAL COMPLEXES FOR USE IN ELECTRONIC DEVICES AND ENVIRONMENTAL SENSORS

A DISSERTATION
SUBMITTED TO THE FACULTY OF THE GRADUATE SCHOOL
OF THE UNIVERSITY OF MINNESOTA
BY

KARI ANN MCGEE

IN PARTIAL FULFILLMENT OF THE REQUIREMENTS
FOR THE DEGREE OF
DOCTOR OF PHILOSOPHY

PROFESSOR KENT R. MANN

DECEMBER 2008

Acknowledgements

The Mann group…what can I say…this group has turned out to be a second family for me, and I want to thank all of the Mann group members with whom I have worked. Daron Janzen deserves so much thanks for drawing me into this group with his excitement for chemistry and thirst for knowledge; he was always willing to answer any question and taught me how to do crystallography the right way. Jason Burney and Michael Burand were my lab buddies in the old lab, the other 2/3 of the Mann Group Trio; they taught me not to take myself or sometimes, chemistry, too seriously. Ted Pappenfus often gave me advice about chemistry (and life) and always had an unending supply of crystals to fuel my obsession. Paul Ewbank (the Ewb) taught me to answer the hardest questions. Raghu Chitta amazed me from day one with his ideas and broad knowledge-base, helping me to expand my mind. The other current Mann group members: Conor Smith, Lisa Koenig, Jon Bohnsack, Kyle Schwartz, Lindsay Hinkle, and Darren Ceckanowicz, my lab buddies in the new lab, I thank for the wonderful discussions (chemistry or not) and all of the good times. I've enjoyed working with each and every one of them!

Most of all in the Mann group I would like to thank Kent. He gave me the perfect amount of free rein and attention that I needed to be successful. He gave me the freedom to pursue the chemistry and techniques in which I was interested but also pushed me to expand my horizons and take my chemistry to the next level. Kent devotes an amazing amount of time and energy to his students, and it shows in his sustained relationships with them after they leave. I thank him for being a wonderful mentor and friend.

I am also indebted to Seth Rasmussen, my undergraduate advisor. He taught me "the ropes" of synthetic chemistry and by encouraging me to attend graduate school, kept me out of clown college. I would also like to thank Benjamin Kucera, Bill Brennessel, and Victor Young for all of their help and patience in solving difficult crystal structures.

I am grateful for my parents and their support of both me and my choices in life; I wouldn't be the person I am without their influence. I thank my brother, Jim, for the Guitar Hero stress-relieving sessions. To my carpool buddy, Alicia Peterson, thank you for all the chemistry talk on the way home and for being a great listener. Thank God for the bus strike!

Last but not least I would like to thank my husband Chris who has been my rock since we first met. He has been the calming influence in my life, always listening to my "shop talk", frustrations, and accomplishments with equal attentiveness. He has been understanding of my tendency to bring chemistry home with me, both in my mind and on my shoes, as well as the sometimes long hours monopolizing the computer! He can always make me smile, even in the worst of times. This is just one of things I love and thank him for.

Kari Ann McGee

334 words

Abstract

This thesis describes the synthesis, structural, and spectroscopic study of ruthenium and iridium complexes for use in environmental sensors or electronic devices. Chapters 1–2 discuss studies of ruthenium polypyridyl (pp) complexes used for detection of oxygen gas. In Chapter 1 the variation of the counterion and its affect on the packing structure and subsequent detection of oxygen is discussed. The anion $tfpb^-$ (tetrakis(bis-3,5-trifluoromethylphenylborate) worked particularly well and provided the inefficient packing structure with desired channels of open space. In Chapter 2 optically pure metal complexes were explored to alter the packing structure. Both means of creating void space enabled oxygen diffusion to give sensitive and reproducible crystalline oxygen sensors.

Chapter 3 describes the dual use of a $[Ru(pp)_3](tfpb)_2$ complex for detection of oxygen and the volatile organic, benzene. The crystalline solid undergoes a reversible vapochromic shift of the emission λ_{max} to higher energy in the presence of benzene. Additionally, in the presence of oxygen the solid exhibits linear Stern-Volmer quenching behavior. This crystalline solid was a practical sensor at low concentrations (0.76%) of benzene vapor.

In Chapter 4, the synthesis of new compounds of the general form [(*p*-cym)Ru(pp)Cl]Cl is discussed. This method allowed the study of a series of Ru(II) complexes, with different polypyridyl and β-diketonate ligands. Modification of the substituent group on the β-diketonate ligand has a pronounced effect on the electronic

and electrochemical properties of these complexes. The presence of channels in the crystal structures of two of these molecules as well as the low Ru(III)/Ru(II) redox couple led to their examination as chlorine sensors.

In Chapter 5, a selective low-temperature synthesis of the highly desired *fac* and *mer* tris-cyclometalated Ir(III) complexes used in OLEDs is discussed. The bis-acetonitrile species, $[Ir(C^N)_2(NCCH_3)_2]PF_6$, and hydroxy-bridged dimers, $[Ir(C^N)_2(OH)]_2$ for two cyclometalating ligands (C^N) were synthesized. The *fac*-$Ir(C^N)_3$ and *mer*-$Ir(C^N)_3$ complexes were synthesized at 100 ºC in *o*-dichlorobenzene from the $[Ir(C^N)_2(NCCH_3)_2]PF_6$ or $[Ir(C^N)_2(OH)]_2$ complexes respectively. A mechanism is proposed that may account for the selectivity observed in the formation of these *fac*-$Ir(C^N)_3$ and *mer*-$Ir(C^N)_3$ isomers.

Table of Contents

Chapter 1

Porous Crystalline Ruthenium Complexes Are Oxygen Sensors

Abstract

Several highly emissive, crystalline salts (ClO_4^-, PF_6^-, BF_4^-, $B(C_6F_5)_4^-$, and $tfpb^-$; $B(C_6F_5)_4^-$ = tetrakis(pentafluorophenyl)borate; $tfpb^-$ = tetrakis(bis-3,5-trifluoromethylphenylborate) of the $Ru(pp)_3^{2+}$ (pp = bpy (2,2'-bipyridine), phen (1,10-phenanthroline), or 4,7-Me_2Phen (4,7-dimethyl-1,10-phenanthroline) lumophore have been tested as oxygen sensors. Oxygen detection by luminescence quenching correlates with the void space in the crystalline lattice, particularly in the case of $[Ru(phen)_3](tfpb)_2$ and $[Ru(4,7\text{-}Me_2Phen)_3](tfpb)_2$ which have channels occupying approximately 136 $Å^3$ and 173 $Å^3$ per Ru in the crystals respectively. The emission intensity and lifetime quenching of $[Ru(phen)_3](tfpb)_2$ displayed strictly linear (R^2 = 0.9996) Stern-Volmer behavior (plots of I_0/I and τ_0/τ vs mole fraction of oxygen) with a slope of 2.43. A single exponential is observed for the emission intensity decay for all oxygen concentrations. Improved emission intensity quenching was displayed for $[Ru(4,7\text{-}Me_2Phen)_3](tfpb)_2$ which exhibited a linear Stern-Volmer plot with a slope of 4.76. The time dependence of the emission of $[Ru(phen)_3](tfpb)_2$ caused by a step function air pressure drop is significantly affected by changing the light penetration depth when different excitation wavelengths are used (at 470 nm, $t_{1/2}$ = 120 ms; at 518 nm, $t_{1/2}$ = 2200 ms). These experiments are consistent with the diffusion of oxygen molecules in $[Ru(phen)_3](tfpb)_2$ crystals with a diffusion coefficient on the order of 10^{-7}–10^{-8} cm^2/s. The technological significance of these crystalline oxygen sensors was demonstrated by long-term stability studies and by the successful calibration of a ballprobe sensor coated with crystalline $[Ru(phen)_3](tfpb)_2$ against a dissolved oxygen Clark electrode.

Introduction

Due to the significance of molecular oxygen, measurement of the concentration of oxygen in air and in water is important. Measuring oxygen in our biosphere provides information about the overall ecological conditions in the environment;[1, 2] additionally, oxygen measurements in the human body are also important. For example, oxygen levels in the blood or exhaled air of a patient are parameters used for judging the general health of a person. Until recently, the Clark electrode, which operates by the electrochemical reduction of oxygen, was the best option for oxygen detection. The several limitations of the Clark electrode, (1) they cannot be readily miniaturized, (2) they suffer from electrical interference, and (3) they detect by electrochemical consumption of oxygen, have led to the search for detection by other means.

The sensing of molecular oxygen in the gas phase and water with optical sensors, as an alternative to electrochemical detection, has generated considerable interest in the past 20 years.[1-5] Optical sensors do not suffer from electrical interference and offer increased reproducibility as the detection mechanism requires the ground state of oxygen to quench triplet emission. This reversible luminescence quenching does not consume oxygen and excitation of the sample using LEDs (light emitting diodes) and fiber-optic cables and detection using a photodiode allows for miniaturization. Solid-state optical sensors developed thus far involve embedding emissive transition metal complexes in polymeric,[1, 6-23] zeolitic,[24, 25] sol gel,[26-30] or other[31-36] support materials that allow oxygen to diffuse to the emissive sites. The metal complex emission is quenched via energy transfer to the oxygen molecules, allowing detection. Fiber-optic sensors are a well-suited alternative for both monitoring oxygen concentrations in the blood vessels or

breath of critical-care patients and environmental applications requiring sensitive, reproducible, and miniaturized sensors.[1, 2]

The mechanism of detection in optical oxygen sensors relies on the production of triplet symmetry metal-to-ligand-charge-transfer (MLCT) excited states which lie close in energy to the ground state of molecular oxygen. Excitation of a metal complex in its ground state (A) by light generates an excited state (A^*). This singlet excited state is converted to a triplet state via intersystem crossing resulting in spin-forbidden relaxation back to the singlet ground state and subsequent phosphorescent emission (Figure 1). The excited state can also relax back to the ground state via non-radiative pathways. A quencher (Q), like oxygen ($^3O_2$), with energy levels near that of the excited state of the metal center, provides an alterative pathway of relaxation to the ground state. Oxygen in particular is a good quencher of triplet MLCT excited states due to the spin-allowed energy transfer to its triplet symmetry ground state. Upon energy transfer to the quencher, the remaining energy of the metal complex excited state decays to the ground state and the quencher is now in its excited state Q^* ($^1O_2$). Q^* decays back to the ground state independent of the metal complex decay. From this scheme one can see how the phosphorescent emission is decreased with increases in oxygen concentration.

$$A + h\nu \longrightarrow {}^1A^* \tag{1}$$

$${}^1A^* \xrightarrow{k_{isc}} {}^3A^* \tag{2}$$

$${}^3A^* \xrightarrow{k_r} A + h\nu \tag{3}$$

$${}^3A^* \xrightarrow{k_{nr}} A + \Delta \tag{4}$$

$${}^3A^* + Q \xrightarrow{k_q[Q]} A + Q^* \tag{5}$$

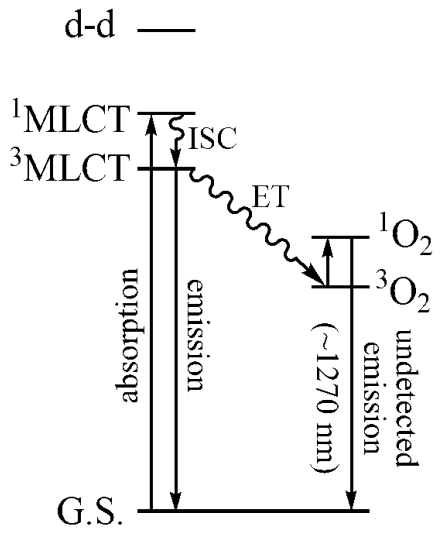

Figure 1. Energy diagram showing the processes involved in quenching of MLCT emission by molecular oxygen, ISC = intersystem crossing, ET = energy transfer.

The use of fiber-optic sensors allows for accurate quantification of the amount of molecular oxygen present in a system as they operate based on the decrease in the luminescence intensity and lifetime as a function of the oxygen concentration. In an ideal homogeneous system with single-exponential lifetime decays this behavior can be described by the Stern-Volmer equation:

$$\frac{I_0}{I} = \frac{\tau_0}{\tau} = 1 + K_{SV}[Q] \tag{6}$$

$$K_{SV} = \frac{k_q}{k_r + k_{nr}} = k_q \tau \tag{7}$$

where I_0 is the emission intensity with no quencher present, I is the emission intensity with some concentration of quencher present, τ_0 is the emission lifetime with no quencher present, τ is the emission lifetime with some concentration of quencher present, K_{SV} is the Stern-Volmer quenching constant, and $[Q]$ is the concentration of quencher present.

Sensors based on these straightforward kinetics are highly desirable compared to those based on electrochemical detection.

Sensors based on the $Ru(bpy)_3^{2+}$ (bpy = 2,2'-bipyridine) lumophore that undergo efficient quenching via energy transfer to produce singlet oxygen have been commercialized[37] for dissolved oxygen (DO) measurements in aqueous solutions. The $Ru(bpy)_3^{2+}$ ion can also be used as a solid-state sensor by adsorption to the large internal surface areas of zeolitic materials[35] to give composites that allow nearly "solution-like" diffusional oxygen quenching. DO measurements with these systems are complicated by matrix effects: the nanoscopic surroundings of each emissive molecule may vary resulting in multiple sites that are quenched to differing extents[7] and by decomposition reactions initiated by the high-energy singlet oxygen produced in the quenching events.[38] These heterogeneous systems result in complicated response and non-linear Stern-Volmer kinetics. Elimination of the need to encapsulate the luminescent species to allow oxygen diffusion could remove the non-linear response observed with previously examined fiber-optic oxygen sensors and allow for more straightforward data analysis.

Our recent work with vapochromic complexes[39-41] suggested that DO measurements could be improved if oxygen molecules could diffuse in and out of a nanoporous crystalline lumophore with a significant fraction of void space. Crystal structures do not typically contain solvent-accessible voids larger than 25 $Å^3$.[42] Often, when present, void space is not well controlled, resulting only from the solvent of crystallization leaving the lattice without disrupting the crystal structure. Two known strategies for generation of void space via control of crystal packing exist: (1) using the shape of the molecular building blocks to dictate the morphology,[43] and (2) using

directional interactions between molecules to induce specific intermolecular interactions which control the pattern of association.[43] Through the combination of propeller-shaped cations with a propeller-shaped anion containing large, bulky trifluoromethyl substituents, we attempt control of molecular packing and subsequent void space.[44] Through the $tfpb^-$ salt of $Ru(phen)_3^{2+}$ as well as several more common anions (PF_6^-, BF_4^-, ClO_4^-) we have investigated the effect of the molecular building block shape on the resultant void space in crystalline solids.

The use of porous crystalline materials offers several advantages over typically used polymer matrices. The crystallographically imposed site symmetry contrasts the multiple sites present in amorphous matrices, a distinct advantage for studies of the quenching processes. Single crystal studies could even be envisioned. The careful design of crystalline matrices (i.e., incorporation of inert fluorous phases[9]) could also mitigate decomposition modes and increase the solubility and perhaps the diffusivity of oxygen molecules in crystals of this type.

Experimental

General Considerations. The following chemicals were purchased as indicated: $[Ru(phen)_3]Cl_2 \cdot x\ H_2O$, $[Ru(bpy)_3]Cl_2 \cdot 6\ H_2O$ (bpy = 2,2'-bipyridine; phen = 1,10-phenanthroline) and $NaBF_4$ from Aldrich Chemical Co.; $NaClO_4$ from Fisher Scientific, NH_4PF_6 from Alfa; 4,7-Me_2Phen (4,7-Me_2Phen = 4,7-dimethyl-1,10-phenanthroline) from Pfaltz and Bauer; $K(B(C_6F_5)_4)$ ($B(C_6F_5)_4$ = tetrakis(pentafluorophenyl)borate) from Boulder Scientific. Na(tfpb) (tfpb = tetrakis (bis-3,5-trifluoromethylphenylborate)) was from a previous study.[45] $Ru(DMSO)_4Cl_2$ was synthesized by the method of Wilkinson et al.[46] $[Ru(4,7\text{-}Me_2Phen)_3]Cl_2$ was synthesized from $Ru(DMSO)_4Cl_2$ by the method of Elliot et al.[47, 48]

Synthesis and Characterization. Salts of the form $[Ru(pp)_3]X_2$ (pp = generic polypyridine ligand) were synthesized by metathesis reactions by adding a solution containing a slight stoichiometric excess of the anion salt to a solution of the $[Ru(pp)_3]Cl_2$ compound. After filtration, the $[Ru(pp)_3]X_2$ compound was purified to remove Ru(III) contaminants by chromatography and then crystallized by slow solvent evaporation. The solvents used for synthesis, chromatography and crystallization are given in Table 1. All compounds gave appropriate ^1H NMR spectra.

Table 1. Summary of solvents used for synthesis, purification, and crystallization.

Compound	Synthesis solvent	Chromatography solvent	Crystallization solvent
$[Ru(bpy)_3](PF_6)_2$	water	CH_2Cl_2/acetone	acetonitrile
$[Ru(bpy)_3](BF_4)_2$	water	CH_2Cl_2/acetone	hot water
$[Ru(bpy)_3](ClO_4)_2$	water	CH_2Cl_2/acetone	hot water
$[Ru(phen)_3](PF_6)_2$	water	CH_2Cl_2/acetone	ethanol
$[Ru(phen)_3](tfpb)_2$	methanol	CH_2Cl_2/acetone	acetonitrile
$[Ru(phen)_3](B(C_6F_5)_4)_2$	acetonitrile/ methanol	diethyl ether	diethyl ether/ methanol
$[Ru(4,7\text{-}Me_2Phen)_3](tfpb)_2$	methanol	diethyl ether	acetonitrile

Single Crystal X-ray Crystallography. The crystal structures of four compounds ($[Ru(phen)_3](tfpb)_2$, $[Ru(phen)_3](B(C_6F_5)_4)_2$, $[Ru(4,7\text{-}Me_2Phen)_3](tfpb)_2$ and $[Ru(bpy)_3](BF_4)_2$) were determined for this study. Relevant crystallographic data are shown in Tables 2 and 3. All crystals were grown by slow evaporation of saturated solutions. All the data for these structure determinations were collected at the X-ray Crystallographic Laboratory (Department of Chemistry, University of Minnesota). Single crystals were attached to glass fibers and mounted on a Bruker SMART Platform CCD ($tfpb^-$ structures) or Siemens SMART Platform CCD ($B(C_6F_5)_4^-$ and BF_4^- structures) for data collection at 100 K ($tfpb^-$ structures) or 173 K ($B(C_6F_5)_4^-$ and BF_4^- structures) using graphite-monochromated Mo Kα radiation (λ = 0.71073 Å). An initial set of cell constants was calculated from reflections harvested from three sets of 20 frames oriented such that orthogonal wedges of reciprocal space were surveyed. Final cell constants were calculated from a minimum set of 3569 strong reflections from the actual data collection. Data were collected to the extent of 1.5–2.0 hemispheres at a resolution of 0.77 Å ($[Ru(phen)_3](tfpb)_2$ and $[Ru(phen)_3](B(C_6F_5)_4)_2$) or 0.84 Å ($[Ru(4,7\text{-}Me_2Phen)_3](tfpb)_2$ and $[Ru(bpy)_3](BF_4)_2$) using ϕ-scans. For all structures, the intensity data were corrected for absorption and decay using SADABS.[49, 50]

Space groups were determined based on systematic absences and intensity statistics. The structures were determined by Patterson or direct-methods solutions. Several full-matrix least-squares/difference Fourier cycles were performed to locate remaining non-hydrogen atoms. All calculations were performed using the SHELXTL-V6.12 suite of programs on Pentium computers.[51] Crystallographic data were also obtained from the Cambridge Structural Database (CSD) for three additional compounds

tested for oxygen sensing: $[Ru(bpy)_3](ClO_4)_2$, $[Ru(bpy)_3](PF_6)_2$ and $[Ru(phen)_3](PF_6)_2$ with CCDC codes HEGMIP, BPYRUF and ZUZSIW, respectively. Packing analysis parameters were measured using PLATON/VOID[52, 53], with more detailed analysis of the void spaces performed with PLATON/CAVITY. Pictorial representations of the solvent channels were done with edited .res files in Mercury.[54] The detection of solvent accessible voids by PLATON/VOID[52, 53] is done in the following way: The unit cell is filled with the atoms from the structural model and each specific atom is assigned its respective van der Waals radius. A grid search generates a list of grid points with a minimum distance of 1.2 Å from the nearest van der Waals surface. This list of grid points is then used to produce a new list of grid points that makes up the solvent accessible areas. For the sets of grid points, the center of gravity and volume of the void are calculated, along with the overall solvent accessible volume.

All of the compounds used in the oxygen sensing studies are stable in air and crystallize without solvent molecules in the lattice with the exception of $[Ru(bpy)_3](BF_4)_2$. In this case, a small amount of electron density, that could not be modeled, remained after refinement. Additional information concerning the residual electron density was obtained with PLATON/SQUEEZE.[52, 53] The void space consists of 67 electrons/cell (about 8 water molecules) amounting to ½ of a water molecule per ruthenium, which in our studies, we speculate is lost without loss of crystallinity. The original data were corrected for the disordered solvent. Crystallographic and physical measurement information relevant to oxygen sensing (*vide infra*) is given in Table 4.

Table 2. Crystallographic data for $[Ru(phen)_3](tfpb)_2$ and $[Ru(phen)_3](B(C_6F_5)_4)_2$.

Compound	**$[Ru(phen)_3](tfpb)_2$**	**$[Ru(phen)_3](B(C_6F_5)_4)_2$**
empirical formula	$C_{100}\ H_{48}\ B_2\ F_{48}\ N_6\ Ru$	$C_{84}\ H_{24}\ B_2\ F_{40}\ N_6\ Ru$
crystal color, morphology	orange, block	red-orange, needle
crystal system	Monoclinic	Tetragonal
space group	$C2/c$	$P4_1$
a, Å	30.846(2)	12.8314(6)
b, Å	14.9030(10)	12.8314(6)
c, Å	24.2010(16)	44.695(4)
α, deg	90	90
β, deg	119.4360(10)	90
γ, deg	90	90
volume, Å^3	9688.9(11)	7358.9(8)
Z	4	4
formula weight, g mol^{-1}	2368.13	1999.78
density (calculated), g cm^{-3}	1.623	1.805
temperature, K	100(2)	173(2)
Absorption coefficient, mm^{-1}	0.306	0.370
$F(000)$	4704	3936
θ range, deg	1.52 to 27.52	1.59 to 27.52
index ranges	$-40 \le h \le 40$	$-16 \le h \le 16$
	$-19 \le k \le 19$	$-16 \le k \le 16$
	$-31 \le l \le 31$	$-57 \le l \le 57$
reflections collected	57467	87407
independent reflections	11134 (R_{int} = 0.0400)	16927 (R_{int} = 0.0610)
weighting factors,[a] *a,b*	0.0609, 39.4382	0.0366, 7.6582
max, min transmission	0.950000, 0.843863	0.940000, 0.848191
Data/restraints/parameters	11134/36/701	16927/1/1198
R_1, wR_2 [$I > 2\sigma(I)$]	0.0469, 0.1198	0.0570, 0.1040
R_1, wR_2 (all data)	0.0567, 0.1290	0.0709, 0.1083
GOF	1.028	1.104
largest diff. peak, hole, eÅ^{-3}	1.475, -1.222	0.571, -0.666

[a] $w = [\sigma^2(F_o^2) + (aP)^2 + (bP)]^{-1}$, where $P = (F_o^2 + 2F_c^2)/3$.

Table 3. Crystallographic data for $[Ru(4,7\text{-}Me_2Phen)_3](tfpb)_2$ and $[Ru(bpy)_3](BF_4)_2$.

Compound	**$[Ru(4,7\text{-}Me_2Phen)_3](tfpb)_2$**	**$[Ru(bpy)_3](BF_4)_2$**
empirical formula	$C_{106}\ H_{60}\ B_2\ F_{48}\ N_6\ Ru$	$C_{30}\ H_{24}\ B_2\ F_8\ N_6\ Ru$
crystal color, morphology	orange, prism	orange, needle
crystal system	Monoclinic	Orthorhombic
space group	*C*2/*c*	*Fdd*2
a, Å	31.074(2)	22.196(5)
b, Å	15.3490(13)	42.772(9)
c, Å	24.411(2)	13.683(3)
α, deg	90	90
β, deg	116.6150(10)	90
γ, deg	90	90
volume, $Å^3$	10409.2(14)	12991(5)
Z	4	16
formula weight, g mol^{-1}	2452.29	743.24
density (calculated), g cm^{-3}	1.565	1.520
temperature, K	100(2)	173(2)
Absorption coefficient, mm^{-1}	0.288	0.560
F(000)	4896	5952
θ range, deg	1.47 to 25.05	1.81 to 25.16
index ranges	$-36 \le h \le 36$	$-26 \le h \le 26$
	$-18 \le k \le 18$	$-50 \le k \le 50$
	$-29 \le l \le 29$	$-16 \le l \le 16$
reflections collected	49908	28807
independent reflections	9210 (R_{int} = 0.0395)	5745 (R_{int} = 0.1112)
weighting factors,[a] *a,b*	0.0582, 45.6846	0.1521, 171.0695
max, min transmission	0.9314, 0.8873	0.980000, 0.800014
Data/restraints/parameters	9210/0/748	5745/475/517
R_1, wR_2 [$I > 2\sigma(I)$]	0.0608, 0.1368	0.0912, 0.2428
R_1, wR_2 (all data)	0.0705, 0.1420	0.1067, 0.2531
GOF	1.148	1.075
largest diff. peak, hole, e$Å^{-3}$	1.512, -0.494	0.913, -0.986

[a] $w = [\sigma^2(F_o^2) + (aP)^2 + (bP)]^{-1}$, where $P = (F_o^2 + 2F_c^2)/3$.

Solid-state quantum yields and oxygen sensing screening. Solid-state quantum yields of the compounds listed in Table 4 (*vide infra*) were obtained by a modification of the method described by Wrighton et al.[55] The diffuse reflectance is captured from a "perfectly" scattering surface to give (after integration and correction for instrument response) a quantity proportional to the incident light intensity (I_0, units of photons/wavenumber). The scatterer is then replaced with the sample and the emission from the sample (I_{emit}, the emitted light) and the remaining scattered intensity from the light source (I, the reduced light source intensity) are captured and corrected. These two measurements allow the solid-state emission quantum yield to be calculated from:

$$\phi = \frac{I_{emit}}{I_0 - I} \tag{8}$$

Photographs of our apparatus are shown below (Figure 2). A bifurcated (six around one) fiber optic probe with an angle tip was used to bring light into and out of the sample. An Ocean Optics CCD spectrophotometer that was calibrated with a standard light source was used to capture the light intensities. The raw intensity values at each wavelength were multiplied by the appropriate correction factor as determined with the standard lamp and then by λ^3 so that the resulting intensity units are proportional to photons/wavenumber.[56] For the studies presented here, we have decreased a major source of error in Wrighton's method by replacing the powdered MgO scatterer (which has a surface that is very difficult to reproduce) with a 1×1 cm piece of Fluorilon[57] scattering target. The Fluorilon target is a NIST standard of fused powdered Teflon with a greater than 99% scattering coefficient across the entire spectral region of interest (350–1000 nm).[57] The surface can be sanded to a reproducible scatter with simple 240 grit

sand paper and reused.[57] The procedure consists of measuring the diffuse reflectance of the Fluorilon target followed by rubbing the freshly grown crystals of interest into the pores of the target with a metal spatula. The light (unabsorbed excitation beam and emission) from the target with the sample embedded in the surface is then collected and the necessary calculations are carried out with an Excel spreadsheet. Samples that are not sensitive to the environment (i.e. air or water) give highly reproducible spectra under ambient conditions. Although we have found that $[(n\text{-}C_2H_5)_4N]MnBr_4$ and especially $[(n\text{-}C_2H_5)_4N]MnCl_4$ (originally suggested as quantum yield standards[55]) can sometimes give values close to those reported by Wrighton, they are actually very sensitive to humidity and are unacceptable as standards. Reproducible results are only obtained by carefully controlling the atmosphere at the surface of the scattering sample by blowing dry gas across the surface. The dry oxygen/nitrogen mixtures used for our studies were produced with two calibrated rotameters (one for oxygen, a second for nitrogen) or for some experiments, with a set of mass-flow control valves under computer control. A representative set of the data required for a quantum yield determination is shown in Figure 3 for $[Ru(phen)_3](tfpb)_2$.

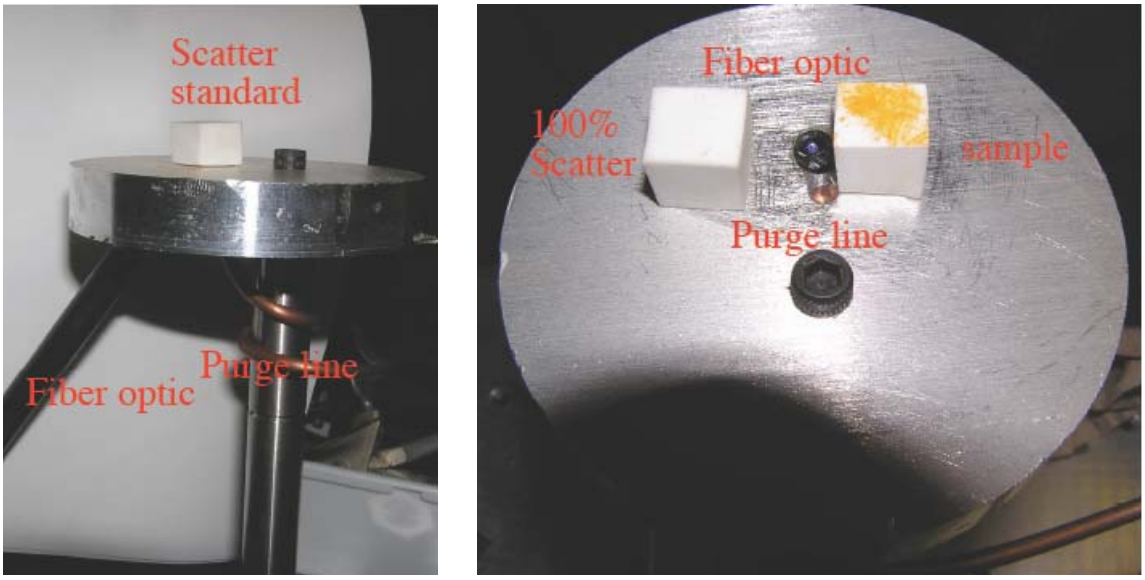

Figure 2. Two views of the solid-state emission quantum yield apparatus. Left: Side view of the table with the white 1×1 cm scattering standard in place. Fiber optic bundle comes in from bottom, left; copper tubing is the surface purge gas line. Right: Top view of the table showing the 100% scatter standard (left) and the sample (right); the fiber optic bundle and purge line come into the table from bottom.

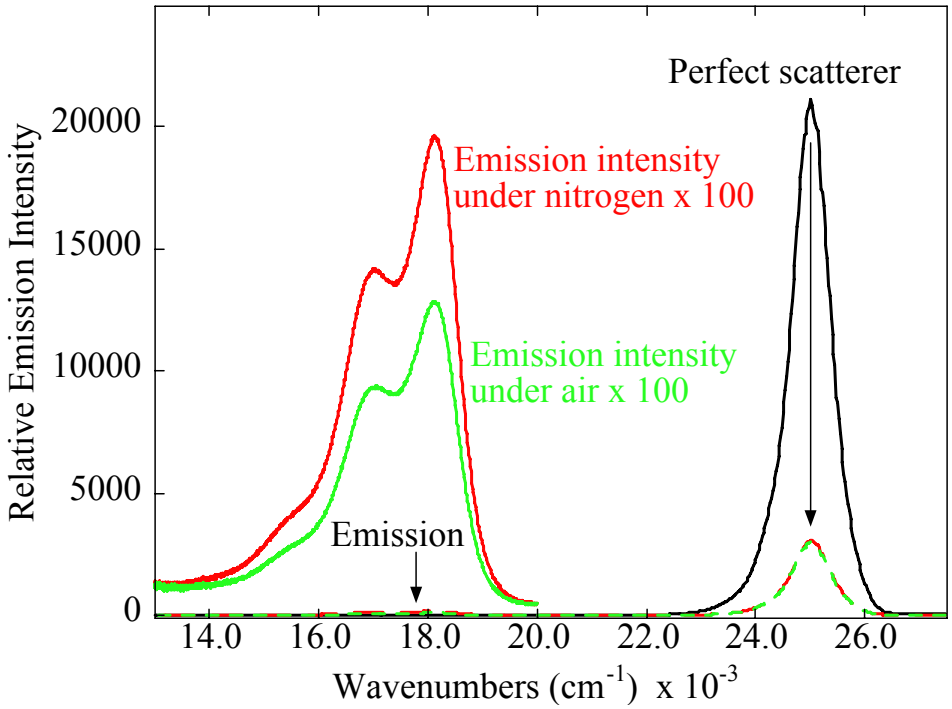

Figure 3. Sample data needed for a solid-state emission quantum yield measurement. Black curve is the scattered LED light from the Flourilon scatter target without the sample applied. The dashed red curve is the scatter and emission in a nitrogen atmosphere for the target with $[Ru(phen)_3](tfpb)_2$ micro crystals applied; the solid red line is a 100× blow up of the emission region between 20,000 and 13,500 cm^{-1}. The green curves are the responses of the target and sample under air. The arrow (at 25,000 cm^{-1}) indicates the decrease in the amount of the exciting light due to absorption by the sample. The quantum yield is the area under the emission spectrum divided by the difference in areas between the scatterer and the scatter from the sample.

Collection of Stern-Volmer emission intensity measurements. Data for the emission intensity Stern-Volmer plot were collected with the apparatus shown in Figure 4. All measurements were made at atmospheric pressure which was 736 Torr. A swage lock cross fitting was used as the cell. One port was used for a ¼ inch diameter delrin rod sample holder. The sample was coated by dissolving the metal complex in acetonitrile and then allowing the solution to slowly crystallize in place on the end of the rod. A photograph taken through a microscope of the actual sample used for many of the measurements made in this study is shown in Figure 5.

A second port (in the 180 degree position relative to the sample to allow front face illumination) was used for a bifurcated (six around one fiber) fiber optic probe. Two other ports were used for gas inlets and outlets. The atmosphere in the cell was controlled as per above (mass-flow controlled valves under computer control). Light from an LED was sent into the cell through one leg of the fiber optic probe to illuminate the sample on the end of the delrin rod. Emitted light was returned through the other leg into an Ocean Optics CCD spectrophotometer.

The emission spectra were integrated and I_o/I (I_o is defined as the integrated intensity for the emission spectrum from the sample under pure nitrogen) was calculated for each oxygen mole fraction measured. At least three replicates were used for each point plotted, collected in a "stair case" fashion with respect to oxygen concentration.

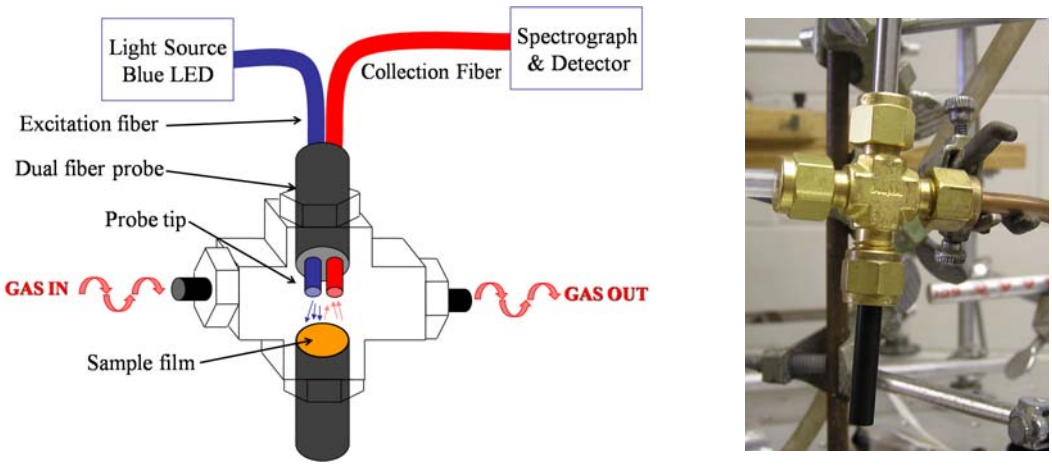

Figure 4. Schematic of swage lock cross cell (left) and actual cell used for emission intensity measurements (right).

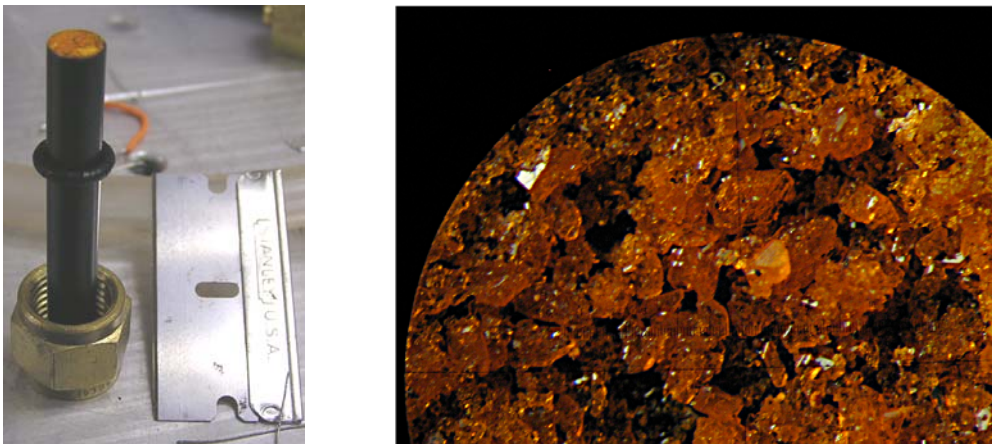

Figure 5. Delrin rod with microcrystalline $[Ru(phen)_3](tfpb)_2$ (left) and photograph of $[Ru(phen)_3](tfpb)_2$ micro crystals at 50× on the end of the ¼ in diameter delrin rod sample holder.

Solid state emission lifetime measurements. Solid state lifetime measurements were made using a swage lock cross cell identical to the one described above for intensity measurements. In this case, a pulsed LED light source (vide infra) was used for excitation. The emitted light (collected through the second fiber optic leg) was filtered (Kodak #8 Wratten) to remove the remaining LED exciting light and then directed to a Hamamatzu R928 PMT run at 1250 V using the last 5 dynodes. The PMT detection circuitry was designed by J. C. Scaiano[58] for high momentary currents with fast response times. The time response of this system was better than 1 ns. The PMT signal was amplified (10x) by a CLC 100 video amplifier and read by a sampling digital oscilloscope (Phillips PM 3323). The oscilloscope was triggered by a logic pulse produced by the LED light source.

The LED light source was constructed in house. It consists of a computer clock, counter, and pulse length generator logic circuit that switches a MIC4422YN MOSFET gate driver which in turn switches a ZVN2110A FET capable of 8 A currents at 100 V with approximately 5 ns on/off times. When the FET was on, current from a charged 100 μF capacitor was allowed to flow through the LED (λ_{ex} = 405 nm[59]). This system allowed variable duty cycle (500 to 4000 Hz) square-wave current pulses of 0–5 A with variable pulse widths (5 ns – 5 μs) to be produced. The current through the LED was monitored as a voltage drop across an in-series 1 ohm resistor; the total impedance of the LED and 1 ohm resistor was approximately 17 ohms. Pulsed operation of the LED produced, in addition to the 405 nm light needed for excitation, a long lived component[59] (centered at λ_{max} = 550 nm) that was removed by passing the LED light through a filter[60]. The filtered light pulses were focused on to the end of the fiber optic inlet leg with a

sapphire ball lens.[61] The two resulting oscilloscope traces (current input pulse and emission intensity rise and decay) were the average of 64 traces, where each trace resulted from many LED light pulses (as per typical sampling oscilloscope methodology). Typically ten of these signals were collected for a given oxygen concentration and further averaged in Microsoft Excel. The weighted plots ($w_i = 1/\sigma_i^2 = I(t)^2$) of ln($I$) vs t were fit to single-exponential decays using the Solver in Excel.

Emission intensity pressure jump measurements. The same swage lock cross cell as described above was used for these experiments. In this case, the input gas stream was from a compressed air tank and the pressure inside the cell was controlled with a manual ball valve at the outlet of the cell. After pressurization, the system was tested to be leak free with the inlet and outlet valves closed. The time constant for pressure leaking out of the cell back to 1 atm ambient was measured by pressurizing the cell to 2 atm, closing the inlet valve and then monitoring the rate of the pressure drop back to 1 atm with a computer interfaced pressure transducer[62] when the outlet valve was opened. The time constant was approximately 2 ms. A similar method was used to measure the time evolution of the emission spectrum except the OceanOptic spectrometer was used to collect emission spectra before and during the pressure release. Spectra could be collected to disk every 30 ms. The total emisson intensity for each spectrum was calculated and $I_{nitrogen}/I$ vs t was plotted for excitation with three different LEDs (400 nm, 470 nm and 518 nm). For a given LED, the results were very reproducible for several identical pressure jumps.

Calibration of $[Ru(phen)_3](tfpb)_2$ for DO measurements. The end of the optical sampling ballprobe[63-65] was coated with a thin layer of $[Ru(phen)_3](tfpb)_2$ microcrystals by dipping it in an acetonitrile solution of $[Ru(phen)_3](tfpb)_2$ followed by evaporation (as shown in Figure 6). Thicker layers could be built up by repeating this procedure. The coated ballprobe was immersed into a cell with water along with the Ox probe Clark electrode (model number D200, Broadley James Corp, Irvine, CA) and the percentage of oxygen was controlled with a mass-flow control valve system. The membrane covered Clark electrode was used as a reference measurement to monitor the DO concentration in the sample cell. Before each experiment the DO probe was immersed in distilled water and bubbled with both oxygen and nitrogen to calibrate at 100% and 0% DO, respectively. Five replicates at each oxygen concentration, in random jumps between concentrations, were collected with both the oxygen sensor and the DO probe. Emission intensity data were collected for each replicate and were analyzed along with the simultaneous measurements from the Clark electrode with a partial least-squares (PLS) model using the program Unscrambler version 8.2 (CAMO, Oslo Norway). The PLS model was created using the emission spectral response to varying oxygen concentration between the wavelengths of 500 to 700 nm.[66] The dissolved oxygen concentrations used for developing the model were; 4, 15, 28, 38, 48, 58, 67, 80, 100, 103 percent DO in distilled water. The 103% DO number was the absolute saturation value achieved after one hour of continuous bubbling of oxygen into the sample cell measured with the Clark electrode. The value of 103% is a slightly elevated artifact, not an absolute concentration number due to a calibration discrepancy of the Clark DO probe.

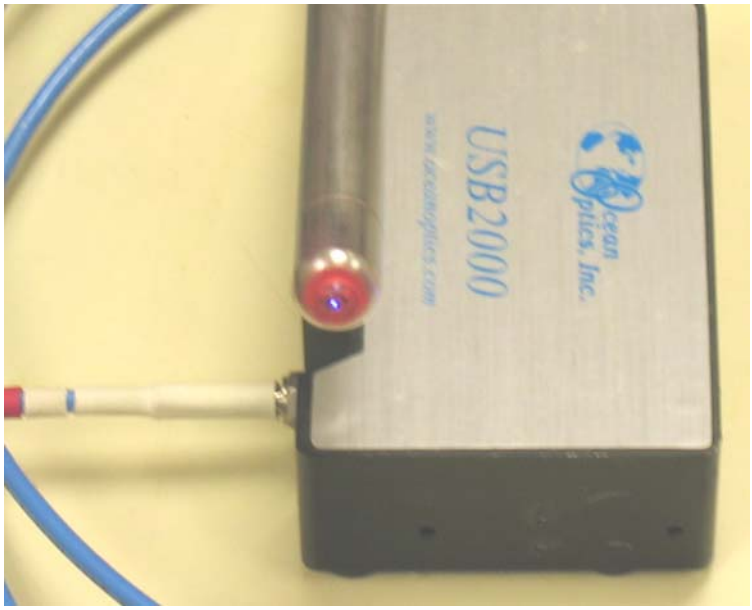

Figure 6. A view of the ballprobe coated with a sensor compound.

Results and Discussion.

Photophysical Studies.

Emission Intensity Quenching Studies.

To examine our theories about the use of bulky counterions as a means of producing void space in crystalline solids and its effect on the diffusion of molecular oxgyen, we screened several simple salts of $Ru(bpy)_3^{2+}$ and $Ru(phen)_3^{2+}$ and three substituted tetraphenylborate salts for solid-state emission quenching by air. Freshly grown crystals were pressed into the surface of a "perfect scatter" Fluorolon target and the absolute emission quantum yield[8] (λ_{ex} = 400 nm) was measured under nitrogen and in air. As expected, all of the compounds emit in the solid state, but surprisingly, even the simple salts (ClO_4^-, PF_6^-, and BF_4^-) showed some emission quenching in air relative to nitrogen; two of the substituted tetraphenylborate salts showed much better behavior.

Table 4. Free volume, quantum yield and oxygen sensing screening.

	Space Group, Z	Cell volume (Å^3)	Free volume (Å^3)	Free volume fraction	$\phi_{nitrogen}$	$\frac{\Delta\phi}{\phi_0}$
$[Ru(bpy)_3](ClO_4)_2$	*C*2/*c*, 4	3021.30	0.0	0.000	0.066(2)	0.0320(2)
$[Ru(bpy)_3](BF_4)_2$	*Fdd*2, 16	12991.00	333.7	0.026	0.14(2)	0.170(2)
$[Ru(bpy)_3](PF_6)_2$	$P\bar{3}c1$, 2	1643.50	14.7	0.009	0.029(2)	0.0620(2)
$[Ru(phen)_3](PF_6)_2$	*C*2/*c*, 8	7074.00	57.9	0.008	0.045(2)	0.0616(2)
$[Ru(phen)_3](tfpb)_2$	*C*2/*c*, 4	9688.90	543.7	0.056	0.071(2)	0.354(2)
$[Ru(4,7\text{-}Me_2Phen)_3](tfpb)_2$	*C*2/*c*, 4	10409.00	693.3	0.067	0.11(2)	0.466(2)
$[Ru(phen)_3](B(C_6F_5)_4)_2$	$P4_1$, 4	7358.90	29.1	0.004	0.075(2)	0.0467(2)

This behavior is quantified using the following relationship, where $\Delta\phi/\phi_0$ represents the fraction of integrated emission quenched in the presence of air:

$$\frac{\Delta\phi}{\phi_0} = \frac{\phi_{nitrogen} - \phi_{air}}{\phi_{nitogen}} = 1 - \frac{\phi_{air}}{\phi_{nitogen}} \qquad (9)$$

where $\phi_{air}/\phi_{nitrogen}$ is also the ratio of the integrated emission intensities under air and nitrogen. Values for $\phi_{nitrogen}$ and $\Delta\phi/\phi_0$ are given in Table 3 along with the fraction of void space calculated from crystallographic data.

These salts show (Figure 7) a monotonic increase in the fraction quenched, $\Delta\phi/\phi_0$ (defined as: $1-(\phi_{air}/\phi_{nitrogen})$) with the fraction of void space calculated from X-ray structural data. This suggests that void space is important for oxygen quenching in these systems, particularly in the case of $[Ru(pp)_3](tfpb)_2$ salts like $[Ru(phen)_3](tfpb)_2$ where the channels (Figure 8) could allow oxygen molecules to freely move in the crystals.

The quenching process(es) in $[Ru(phen)_3](tfpb)_2$ was examined further. A gas mixing apparatus constructed with mass-flow control valves was used to produce specific concentrations of oxygen in nitrogen at ~1 atm. Emission intensity data for microcrystalline $[Ru(phen)_3](tfpb)_2$ were collected and are examined according to the Stern-Volmer relationship:

$$\frac{I_0}{I} = 1 + K_{SV}[O_2] \tag{10}$$

where I_0 is the integrated intensity under nitrogen and I is the integrated intensity under varying concentrations of oxygen, $[O_2]$. These intensity data are displayed as a Stern-Volmer plot (I_0/I vs mole fraction of oxygen, ○ points) (Figure 9) with strictly linear (R^2 = 0.9996) behavior and a slope of 2.43. A second Stern-Volmer determination nearly a year later with the *same* sample but with a slightly different apparatus gave a slope of 2.41, identical within experimental error. Microscopic examination of the sample before and after the Stern-Volmer studies showed no apparent decomposition or change in crystallinity; long-term stability tests under continuous illumination in the presence or

absence of oxygen over a 24 h period showed no change in emission intensity. A second sample was used for many oxygen-sensing experiments for more than a year with no apparent change in responsivity.

Emission intensity data for microcrystalline $[Ru(4,7\text{-}Me_2Phen)_3](tfpb)_2$ were also collected and examined according to the Stern-Volmer relationship. These intensity data are displayed as a SV plot (I_0/I vs mole fraction of oxygen) (Figure 10) with linear (R^2 = 0.9987) behavior and a slope of 4.76. The improved performance of this crystalline salt towards detection of oxygen warrants further investigation.

The oxygen detection capabilities of the $[Ru(phen)_3](tfpb)_2$ and $[Ru(4,7\text{-}Me_2Phen)_3](tfpb)_2$ salts correlate with the amount of void space in the crystalline lattice as was previously discussed and is shown in Figure 7. The amount of void space in the crystalline lattices of these two salts can be compared pictorially in Figure 10 where the red spheres represent the volume of void space. The appreciable difference in the amount of void space present in these two crystalline solids is obvious from these views down the a- and c-axes. Crystals of $[Ru(phen)_3](tfpb)_2$ contain 5.6 % void space or 136 $Å^3$ per ruthenium while crystals of $[Ru(4,7\text{-}Me_2Phen)_3](tfpb)_2$ contain 6.7 % void space and 173 $Å^3$ per ruthenium. It is easy to imagine that the larger portion of void space present in crystals of $[Ru(4,7\text{-}Me_2Phen)_3](tfpb)_2$ could not only allow more oxygen to enter the crystal but also allow for facile diffusion of oxygen within the crystal resulting in the improved sensitivity of this salt towards oxygen (K_{sv} = 4.76) as compared with that of the unsubstituted version, $[Ru(phen)_3](tfpb)_2$ (K_{sv} = 2.43).

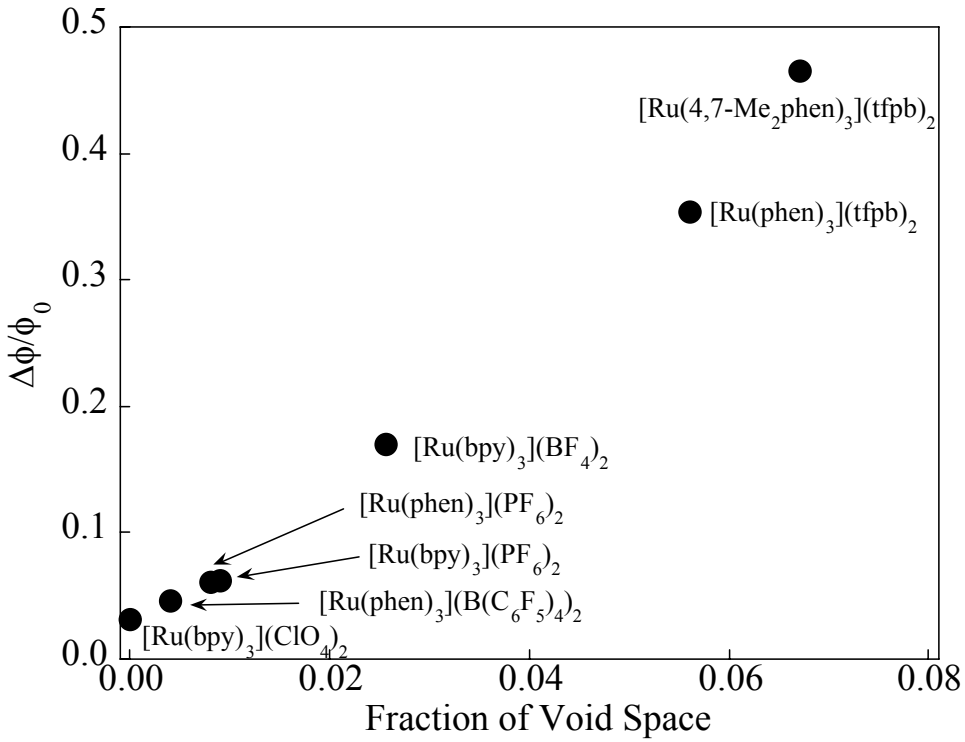

Figure 7. Graph of $\Delta\phi/\phi_0$ vs void space for some $Ru(pp)_3^{2+}$ salts.

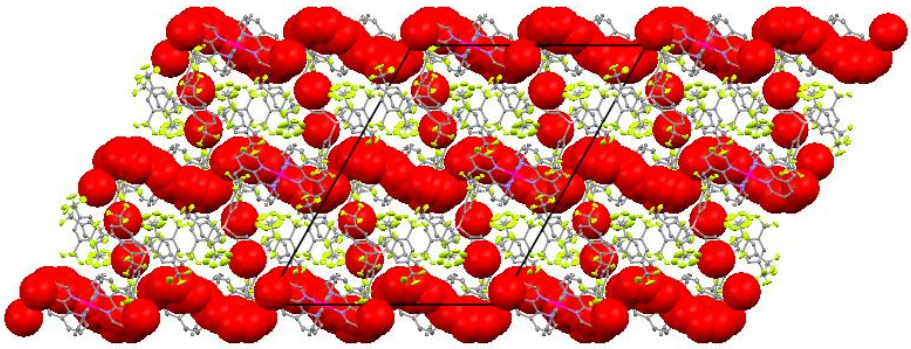

Figure 8. View down the b-axis of $[Ru(phen)_3](tfpb)_2$ showing alternating layers of cations and anions. The void space channels (red spheres, 136 $Å^3$ per Ru) run through the cationic layers. Hydrogen atoms are omitted for clarity.

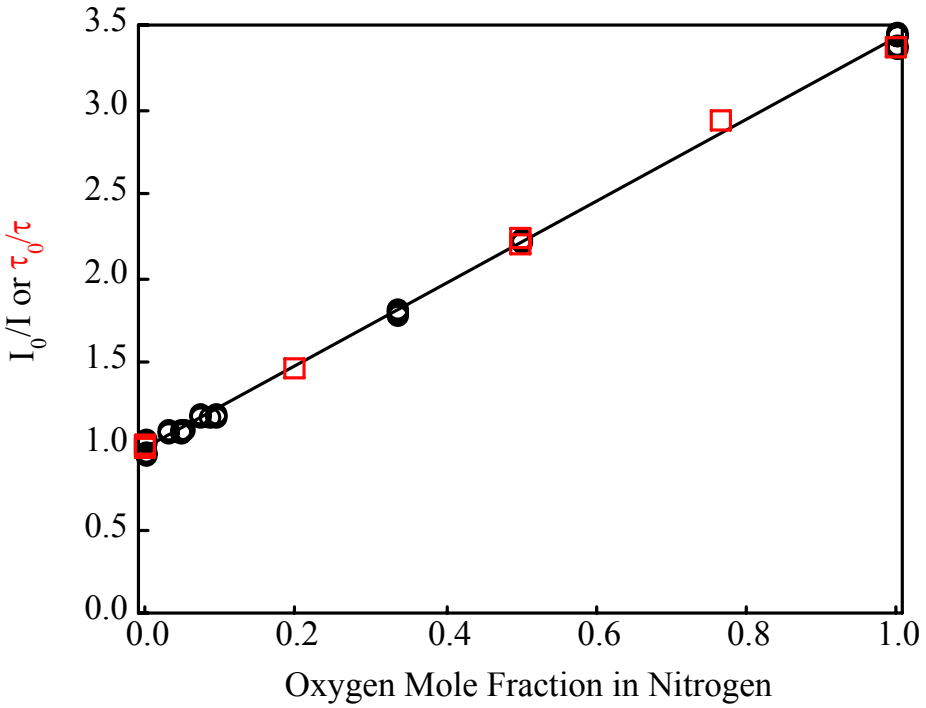

Figure 9. Stern-Volmer plot of I_0/I, (○) and τ_0/τ (□) vs oxygen mole fraction for $[Ru(phen)_3](tfpb)_2$.

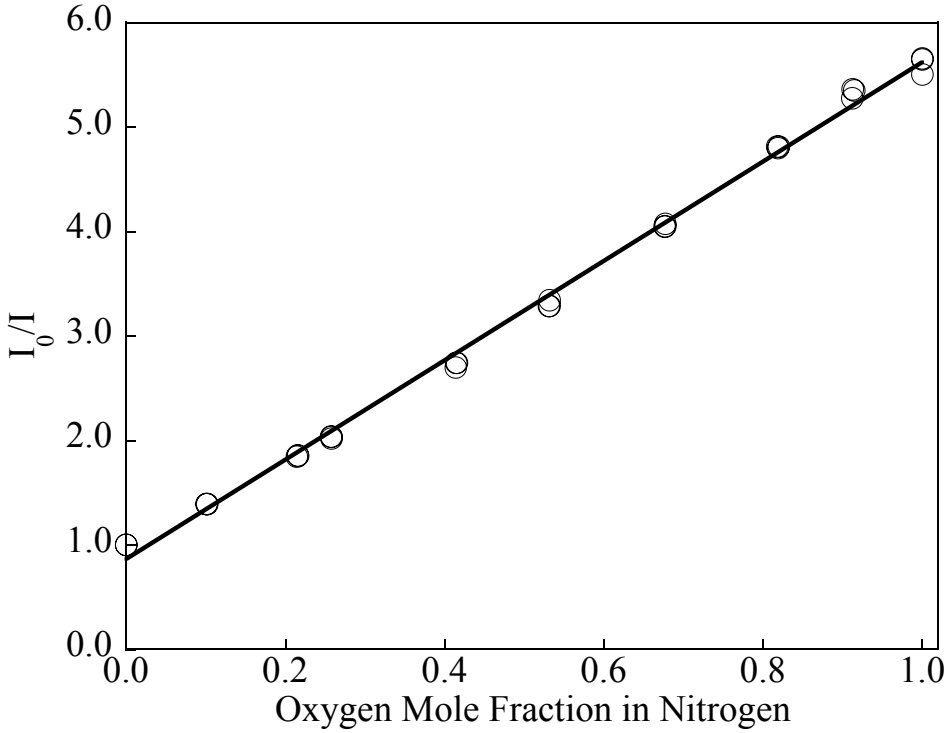

Figure 10. Stern-Volmer plot of I_0/I for $[Ru(4,7\text{-}Me_2Phen)_3](tfpb)_2$.

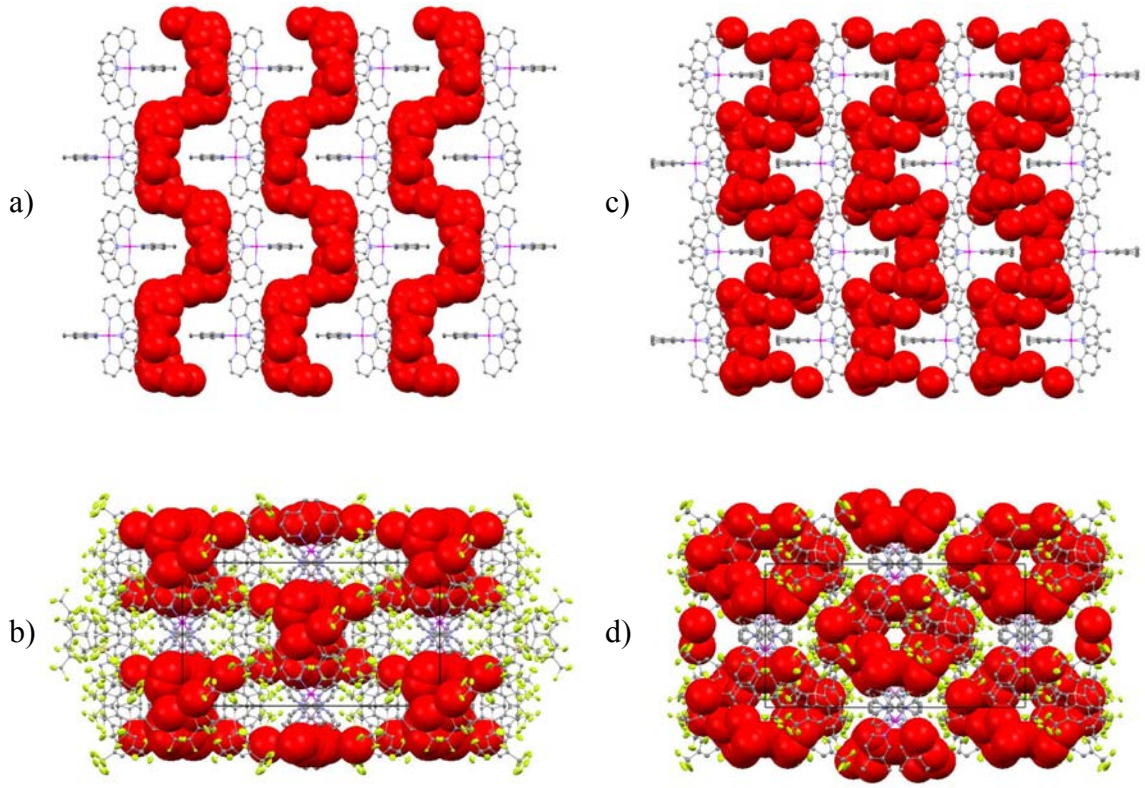

Figure 11. Packing diagrams of $[Ru(phen)_3](tfpb)_2$ (a and b) and $[Ru(4,7\text{-}Me_2Phen)_3](tfpb)_2$ (c and d) down the a-axis (top, a and c, cation layer only) and c-axis (bottom, b and d). Hydrogen atoms are omitted for clarity.

Support for Oxygen Diffusion

Solid state emission lifetime measurements.

Stern-Volmer quenching determined by emission intensity can (among other things) be a result of static quenching, diffusional quenching, or both. Stern-Volmer quenching by emission lifetime, on the other hand, does not exhibit a static component. Solid-state emission lifetime measurements of $[Ru(phen)_3](tfpb)_2$ show that the emission can be fit at all oxygen concentrations for at least 6 half-lives to a single-exponential decay (τ = 640 ns under pure nitrogen) that is significantly faster (τ = 190 ns) under pure oxygen. A typical current pulse and the resulting emission rise and decay are illustrated in Figure 12. The lifetimes (in nanoseconds) for different oxygen concentrations are: 640(4), 438(4), 289(4), 219(4) and 190(4) ns for oxygen mole fractions of 0, 0.2, 0.5, 0.77 and 1.00, respectively at an atmospheric pressure of 736 Torr. Plots of ln(I) vs t are shown for $[Ru(phen)_3](tfpb)_2$ under pure nitrogen and pure oxygen atmospheres in Figure 13.

The observation of a single-exponential decay suggests that identical emitting sites in one crystalline phase produce the emission and the oxygen concentration is uniform at least throughout the penetration depth of the light. The Stern-Volmer plot for these lifetime data (Figure 9, □) is linear and shows the same K_{sv} as the intensity data. The agreement in K_{sv} for the two techniques shows that the quenching is dynamic in nature.

Solid-state lifetime measurements were also completed for $[Ru(4,7\text{-}Me_2Phen)_3](tfpb)_2$ under nitrogen and oxygen. The emission decay of this solid was more complex than the single-exponential decay of $[Ru(phen)_3](tfpb)_2$ instead requiring

biexponential modeling. Emission decays that exhibit biexponential behavior result from two emitting species. Stern–Volmer treatment of this type of data is not straightforward. This will be further addressed in Appendices B and C, however, the preexponential weighted mean lifetime, $\tau_{M,}$ has been shown to give suitable expressions of the "average" lifetime allowing comparison of long pulse ($t_{pulse} >> \tau$) multiexponential lifetime data to intensity data.

$$\tau_M = \frac{\alpha_a \tau_a + \alpha_b \tau_b}{\alpha_a + \alpha_b} \tag{11}$$

In this expression τ_a and τ_b represent the emission lifetimes of the two different excited states. The preexponential factors, α_a and α_b, describe the contribution of each excited state to the signal at t=0 and depend on many factors. The expression $\alpha_a + \alpha_b$ is equal to one. The lifetime decays of $[Ru(4,7\text{-}Me_2Phen)_3](tfpb)_2$ were collected with 10 μs (nitrogen) and 2 μs (oxygen) pulse widths which as are significantly longer than the mean lifetimes at these oxygen concentrations. Plots of ln(I) vs t are shown for $[Ru(4,7\text{-}Me_2Phen)_3](tfpb)_2$ under pure nitrogen and pure oxygen atmospheres in Figure 14. Significant quenching of the excited is evident from the τ_M values for these biexponential decays, 1.893 μs for nitrogen and 0.318 μs for oxygen. Even though a full Stern-Volmer plot cannot be made due to the absence of other lifetime decays at intermediate oxygen concentrations, K_{SV} can be estimated by substituting the pure nitrogen and pure oxygen τ_M values into the one-site Stern-Volmer equation (Equation 6). Substituting these values into Equation 6 gives a lifetime-based K_{SV} of 4.95, in excellent agreement with the value of 4.76 for a full set of intensity data. Again, the agreement in K_{sv} for the two techniques shows that the quenching is dynamic in nature.

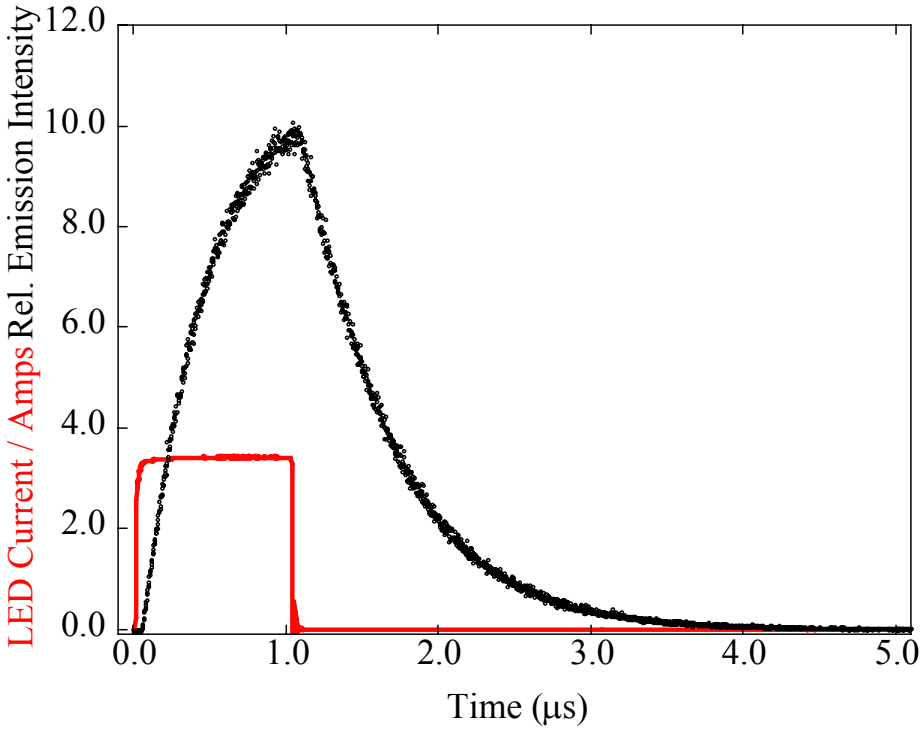

Figure 12. LED current pulse (red) and relative emission intensity (black) for $[Ru(bpy)_3]Cl_2$ dissolved in deoxygenated water.

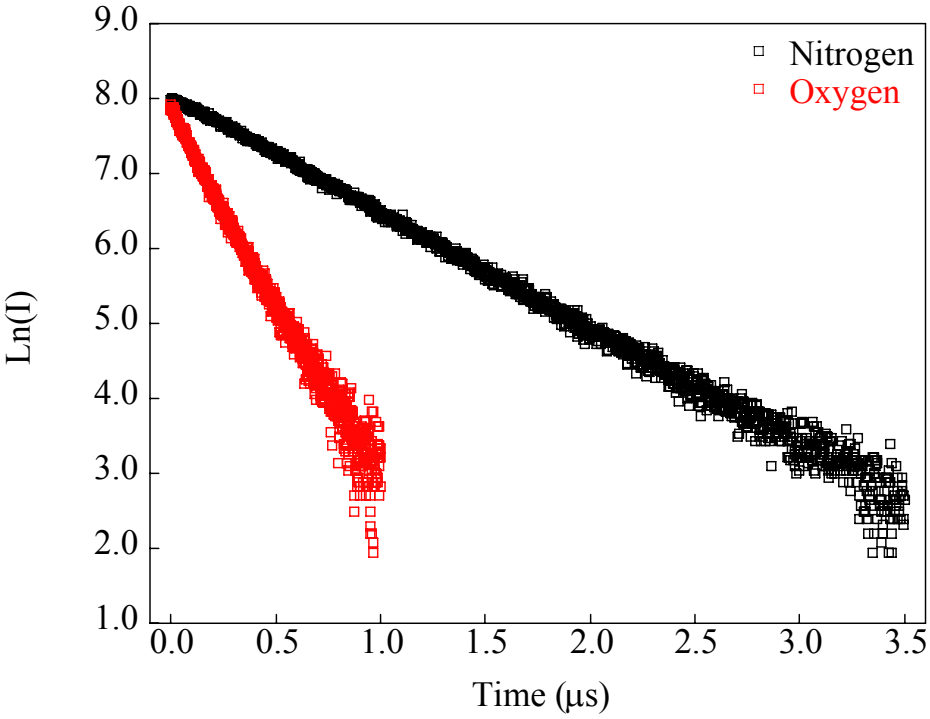

Figure 13. Plots of ln(emission intensity) for a microcrystalline sample of $[Ru(phen)_3](tfpb)_2$ under pure nitrogen (black points) and under pure oxygen (red points).

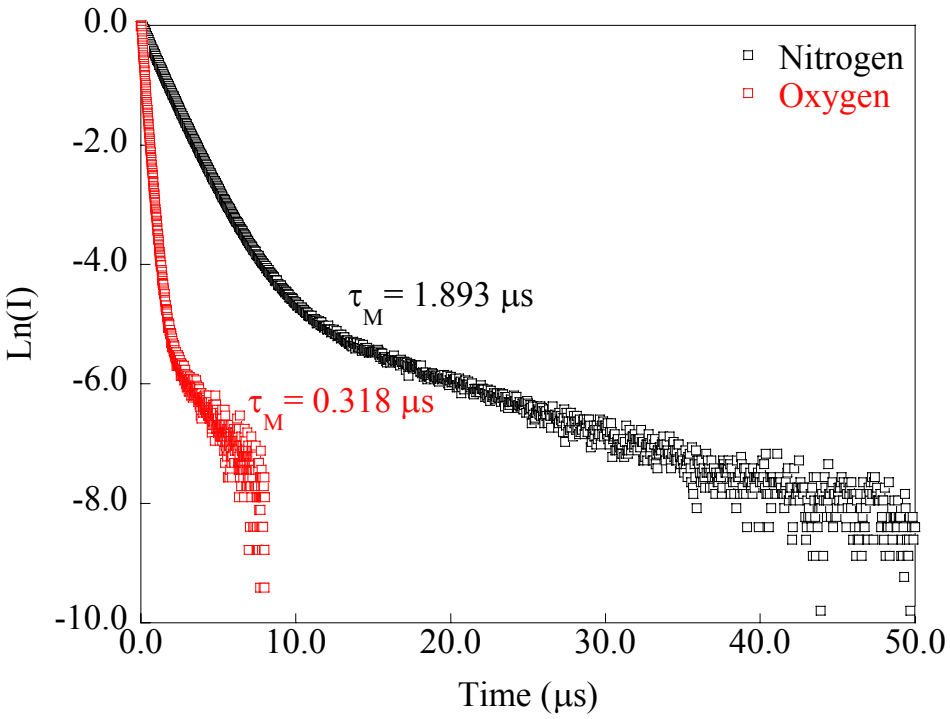

Figure 14. Plots of ln(emission intensity) for a microcrystalline sample of [Ru(4,7-Me_2Phen)$_3$](tfpb)$_2$ under pure nitrogen (black points) and under pure oxygen (red points). The decays fit the general equation $I(t) = \alpha_a \exp(-t/\tau_a) + \alpha_b \exp(-t/\tau_b)$. The decay under nitrogen is $I(t)$ = 0.985exp(-t/1.75 μs) + 0.015exp(-t/11.3 μs) while the curve under oxygen is $I(t)$ = 0.988exp(-t/0.298 μs) + 0.012exp(-t/2.49 μs). The long-lived excited state is present in a much smaller amount as compared to the shorter-lived excited state.

The emission lifetime, as well as other variables, of a complex can affect the oxygen sensitivity to a large extent. The intensity Stern-Volmer equation can be expressed more exhaustively by expanding K_{sv} into its composite terms:[67]

$$\frac{I_o}{I} = 1 + K_{sv}[O_2] = 1 + \tau_0 k_q [O_2] = 1 + \tau_0 f N_A 4\pi D_{O_2} (r_L + r_{O_2}) S_{O_2} p_{O_2} \qquad (12)$$

where constants in this equation are, f, a statistical factor incorporating the probability of oxygen reaching the emissive site and N_A, Avogadro's number. The variables in this equation are τ_0, the lifetime of the molecule in the absence of quencher; D_{O_2}, the oxygen diffusion constant; r_L and r_{O_2}, the encounter radii of oxygen and the lumiphore; S_{O_2}, the solubility coefficient of oxygen; and p_{O_2}, the partial pressure of oxygen. The quenching rate constant, k_q, equals $f N_A 4\pi D_{O_2} (r_L + r_{O_2})$ and the concentration of oxygen [O_2] in the solid equals $S_{O_2} p_{O_2}$. From this equation it is easy to see that changes in the amount of void space could have large effects on the oxygen diffusion coefficient, greatly influencing the k_q and subsequently the K_{SV}. The lifetime, as well, can change drastically with lumiphore, affecting K_{SV}. Applying these concepts, we can in a rudimentary manner, examine the reasons for the differences in the oxygen sensitivity of $[Ru(phen)_3](tfpb)_2$ and $[Ru(4,7\text{-}Me_2Phen)_3](tfpb)_2$. The question of the relative importance of the void space and the lifetime, where the lumiphore with the better *Ksv* ($[Ru(4,7\text{-}Me_2Phen)_3](tfpb)_2$) has larger values for both, is particularly interesting. Using the relationship for the Stern-Volmer constant, $K_{SV} = k_q \tau$, the pseudo-first-order rate constant for quenching can be calculated (Table 5).

Table 5. Compilation of Stern-Volmer parameters for $[Ru(phen)_3](tfpb)_2$ and $[Ru(4,7\text{-}Me_2Phen)_3](tfpb)_2$

	$[Ru(phen)_3](tfpb)_2$	**$[Ru(4,7\text{-}Me_2Phen)_3](tfpb)_2$**
τ_0[a] or τ_{M0}[b] (μs)	0.640[a]	1.89[b]
K_{SV}	2.43	4.95
k_q (s^{-1})[c]	3.8	2.6
Void space fraction	0.056	0.067

[a]microseconds, τ_0. [b]microseconds, τ_{0M}. [c]Rate constants do not have typical units of $L \cdot mol^{-1} \cdot s^{-1}$ (for $[O_2]$) or $Torr^{-1} \cdot s^{-1}$ (p_{O_2}) due to the use of mole fraction to express the concentration of oxygen.

The results shown here indicate that increases in emission lifetime may be more important than increases in void space. While $[Ru(phen)_3](tfpb)_2$ has a smaller K_{sv} with a shorter lifetime and less open space than that of $[Ru(4,7\text{-}Me_2Phen)_3](tfpb)_2$, it has a larger quenching rate constant, k_q. The better sensitivity towards oxygen of $[Ru(4,7\text{-}Me_2Phen)_3](tfpb)_2$ but smaller k_q indicates that increases in τ must be more important than increases in void space, or at the least that increases in void space do not always result in a straightforward proportional increase in K_{sv}. In this case, there is some effect that is limiting the diffusion of oxygen in the crystals (affecting k_q) and/or the solubility of oxygen (which is a component of $[O_2]$ that we have not taken into account) in $[Ru(4,7\text{-}Me_2Phen)_3](tfpb)_2$. Perhaps the oxygen could "stick" to the channel walls more in the $[Ru(4,7\text{-}Me_2Phen)_3](tfpb)_2$ structure, because of either flow inhibition due to channel shape or to enhanced association of oxygen to some portion of the molecule along the channel that results in a decreased diffusion coefficient. Conceivably the solubility of oxygen could also be lower in the less fluorous[68] $[Ru(4,7\text{-}Me_2Phen)_3](tfpb)_2$ salt compared with the more fluorous[68] $[Ru(phen)_3](tfpb)_2$ compound. In effect this examination of the quenching rate constant has at minimum shown that all void space may not be created equal and should lead to further examination of what factors most

influence the oxygen sensitivity of a crystalline compound. Studies of the lifetimes of other ruthenium salts, such as those whose correlation of oxygen sensitivity to void space was already examined in Figure 7, could shed more light on the importance the variable terms in Equation 12 and allow for more informed decisions regarding molecular design of crystalline oxygen sensors.

Validity of energy transfer via excitonic hopping of excited states

Previous studies[69] of solid-state emission from several $Ru(bpy)_3^{2+}$ salts that vary the Ru–Ru distance suggest that in simple salts (PF_6^-, ClO_4^-, Cl^-) excitonic hopping from one Ru site to another can occur. To further support oxygen diffusion, elimination of the mechanism of energy transfer to oxygen via excitonic hopping of the excited state to the surface of the crystals is necessary. An estimate for the hopping rate constant k_{hop} in $[Ru(phen)_3](tfpb)_2$ is calculated from the following equation:[69]

$$\ln k_{hop} = \ln k^0_{hop} - \beta(R - R_0) \tag{13}$$

where β, R, and k^0_{hop} are an attenuation factor, the center-to-center distance between ruthenium atoms in the crystal and the hopping rate constant at the van der Waals distance (R_0 = 6.1 Å), respectively. The parameters β = 45 nm^{-1} and k^0_{hop} = 6.8 x 10^{12} s^{-1} were evaluated previously from measurements made for $[Ru(bpy)_3](X)_2$ where X^- = Cl^-, ClO_4^-, and PF_6^-.[69] The value calculated for k_{hop} at the closest Ru–Ru distance (R = 12.349 Å) found in the $[Ru(phen)_3](tfpb)_2$ crystal is 4.2 s^{-1}. This value allows the excited state diffusion coefficient to be estimated from:

$$D = \frac{k_{hop} R^2}{2} \tag{14}$$

which gives for R = 12.349 Å and k_{hop} = 4.2 s^{-1} a D of 3.2 x 10^{-14} cm^2 s^{-1}. The average diffusion distance ($l_{diffusion}$) of an excited state during its lifetime (τ) is approximately:

$$l_{diffusion} = \sqrt{D\tau} \tag{15}$$

For the τ value of $[Ru(phen)_3](tfpb)_2$ in the crystal (640 ns) and D of 3.2 x 10^{-14} cm^2 s^{-1}, $l_{diffusion}$ is 0.014 Å. This result is consistent with essentially no excited state movement during its lifetime, so significant quenching by oxygen only at the illuminated surface or by excitonic hopping of the excited state to trapped oxygen molecules near the surface can be ruled out.[70] In conclusion, excitonic hopping of the excited state to trapped oxygen molecules is too slow ($D \approx 10^{-14}$ cm^2/s) to account for the quenching in solid $[Ru(phen)_3](tfpb)_2$. Our conjecture that oxygen molecules diffuse in and out of $[Ru(phen)_3](tfpb)_2$ crystals will be further supported by pressure jump experiments.

Emission intensity pressure jump measurements.

A crystalline sample of $[Ru(phen)_3](tfpb)_2$ was pressurized with air to about 2 atm in a pressure cell that allowed "front face" emission spectra to be acquired as a function of time. At time zero the pressure was allowed to escape ($t_{1/2}$ = 5 ms) back to 1 atm and the emission spectra as a function of time were acquired. Plots of $I_{nitrogen}/I$ vs t are shown in Figure 15. The time for ½ response, $t_{1/2}$ for 400 nm excitation is <20 ms and the characteristic shape of the $I_{nitrogen}/I$ vs t curve expected for a diffusional process is readily apparent (fast change at early times with a characteristic long tail at later times). The apparent diffusion time was increased (at 470 nm, $t_{1/2}$ = 120 ms; at 518 nm, $t_{1/2}$ = 2200 ms) by changing the excitation to longer wavelengths where the extinction coefficient is significantly smaller and the penetration depth of the light is greater. These measurements are consistent with an oxygen diffusion coefficient on the order of

10^{-7}–10^{-8} cm^2/s in the solid (see Appendix A). Further data analysis is planned to fit these curves to the characteristic functions previously used by Demas et al.[71] in their study of oxygen diffusion in polymer films.

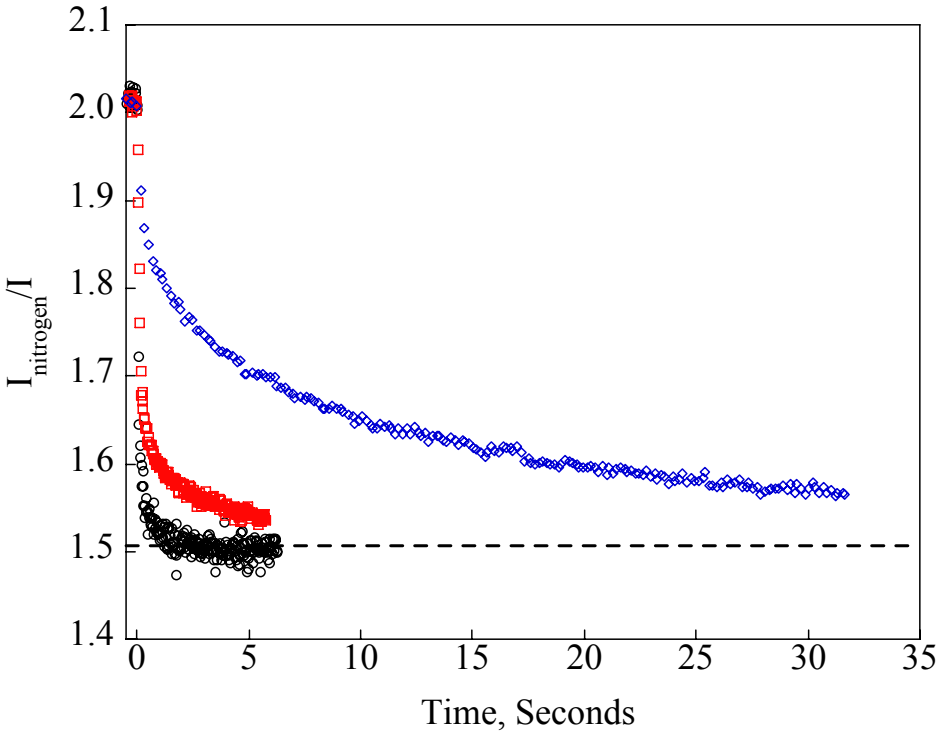

Figure 15. Plot of $I_{nitrogen}/I$ vs time for air pressure jump from 2 to 1 atmosphere. The ◊, □, and ○, points are 518, 470 and 400 nm excitation respectively; dashed line is the $I_{nitrogen}/I$ infinity value for all data.

Calibration of probe and DO measurements.

Dissolved oxygen (DO) sensing in aqueous media is an important application for oxygen sensing materials.[36] A fiber optically coupled ball probe with a thin film of crystalline $[Ru(phen)_3](tfpb)_2$ deposited on the end was immersed in water saturated with different oxygen/nitrogen mixtures. A partial least-squares (PLS) model with a single principle component calibrated against a Clark DO electrode is shown in Figure 16. After the ballprobe was calibrated, the ballprobe dissolved oxygen sensor agreed very well with the relative DO results indicating effective calibration. The successful calibration of this sensor against the Clark electrode could allow the use of this crystalline sensor in applications where the Clark electrode is currently employed or more importantly, in situations where the Clark electrode cannot be used. Future miniaturization of these crystalline oxygen sensors could be exceptionally useful, permitting detection of oxygen in settings that currently are devoid of an oxygen sensor.

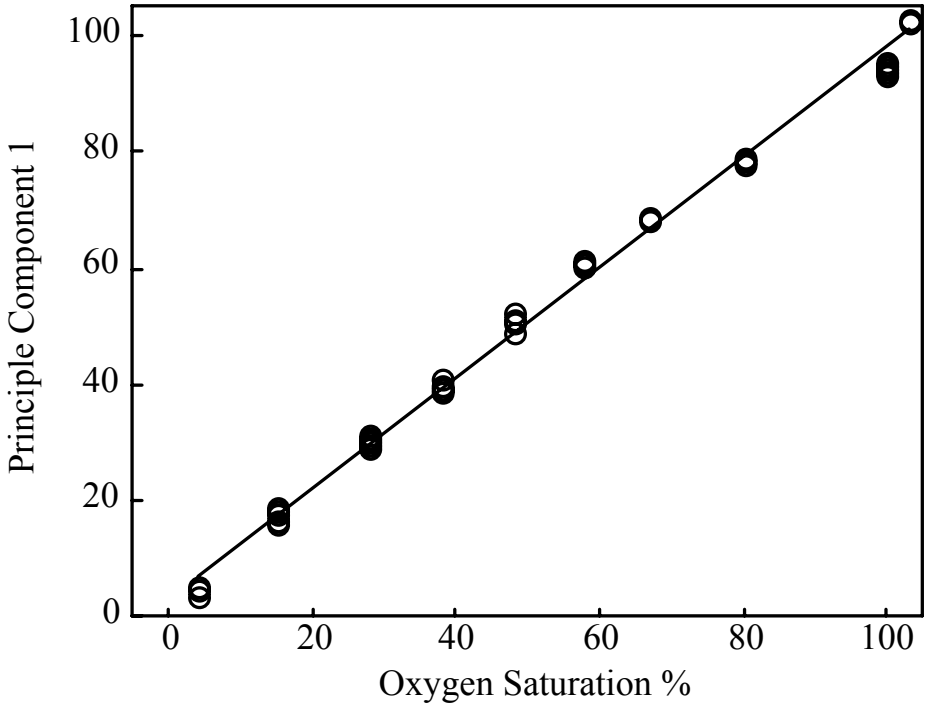

Figure 16. Plot of Principle Component 1 vs the oxygen saturation level measured by a Clark electrode. Each concentration was measured 5 times.

Conclusions.

In summary, we have shown that crystals of emissive ruthenium complexes with significant void space are oxygen sensors. $[Ru(phen)_3](tfpb)_2$ with the partially fluorinated $tfpb^-$ counterion shows simple behavior as a gas phase and aqueous solution oxygen molecule detector. The linear Stern-Volmer plots for both emission intensity and emission lifetime measurements and the pressure jump studies are readily explained by assuming that oxygen molecules enter the crystal lattice of $[Ru(phen)_3](tfpb)_2$ and are able to diffuse internally with an effective diffusion coefficient on the order of 10^{-7}–10^{-8} cm^2/s. Additionally $[Ru(4,7\text{-}Me_2Phen)_3](tfpb)_2$ was examined and found to have an even greater K_{sv} than that of $[Ru(phen)_3](tfpb)_2$. A correlation exists between the amount of void space present in the crystalline solids and the detection ability of the materials, with greater amounts of void space resulting in better sensors. $[Ru(phen)_3](tfpb)_2$ was examined as a potential sensor for DO and was successfully calibrated against the Clark electrode. Optimization and miniaturization of crystalline sensors has the potential to allow detection of oxygen in media previously unexamined.

References.

1. Demas, J. N.; DeGraff, B. A.; Coleman, P. B., *Anal. Chem.* **1999**, *71*, 793A.

2. Mills, A., *Platinum Met. Rev.* **1997**, *41*, 115.

3. Ando, M., *TrAC, Trends Anal. Chem.* **2006**, *25*, 937.

4. Demas, J. N.; DeGraff, B. A., *Coord. Chem. Rev.* **2001**, *211*, 317.

5. Zhao, Y.; Richman, A.; Storey, C.; Radford, N. B.; Pantano, P., *Anal. Chem.* **1999**, *71*, 3887.

6. Amao, Y.; Okura, I., *Sens. Actuators, B* **2003**, *B88*, 162.

7. Demas, J. N.; DeGraff, B. A.; Xu, W., *Anal. Chem.* **1995**, *67*, 1377.

8. Draxler, S.; Lippitsch, M. E.; Klimant, I.; Kraus, H.; Wolfbeis, O. S., *J. Phys. Chem.* **1995**, *99*, 3162.

9. Ertekin, K.; Kocak, S.; Sabih Ozer, M.; Aycan, S.; Cetinkaya, B., *Talanta* **2003**, *61*, 573.

10. Fuller, Z. J.; Bare, W. D.; Kneas, K. A.; Xu, W. Y.; Demas, J. N.; DeGraff, B. A., *Anal. Chem.* **2003**, *75*, 2670.

11. Garcia-Fresnadillo, D.; Marazuela, M. D.; Moreno-Bondi, M. C.; Orellana, G., *Langmuir* **1999**, *15*, 6451.

12. Hartmann, P.; Leiner, M. J. P.; Lippitsch, M. E., *Anal. Chem.* **1995**, *67*, 88.

13. Huynh, L.; Wang, Z.; Yang, J.; Stoeva, V.; Lough, A.; Manners, I.; Winnik, M. A., *Chem. Mater.* **2005**, *17*, 4765.

14. Kneas, K. A.; Demas, J. N.; Nguyen, B.; Lockhart, A.; Xu, W.; DeGraff, B. A., *Anal. Chem.* **2002**, *74*, 1111.

15. Kneas, K. A.; Xu, W.; Demas, J. N.; DeGraff, B. A., *Appl. Spectrosc.* **1997**, *51*, 1346.

16. McMurray, H. N.; Douglas, P.; Busa, C.; Garley, M. S., *J. Photochem. Photobiol. A* **1994**, *80*, 283.

17. McNamara, K. P.; Li, X.; Stull, A. D.; Rosenzweig, Z., *Anal. Chim. Acta* **1998**, *361*, 73.

18. Mills, A., *Analyst* **1998**, *123*, 1135.

19. Morin, A. M.; Xu, W.; Demas, J. N.; DeGraff, B. A., *J. Fluoresc.* **2000**, *10*, 7.

20. Navarro-Villoslada, F.; Orellana, G.; Moreno-Bondi, M. C.; Vick, T.; Driver, M.; Hildebrand, G.; Liefeith, K., *Anal. Chem.* **2001**, *73*, 5150.

21. Preininger, C.; Klimant, I.; Wolfbeis, O. S., *Anal. Chem.* **1994**, *66*, 1841.

22. Ruffolo, R.; Evans, C. E. B.; Liu, X.-H.; Ni, Y.; Pang, Z.; Park, P.; McWilliams, A. R.; Gu, X.; Lu, X.; Yekta, A.; Winnik, M. A.; Manners, I., *Anal. Chem.* **2000**, *72*, 1894.

23. Wang, Z.; McWilliams, A. R.; Evans, C. E. B.; Lu, X.; Chung, S.; Winnik, M. A.; Manners, I., *Adv. Funct. Mater.* **2002**, *12*, 415.

24. Coutant, M. A.; Payra, P.; Dutta, P. K., *Microporous Mesoporous Mater.* **2003**, *60*, 79.

25. Meier, B.; Werner, T.; Klimant, I.; Wolfbeis, O. S., *Sens. Actuators, B* **1995**, *B29*, 240.

26. Bukowski, R. M.; Ciriminna, R.; Pagliaro, M.; Bright, F. V., *Anal. Chem.* **2005**, *77*, 2670.

27. Bukowski, R. M.; Davenport, M. D.; Titus, A. H.; Bright, F. V., *Appl. Spectrosc.* **2006**, *60*, 951.

28. Leventis, N.; Elder, I. A.; Rolison, D. R.; Anderson, M. L.; Merzbacher, C. I., *Chem. Mater.* **1999**, *11*, 2837.

29. Leventis, N.; Rawashdeh, A.-M. M.; Elder, I. A.; Yang, J.; Dass, A.; Sotiriou-Leventis, C., *Chem. Mater.* **2004**, *16*, 1493.

30. Murtagh, M. T.; Shahriari, M. R.; Krihak, M., *Chem. Mater.* **1998**, *10*, 3862.

31. Cheng, Z.; Aspinwall, C. A., *Analyst* **2006**, *131*, 236.

32. Chu, B. W.-K.; Yam, V. W.-W., *Langmuir* **2006**, *22*, 7437.

33. Jorge, P. A. S.; Mayeh, M.; Benrashid, R.; Caldas, P.; Santos, J. L.; Farahi, F., *Appl. Opt.* **2006**, *45*, 3760.

34. Kocincova, A. S.; Borisov, S. M.; Krause, C.; Wolfbeis, O. S., *Anal. Chem.* **2007**, *79*, 8486.

35. Krenske, D.; Abdo, S.; Van Damme, H.; Cruz, M.; Fripiat, J. J., *J. Phys. Chem.* **1980**, *84*, 2447.

36. Xiong, X.; Xiao, D.; Choi, M. M. F., *Sens. Actuators, B* **2006**, *B117*, 172.

37. FOXY Fiber Optic Oxygen Sensors; OceanOptics: Dunedin, F.

38. Carraway, E. R.; Demas, J. N.; DeGraff, B. A.; Bacon, J. R., *Anal. Chem.* **1991**, *63*, 337.

39. Drew, S. M.; Janzen, D. E.; Mann, K. R., *Anal. Chem.* **2002**, *74*, 2547.

40. Drew, S. M.; Mann, J. E.; Marquardt, B. J.; Mann, K. R., *Sens. Actuators, B* **2004**, *B97*, 307.

41. Grate, J. W.; Moore, L. K.; Janzen, D. E.; Veltkamp, D. J.; Kaganove, S.; Drew, S. M.; Mann, K. R., *Chem. Mater.* **2002**, *14*, 1058.

42. Spek, A. L. PLATON/CALC VOID. http://www.weizmann.ac.il/Chemical_Research Support/xraylab/manuals/Platon/platon/pl000302.html (accessed 03/02/05).

43. *Crystal Engineering: From Molecules and Crystals to Materials*. Kluwer Academic: Dordrecht, **1999**; Vol. 538.

44. *Inclusion Compounds Volume 1*. Academic Press: London, **1984**.

45. Exstrom, C. L.; Britton, D.; Mann, K. R.; Hill, M. G.; Miskowski, V. M.; Schaefer, W. P.; Gray, H. B.; Lamanna, W. M., *Inorg. Chem.* **1996**, *35*, 549.

46. Evans, I. P.; Spencer, A.; Wilkinson, G., *J. Chem. Soc., Dalton Trans.* **1973**, 204.

47. Cooley, L. F.; Headford, C. E. L.; Elliott, C. M.; Kelley, D. F., *J. Am. Chem. Soc.* **1988**, *110*, 6673.

48. Lacour, J.; Goujon-Ginglinger, C.; Troche-Haldimann, S.; Jordry, J. J., *Angew. Chem., Int. Ed.* **2000**, *39*, 3695.

49. Blessing, R. H., *Acta Crystallogr., Sect. A: Found. Crystallogr.* **1995**, *A51*, 33.

50. Sheldrick, G. *SADABS*, v.2.10; 2002.

51. *SHELXTL*, v.6.12; Bruker AXS, Madison, WI, 2001.

52. Spek, A. L., *J. Appl. Crystallogr.* **2003**, *36*, 7.

53. Spek, A. L. *PLATON*, Utrecht University, Utrecht, The Netherlands, 2005.

54. Bruno, I. J.; Cole, J. C.; Edgington, P. R.; Kessler, M.; Macrae, C. F.; McCabe, P.; Pearson, J.; Taylor, R., *Acta Crystallographica, Section B: Structural Science* **2002**, *B58*, 389.

55. Wrighton, M. S.; Ginley, D. S.; Morse, D. L., *J. Phys. Chem.* **1974**, *78*, 2229.

56. Demas, J. N.; Crosby, G. A., *J. Phys. Chem.* **1971**, *75*, 991.

57. Avian Technolgies, 1 Worthington Rd., P.O. Box 822, Wilmington, OH 45177, USA; http://www.aviantechnologies.com/faq.html.

58. Private communication, Paul F. Barbara.

59. LED is ETG-5UV 405-30 from ETG Corporation, 8599 Venice Blvd, Unit K, Los Angeles, CA 90034.

60. The filter is a FF01-406/15-25 from Semrock, 3625 Buffalo Road, Rochester, NY 14624.

61. Araki, T.; Fujisawa, Y.; Hashimoto, M., *Rev. Sci. Instrum.* **1997**, *68*, 1365.

62. Logger Pro software: Vernier Software & Technology, 13979 SW Millikan Way, Beaverton, OR 97005-2886.

63. Marquardt, B. J.; Burgess, L. W. Optical Immersion Probe Incorporating a Spherical Lens. US patent # 6,831,745 B2, 2004.

64. Marquardt, B. J.; Le, T.; Burgess, L. W., *SPIE Proceedings* **2001**, *4469*, 62.

65. Wold, J. P.; Marquardt, B. J.; Dable, B. K.; Robb, D.; Hatlen, B., *Appl. Spectrosc.* **2004**, *58*, 395.

66. Beebe, K. R.; Pell, R. J.; Seasholtz, M. B., *Chemometrics: A Practical Guide*. John Wiley and Sons, Inc.: New York, NY, **1998**; p 278-335.

67. Douglas, P.; Eaton, K., *Sens. Actuators, B* **2002**, *B82*, 200.

68. Gladysz, J. A.; Curran, D. P.; Horvath, I. T.; Editors, *Handbook of Flurorous Chemistry*. **2004**; p 594 pp.

69. Ikeda, N.; Yoshimura, A.; Tsushima, M.; Ohno, T., *J. Phys. Chem. A* **2000**, *104*, 6158.

70. Kalinowski, J.; Fattori, V.; Di Marco, P., *Chem. Phys.* **2001**, *266*, 85.

71. Bowyer, W. J.; Xu, W.; Demas, J. N., *Anal. Chem.* **2004**, *76*, 4374.

Chapter 2

Inefficient Crystal Packing in Chiral $[Ru(phen)_3](PF_6)_2$ Enables Oxygen Molecule Quenching of the Solid-State MLCT Emission

Abstract

The molecular oxygen quenching of the solid-state emission from pure crystals of Δ-$[Ru(phen)_3][PF_6]_2$, Λ-$[Ru(phen)_3][PF_6]_2$, and racemic $Ru(phen)_3(PF_6)_2$ was studied by emission spectroscopy (phen = 1,10-phenanthroline). Crystals of the pure enantiomers exhibit significant and nearly identical emission intensity quenching (0.36(2) and 0.33(2) respectively) in the presence of air (where the fraction quenched is $(I_{nitrogen}-I_{air})/I_{nitrogen}$); in comparison the racemic compound shows a much lower value (0.05(2)). The large differences in the quenching behavior are a result of major structural differences between the two chiral and racemic salts. The chiral compounds crystallize in $P4_1$ and $P4_3$ respectively with toluene and acetonitrile molecules in the lattice that can be partially removed to create void space channels. These open channels allow the diffusion of oxygen molecules within the crystals and enable efficient emission quenching that is not possible in the closely packed racemic salt. Lifetime measurements, thermal gravimetric analysis (TGA), and single crystal X-ray structure determinations support these conclusions.

Introduction

The sensing of molecular oxygen in the gas phase and water with optical sensors has generated considerable interest in the past 20 years because optical sensing offers several advantages over electrochemical detection (i.e. Clark electrode).[1-5] Solid-state optical sensors have been developed by embedding emissive transition metal complexes in polymeric,[3, 6-23] zeolitic,[24, 25] sol gel,[26-30] or other[31-36] support materials that allow oxygen to diffuse to the emissive sites. The metal complex emission is quenched via energy transfer to the oxygen molecules, allowing detection. Specifically, sensors utilizing $Ru(bpy)_3^{2+}$ (bpy = 2,2'-bipyridine) derivatives as the lumiphore have been commercialized.[37] Unfortunately, in these systems the nanoscopic surroundings of each emissive molecule may be different, resulting in heterogeneous emissive sites and complications that can result from the photoinstability of many of the support materials as well as the metal complex itself.[10, 14, 16, 17, 21, 22, 29]

We have recently reported the use of pure nanoporous crystalline solids, such as $[Ru(phen)_3](tfpb)_2$ (tfpb = tetrakis(bis-3,5-trifluoromethylphenylborate), as oxygen sensors. These crystalline materials contain void space channels which allow the diffusion of oxygen and can eliminate problems of heterogeneity and subsequent inconsistent sensor response.[38] Compared to sensors that use polymeric support materials, sensors based on crystalline solids can have enhanced stability and consistent emissive sites due to the uniformity of the repeat unit in the crystals. Bulky fluorinated counterions, like $tfpb^-$, promote the formation of void space within the crystals and allow higher permeability to oxygen.[38]

We recently became aware of another potential method to generate void space within crystalline solids that eliminates the need of large counterions. Wallach's rule states that racemic crystals tend to be more dense than their chiral counterparts. The decrease in density implies the presence of increased void space in the crystals of enantiomorphic species due to less efficient packing. Of course, these void spaces may be filled with solvent molecules that may be subsequently removed as is observed in the case of comparison of salts of tris(diimine) complexes of Ru(II).[ref] It is favorable for our purposes here that these small molecules may be removed from the crystals to produce void space channels that may enable oxygen molecules access to the interior of the crystals.

The Δ and Λ forms of $Ru(phen)_3^{2+}$ can be separated and independently combined with simple counterions to give compounds with different crystalline structures and properties than those of the racemic form.[39] As has been previously observed, pure crystals of the Δ and Λ forms often do not pack as efficiently in the crystal as the racemic mixture, which can lead to a porous structure.[40-42] Herein, we describe the use of microcrystalline samples of simple salts of chiral metal complexes as oxygen sensors. We have separated and studied the pure Δ and Λ forms of $Ru(phen)_3^{2+}$ as PF_6^- salts and compare the crystalline forms and oxygen sensing ability of these chiral salts to racemic $[Ru(phen)_3][PF_6]_2$.

Experimental

General Considerations. Racemic $[Ru(phen)_3]Cl_2 \cdot x\ H_2O$ and potassium antimony tartrate ($K_2[Sb_2\{(+)\text{-tartrate}\}_2] \cdot 3H_2O$) were purchased from Aldrich Chemical Co. Sodium hydroxide (NaOH) and ammonium hexafluorophosphate (NH_4PF_6) were purchased from Mallinckrodt Chemicals and Aldrich respectively. Deionized water was used in all cases. All reagents were used without further purification. Racemic-$[Ru(phen)_3][PF_6]_2$ was synthesized in a previous study by a metathesis reaction of $[Ru(phen)_3]Cl_2 \cdot x\ H_2O$ with NH_4PF_6.[38]

Optical resolution of $[Ru(phen)_3]^{2+}$. In general, our procedure follows the method of Nakamura et al. $[Ru(phen)_3]Cl_2$ (0.356 g, 0.500 mmol) was dissolved in water (24.5 mL).[39] Potassium antimony tartrate (0.334 g, 0.500 mmol) was dissolved with warming in water (12.5 mL) and added to the solution of $[Ru(phen)_3]Cl_2$. Orange solid began precipitating after only a few mL of the antimony tartrate solution was added. The solution was heated during the addition of the remaining antimony tartrate solution. Upon completion of the addition of the resolving agent, water (10 mL) was added and the solution was again heated. Upon cooling to room temperature overnight, Λ-$[Ru(phen)_3][Sb_2\{(+)\text{-tartrate}\}_2]$ crystallized as an orange solid which was collected by filtration (0.283 g, 96 % yield). The filtrate that contained Δ-$[Ru(phen)_3]^{2+}$ was saved for further reaction.

Λ-$[Ru(phen)_3][PF_6]_2$. Λ-$[Ru(phen)_3][Sb_2\{(+)\text{-tartrate}\}_2]$ (0.1428 g, 0.1213 mmol) was dissolved in 25 mL of hot NaOH solution (0.05 M). Filtration was performed to remove an off-white solid which was rinsed with an additional 3 mL of 0.05 M NaOH. A 5 mL solution of NH_4PF_6 (1.132 g, 6.945 mmol) was added dropwise to give an immediate

precipitate of a light orange solid (0.070 g, 62 % yield), Λ-$[Ru(phen)_3][PF_6]_2$. The optical purity (enantiomeric excess) of the Λ-$[Ru(phen)_3][PF_6]_2$ was determined by HPLC as 95 %. X-ray quality crystals were grown by recrystallization of the orange solid from an acetonitrile/toluene mixture.

Δ-$[Ru(phen)_3][PF_6]_2$. A 20 mL solution of NH_4PF_6 (2.50 g, 15.4 mmol) was added dropwise to the potassium antimony tartrate filtrate containing Δ-$[Ru(phen)_3]^{2+}$ from the optical resolution of the racemic mixture. Δ-$[Ru(phen)_3][PF_6]_2$ precipitated as an orange solid (0.204 g, 88 % yield) with an optical purity (enantiomeric excess) as determined by HPLC of 99 %. X-ray quality crystals were grown by recrystallization of the orange solid from an acetonitrile/toluene mixture.

HPLC Analysis. The optical purity of the complexes was determined by HPLC on a 1100 Series Agilent liquid chromatograph equipped with a UV-absorbance detector, and a Chiralcel OD (4.6 mm inner diameter × 25 mm long with 10 micron particles) normal phase column that was converted to reverse phase by flushing with acetonitrile/water. The mobile phase was a 50:50 mixture, by volume, of aqueous 0.1 M $NaPF_6$ and acetonitrile with a flow rate of 0.75 mL/min, an injection volume of 50 μL, and a detection wavelength of 400 nm.

Spectroscopic and Photophysical Studies. Solid-state UV-Vis spectra were acquired from films made from samples used for oxygen sensitivity studies (*vide infra*) on a custom built zirconium oxide attenuated total reflectance (ATR) crystal. The solid-state emission spectra were acquired using an apparatus similar to one described previously.[38] A bifurcated (six-around-one) fiber optic probe (Ocean Optics) was used to excite the sample and also to collect the emitted light. The excitation light was provided by a 400

nm LED. Spectra were corrected for detector response with an Ocean Optics CCD spectrophotometer that was calibrated with a standard light source.[38] Samples used for oxygen detection were made by dissolving mg quantities of the Ru complex in acetonitrile and adding the resulting solution to 3 mL of toluene. Precipitation of microcrystalline samples resulted, which were then centrifuged. These solid samples were removed from the mother liquor and either placed on the tip of a Delrin® rod or placed in a depression in the center of a thermistor (Digi-Key, Allied Electronics) that allowed fast (10 s) heating to approximately 80°C (Figure 1). The samples were fitted into a sample compartment which allowed gas flow over the sample. Known percentages of oxygen were made with in-house built gas mixing setups using mass-flow control valves. The oxygen concentrations for the Stern-Volmer plots reported here are expressed in terms of mole fraction at the standard atmospheric pressure of Minneapolis-St. Paul, MN of 0.97 atm. Data were collected either with Ocean Optics OOIBase32 or with custom-written Labview programs that also controlled the oxygen fraction. Solid-state quantum yields and emission lifetimes were collected as previously described.[38]

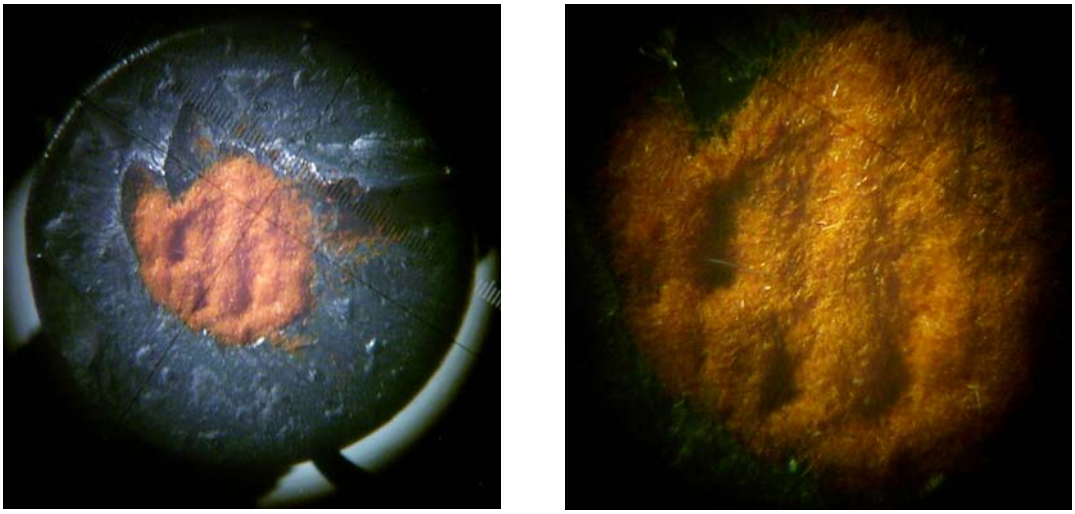

Figure 1. Photograph of thermistor with sample of Δ-$[Ru(phen)_3](PF_6)_2$ at 25× (left) and 50× (right) showing microcrystalline state of sample.

Single Crystal X-ray Crystallography. The crystal structure of Λ-$[Ru(phen)_3][PF_6]_2$ has been previously reported as a 2:1 acetonitrile: diethyl ether solvate.[43] A crystal of Δ-$[Ru(phen)_3][PF_6]_2$ grown from an acetonitrile/toluene solvent mixture was attached to a glass capillary fiber and mounted on a Siemens SMART Platform CCD diffractometer for a data collection at 173(2) K using a graphite monochromator and Mo Kα radiation (λ = 0.71073 Å). An initial set of cell constants was calculated from 93 reflections harvested from three sets of 20 frames such that orthogonal wedges of reciprocal space were surveyed. Final cell constants were calculated from the xyz centroids of 3417 strong reflections from the actual data collection. Data were collected to the extent of 1.5 hemispheres to a resolution of 0.84 Å. Three major sections of frames were collected with 0.30° steps in ω. The intensity data were corrected for absorption and decay using SADABS.[44, 45] The space group was determined to be $P4_1$ based on systematic absences and intensity statistics. The absolute structure was determined by confirming the space group was $P4_1$ and not $P4_3$ by solving the structure in both space groups and then analyzing the resulting absolute structure parameter (the Flack parameter (x)), in each case. The Flack parameter is near zero when the absolute structure is correct and near one when the structure should be inverted. In this case when the structure was solved in $P4_1$, x = 0.0066 with an estimated standard deviation (ESD) of 0.0386. When solved in $P4_3$, x = 0.9700 with an estimated standard deviation (ESD) of 0.0402 indicating a need to reinvert to the space group $P4_1$ confirming the presence of the Δ enantiomer as expected. A direct-methods solution provided the positions of most of the non-hydrogen atoms. Full-matrix least-squares/difference Fourier cycles were performed to locate the remaining non-hydrogen atoms. All non-hydrogen atoms were refined with anisotropic

displacement parameters and all hydrogen atoms were placed in idealized positions and refined as riding atoms with relative isotropic displacement parameters. All calculations were performed with the SHELXTL suite of programs.[46] Packing analysis parameters were measured using PLATON/VOID, with more detailed analysis of the void spaces performed with PLATON/CAVITY.[47, 48] Pictorial representations of the solvent channels were done with edited .res files in Mercury.[49] Details of the refinement are given in Table 1.

Thermogravimetric Analysis. Investigation of mass loss was completed with a Perkin Elmer Diamond TG/DTA with an inert nitrogen gas flow. Samples were prepared identically to those used for emission studies and were taken directly from the mother liquor. A 15 min hold time was programmed at the beginning of the run to monitor evaporation of the excess mother liquor to produce dry, solvated samples of 0.5-3 mg. The dry samples were then heated at a rate of 10 °C/min from 20 °C to 400 °C and the mass loss was recorded.

Table 1. Crystallographic data and refinement parameters.

Compound	**2 Δ-[Ru(phen)$_3$][PF$_6$]$_2$ ·2CH$_3$CN·toluene**	**2 Λ-[Ru(phen)$_3$][PF$_6$]$_2$ ·2CH$_3$CN·Et$_2$O** ‡
empirical formula	C_{83} H_{62} F_{24} N_{14} P_4 Ru_2	C_{80} H_{64} F_{24} N_{14} O P_4 Ru_2
crystal color, morphology	orange, needle	orange, parallelepiped
crystal system	Tetragonal	Tetragonal
space group	*P4$_1$*	*P4$_3$*
a, Å	25.5737(9)	25.372(1)
b, Å	25.5737(9)	25.372(1)
c, Å	12.5736(9)	12.726(2)
α, deg	90	90
β, deg	90	90
γ, deg	90	90
volume, Å^3	8223.3(7)	8192.2(2)
Z	4	4
formula weight, g mol^{-1}	2037.49	2019.48
density (calculated), g cm^{-3}	1.646	1.637
temperature, K	173(2)	183(2)
Absorption coefficient, mm^{-1}	0.556	0.558
F(000)	4088	4056
θ range, deg	0.80 to 25.04	5.08 to 16.48
index ranges	$-22 \le h \le 30$ $-30 \le k \le 26$ $-14 \le l \le 14$	$-30 \le h \le 30$ $-30 \le k \le 30$ $-15 \le l \le 15$
reflections collected	38214	15846
independent reflections	14398 (R_{int} = 0.0849)	14413 (R_{int} = 0.030)
weighting factors[a] *a,b*	0.0873, 0.0	
max, min transmission	0.9835, 0.7686	0.774, 0.695
Data/restraints/parameters	14398/58/1130	14413/0/1124
R_1, wR_2 [$I > 2\sigma(I)$]	0.0730, 0.1549	0.063, 0.160
R_1, wR_2 (all data)	0.1209, 0.1755	
GOF	1.027	1.075
largest diff. peak, hole, eÅ^{-3}	0.731, -0.502	0.66, -0.55

[a] $w = [\sigma^2(F_o^2) + (aP)^2 + (bP)]^{-1}$, where $P = (F_o^2 + 2F_c^2)/3$.

‡ previously determined[43]

Results and Discussion.

Optical Resolution of rac-$[Ru(phen)_3]^{2+}$.

The racemic mixture of $[Ru(phen)_3]Cl_2$ was chemically resolved into the Δ and Λ enantiomers by treatment with potassium antimony tartrate ($K_2[Sb_2\{(+)\text{-tart}\}$) by the method of Nakamura et al.[39] The Λ enantiomer crystallized as an orange antimony tartrate salt while the the Δ enantiomer remained in solution (Equation 1). The PF_6^- salts of the resulting enantiomers were then isolated by decomposition of the antimony tartrate anion with NaOH followed by precipitation with NH_4PF_6 (Equations 2 and 3) to give Δ-$[Ru(phen)_3][PF_6]_2$ and Λ-$[Ru(phen)_3][PF_6]_2$ in 99 % and 95 % enantiomeric excess respectively as determined by chiral column HPLC (Figure 2). Solid samples of both enantiomers that were stored for 9 months showed no signs of racemization as determined by HPLC.

$$\Delta\text{-},\Lambda\text{-}[Ru(phen)_3]Cl_2 \xrightarrow[H_2O,\,\Delta]{K_2[Sb_2\{(+)\text{-tart}\}_2]} \Lambda\text{-}[Ru(phen)_3][Sb_2\{(+)\text{-tart}\}_2]_{(s)} + \Delta\text{-}[Ru(phen)_3]^{2+}{}_{(aq)} + 2\,Cl^- \quad (1)$$

$$\Lambda\text{-}[Ru(phen)_3][Sb_2\{(+)\text{-tart}\}_2] \xrightarrow[NH_4PF_6]{0.05\ M\ NaOH} \Lambda\text{-}[Ru(phen)_3][PF_6]_2 \quad (2)$$

$$\Delta\text{-}[Ru(phen)_3]^{2+}{}_{(aq)} \xrightarrow{NH_4PF_6} \Delta\text{-}[Ru(phen)_3][PF_6]_2 \quad (3)$$

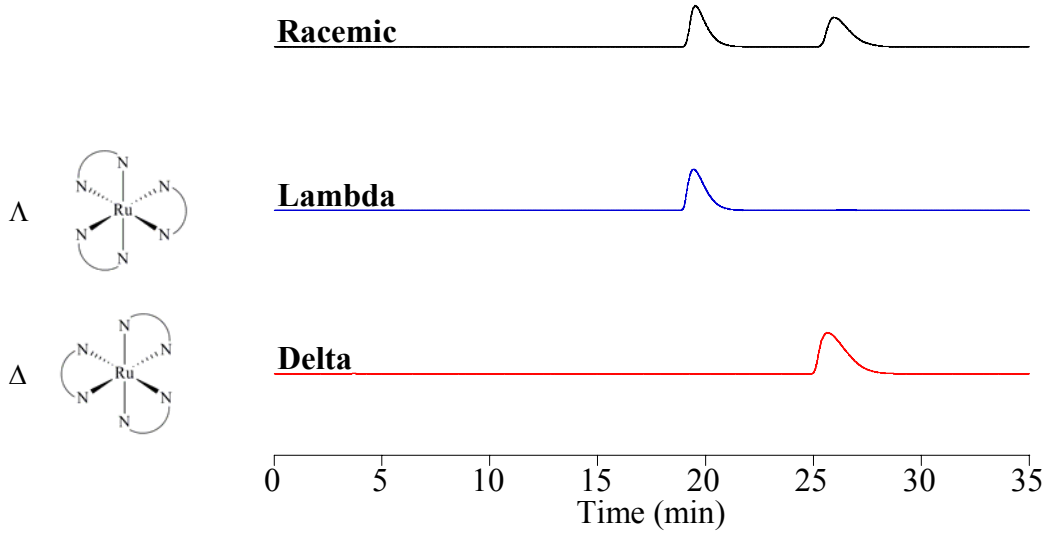

Figure 2. HPLC chromatograms showing the racemic, Λ-, and Δ-$[Ru(phen)_3](PF_6)_2$.

X-ray Crystallography.

Unfortunately our attempts to grow crystals from water/acetone mixtures to match exactly the previously determined 100 K structure[39] of the hydrated Λ enantiomer which loses the water molecules but maintains the crystalline structure at 298 K were unsuccessful; however, crystals of the Δ enantiomer were grown from a combination of acetonitrile and toluene that enabled the absolute configuration of the Δ enantiomer to be determined by a single crystal x-ray structure. The crystal structure of the Λ enantiomer has also previously been completed with crystals grown from diethyl ether diffused into acetonitrile.[43] These crystals were reported to undergo facile loss of the interstitial solvent leading to our modification in crystal growth, replacing diethyl ether with the higher boiling toluene. The unit cell parameters and volume of the Δ enantiomer are very similar to that of the Λ enantiomer as reported by Maloney (Table 1) and upon closer investigation the packing of the ions is almost identical, with helical columns of the chiral complex progressing through the cell.[43] The Δ enantiomer has two formula units in the asymmetric unit with the Ru cations related by a pseudo-2-fold screw axis, as is the case in the structure of the Λ enantiomer.[43]

The cations contain pseudooctahedral Ru. The average Ru–N bond lengths (2.066 Å) and angles between least-squares planes made from the ligands (Ru1 – 82.4, 88.8, 81.5º and Ru2 – 86.0, 85.0, 85.9º) correlate well with the literature values reported for the Λ enantiomer (2.067 Å average Ru–N) (Ru1 – 80, 86, 90º and Ru2 – 86, 90, 87º).[43] The Δ enantiomer crystallizes as a solvate with two acetonitrile molecules and one toluene per asymmetric unit. Due to the close similarity of our structure with the

literature structure of the Λ enantiomer, we make the assumption that when Λ-$[Ru(phen)_3](PF_6)_2$ is crystallized from acetonitrile and toluene, the same structure with two co-crystallized acetonitrile molecules and one toluene is realized.

Examination of the molecular packing of the structures of the Δ and Λ enantiomers shows a narrow channel of open space running though the structure, as well as another larger channel partially occupied by the acetonitrile and toluene solvent molecules (Figure 3, top). One can envision that the loss of some of this co-crystallized solvent will significantly increase the amount of void space accessible to small molecules. The channels observed in the chiral structures are in contrast to the structure of racemic-$[Ru(phen)_3](PF_6)_2$[50] which contains no solvent molecules and a much smaller amount of open space in the form of isolated voids (Figure 3, bottom). The channels observed in the chiral structures could allow diffusion of small molecules like oxygen into and out of the crystal allowing their use as sensors. Conversely the presence of small isolated voids in the racemic crystal may not enable diffusion of oxygen to the interior; hence we expect poor oxygen sensing in this case (*vide infra*).

a)

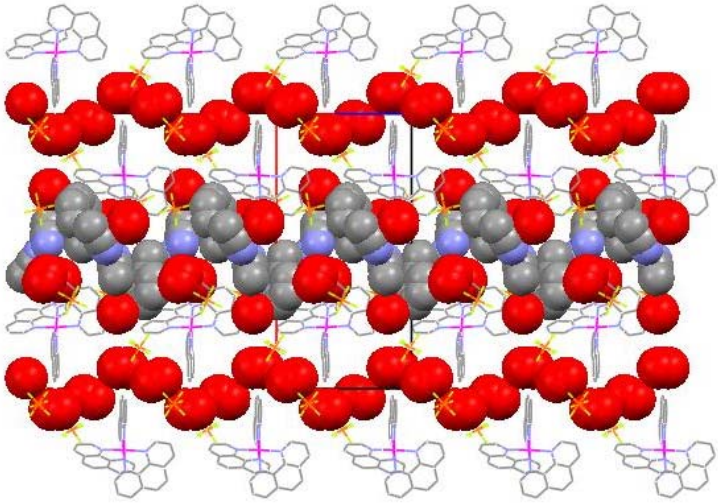

b)

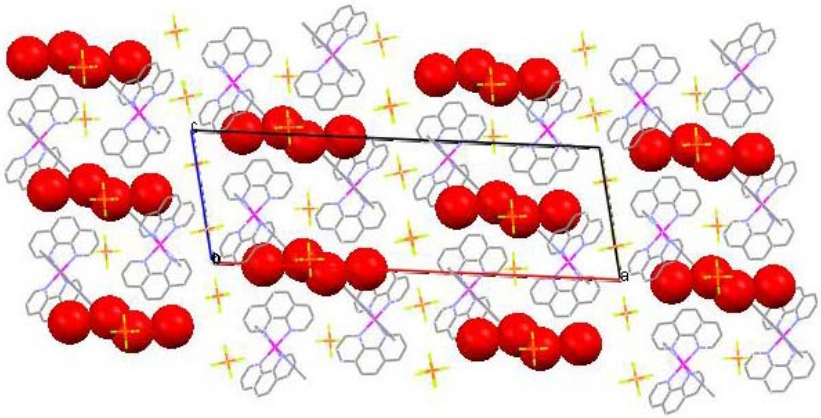

Figure 3. Packing diagrams of crystal structures, down the b-axis, of a) Δ-[Ru(phen)$_3$](PF$_6$)$_2$·toluene·2CH$_3$CN and b) racemic-[Ru(phen)$_3$](PF$_6$)$_2$[50]. Red spheres, with an average diameter of approximately 2.4 Å, represent open space.

Thermogravimetric Analysis.

Samples prepared identically to those analyzed for oxygen sensitivity were investigated by TGA (Figure 4). A gradual loss of mass occurred upon heating with three ill-defined inflection points. The first inflection at 40 °C corresponds to loss of 0.25 acetonitrile molecules per Ru which we believe leaves from the smaller channel in the crystal structure. We believe the loss of this portion of solvent also occurs readily at room temperature in air for bulk samples and was not present in the lattice during the crystallographic data collection or at the beginning of the oxygen sensitivity studies. The next two inflection points occur at approximately 60° and 80 °C and correspond to the loss of 0.5 acetonitrile molecules per Ru at each point. A further mass loss of 0.5 toluene molecules per Ru occurs until about 140 °C after which the mass loss is minimal until the temperature reaches 380 °C where the samples undergo decomposition. The total mass lost between 40° and 140 °C corresponds to 1.0 acetonitrile molecule and 0.5 toluene molecules per $[Ru(phen)_3](PF_6)_2$ in excellent agreement with the crystal structure. Under the constant heating rate conditions of the TGA experiment, the acetonitrile molecules in the structure are lost in 8–9 minutes between 25°–80 °C.

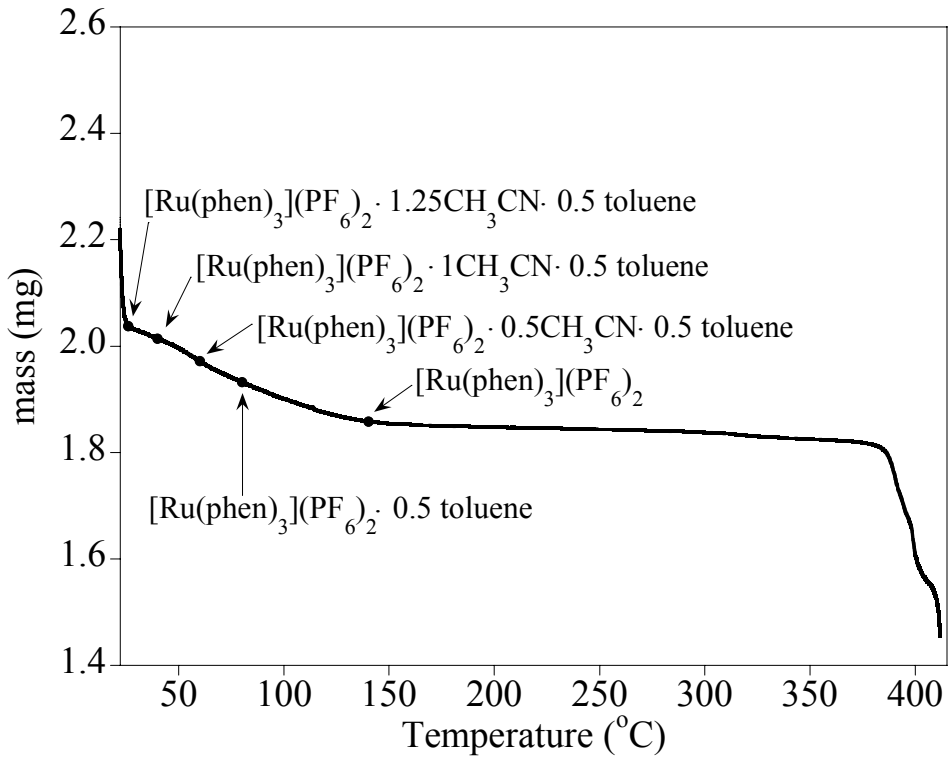

Figure 4. TGA plot of the mass in mg of the Δ-$[Ru(phen)_3](PF_6)_2$ sample versus sample temperature. Heating rate is 10 °C/minute.

Photophysical Studies.

The room temperature solid-state absorption and emission spectra for the three salts (racemic, pure Δ and pure Λ enantiomer $[Ru(phen)_3](PF_6)_2$ salts) were collected under nitrogen. The λ_{max} values (along with absolute emission quantum yields and mean lifetimes (τ_M)) are reported in Table 2. The respective λ_{max} values for absorption and emission of the two pure enantiomers are nearly identical and shifted to the red (approximately 6 nm for absorption and 10 nm for emission) of the racemic compound, likely a result of interactions between the cations and solvent molecules in the pure chiral compounds that are not present in the racemic crystals. This pattern of physical property results (pure Δ and pure Λ enantiomers the same, racemic different) is expected and is confirmed for all of the solid-state measurements we report herein.

Solid-state absolute emission quantum yields were collected for racemic and the pure Δ and Λ enantiomer $[Ru(phen)_3](PF_6)_2$ salts as described previously[38] using a Fluorilon scattering target[51]. The quantum yields were found to be very dependent on the treatment of the solids[38] with much lower values resulting when the measurements were taken of solids that had been evaporated from acetonitrile containing no toluene. The values reported in Table 2 were taken of 10–20 mg samples that had been dissolved in acetonitrile (0.05 mL) and added to toluene (3 mL) resulting in a crystalline precipitate.

Table 2. Spectroscopic and photophysical data.

	Absorbance λ_{max} **(nm)**	**Emission** λ_{max} **(nm)**	$\tau_{M\ nitrogen}$ **(ns)**	$\phi_{nitrogen}$	$\frac{\Delta\phi}{\phi_0}$
Δ-$[Ru(phen)_3](PF_6)_2$	465	599	462	0.05(2)	0.36(2)
Λ-$[Ru(phen)_3](PF_6)_2$	466	601	464	0.05(2)	0.33(2)
Δ, Λ-$[Ru(phen)_3](PF_6)_2$	459	590	392	0.04(2)	0.05(2)

Emission Intensity Quenching Studies.

Due to the presence of void space in the crystalline lattice both Δ and Λ enantiomers were examined for their utility as oxygen sensors. Additionally, for comparison, racemic $[Ru(phen)_3](PF_6)_2$ was also investigated. The quenching effect of air on the solid-state emission was examined by emission intensity measurements under nitrogen and air (Figure 5). The extent of emission quenching in the presence of air is quantified using the integrated intensities of the emission to give a fraction of emission quenched according to equation 4, I_0 is the normal Stern-Volmer intensity with no quencher present and I is the Stern-Volmer intensity with air present.

$$\textbf{Fraction of integrated emission quenched} = \frac{I_0 - I}{I_0} = \frac{\Delta I}{I_0} = \frac{\Delta \phi}{\phi_0} \qquad (4)$$

The solid-state emission of both pure enantiomers was reversibly quenched in the presence of air compared with nitrogen (Figure 5). The fractions of emission quenched were 0.36(2) and 0.33(2) for the Δ and Λ enantiomers after conditioning (*vide infra*). In contrast, the racemic salt gave a very small fraction quenched (0.05(2)). The sensitivity of these chiral crystalline solids to oxygen is similar to racemic salts with significant void space that we have previously studied, for example $[Ru(phen)_3](tfpb)_2$, which exhibits a fraction of emission quenched of 0.354 in air.[38] Immediately after samples of the enantiomers were removed from the crystallization mixture and prepared for measurements, the sensing behavior was lower than the steady state values reported in Table 2 with fractions of emission quenched under air of 0.15(2). The table values are obtained if samples are conditioned either under a flow of nitrogen for long times (days) or heated in several 10 s increments on a thermistor to more rapidly remove a portion of the acetonitrile of crystallization. The emission quenching of the freshly prepared

samples in the presence of air increases, resulting in a stable sensor when a portion of the loosely held solvent of crystallization is released. We believe that loss of 0.5 equivalents of acetonitrile per Ru (1 acetonitrile per asymmetric unit, half of the acetonitrile present) results in the generation of an equivalent amount of void space and a stable sensing state.

The oxygen sensing ability of the chiral salts correlates well with the fraction of emission quenched found for previously studied crystalline Ru salts as oxygen sensors (Figure 6). The fraction quenched of 0.15(2), for the preconditioned state, fits on the correlation line (Figure 6) assuming that oxygen may only diffuse in the small channel of the structure. The mild thermistor heating results in loss of half of the cocrystallized acetonitrile, additional void space, and a higher fraction quenched, again in good agreement with the previous correlation. Additional heating of the sample results in further solvent loss and diminished sensitivity to oxygen, most likely due to the collapse of the structure and loss of crystallinity. It is worthy to note that occasionally a solvation state was observed that was more sensitive to air. These samples exhibited fractions of emission quenched on the order of 0.41–0.45. We believe this state results from a slower heating rate, but repeated attempts to produce this state, on demand, were unsuccessful.

The quenching behavior of these salts was investigated further by using mass-flow control valves to produce specific concentrations of oxygen in nitrogen. Emission intensity measurements for microcrystalline samples of both pure enantiomers, as well as racemic-$[Ru(phen)_3](PF_6)_2$, were collected and are displayed as a Stern-Volmer plot (I_0/I vs mole fraction of oxygen in nitrogen at atmospheric pressure) in Figure 7. The importance of void space as an enabling structural feature for excited state quenching by molecular oxygen in these crystalline materials is obvious.

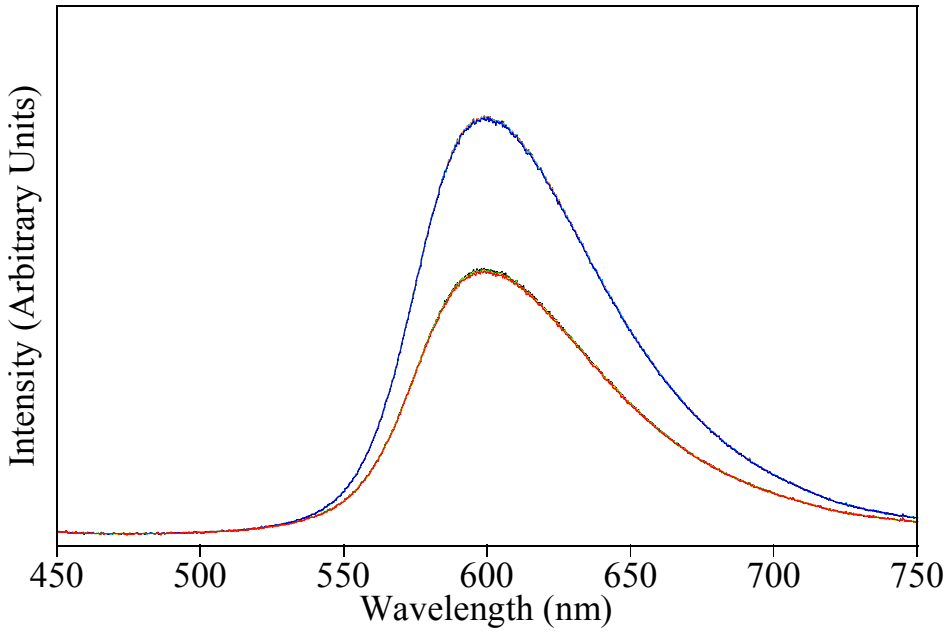

Figure 5. Emission spectra of solid Δ-$[Ru(phen)_3](PF_6)_2$ under nitrogen (blue) and under air (red) showing the quenching of the emission in the presence of oxygen and the reversibility of the sensor. Each exposure level contains 5 overlayed spectra collected in an alternating fashion.

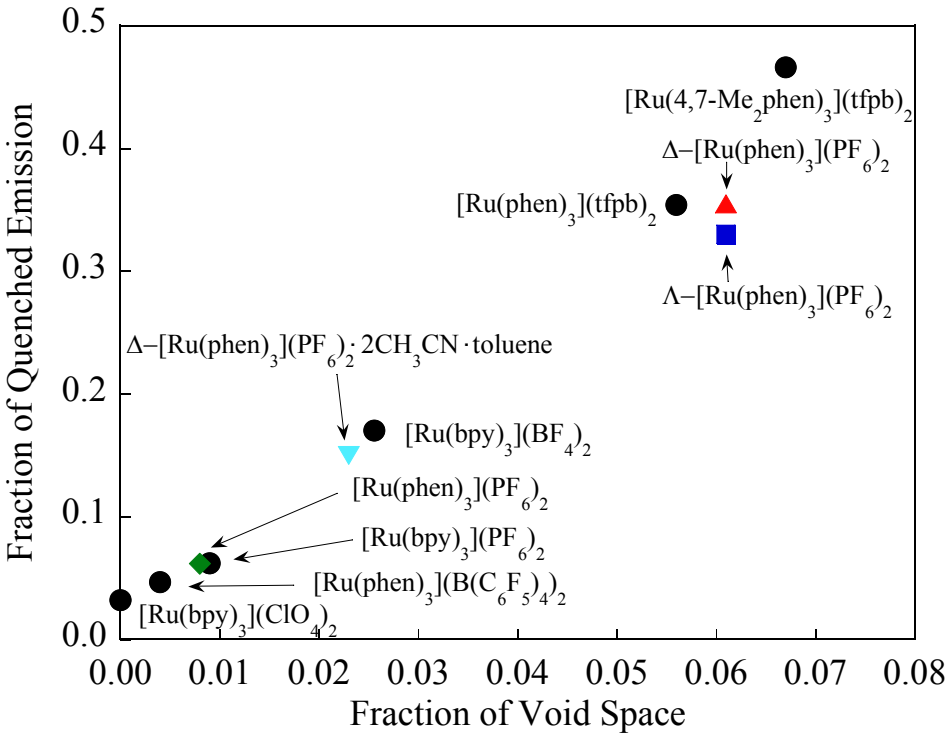

Figure 6. Comparison of the Δ-$[Ru(phen)_3](PF_6)_2$ (▲) and Λ-$[Ru(phen)_3](PF_6)_2$ (■) salts to the correlation of the fraction of emission quenched in the presence of air to the fraction of void space present for several $Ru(bpy)_3^{2+}$ and $Ru(phen)_3^{2+}$ salts including racemic $[Ru(phen)_3](PF_6)_2$ (◆). Fraction of quenched emission immediately after samples of the enantiomers were removed from the crystallization mixture (▼).

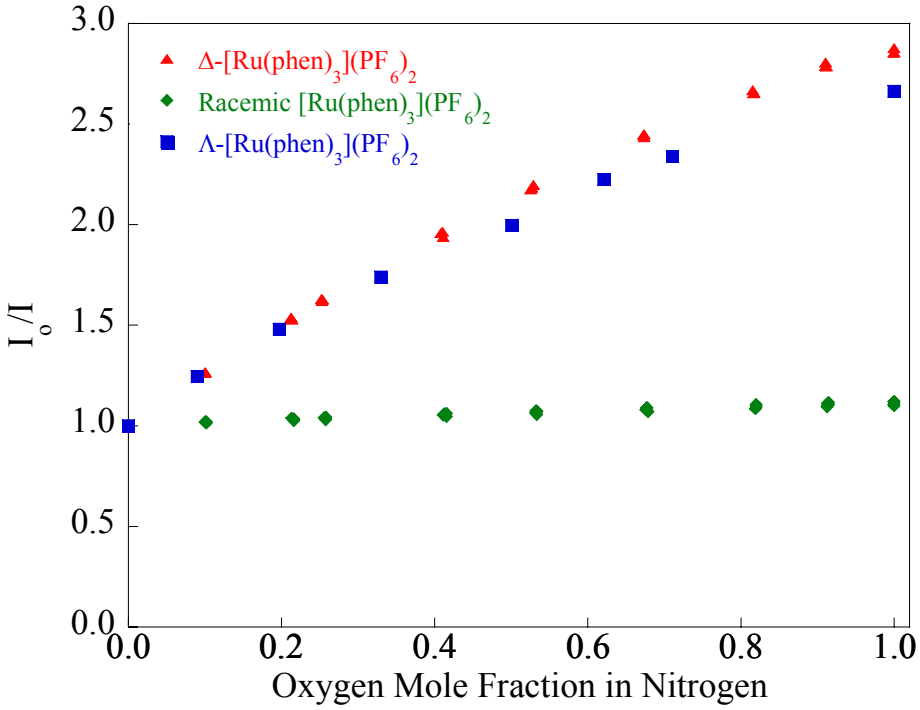

Figure 7. Stern-Volmer intensity plot of I_0/I vs oxygen mole fraction for Δ-$[Ru(phen)_3](PF_6)_2$ (▲), Λ-$[Ru(phen)_3](PF_6)_2$ (■), and the racemic mixture (◆).

The Δ and Λ enantiomers that exhibit void space channels and solvent molecules in the crystalline lattice allow the diffusion of oxygen into the solid and subsequent quenching of the emission of the complex while the racemic-$[Ru(phen)_3](PF_6)_2$ salt, with smaller isolated voids, does not allow significant oxygen diffusion and exhibits very little quenching. The curved Stern-Volmer plots seen for the Δ and Λ enantiomers can be fit to a two-site Stern-Volmer model according to equation 5 where I_0 is the normal Stern-Volmer intensity with no quencher present, I is the Stern-Volmer intensity with some concentration of O_2 present, f is the fractional contribution to the unquenched emission where $f_1 + f_2 = 1$, K_{SV1} and K_{SV2} are the different Stern-Volmer quenching constants, and $[O_2]$ is the concentration of oxygen.

$$\frac{I_0}{I} = \frac{1}{\frac{f_1}{1 + K_{SV1}[O_2]} + \frac{f_2}{1 + K_{SV2}[O_2]}} \tag{5}$$

In an ideal system with only dynamic quenching of a single emitting site ($f_2 = 0$), the Stern-Volmer quenching will give a linear relationship between I_0/I and the concentration of oxygen. The curvature of the pure enantiomer Stern-Volmer plots indicates more complicated behavior. For the Δ isomer the two-site model results in a fit where one emitting species has a K_{SV} of 3.31 and a fractional contribution (f_1) of 0.85 to the total emission; a second emitting species has a K_{SV} of ~0 with a fractional contribution ($f_2 = 1 - f_1$) of 0.15. Similar results are presented in Table 3 for the Λ isomer. The simulated Stern-Volmer plots are in excellent agreement with the experimental intensity data for the Δ (Figure 8) and Λ (Figure 9) enantiomers. In comparison, the racemic salt exhibits linear Stern-Volmer quenching behavior ($f_2 \approx 0$) with a very small K_{SV} of ~0.110.

Table 3. Fitting parameters for the fit of the intensity data for the pure Δ and Λ enantiomers and the racemic mixture to the two-site Stern-Volmer model.

	Δ-[Ru(phen)$_3$](PF$_6$)$_2$	**Λ-[Ru(phen)$_3$](PF$_6$)$_2$**	**Δ, Λ-[Ru(phen)$_3$](PF$_6$)$_2$**
K_{SV1}	3.305	3.513	0.110
f_1	0.852	0.782	1.00
K_{SV2}	0	0.0812	0
f_2	0.148	0.218	0

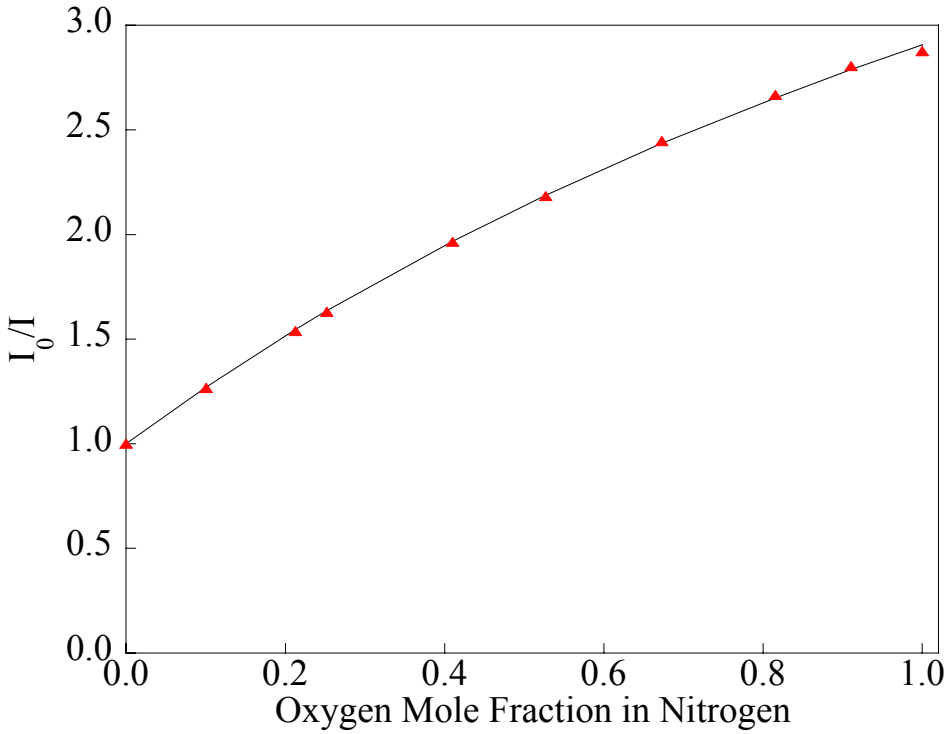

Figure 8. Stern-Volmer intensity plot of I_0/I vs oxygen mole fraction for [Δ-Ru(phen)$_3$](PF$_6$)$_2$. Filled red triangles (▲) are experimental data, black line is the two-site model fit of the data.

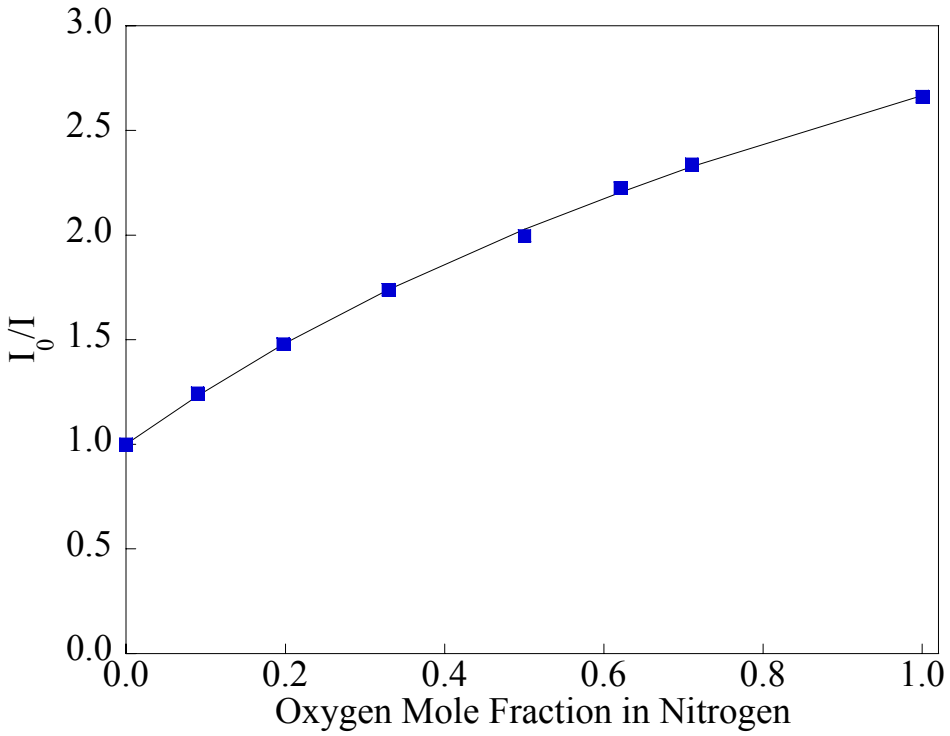

Figure 9. Stern-Volmer intensity plot of I_0/I vs oxygen mole fraction for [Λ-Ru(phen)$_3$](PF$_6$)$_2$. Filled blue squares (■) are experimental data, black line is the two-site model fit of the data.

Emission Lifetime Studies.

Solid-state emission lifetime data for the pure Δ and Λ enantiomers as well as the racemic salt were collected and are summarized with other spectroscopic and photophysical data in Table 4. Emission decay data were taken with samples under a nitrogen atmosphere and various concentrations of oxygen (Figure 10). Mono- and biexponential modeling of the emission decay data provided inadequate fits in each case. The emission decay data for all complexes and oxygen concentrations were satisfactorily modeled using three weighted exponentials. Data for both pure enantiomers were modeled independently with very similar sets of parameters. Data for pure nitrogen and pure oxygen are given in Table 4. In each case the emission decay is dominated by two decays (~630 and 205 ns under nitrogen) that are significantly quenched to differing extents in the presence of oxygen. The inclusion of a very small amount (0.05–3%) of a long-lived (~2 μs) third component that is not quenched in the presence of oxygen is needed to adequately model the time response of the decay. It is not known whether this long-lived component which is common to all samples, is an impurity or an instrumental artifact.

Table 4. Emission decay lifetimes and fractional components for 0 and 100 % oxygen for the chiral and racemic salts.

	Δ-[Ru(phen)$_3$](PF$_6$)$_2$		**Λ-[Ru(phen)$_3$](PF$_6$)$_2$**		**Δ, Λ-[Ru(phen)$_3$](PF$_6$)$_2$**	
Mole fraction O$_2$	0	1	0	1	0	1
α_a	0.448	0.711	0.510	0.683	0.882	0.408
τ_a (ns)	207	65.8	206	89.7	320	183
α_b	0.535	0.283	0.455	0.304	0.114	0.583
τ_b (ns)	631	300	664	284	765	384
α_c	0.0171	0.00606	0.0354	0.0129	0.00360	0.00887
τ_c (μs)	1.88	1.96	1.99	2.12	6.30	2.55
τ_M	0.462	0.143	0.464	0.175	0.392	0.321

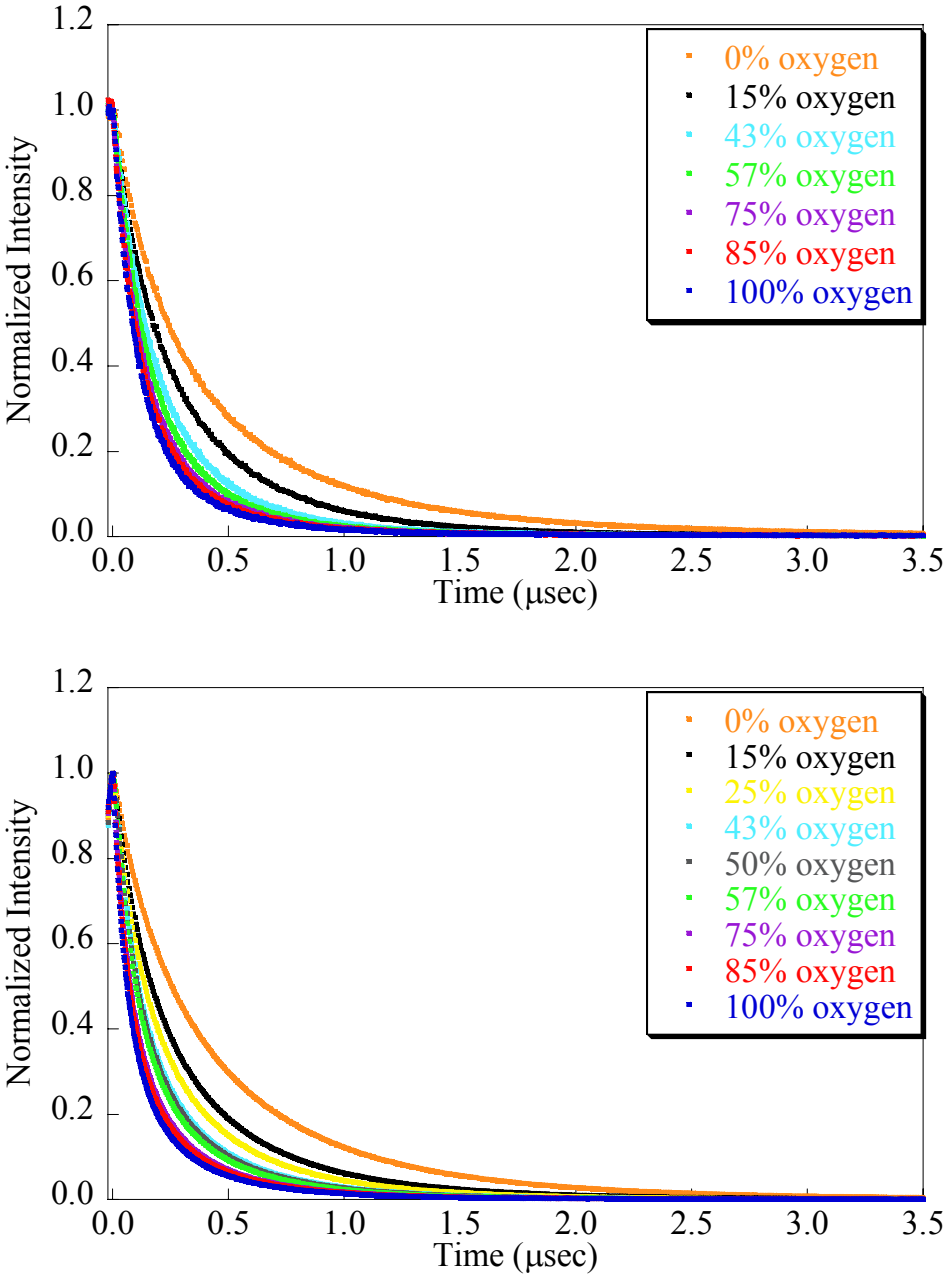

Figure 10. Normalized emission lifetime intensity decay of Λ-[Ru(phen)$_3$](PF$_6$)$_2$ (top) and Δ-[Ru(phen)$_3$](PF$_6$)$_2$ (bottom) at varying concentrations of oxygen.

The preexponential weighted mean lifetime, τ_M, as defined by Carraway and Demas, was used to compare the intensity and lifetime quenching data for evidence of static quenching.[52, 53]

$$\tau_M = \frac{\sum \alpha_i \tau_i}{\sum \alpha_i} \tag{6}$$

This weighted lifetime is calculated from the three exponential fit of the intensity decay curve where α_i are the normalized preexponential factors and τ_i are the observed lifetimes. If only dynamic (diffusional) quenching occurs then:

$$\frac{\tau_{M0}}{\tau_M} = \frac{I_0}{I} = \frac{1}{\frac{f_1}{1+K_{SV1}[O_2]} + \frac{f_2}{1+K_{SV2}[O_2]}} \tag{7}$$

and a Stern-Volmer plot using τ_{M0}/τ_M will closely match the intensity Stern-Volmer plot. The weighted emission lifetime Stern-Volmer plots for the Δ (Figure 11) and especially the Λ enantiomer (Figure 12) match the respective intensity plots quite well, ruling out any significant contribution of static quenching in the mechanism. The nearly identical behavior of the two chiral salts suggest that the underlying photophysical kinetics in the pure solid Δ and Λ enantiomers are virtually identical. It is interesting that the lifetime data require more fitting parameters than the intensity data would suggest, a situation that has been discussed by Demas *et al* as well as others.[18, 53-55] As Demas has suggested for oxygen quenching of ruthenium polypyridyls in polymer matrices, the parameters from the lifetime fitting are not necessarily directly interpretable but are more likely composites of the real parameters that result from a more complicated photophysical mechanism.[53] Further efforts are underway to derive an underlying photophysical model.

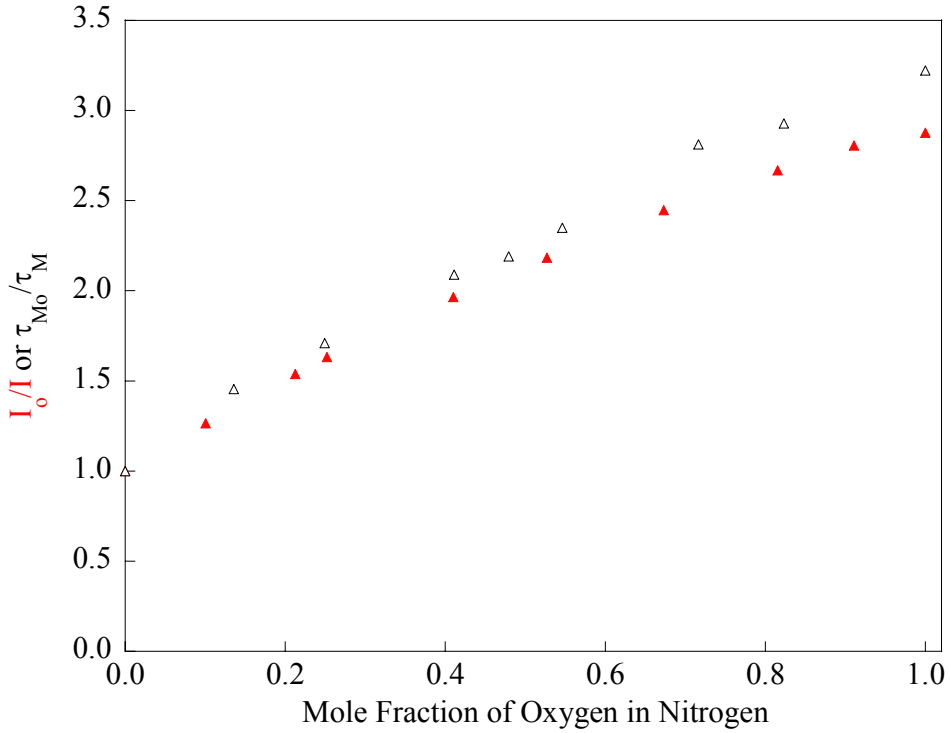

Figure 11. Overlayed intensity (▲) and preexponential weighted mean lifetime (△) Stern-Volmer data for Δ-$[Ru(phen)_3](PF_6)_2$.

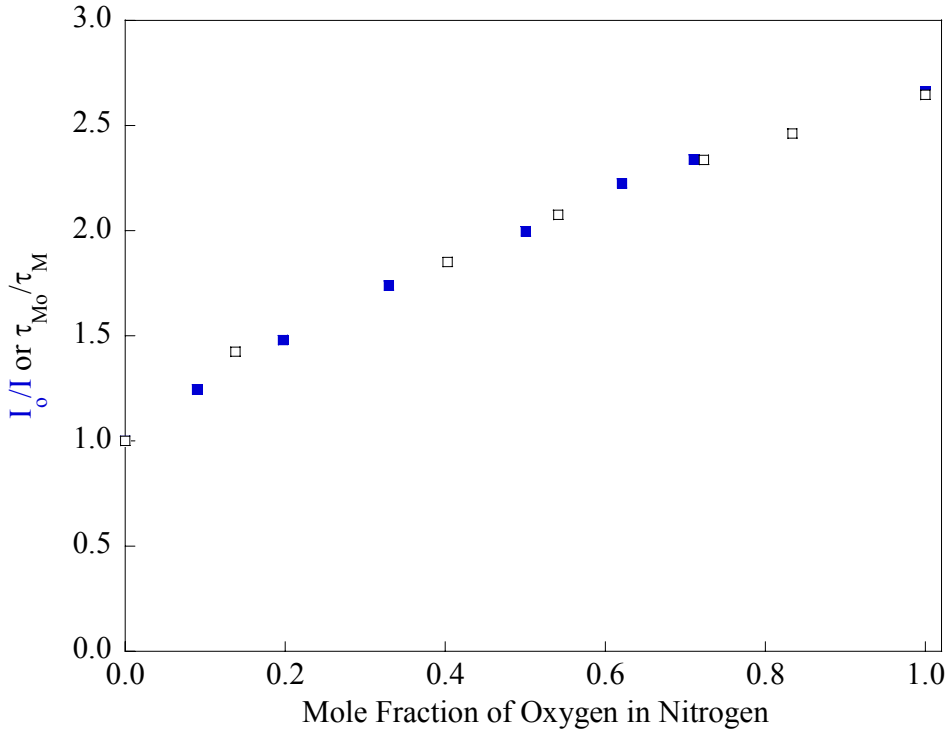

Figure 12. Overlayed intensity (■) and preexponential weighted mean lifetime (□) Stern-Volmer data for Λ-$[Ru(phen)_3](PF_6)_2$.

Calculation of the excited state hopping rate in $[Ru(phen)_3](tfpb)_2$.

Energy migration via excited state hopping between the two crystallographically distinct sites with different oxygen quenching rates was examined as a viable model to explain the complicated photophysics observed. Estimation of the hopping rate constant k_{hop} in the chiral $[Ru(phen)_3](PF_6)_2$ species was calculated in an analogous manner to that of $[Ru(phen)_3](tfpb)_2$ (Chapter 1) from the following equation:[56]

$$\ln k_{hop} = \ln k^0{}_{hop} - \beta(R - R_0) \tag{8}$$

where β, R, and $k^0{}_{hop}$ are an attenuation factor, the center-to-center distance between ruthenium atoms in the crystal and the hopping rate constant at the van der Waals distance (R_0 = 6.1 Å), respectively. The parameters β = 45 nm^{-1} and $k^0{}_{hop}$ = 6.8 x 10^{12} s^{-1} were evaluated previously from measurements made for $[Ru(bpy)_3](X)_2$ where X^- = Cl^-, ClO_4^- and PF_6^- and are the same as those used previously for $[Ru(phen)_3](tfpb)_2$ (Chapter 1).[56] The value calculated for k_{hop} at the closest Ru–Ru distance (R = 9.192 Å, between two crystallographically equivalent ruthenium cations) found in the Δ-$[Ru(phen)_3](PF_6)_2$ crystal is 6.2 x 10^6 s^{-1}. This value allows the excited state diffusion coefficient to be estimated from equation 9:

$$D = \frac{k_{hop} R^2}{2} \tag{9}$$

which gives for R = 9.192 Å and k_{hop} = 6.2 x 10^6 s^{-1} a D of 2.6 x 10^{-8} cm^2 s^{-1}. For the two different τ values of Δ-$[Ru(phen)_3](PF_6)_2$ in the crystal (630 and 207 ns), k_{rad} = 1.6 x 10^6 and 4.8 x 10^6 s^{-1}. The average diffusion distance ($l_{diffusion}$) of an excited state during its lifetime (τ) is approximated by equation 10:

$$l_{diffusion} = \sqrt{D\tau} \tag{10}$$

For the two different τ values of Δ-[Ru(phen)$_3$](PF$_6$)$_2$ in the crystal (630 and 207 ns) and D of 2.6 x 10^{-8} cm^2 s^{-1}, $l_{diffusion}$ is 12.8 and 7.3 Å respectively.

Examining the nearest neighbor crystallographically inequivalent Ru cations with a distance of R = 10.42 Å we find k_{hop} = 2.5 x 10^4 s^{-1}, D = 1.3 x 10^{-10} s^{-1}, k_{rad} = 1.6 x 10^6 (630 ns) and 4.8 x 10^6 s^{-1} (207 ns), and $l_{diffusion}$ = 0.92 and 0.53 Å.

It appears that energy migration via two crystallographically inequivalent Ru sites would be unlikely as the rate constant for radiative decay is two orders of magnitude faster than that of energy transfer via excited state hopping. However, energy transfer between crystallographically equivalent sites is more likely as the rate constants for hopping and radiative decay are of the same order of magnitude, 10^6. Without a clear preference for energy migration via hopping of excited states, i.e. $k_{hop} >> k_{rad}$, we cannot conclusively say whether quenching by oxygen only at the illuminated surface or by excitonic hopping of the excited state to trapped oxygen molecules near the surface is occurring.

Conclusions.

$[Ru(phen)_3]Cl_2$ was chemically resolved into Δ and Λ enantiomers and then metathesized to PF_6^- salts. Pure Δ-$[Ru(phen)_3](PF_6)_2$ and Λ-$[Ru(phen)_3](PF_6)_2$ salts exhibit the same crystalline structure and contain a narrow channel of open space running though the structure, as well as another larger channel occupied by co-crystallized solvent molecules. In contrast, crystals of the racemic mixture contain a much smaller amount of open space in the form of isolated voids which do not allow significant oxygen diffusion. The chiral salts exhibit increased sensitivity to oxygen with mild heating; thermogravimetric experiments support the loss of acetonitrile which increases the fraction of void space in the crystals. The Stern-Volmer quenching behavior of these materials correlates with the oxygen accessible volume; the chiral salts exhibit significant quenching with increasing oxygen concentration while the racemic salt exhibits very little quenching. These systems demonstrate that chiral packing offers an alternative to the bulky fluorinated counterions used previously to generate the void space channels within crystalline solids necessary for oxygen diffusion and detection.

References.

1. Ando, M., *TrAC, Trends Anal. Chem.* **2006**, *25*, 937.

2. Demas, J. N.; DeGraff, B. A., *Coord. Chem. Rev.* **2001**, *211*, 317.

3. Demas, J. N.; DeGraff, B. A.; Coleman, P. B., *Anal. Chem.* **1999**, *71*, 793A.

4. Mills, A., *Platinum Met. Rev.* **1997**, *41*, 115.

5. Zhao, Y.; Richman, A.; Storey, C.; Radford, N. B.; Pantano, P., *Anal. Chem.* **1999**, *71*, 3887.

6. Amao, Y.; Okura, I., *Sens. Actuators, B* **2003**, *B88*, 162.

7. Demas, J. N.; DeGraff, B. A.; Xu, W., *Anal. Chem.* **1995**, *67*, 1377.

8. Draxler, S.; Lippitsch, M. E.; Klimant, I.; Kraus, H.; Wolfbeis, O. S., *J. Phys. Chem.* **1995**, *99*, 3162.

9. Ertekin, K.; Kocak, S.; Sabih Ozer, M.; Aycan, S.; Cetinkaya, B., *Talanta* **2003**, *61*, 573.

10. Fuller, Z. J.; Bare, W. D.; Kneas, K. A.; Xu, W. Y.; Demas, J. N.; DeGraff, B. A., *Anal. Chem.* **2003**, *75*, 2670.

11. Garcia-Fresnadillo, D.; Marazuela, M. D.; Moreno-Bondi, M. C.; Orellana, G., *Langmuir* **1999**, *15*, 6451.

12. Hartmann, P.; Leiner, M. J. P.; Lippitsch, M. E., *Anal. Chem.* **1995**, *67*, 88.

13. Huynh, L.; Wang, Z.; Yang, J.; Stoeva, V.; Lough, A.; Manners, I.; Winnik, M. A., *Chem. Mater.* **2005**, *17*, 4765.

14. Kneas, K. A.; Demas, J. N.; Nguyen, B.; Lockhart, A.; Xu, W.; DeGraff, B. A., *Anal. Chem.* **2002**, *74*, 1111.

15. Kneas, K. A.; Xu, W.; Demas, J. N.; DeGraff, B. A., *Appl. Spectrosc.* **1997**, *51*, 1346.

16. McMurray, H. N.; Douglas, P.; Busa, C.; Garley, M. S., *J. Photochem. Photobiol. A* **1994**, *80*, 283.

17. McNamara, K. P.; Li, X.; Stull, A. D.; Rosenzweig, Z., *Anal. Chim. Acta* **1998**, *361*, 73.

18. Mills, A., *Analyst* **1998**, *123*, 1135.

19. Morin, A. M.; Xu, W.; Demas, J. N.; DeGraff, B. A., *J. Fluoresc.* **2000**, *10*, 7.

20. Navarro-Villoslada, F.; Orellana, G.; Moreno-Bondi, M. C.; Vick, T.; Driver, M.; Hildebrand, G.; Liefeith, K., *Anal. Chem.* **2001**, *73*, 5150.

21. Preininger, C.; Klimant, I.; Wolfbeis, O. S., *Anal. Chem.* **1994**, *66*, 1841.

22. Ruffolo, R.; Evans, C. E. B.; Liu, X.-H.; Ni, Y.; Pang, Z.; Park, P.; McWilliams, A. R.; Gu, X.; Lu, X.; Yekta, A.; Winnik, M. A.; Manners, I., *Anal. Chem.* **2000**, *72*, 1894.

23. Wang, Z.; McWilliams, A. R.; Evans, C. E. B.; Lu, X.; Chung, S.; Winnik, M. A.; Manners, I., *Adv. Funct. Mater.* **2002**, *12*, 415.

24. Coutant, M. A.; Payra, P.; Dutta, P. K., *Microporous Mesoporous Mater.* **2003**, *60*, 79.

25. Meier, B.; Werner, T.; Klimant, I.; Wolfbeis, O. S., *Sens. Actuators, B* **1995**, *B29*, 240.

26. Bukowski, R. M.; Ciriminna, R.; Pagliaro, M.; Bright, F. V., *Anal. Chem.* **2005**, *77*, 2670.

27. Bukowski, R. M.; Davenport, M. D.; Titus, A. H.; Bright, F. V., *Appl. Spectrosc.* **2006**, *60*, 951.

28. Leventis, N.; Elder, I. A.; Rolison, D. R.; Anderson, M. L.; Merzbacher, C. I., *Chem. Mater.* **1999**, *11*, 2837.

29. Leventis, N.; Rawashdeh, A.-M. M.; Elder, I. A.; Yang, J.; Dass, A.; Sotiriou-Leventis, C., *Chem. Mater.* **2004**, *16*, 1493.

30. Murtagh, M. T.; Shahriari, M. R.; Krihak, M., *Chem. Mater.* **1998**, *10*, 3862.

31. Cheng, Z.; Aspinwall, C. A., *Analyst* **2006**, *131*, 236.

32. Chu, B. W.-K.; Yam, V. W.-W., *Langmuir* **2006**, *22*, 7437.

33. Jorge, P. A. S.; Mayeh, M.; Benrashid, R.; Caldas, P.; Santos, J. L.; Farahi, F., *Appl. Opt.* **2006**, *45*, 3760.

34. Kocincova, A. S.; Borisov, S. M.; Krause, C.; Wolfbeis, O. S., *Anal. Chem.* **2007**, *79*, 8486.

35. Krenske, D.; Abdo, S.; Van Damme, H.; Cruz, M.; Fripiat, J. J., *J. Phys. Chem.* **1980**, *84*, 2447.

36. Xiong, X.; Xiao, D.; Choi, M. M. F., *Sens. Actuators, B* **2006**, *B117*, 172.

37. FOXY Fiber Optic Oxygen Sensors; OceanOptics: Dunedin, F.

38. McGee, K. A.; Veltkamp, D. J.; Marquardt, B. J.; Mann, K. R., *J. Am. Chem. Soc.* **2007**, *129*, 15092.

39. Nakamura, A.; Sato, T.; Kuroda, R., *Chem. Commun.* **2004**, 2858.

40. Brock, C. P.; Schweizer, W. B.; Dunitz, J. D., *J. Am. Chem. Soc.* **1991**, *113*, 9811.

41. Herbstein, F. H., Crystalline Molecular Complexes and Compounds. In *IUCr Monographs on Crystallography - 18*, Oxford University Press: Oxford, 2005; Vol. 1, pp 571-574.

42. Lancaster, R. W.; Karamertzanis, P. G.; Hulme, A. T.; Tocher, D. A.; Covey, D. F.; Price, S. L., *Chem. Commun.* **2006**, 4921.

43. Maloney, D. J.; MacDonnell, F. M., *Acta Crystallogr., Sect. C: Cryst. Struct. Commun.* **1997**, *C53*, 705.

44. Blessing, R. H., *Acta Crystallogr., Sect. A: Found. Crystallogr.* **1995**, *A51*, 33.

45. Sheldrick, G. *SADABS*, v.2.03; 2002.

46. *SHELXTL*, v.6.12; Bruker AXS, Madison, WI, 2001.

47. Spek, A. L., *J. Appl. Crystallogr.* **2003**, *36*, 7.

48. Spek, A. L. *PLATON*, Utrecht University, Utrecht, The Netherlands, 2005.

49. Bruno, I. J.; Cole, J. C.; Edgington, P. R.; Kessler, M.; Macrae, C. F.; McCabe, P.; Pearson, J.; Taylor, R., *Acta Crystallographica, Section B: Structural Science* **2002**, *B58*, 389.

50. Breu, J.; Stoll, A. J., *Acta Crystallogr., Sect. C: Cryst. Struct. Commun.* **1996**, *C52*, 1174.

51. Avian Technolgies, 1 Worthington Rd. , P.O. Box 822 , Wilmington, OH 45177, USA; http://www.aviantechnologies.com/faq.html.

52. Carraway, E. R.; Demas, J. N.; DeGraff, B. A., *Anal. Chem.* **1991**, *63*, 332.

53. Carraway, E. R.; Demas, J. N.; DeGraff, B. A.; Bacon, J. R., *Anal. Chem.* **1991**, *63*, 337.

54. Demas, J. N.; DeGraff, B. A., *Sens. Actuators, B* **1993**, *B11*, 35.

55. Klimant, I.; Wolfbeis, O. S., *Anal. Chem.* **1995**, *67*, 3160.

56. Ikeda, N.; Yoshimura, A.; Tsushima, M.; Ohno, T., *J. Phys. Chem. A* **2000**, *104*, 6158.

Chapter 3

Concurrent Sensing of Benzene and Oxygen by a Crystalline Salt of Tris(5,6-dimethyl-1,10-phenanthroline)ruthenium(II)

Abstract

The complex $[Ru(5,6\text{-}Me_2Phen)_3](tfpb)_2$ has been examined as a solid-state benzene and oxygen sensor. The crystalline solid undergoes a reversible vapochromic shift of the emission λ_{max} to higher energy in the presence of benzene. Additionally, in the presence of oxygen the solid exhibits linear Stern-Volmer quenching behavior. When simultaneously exposed to benzene vapor and oxygen the crystals uptake benzene which inhibits the diffusion of oxygen in the lattice; very little quenching is observed. However, when benzene is removed from the carrier gas, partial loss of benzene occurs and oxygen diffusion is restored resulting in quenching of the emission. The practicality of this crystalline solid as a benzene sensor was investigated by examination of a low concentration of benzene vapor (0.76%).

Introduction

Volatile organic compounds (VOCs) such as benzene, toluene, chloroform, and methylene chloride are common organic pollutants emitted as gases from household products. Exposure by inhalation or skin contact to these VOCs, as well as others, can result in both short- and long-term adverse health effects.[1] At this time not much is known about the health effects from the levels of VOCs found in homes and workplaces, though the resultant cancer in animals caused by many organics makes determination of this information a priority. It *is* known that concentrations of many VOCs are consistently higher indoors than outdoors (up to 10 times higher).[1] Benzene, found in tobacco smoke, stored fuels and paint supplies, and automobile emissions is a concern due to its classification in human carcinogen group A by the US EPA.[1, 2] The very low recommended exposure limits and toxicity of benzene require advanced sensing technology with low detection limits to be a priority.[3]

Optical technologies are promising candidates for detection of many analytes including VOCs. Optical sensors offer many advantages over currently used sensors utilizing gas chromatography/mass spectrometry (GC/MS) which require longer assay time and expensive reagents and apparatus.[4, 5] Optical sensors offer the possibility of fast response time, high sensitivity, and remote controllability as well as compactness due to employment of fiber optics and LED excitation sources. Optical technologies have been explored by several groups for detection of benzene including use of absorbance[6, 7], fluorescence[8-10], and infrared[11] spectroscopies as well as other methods[12-14].

Transition-metal complexes that exhibit low-lying excited states (i.e. metal-to-ligand charge-transfer (MLCT) excitations) can make them particularly well-suited for

the detection of small molecules with environmental or industrial relevance.[15-23] Optical sensors built around metal complexes of this type have become increasingly popular.[15, 19, 23] The detection of gases with crystalline platinum salts that can uptake VOCs[24-26] has been an area of interest to us for several years. The reversible change in the unit cell composition results in a perturbation of the Pt–Pt distance which controls the color of the complexes ("vapochromism").[27, 28] Many of these compounds also show a dramatic reversible shift in the position and/or intensity of the luminescence ("vapoluminescence") that may be excited by light-emitting diodes and detected with inexpensive photodiode array spectrometers.

More recently, we have reported an alternative to the currently used polymer-supported sensors for luminescence quenching-based oxygen detection that relies on crystalline salts of $Ru(phen)_3^{2+}$. These salts have void space channels that allow oxygen to diffuse freely through the crystal to quench the luminescence.[29] These channels are produced by the poor packing of bulky anions with the propeller-shaped cations.[29]

We hypothesized that these two crystalline sensing systems might be combined into a single system that could sense VOCs and oxygen through their respective mechanisms by choosing a solvatochromic chromophore (MLCT) with a long lifetime that could undergo oxygen quenching but also exhibit a vapoluminescent shift upon solvent molecule uptake into the crystal lattice. The melding of these two sensor mechanisms into a functioning example has been realized. We report here the preliminary investigation of $[Ru(5,6\text{-}Me_2Phen)_3](tfpb)_2$ (5,6-Me_2Phen = 5,6-dimethyl-1,10-phenanthroline; $tfpb^-$ = tetrakis(bis-3,5-trifluoromethylphenylborate), a crystalline complex that senses benzene and oxygen, simultaneously, by different mechanisms.

Experimental

General Considerations. NMR spectra were recorded on Varian Unity (300 MHz) or Varian Inova (300 MHz) instruments. The following chemicals were purchased as indicated: $[Ru(phen)_3]Cl_2 \cdot x\ H_2O$ (phen = 1,10-phenanthroline) : Aldrich Chemical Co.; 5,6-Me_2Phen (5,6-Me_2Phen = 5,6-dimethyl-1,10-phenanthroline) from Pfaltz and Bauer; Na(tfpb) (tfpb = tetrakis(bis-3,5-trifluoromethylphenylborate)) was synthesized in a previous study.[30] $Ru(DMSO)_4Cl_2$ was synthesized[31] by the method of Wilkinson et al. $[Ru(5,6\text{-}Me_2Phen)_3]Cl_2$ was synthesized[32, 33] from $Ru(DMSO)_4Cl_2$ by the method of Elliot et al.

$[Ru(5,6\text{-}Me_2Phen)_3](tfpb)_2$. The salt $[Ru(5,6\text{-}Me_2Phen)_3](tfpb)_2$ was synthesized by a methathesis reaction by adding a slight stoichiometric excess of a solution of Na(tfpb) in methanol to a methanolic solution of the $Ru(5,6\text{-}Me_2Phen)_3Cl_2$ compound. The addition of water to this solution resulted in the precipitation of $[Ru(5,6\text{-}Me_2Phen)_3](tfpb)_2$. After filtration, $[Ru(5,6\text{-}Me_2Phen)_3](tfpb)_2$ was purified to remove Ru(III) contaminants by chromatography on neutral alumina with CH_2Cl_2/acetone and then crystallized by slow evaporation of CH_2Cl_2/benzene. ^{1}H NMR (CD_3CN): δ 8.69 (dd, 6 H, J = 1.2, 8.7 Hz), 7.90 (dd, 6 H, J = 0.9–1.2, 5.3 Hz), 7.68 (m, 24 H), 7.58 (dd, 6 H, J = 5.1, 8.4 Hz), 2.82 (s, 18 H). ^{19}F NMR (CD_3CN): δ -63.85 (s).

Collection of Stern-Volmer emission intensity measurements and benzene detection. Data for the emission intensity Stern-Volmer plot were collected with the apparatus shown in Figure 1. All measurements were made at atmospheric pressure which was 736 Torr. A swage cross fitting was used as the cell. One port was used to hold a 100 °C thermistor with a small depression to hold the solid. The microcrystalline solid was

finely ground to maximize the surface area and was then placed on the thermistor and adhered with benzene which was allowed to evaporate. A photograph taken through a microscope of the actual sample used for many of the measurements made in this study is shown in Figure 2. A second port (in the 90 degree position relative to the sample to allow front face illumination) was used for a bifurcated (six-around-one fiber) fiber optic probe. Two other ports were used for gas inlets and outlets. The atmosphere in the cell was controlled by mass-flow controlled valves under computer control. Light from a 400 nm LED was sent into the cell through one leg of the fiber optic probe to illuminate the sample on the thermistor. Emitted light was returned through the other leg into an Ocean Optics CCD spectrophotometer. The emission spectra were integrated and I_0/I (I_0 is defined as the integrated intensity for the emission spectrum from the sample under pure nitrogen) was calculated for each oxygen mole fraction measured. At least three replicates were used for each point plotted, collected in a "stair case" fashion with respect to oxygen concentration. To make a benzene saturated atmosphere for study of the benzene sensitivity, the carrier gas was purged through liquid benzene. For lower concentrations this benzene saturated stream was then diluted with another inlet of pure carrier gas.

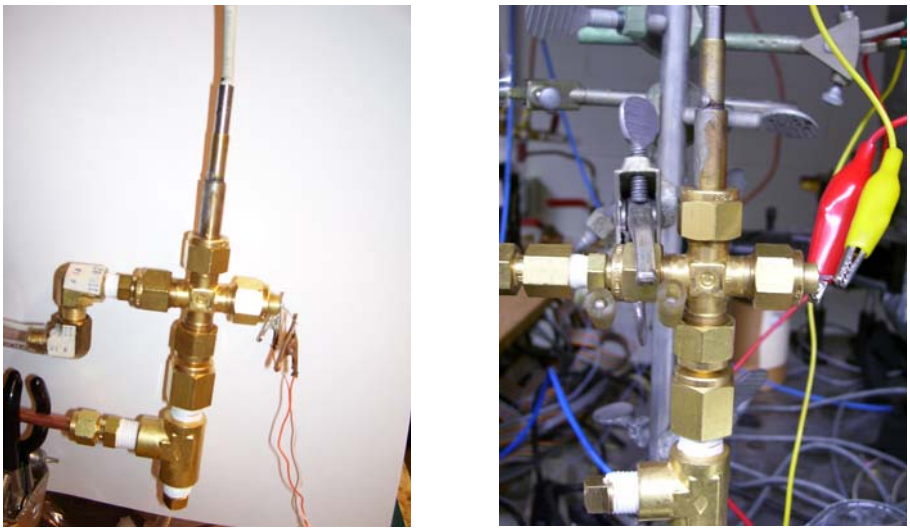

Figure 1. Swagelok cross cell (left) used for benzene detection measurements and Swagelok cross cell (right) used for Stern-Volmer oxygen data collection.

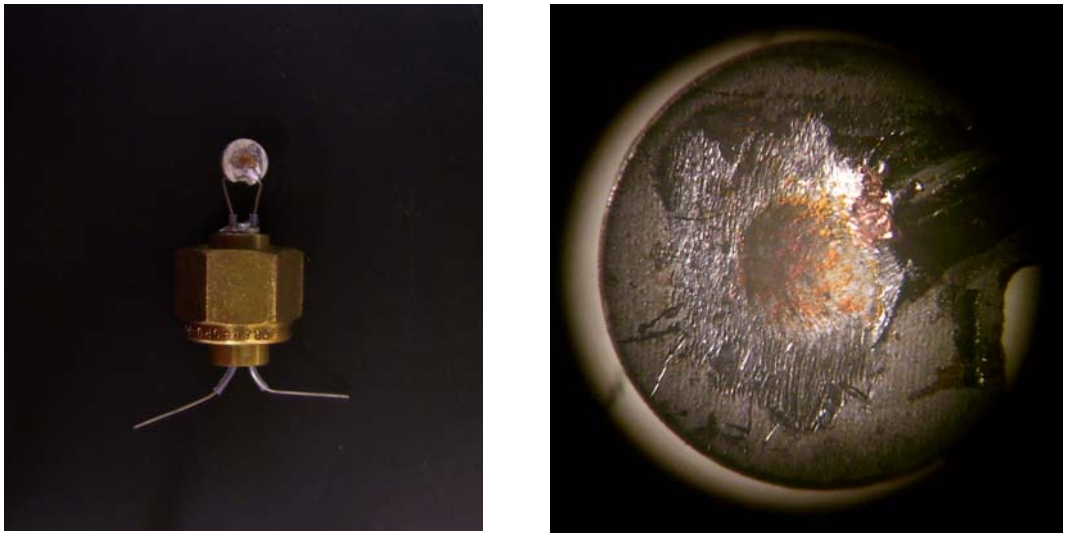

Figure 2. Photograph of thermistor with sample (left) and $[Ru(5,6\text{-}Me_2Phen)_3](tfpb)_2$ microcrystals at 25x in the depression of a 100 °C thermistor (right).

Principle Component Analysis. A series of emission spectra were taken while cycling between the carrier gases (either air or nitrogen), benzene vapor plus the carrier gas, and again the carrier gas after exposing the crystals to benzene. Thirteen cycles (6 with air and 7 with nitrogen) for a total of 39 spectra were taken over a period of 2 hours. Each spectrum consists of an intensity at each of the 2048 wavelengths (from 177.5 to 875 nm). The data were processed with a Notebook written in Mathematica (version 5.2) to perform PCA as discussed in reference 12.[34] Every tenth wavelength was used in the PCA analysis (a total of 205). These data were mean centered and decomposed into principle components (scores). The first three scores represent 74.1, 24.4 and 1.47 % of the variance; the first two scores are plotted in Figure 7. The loading plots, which show where the differences are between spectra, for scores 1 and 2 (Figures 8 and 9) show them to be mainly a wavelength shift (score 1) and an intensity change (score 2) that correlate with a change from no benzene to benzene present and nitrogen to air, respectively.

Single Crystal X-ray Crystallography. The crystal structure of [Ru(5,6-Me_2Phen)$_3$](tfpb)$_2$ was determined for this study. Relevant crystallographic data are shown in Table 1. Crystals were grown by slow evaporation of a saturated solution of CH_2Cl_2 and benzene. The data for the structure determination was collected at the X-ray Crystallographic Laboratory (Department of Chemistry, University of Minnesota).[35]

A single crystal was attached to a glass fiber and mounted on a Bruker SMART Platform CCD for data collection at 173 K using graphite-monochromated Mo Kα radiation (λ = 0.71073 Å). An initial set of cell constants was calculated from 266 reflections harvested from three sets of 20 frames oriented such that orthogonal wedges

of reciprocal space were surveyed. Final cell constants were calculated from 3610 strong reflections from the actual data collection. Data were collected to the extent of 1.5–2.0 hemispheres at a resolution of 0.84 Å using ϕ-scans. The intensity data were corrected for absorption and decay using SADABS.[36, 37]

Table 1. Crystallographic information for $[Ru(5,6\text{-}Me_2Phen)_3](tfpb)_2$.

Compound	$[Ru(5,6\text{-}Me_2Phen)_3](tfpb)_2$
empirical formula	$C_{225}\ H_{134}\ B_4\ Cl_2\ F_{96}\ N_{12}\ Ru_2$
crystal color, morphology	orange-red, block
crystal system	Monoclinic
space group	$P2_1/c$
a, Å	27.231(2)(2)
b, Å	16.6067(14)
c, Å	24.790(2)
α, deg	90
β, deg	93.714(2)
γ, deg	90
volume, Å^3	11186.8(16)
Z	4
formula weight, g mol^{-1}	2572.86
density (calculated), g cm^{-3}	1.528
temperature, K	173(2)
Absorption coefficient, mm^{-1}	0.295
F(000)	5148
θ range, deg	1.50 to 25.07
index ranges	$-32 \le h \le 32$
	$-19 \le k \le 19$
	$-29 \le l \le 29$
reflections collected	108033
independent reflections	19818 (R_{int} = 0.0435)
weighting factors[a] *a,b*	0.101600, 2.735200
max, min transmission	0.970000, 0.849770
Data/restraints/parameters	19818/456/1882
R_1, wR_2 [$I > 2\sigma(I)$]	0.0575, 0.1726
R_1, wR_2 (all data)	0.0791, 0.1861
GOF	1.241
largest diff. peak, hole, eÅ^{-3}	1.845, -1.087

[a] $w = [\sigma^2(F_o^2) + (aP)^2 + (bP)]^{-1}$, where $P = (F_o^2 + 2F_c^2)/3$.

The space group $P2_1/c$ was determined based on systematic absences and intensity statistics. The structure was determined by a direct-methods solution. Several full-matrix least-squares/difference Fourier cycles were performed to locate remaining non-hydrogen atoms. All calculations were performed using the SHELXTL-V6.12 suite of programs[38] on Pentium computers. Packing analysis parameters and solvent accessible void dimensions were measured using PLATON/VOID and PLATON/CAVITY[39, 40] with pictorial representations of the solvent channels made with edited .res files in Mercury[41]. The detection of solvent accessible voids by PLATON/VOID and PLATON/CAVITY[39, 40] is done in the following way: The unit cell is filled with the atoms from the structural model and each specific atom is assigned its respective van der Waals radius. A grid search generates a list of grid points with a minimum distance of 1.2 Å from the nearest van der Waals surface. This list of grid points is then used to produce a new list of grid points that makes up the solvent accessible areas. For the sets of grid points, the center of gravity and volume of the void are calculated. The overall solvent accessible volume is calculated along with the volume and center of gravity of individual 'voids'.

Solvent channels which hold benzene molecules and isolated voids containing dichloromethane exist in the structure. One benzene molecule, which is near a ruthenium cation in the solvent channel, was able to be placed in the asymmetric unit. This benzene molecule was restrained to be planar using a FLAT statement. Another benzene molecule which lies in the center of the solvent channel, only near other benzene molecules, was highly disordered over a special position. The electron density of this benzene molecule was not able to be sufficiently modeled and additional information concerning the residual electron density was obtained with PLATON/SQUEEZE[39, 40].

The void space consists of 153 electrons per cell (about 2 benzene molecules) which occupy 539.5 $Å^3$, amounting to one-half of a benzene molecule per ruthenium atom. The original data were corrected for the disordered solvent. The dichloromethane molecule lies in close proximity (less than the van der Waal's (VDW) radii of the atoms) to a rotationally disordered trifluoromethyl group of one of the $tfpb^-$ counterions and had extremely large ellipsoids as is sometimes seen when a partially occupied atom is modeled as fully occupied. The components of the disordered trifluoromethyl groups refined to near 50:50. It is likely that when the trifluoromethyl group is in the conformation in which no less-than-VDW contacts exist, the dichloromethane is present in the cell, while when the trifluoromethyl group is in the second conformation (which leads to the less-than-VDW contacts) the dichloromethane molecule is absent. Therefore, the dichloromethane and the trifluoromethyl groups were modeled as half occupied.

Thermal rotation of the trifluoromethyl groups of the $tfpb^-$ counterions was problematic leading to large ellipsoids. The fluorine atoms were split into two parts and their occupancies were allowed to refine with a free variable. To originally lock the fluorine atoms into place an AFIX 127 command was applied to constrain the fluorine atoms to be at 60° from each other and to ride on the preceding atom, rotating about the C–X bond (C–C in the case of $tfpb^-$). This bond distance was constrained to be 1.3361 Å. Pairs of fluorine atoms on three of the four disordered trifluoromethyl groups were constrained to have the same thermal parameters using an EADP command. The disordered fluorine atoms of the remaining trifluoromethyl group were restrained to have similar thermal parameters using a SIMU restraint. The AFIX 127 commands were then removed and the fluorines were allowed to refine freely.

Results and Discussion.

$Ru(5,6\text{-}Me_2Phen)_3]Cl_2$ was synthesized by a standard method[32, 33] and converted to the $tfpb^-$ salt (Figure 3) which was characterized by ^1H NMR and an X-ray crystal structure (*vida infra*). The emission behavior of a solvent-free crystalline sample of $[Ru(5,6\text{-}Me_2Phen)_3](tfpb)_2$ in the presence of different oxygen concentrations in nitrogen was investigated. Significant quenching of the solid-state emission was observed, and the resulting Stern-Volmer plot is linear with a slope of 0.83 (Figure 4).[42] The slope is less than that found for the recently studied $[Ru(phen)_3](tfpb)_2$ system but $[Ru(5,6\text{-}Me_2Phen)_3](tfpb)_2$ is still a significant oxygen sensor relative to many of the solid ruthenium polypyridine complexes that we examined.[29]

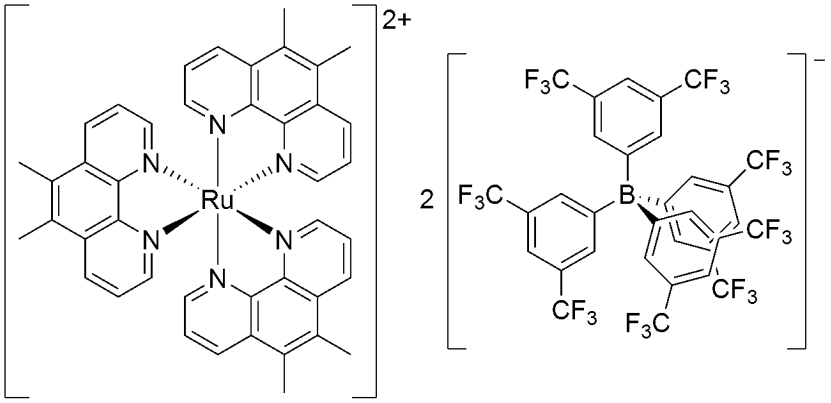

Figure 3. Structure of $[Ru(5,6\text{-}Me_2Phen)_3](tfpb)_2$.

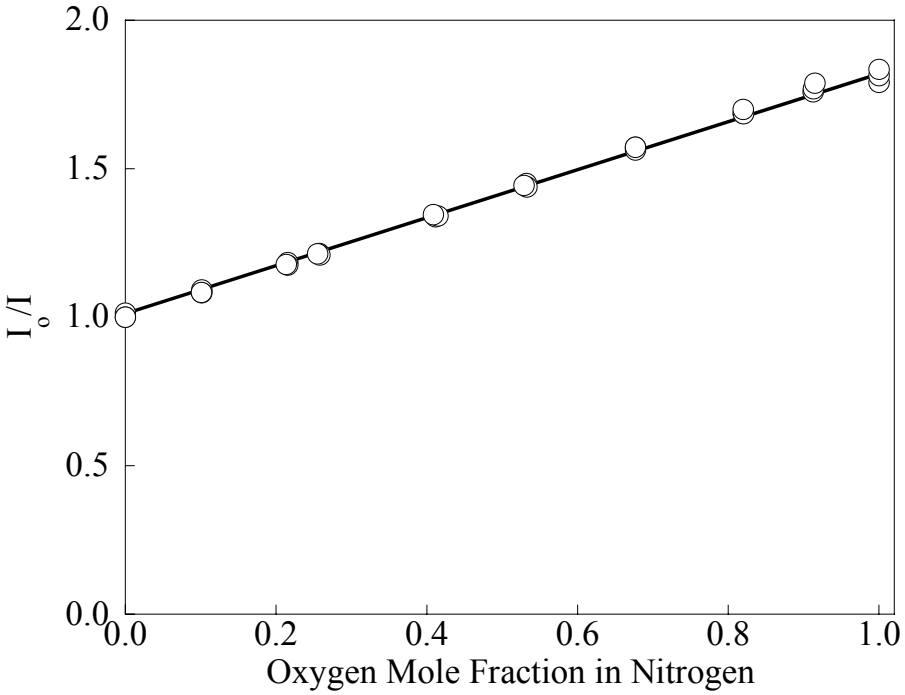

Figure 4. Stern-Volmer plot of I_0/I versus oxygen mole fraction for [Ru(5,6-Me_2Phen)$_3$](tfpb)$_2$.

Benzene Detection.

A sample was studied to measure the spectroscopic changes in the emission spectrum in the presence of benzene. The microcrystalline solid was finely ground to maximize the surface area and then placed in a small depression in the center of a 100 °C thermistor. After an initial heating cycle to 100 °C, followed by cooling to room temperature, the sample was exposed to nitrogen gas saturated with benzene vapor. The resulting spectral changes are shown in Figure 5. A fast spectral change that is dominated by a shift in λ_{max} from 572 to 558 nm is apparent. This change is fast (less than 50 s to reach 90% of the total change). The reverse process that results from purging of the benzene-loaded sample with pure nitrogen is slower (1 h to reach 90% of the total change). The sample can be repeatedly cycled with no loss of emission intensity. Heating the benzene-loaded sample with the thermistor results in a much more rapid reversal (90 s, including cooling time) to the solvent-free state; again, the sample may be cycled repeatedly. Of initial interest here is the cause of the large reversible shift in the emission λ_{max}. We suggest that this spectral change is a vapoluminescence effect that occurs as a result of the interaction of benzene with the luminescent cation.

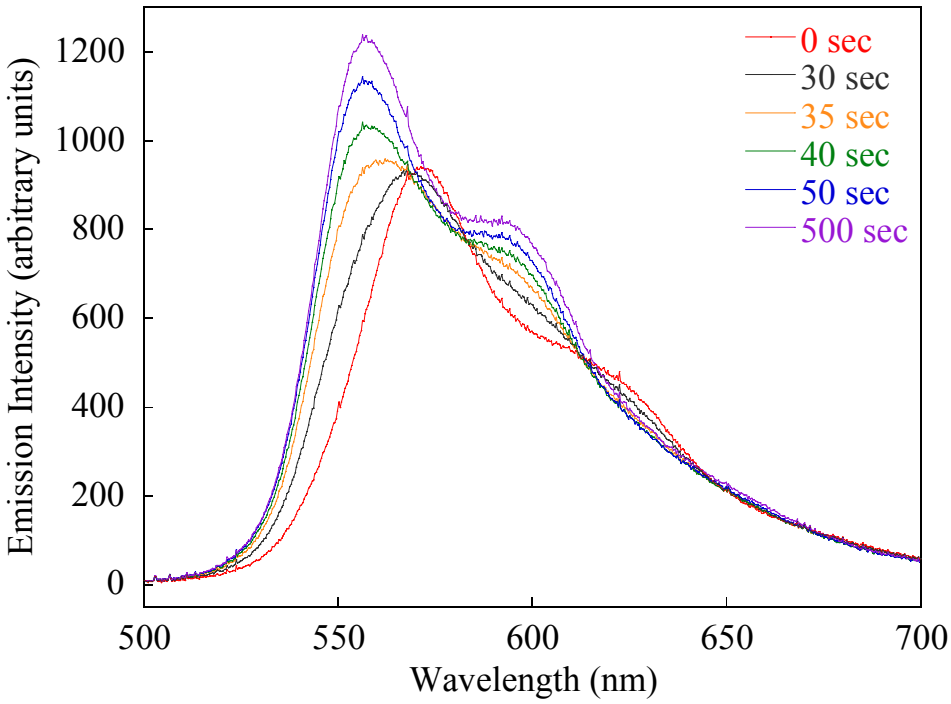

Figure 5. Emission spectral change that results from $[Ru(5,6\text{-}Me_2Phen)_3](tfpb)_2$ in the presence of nitrogen saturated with benzene.

Cross Sensitivity to Benzene and Oxygen.

To determine the applicability and cross-sensitivities of [Ru(5,6-Me_2Phen)$_3$](tfpb)$_2$ for the simultaneous sensing of benzene and oxygen, a series of emission spectra were taken while cycling between the carrier gases (either air or nitrogen), benzene vapor plus the carrier gas, and again the carrier gas after exposure of the crystals to benzene. A total of 13 cycles (6 with air and 7 with nitrogen) for a total of 39 spectra were taken over a period of 2 h. First a sequence of spectra were taken at room temperature in the following order: under a nitrogen atmosphere (**A**), while under a benzene saturated nitrogen atmosphere (**X**), and lastly under a nitrogen atmosphere with the benzene again removed from the flow (**G**) (Scheme 1, top). A heating cycle under a pure nitrogen purge returned the sample from **G** to the original solvation state (**A**) and the process could be repeated. A second sequence (Scheme 1, bottom) was also completed with air instead of nitrogen as the purge gas to give the same benzene solvation states in an air atmosphere (**B**, **Y**, **H**). The pair wise comparisons between the two cycles (**A** with **B**, **X** with **Y**, and **G** with **H**) show the changes in oxygen sensitivity with varying concentrations of benzene in the crystalline lattice. Representative spectra from each exposure condition are shown in Figure 6.

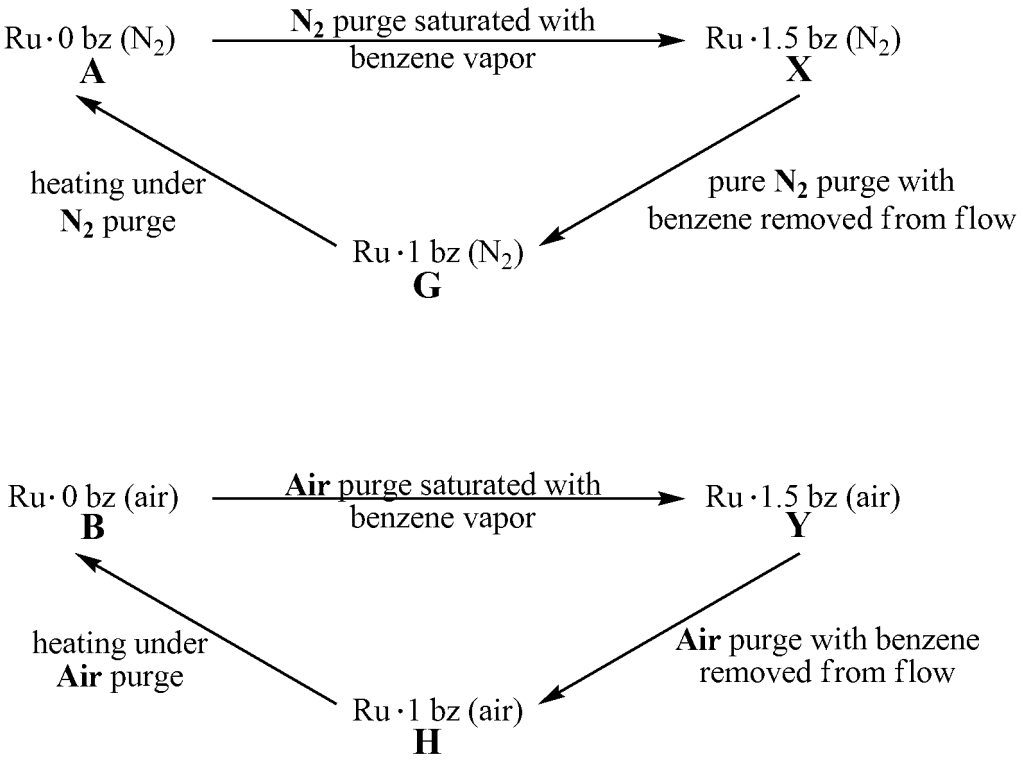

Scheme 1. Experimental procedure for examining the cross sensitivity of [Ru(5,6-Me_2Phen)$_3$](tfpb)$_2$ to benzene and oxygen. Top, cycling of benzene solvation states under a nitrogen atmosphere. Bottom, same cycling of benzene solvation states under an air atmosphere. The representative letter for each state matches that in the emission spectral graph (Figure 6) and the PCA analysis graph (Figure 7).

These data were analyzed via a principle component analysis (PCA). Almost all of the variance (98%) was modeled with two principle components. A score plot (score 2 vs score 1) is shown in Figure 7. The data show a high degree of reversibility, and the six different data clusters that correspond to each of the six different conditions generated by the experimental design are apparent. The small systematic drift of data points within each cluster may be due to a slight loss in reversibility due to the rapid heating employed. The loading plots of score 1 and score 2 show that score 1 is associated with benzene sensing (a spectral shift) and score 2 (an intensity change) with oxygen sensing (Figures 8 and 9). Switching the nonsolvated form from a nitrogen atmosphere to air (cluster **A** to **B**) causes a large shift along the score 2 axis, consistent with the simple Stern-Volmer oxygen sensing behavior reported above. A similar exposure change between nitrogen and air but with the carrier gas saturated with benzene (cluster **X** to **Y**) results in a much smaller excursion along the score 2 axis, with both conditions significantly shifted along the score 1 axis. Finally, the prior loading of benzene into the sample with nitrogen followed by a removal of benzene from the purge at room temperature results in a change from cluster **X** to **G**; subsequent change in purge gas between nitrogen and air without benzene in the purge (cluster **G** to **H**) retains the similar large excursion along score 1, but now the large change along the score 2 axis is mostly restored.

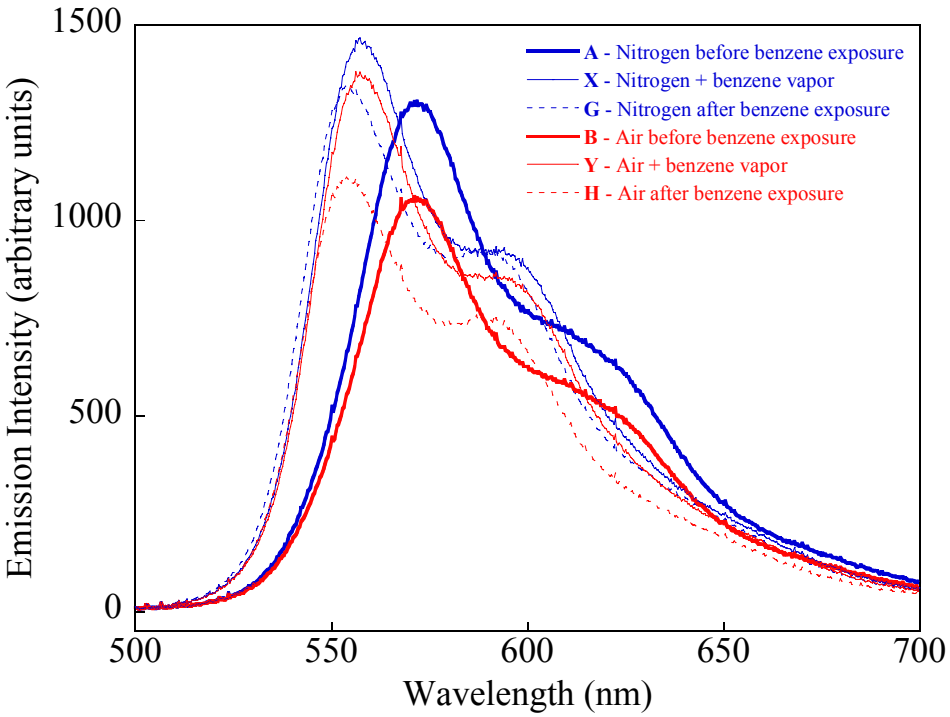

Figure 6. Emission spectra of $[Ru(5,6\text{-}Me_2Phen)_3](tfpb)_2$ taken during cross sensitivity studies. The wavelength shift due to benzene absorption into the crystal lattice and emission quenching effect due to the accessibility of the solid to oxygen is apparent.

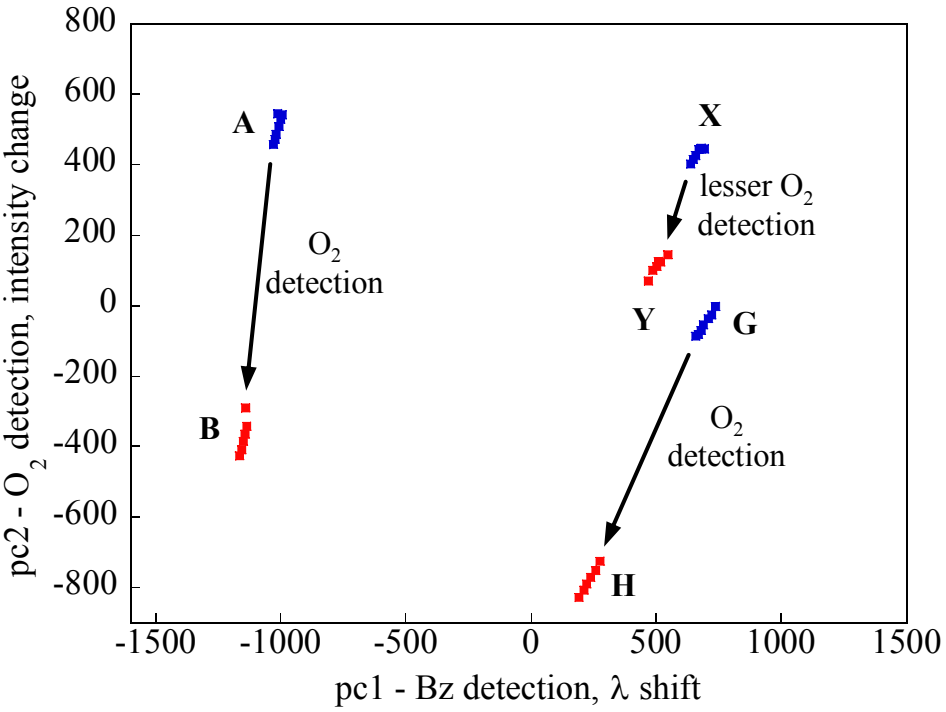

Figure 7. PCA score plot. Blue squares indicate data collected under nitrogen and red squares indicate data collected under air. In each case, the arrows indicate a purge gas change of nitrogen to air for a particular benzene solvation state.

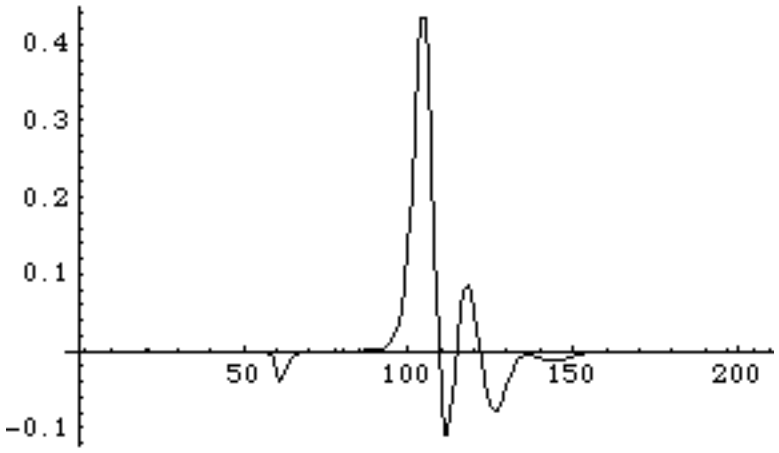

Figure 8. Loading plot for score 1. X-axis runs from wavelength 0 to wavelength 205 (approximately 3.5 nm between points).

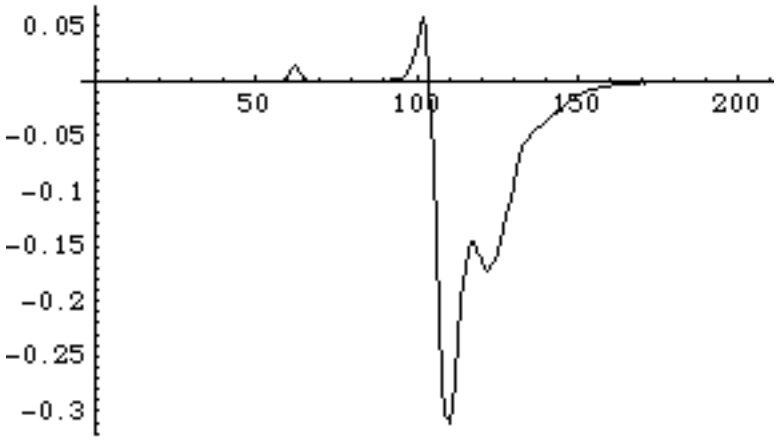

Figure 9. Loading plot for score 2. X-axis runs from wavelength 0 to wavelength 205 (approximately 3.5 nm between points).

X-ray Crystallography.

A model that is consistent with this sensing behavior can be formulated by examining the X-ray crystal structure of $[Ru(5,6\text{-}Me_2Phen)_3](tfpb)_2$. Solvated crystals that contain one half-occupied CH_2Cl_2 and 1.5 benzene molecules per Ru unit were grown by slow evaporation of a CH_2Cl_2/benzene solution. The structure consists of discrete cations and anions separated by the benzene molecules, which lie in a channel, and the methylene chloride molecules, which occupy isolated void chambers in the structure. One of the benzene molecules is ordered, while the other is approximately centered in the channel and is highly disordered over a special position. This disordered benzene molecule was removed from the structure with PLATON SQUEEZE to improve the structural refinement.[40] We suggest that the disordered benzene molecule is not tightly held and easily leaves the crystal lattice under a carrier gas flow absent of benzene vapor; the second, ordered benzene molecule, is held much more tightly by the lattice and is lost much more slowly. These structural data are consistent with three different benzene solvation states for the crystalline solid (after the methylene chloride is removed and never replaced) that are produced in the sensing experiments: one state that contains no benzene (**Ru·0 bz**, where Ru is $Ru(5,6\text{-}Me_2Phen)_3](tfpb)_2$), formed under pure carrier gas prior to benzene exposure; a fully solvated form with 1.5 benzene molecules per Ru (**Ru·1.5 bz**) formed when the carrier gas is saturated with benzene vapor; and an intermediate form that contains only the tightly held benzene molecule (**Ru·1 bz**) which is formed under pure carrier gas after benzene exposure.

The behavior of the emission data illustrated in the score plot can be understood within the structural context if the oxygen diffusion though the crystalline solid is

significant for the form with no benzene (**A** = **Ru·0 bz**) or with only the tightly held benzene molecule (**G** = **Ru·1 bz**) present. In these two cases, a significant channel is still present in the solid for oxygen molecules to diffuse through to enable emission quenching (Figure 10). If the last benzene is loaded into the crystal to form the **Ru·1.5 bz** phase (cluster **X**), the channel is significantly blocked and the oxygen diffusion is greatly diminished. Again, all three of these forms can be interconverted and tested for oxygen sensing by exposure of the crystalline solid to a proper sequence of carrier gas/benzene/heating.

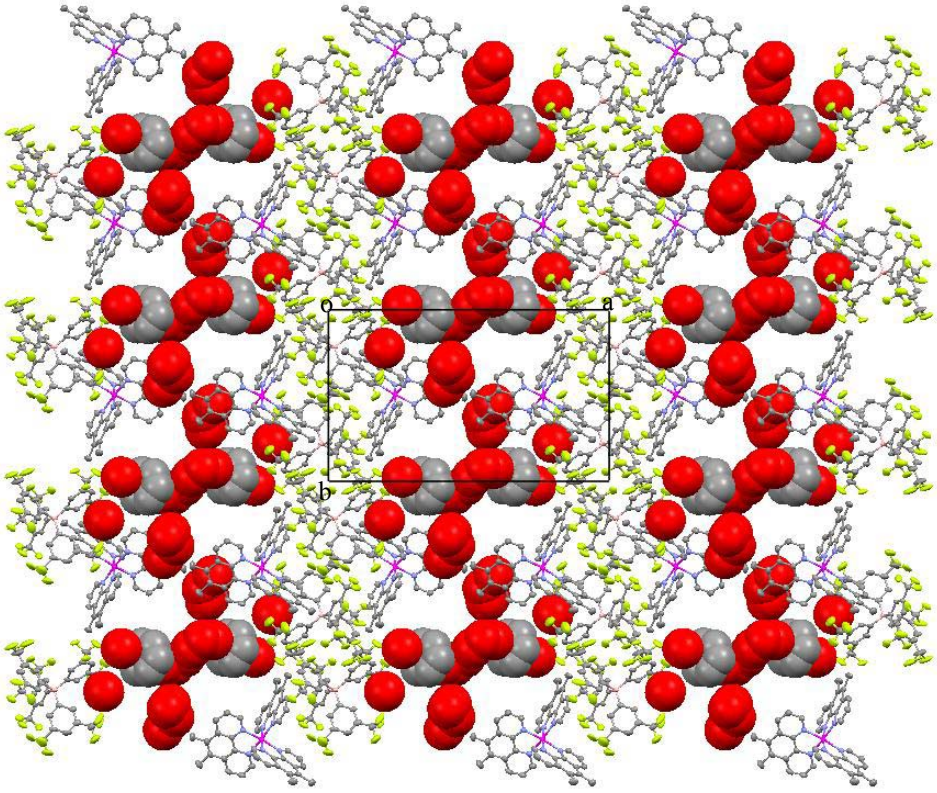

Figure 10. View down the c-axis of the **Ru·1 bz** phase showing the channels running though the structure. The red spheres represent void space while the gray spheres represent benzene molecules which may be present or removed in stages to contribute to the void space. Hydrogen atoms are omitted for clarity.

Utility as a Benzene Sensor.

Of final interest is an estimation of the sensitivity of $Ru(5,6\text{-}Me_2Phen)_3](tfpb)_2$ to lower levels of benzene. Assuming the vapor pressure of benzene at 20 °C is ~75 Torr with an atmospheric pressure at 760 Torr, the concentration of benzene in a saturated nitrogen stream is about 9.9%, a very high value. A lower concentration was made by saturating a known gas flow with benzene by bubbling the gas through liquid benzene and then diluting this stream with a much larger known flow of carrier gas. By this method, the sensitivity of the vapochromic shift of $Ru(5,6\text{-}Me_2Phen)_3](tfpb)_2$ was investigated at a lower concentration of 0.76% (7600 ppm). Relative to the 9.9% data, a slower response was observed. Including the data for the full response of the 0.76% point in a PCA study of the time response of the sample to the 9.9% benzene concentration suggests that approximately the same level of change is observed for 0.76% as for **Ru·1 bz** (Figure 11). Thus, we infer that a greatly improved version of $Ru(5,6\text{-}Me_2Phen)_3](tfpb)_2$ might allow optical measurement of low concentrations of benzene in air.[3] Further studies to fully explore the benzene sensing properties of $Ru(5,6\text{-}Me_2Phen)_3](tfpb)_2$ are underway.

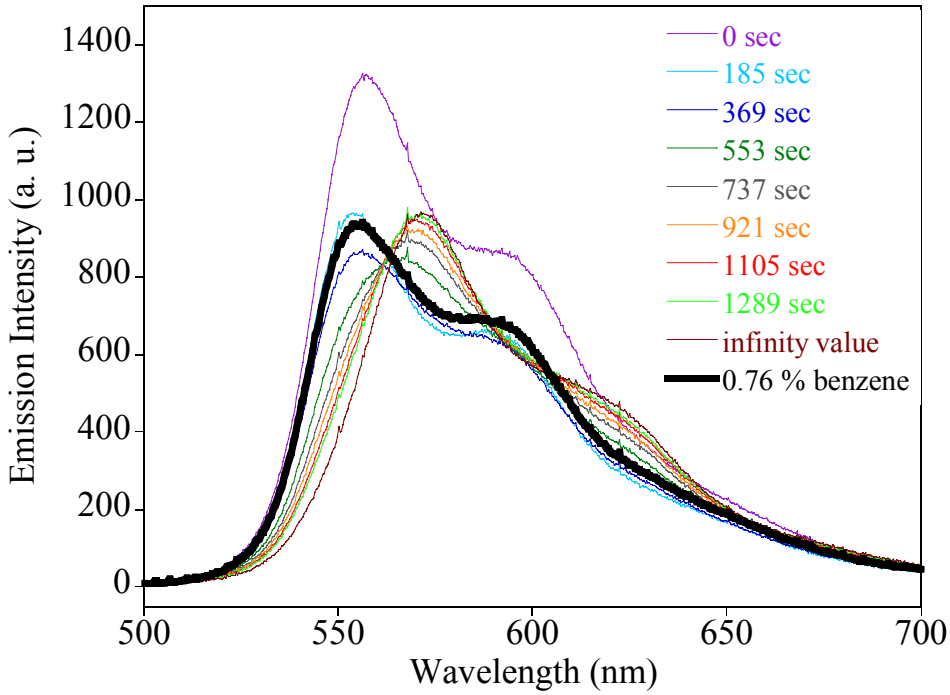

Figure 11. Plot showing loss of benzene from **Ru·1.5 bz** to **Ru·1 bz** (spectra at 0 and 185 s) and from **Ru·1 bz** to **Ru·0 bz** (spectra at 185 s to infinity) under air flow. The spectrum for detection of 0.76% benzene (thick black line) is very near the **Ru·1.0 bz** form (185 s).

Conclusions.

The complex $[Ru(5,6\text{-}Me_2Phen)_3](tfpb)_2$ was examined as a solid-state sensor for detection of the VOC benzene and oxygen. It exhibits a vapochromic shift of its emission to higher energy in the presence of benzene vapor. It also exhibits linear Stern-Volmer quenching behavior in the presence of oxygen. When exposed to benzene and oxygen vapor at the same time the crystals uptake benzene, inhibiting the diffusion of oxygen and subsequent quenching of the excited state. When benzene is removed from the carrier flow, a portion of benzene is removed from the crystals and oxygen is able to diffuse resulting in quenching of the emission. When the sample is heated the remaining benzene molecules leave and the channels are fully accessible to oxygen. Analysis by PCA showed three distinct sensing states in this process. This crystalline Ru complex was examined as a sensor and was found to detect 0.76% benzene in nitrogen. Further examination of these types of complexes could lead to the desired optical sensors with lower detection limits.

References.

1. EPA, *Indoor Air Quality, Sources of Air Pollution - Organic Gases (Volatile Organic Compounds - VOCs)*. updated on October 10, 2008. http://www.epa.gov/iaq/voc.html.

2. EPA, *Technology Transfer Network, Air Toxics Website, Benzene*. updated February 4, 2008. http://www.epa.gov/ttn/atw/hlthef/benzene.html.

3. NIOSH Recommended Exposure Limit (REL): 0.1 ppm (8 h), 1 ppm (15 min), ACGIH Threshold Limit Values (TLV): 0.5 ppm (8 h), 2.5 ppm (15 min), OSHA Permissible Exposure Limits (PEL): 1 ppm (8h), 5 ppm (15 min) from Benzene; CHEMINFO, Canadian Centre for Occupational Health and Safety, http://ccinfoweb2.ccohs.ca (accessed 8/29/08).

4. Dincer, F.; Odabasi, M.; Muezzinoglu, A., *J. Chromatogr., A* **2006**, *1122*, 222.

5. Wu, C.-H.; Feng, C.-T.; Lo, Y.-S.; Lin, T.-Y.; Lo, J.-G., *Chemosphere* **2004**, *56*, 71.

6. Yamada, Y.; Nakamura, T.; Yano, K., *Langmuir* **2008**, *24*, 2779.

7. Endo, T.; Yanagida, Y.; Hatsuzawa, T., *Sens. Actuators, B* **2007**, *B125*, 589.

8. Plante, J. P.; Glass, T. E., *Org. Lett* **2006**, *8*, 2163.

9. Dickinson, T. A.; White, J.; Kauer, J. S.; Walt, D. R., *Nature* **1996**, *382*, 697.

10. White, J.; Kauer, J. S.; Dickinson, T. A.; Walt, D. R., *Anal. Chem.* **1996**, *68*, 2191.

11. Silva, A. M. S.; Pimentel, M. F.; Raimundo, I. M., Jr.; Almeida, Y. M. B., *Vib. Spectrosc.* **2008**, *46*, 39.

12. Ablat, H.; Yimit, A.; Mahmut, M.; Itoh, K., *Anal. Chem.* **2008**, *80*, 7678.

13. Silva, L. I. B.; Rocha-Santos, T. A. P.; Duarte, A. C., *Sens. Actuators, B* **2008**, *B132*, 280.

14. Casalini, R.; Wilde, J. N.; Nagel, J.; Oertel, U.; Petty, M. C., *Sens. Actuators, B* **1999**, *B57*, 28.

15. Ando, M., *TrAC, Trends Anal. Chem.* **2006**, *25*, 937.

16. Borisov, S. M.; Klimant, I., *Anal. Chem.* **2007**, *79*, 7501.

17. Carraway, E. R.; Demas, J. N.; DeGraff, B. A.; Bacon, J. R., *Anal. Chem.* **1991**, *63*, 337.

18. Chu, C.-S.; Lo, Y.-L., *IEEE Photonics Technology Letters* **2008**, *20*, 63.

19. Demas, J. N.; DeGraff, B. A., *Coord. Chem. Rev.* **2001**, *211*, 317.

20. Demas, J. N.; DeGraff, B. A.; Coleman, P. B., *Anal. Chem.* **1999**, *71*, 793A.

21. Demas, J. N.; Harris, E. W.; McBride, R. P., *J. Am. Chem. Soc.* **1977**, *99*, 3547.

22. Draxler, S.; Lippitsch, M. E.; Klimant, I.; Kraus, H.; Wolfbeis, O. S., *J. Phys. Chem.* **1995**, *99*, 3162.

23. Mills, A., *Platinum Met. Rev.* **1997**, *41*, 115.

24. Drew, S. M.; Janzen, D. E.; Mann, K. R., *Anal. Chem.* **2002**, *74*, 2547.

25. Drew, S. M.; Mann, J. E.; Marquardt, B. J.; Mann, K. R., *Sens. Actuators, B* **2004**, *B97*, 307.

26. Grate, J. W.; Moore, L. K.; Janzen, D. E.; Veltkamp, D. J.; Kaganove, S.; Drew, S. M.; Mann, K. R., *Chem. Mater.* **2002**, *14*, 1058.

27. Nagel, C. C. Preparation of thermochromic double-complex salts. 88-300781 277032, 19880129., 1988.

28. Nagel, C. C. Preparation of vapochromic double-complex salts. 88-300782 277033, 19880129., 1988.

29. McGee, K. A.; Veltkamp, D. J.; Marquardt, B. J.; Mann, K. R., *J. Am. Chem. Soc.* **2007**, *129*, 15092.

30. Exstrom, C. L.; Britton, D.; Mann, K. R.; Hill, M. G.; Miskowski, V. M.; Schaefer, W. P.; Gray, H. B.; Lamanna, W. M., *Inorg. Chem.* **1996**, *35*, 549.

31. Evans, I. P.; Spencer, A.; Wilkinson, G., *J. Chem. Soc., Dalton Trans.* **1973**, 204.

32. Cooley, L. F.; Headford, C. E. L.; Elliott, C. M.; Kelley, D. F., *J. Am. Chem. Soc.* **1988**, *110*, 6673.

33. Lacour, J.; Goujon-Ginglinger, C.; Troche-Haldimann, S.; Jordry, J. J., *Angew. Chem., Int. Ed.* **2000**, *39*, 3695.

34. Beebe, K. R.; Pell, R. J.; Seasholtz, M. B., *Chemometrics: A Practical Guide*. John Wiley and Sons, Inc.: New York, NY, **1998**; p 26-182.

35. The authors acknowledge Dr. Victor G Young Jr. and Benjamin E. Kucera at the X-ray Crystallography Laboratory in the Department of Chemistry at the University of Minnesota.

36. Blessing, R. H., *Acta Crystallogr., Sect. A: Found. Crystallogr.* **1995**, *A51*, 33.

37. Sheldrick, G. *SADABS*, v.2.03; 2002.

38. *SHELXTL*, v.6.12; Bruker AXS, Madison, WI, 2001.

39. Spek, A. L., *J. Appl. Crystallogr.* **2003**, *36*, 7.

40. Spek, A. L. *PLATON*, Utrecht University, Utrecht, The Netherlands, 2005.

41. Bruno, I. J.; Cole, J. C.; Edgington, P. R.; Kessler, M.; Macrae, C. F.; McCabe, P.; Pearson, J.; Taylor, R., *Acta Crystallogr., Sect. B: Struct. Sci.* **2002**, *B58*, 389.

42. Oxygen concentration expressed as mole fraction in nitrogen at atmospheric pressure = 0.97 atm.

Chapter 4

Examination of the Detection Abilities of Solid-State Ruthenium(II) Polypyridine Complexes Towards Chlorine

Abstract

The synthesis of new compounds of the general form [(*p*-cym)Ru(pp)Cl]Cl (where *p*-cym = η^6-*p*-cymene and pp = polypyridyl) was developed. This method allowed the study of a series of Ru(II) complexes by varying polypyridyl (bpy = 2,2'-bipyridine, phen = 1,10-phenanthroline, dpdp = 4,4'-diphenyl-2,2'-dipyridyl, dppz = dipyrido[3,2-a:2',3'-c]phenazine) and substituted monoanionic oxygen donor (β-diketonate) ligands (hfacac = hexafluoroacetylacetonate, dbm = dibenzoylmethane). Modification of the substituent group on the β-diketonate ligand has a pronounced effect on the electronic and electrochemical properties of these complexes with electron withdrawing substituents resulting in higher energy $d\pi \rightarrow \pi^*$ absorption. Additionally, cyclic voltammetry has allowed the observation of large effects on the Ru(II) to Ru(III) oxidation of these complexes between hfacac ($E^0 \sim 0.85$ V) and dbm ($E^0 \sim 0$ V). Examination of these complexes by single crystal X-ray crystallography shows solid-state packing involving π-π intermolecular interactions. The hfacac derivatives also display fluorine-fluorine interactions in the solid-state which have a large effect on the overall packing. Two of the dbm derivatives exhibit infinite π-stacks and have large channels of void space in the structure. The presence of channels as well as the low Ru(III)/Ru(II) redox couple led us to examine the utility of these complexes as chlorine sensors.

Introduction

The redox chemistry and photophysics of ruthenium(II) tris-polypyridine (pp) complexes have been extensively studied and are well understood. The easy adjustment of the electronic and redox properties of the $Ru(II)(pp)_3$ systems by modification of the ligand environment makes them particularly appealing for materials applications such as solar cells, LEDs, and optical sensors.[1-13]

Another potential use for these compounds arises because the MLCT state in $Ru(II)(pp)_3$ can exhibit solvatochromism and in some cases vapochromic behavior. As these complexes are susceptible to changes in environment they could function as sensors. In particular, the facile redox chemistry indicated by a low Ru(III)/Ru(II) redox couple near 0 V would lend itself to the detection of the noxious gas, chlorine (Cl_2), which is a powerful oxidant.[14, 15] The detection of Cl_2 is important due to its widespread use in industrial processes coupled with the health concerns inherent in the hazards associated with inhalation of a reactive gas.[16-19] Colorimetric detection, a simple method for Cl_2 sensing, has been reported where the uptake of Cl_2 into the host lattice of Ru(II) with polypyrazolylborato ligands produces a redox reaction of Ru(II) to Ru(III) and Cl^- becomes a counterion.[15]

The use of solid-state transition metal complexes for sensing of gases has long been a goal in our group. Often this is accomplished by design of crystalline materials that pack with channels of void space which allow the diffusion of small gaseous molecules through the solid. Sensing is completed by an accompanying color change. Two strategies that have been adopted for attempted control of the crystal structure are: (1) by using the shape of the molecular building block to dictate the inefficient packing or

(2) by using directionally sensitive interactions between the molecules to induce specific intermolecular interactions to control the pattern of association in the crystal structure.[20] The Ru(II) molecules of interest are propeller-shaped, a conformation that has been shown to give crystalline lattices with a large amount of empty space.[21] These molecules also exhibit strong intermolecular interactions in one direction (π-stacking), which also can lead to large void spaces within the crystalline lattice.

Modification of the electronic properties of Ru(II) pp species can be accomplished by replacing some of the pp ligands with ligands of another type, such as monoanionic oxygen donors. Previous studies of the complex $Ru(bpy)(sal)_2$, where bpy = 2,2'-bipyridine and sal = salicylaldehyde, have shown that the three isomers exhibit Ru(III)/Ru(II) redox couples at 0.042, 0.026, and -0.017 V.[22] $Ru(bpy)(acac)_2$ (acac = acetylacetone) has also been previously synthesized and exhibits a Ru(III)/Ru(II) redox couple with E^0=-0.05 V.[23] The acac ligand is even less π-accepting than sal leading to a more negative oxidation potential. All of these values are well negative of $[Ru(bpy)_3]^{2+}$ which exhibits an oxidation of Ru(II) to Ru(III) at 1.29 V[24] making these heteroleptic complexes advantageous for applications like solar cells, LEDs, and sensors relying on the Ru(II) to Ru(III) oxidation. [1, 3, 22] However, redox potentials near or below zero may account for the instability of the $Ru(bpy)(sal)_2$ and $Ru(bpy)(acac)_2$ complexes in air. Further investigation of Ru(pp)(β-diketonate)$_2$ complexes with β-diketonates substituted with electron withdrawing groups could eliminate the air sensitivity by reducing the electron density at the metal, altering the Ru(III)/Ru(II) couple and desensitizing these complexes to oxidation by air.

Herein we report further investigation of Ru(pp)(β-diketonate)$_2$ chemistry by examining the effect of substituted β-diketonate ligands on the electrochemical and photophysical properties of Ru(II) pp systems. The substituent group on the β-diketonate ligand was found to have a pronounced effect on these properties. Additionally, two of these complexes crystallize with void space channels that might allow small molecules to move in and out of the crystal with ease.[13] The sensitivity of these complexes to chlorine gas will also be discussed.

Experimental

General Considerations. All synthetic procedures were performed under an inert N_2 atmosphere unless otherwise noted. The compounds 2,2'-bipyridine (bpy), 1,10-phenanthroline (phen), 4,4'-diphenyl-2,2'-dipyridyl (dpdp), dibenzoylmethane (dbm), and hexafluoroacetylacetone (hfacac) were purchased from Aldrich Chemical Co. $RuCl_3 \cdot xH_2O$ was purchased from Alfa and α-phellandrene was purchased from Pfaltz and Bauer. (TBA)(PF_6) (TBA = tetra-*n*-butylammonium) was purchased from Southwestern Analytical Chemicals. Dipyrido[3,2-a:2',3'-c]phenazine[25] (dppz) was prepared according to literature procedures via 1,10-phenanthroline-5,6-dione[26] and phenylenediamine. The [Ru(*p*-cym)Cl_2]$_2$ [27, 28] (*p*-cym = η^6-*p*-cymene) dimer and [Ru(bpy)(*p*-cym)Cl]Cl[22, 29] were prepared as previously reported. All solvents were used as received.

NMR spectra were recorded on Varian Unity (200 MHz), Varian Unity (300 MHz), or Varian Inova (300 MHz) instruments. Chemical shifts are reported in parts per million (ppm) and referenced to the residual dichloromethane peak (5.32 ppm) or methanol peak (2.05 ppm). All coupling constants are reported in hertz. High-resolution mass spectrometry was carried out on a Bruker BioTOF II mass spectrometer. Solid and solution UV-Vis spectra were acquired with an Ocean Optics CCD array spectrometer. Solid-state UV-Vis spectra were acquired as films cast from CH_2Cl_2 on a custom built zirconium oxide attenuated total reflectance (ATR) crystal. Electrochemical experiments were performed with a BAS 100B electrochemical analyzer using methods previously described.[30, 31] Potentials are reported versus aqueous Ag/AgCl and are not corrected for the junction potential. The E^0 value for the ferrocenium/ferrocene couple for

concentrations similar to those used in this study was +0.48 V for dichloromethane solutions at a glassy carbon electrode with 0.1M (TBA)(PF_6) as the electrolyte.

Chlorine exposures were carried out by filling a vessel containing fifteen 1.5-2 inch pieces of Tygon tubing with chlorine gas (either from a chlorine lecture bottle or by generating chlorine gas via mixing of hydrochloric acid and bleach) then allowing the gas and tubing to equilibrate for 15 min. Flushing the system with nitrogen gas for 10 minutes at a flow rate of 25 mL/min removed unadsorbed chlorine gas. Bubbling nitrogen gas at a rate of 10 mL/min through the flask and into the sample chamber allowed exposure of the sample to diluted chlorine gas due to the extended release capability of the Tygon tubing. The concentration of chlorine was determined by iodometric titration. A known flow rate of diluted chlorine was bubbled through a 0.1 M KI solution (2 mL) acidified with 3–6 drops of 6 M H_2SO_4 for a predetermined amount of time. Titration with known concentration (0.005–5 mM) $Na_2S_2O_3$ solutions with a starch indicator allowed calculation of the concentration of chlorine gas. Chlorine concentration was measured before and after sample exposures.

[Ru(phen)(*p*-cym)Cl]Cl. [Ru(phen)(*p*-cym)Cl]Cl was prepared by a method previously reported.[22, 29] The ^{1}H NMR was consistent with previously reported values.[32, 33]

[Ru(dpdp)(*p*-cym)Cl]Cl. [Ru(dpdp)(*p*-cym)Cl]Cl was prepared by a method previously reported.[22, 29] ^{1}H NMR (CD_2Cl_2): δ 9.75 (d, 2 H, *J* = 5.7 Hz), 8.51 (s, 2 H), 7.95 (d, 2 H, *J* = 5.1 Hz), 7.86 (d, 2 H, *J* = 5.7 Hz), 7.86 (dd, 2 H, *J* = 3.6–3.9, 5.6 Hz), 7.60 (m, 3 H), 6.21 (d, 2 H, *J* = 6.0 Hz), 6.06 (d, 2 H, *J* = 6.0 Hz), 2.75 (septuplet, 1 H, *J* = 6.9 Hz), 2.32 (s, 3 H), 1.10 (d, 6 H, *J* = 6.9 Hz). HRESIMS (M^+): calcd for $C_{32}H_{30}ClN_2Ru$, 579.1141; found, 579.1144.

[Ru(dppz)(*p*-cym)Cl]Cl. [Ru(dppz)(*p*-cym)Cl]Cl was prepared by a method previously reported.[22, 29] ^{1}H NMR (CD_3OH): δ 9.89 (d, 2 H, *J* = 5.4 Hz), 9.72 (d, 2 H, *J* = 8.1 Hz), 8.31 (dd, 2 H, *J* = 3.3–3.6, 6.5 Hz), 8.21 (dd, 2 H, *J* = 5.4, 8.1 Hz), 8.01 (dd, 2 H, *J* = 3.3, 6.6 Hz), 6.26 (d, 2 H, *J* = 6.3 Hz), 6.04 (d, 2 H, *J* = 6.0 Hz), 6.06 (d, 2 H, *J* = 6.0 Hz), 2.74 (septuplet, 1 H, *J* = 6.6 Hz), 2.27 (s, 3 H), 1.07 (d, 6 H, *J* = 6.9 Hz). HRESIMS (M^+): calcd for $C_{28}H_{24}ClN_4Ru$, 553.0732; found, 553.0737.

Ru(bpy)(hfacac)$_2$ (1).[34] **[**Ru(*p*-cym)(bpy)Cl]Cl (0.500 g, 1.08 mmol) and finely ground K_2CO_3 (1.517 g, 10.97 mmol) were combined in 95% ethanol. An ethanolic solution of hfacac (2.079 g, 10.00 mmol) was added to give a total of 150 mL of solvent and the reaction mixture was placed under a nitrogen atmosphere. The mixture was heated in a water bath to 55–65 °C for 5 h. After 10 min the color had changed from light yellow to dark orange and finally to deep purple. The ethanol was removed from the final dark purple reaction mixture and the solid was recrystallized by placing a solution in an ethanol/hexanes mixture in the freezer. The maroon precipitate was then collected by vacuum filtration and washed with water (to remove residual base) and then hexanes. The solid was dried under vacuum to give 0.658 g (91% yield) of product. X-ray quality crystals were grown by slow evaporation of an acetone solution. ^{1}H NMR (CD_2Cl_2): δ 8.59 (ddd, 2 H, *J* = 0.4–0.8, 1.5, 5.6 Hz), 8.24 (dd, 2 H, *J* = 0.4, 8.0 Hz), 7.90 (dd, 2 H, *J* = 1.4–1.6, 7.7–7.9, 7.8 Hz), 7.43 (ddd, 2 H, *J* = 1.2–1.8, 5.8, 7.4 Hz), 6.16 (s, 2 H). HRESIMS (M + Na^+): calcd for $NaC_{20}H_{10}F_{12}N_2O_4Ru$, 694.9390; found, 694.9394.

Ru(phen)(hfacac)$_2$ (2). **[**Ru(*p*-cym)(phen)Cl]Cl (0.0507 g, 0.104 mmol) and finely ground K_2CO_3 (0.145 g, 1.05 mmol) were combined in 95% ethanol. An ethanolic solution of hfacac (0.261 g, 1.26 mmol) was added to give a total of 25 mL of solvent and

the reaction mixture was placed under a nitrogen atmosphere. The mixture was heated in a water bath to 60–70 °C for 5.5 h. After 10 min the color had changed from light yellow to orange to deep purple. The ethanol was removed from the final dark purple reaction mixture. The solid was dissolved in a smaller portion of ethanol and hexanes was added at which point the solution was placed in the freezer overnight. The maroon precipitate was then collected by vacuum filtration and washed with water (to remove residual base) and then hexanes. The solid was dried under vacuum to give 0.0684 g (94% yield) of product. X-ray quality crystals were grown by slow evaporation of an acetone solution. ^{1}H NMR (CD_2Cl_2): δ 8.92 (ddd, 2 H, J = 0.3–0.6, 1.2, 5.2 Hz), 8.38 (ddd, 2 H, J = 0.3, 1.2, 8.4 Hz), 8.08 (s, 2 H), 7.78 (dd, 2 H, J = 5.1, 8.3 Hz), 6.20 (s, 2 H). HRESIMS (M + Na^+): calcd for $NaC_{22}H_{10}F_{12}N_2O_4Ru$, 718.9391; found, 718.9393.

Ru(bpy)(dbm)$_2$ (3). [Ru(*p*-cym)(bpy)Cl]Cl (0.0509 g, 0.110 mmol) and dbm (0.250 g, 1.11 mmol) were dissolved in 95% ethanol (25 mL) and placed under a nitrogen atmosphere. Finely ground K_2CO_3 (0.153 g, 1.11 mmol) was then added as a solid and the mixture was heated in a water bath to 60–65 °C for 5 h. After 5 min the color had changed from light yellow to a brown which deepened in color as the reaction progressed. The brown reaction mixture was filtered onto a frit to give a black solid which was rinsed with water (50 mL) to remove residual base and then hexanes. The solid was dried under vacuum to give 0.0509 g (66% yield) of product. X-ray quality crystals were grown by slow evaporation of an acetone solution. ^{1}H NMR (CD_2Cl_2): δ 8.97 (d, 2 H, J = 4.8 Hz), 8.15 (dd, 2 H, J = 1.2, 8.1 Hz), 8.03 (dd, 4 H, J = 1.2–1.5, 8.3 Hz), 7.61 (m, 6 H), 7.38 (m, 8 H), 7.21 (m, 6 H), 6.65 (broad s, 2 H). HRESIMS (M^+): calcd for $C_{40}H_{30}N_2O_4Ru$, 704.1255; found, 704.1279.

Ru(phen)(dbm)$_2$ (4). [Ru(*p*-cym)(phen)Cl]Cl (0.0502 g, 0.103 mmol) and dbm (0.240 g, 1.07 mmol) were dissolved in 95% ethanol (25 mL) and placed under a nitrogen atmosphere. Finely ground K_2CO_3 (0.143 g, 1.04 mmol) was then added as a solid and the mixture was heated in a water bath to 60–65 °C for 5 h. After 5 min the color had changed from light yellow to a brown which deepened in color as the reaction progressed. The final red-brown reaction mixture was filtered onto a frit to give a deep purple solid which was rinsed with water (50 mL) to remove residual base. The solid was dried under vacuum to give 0.0484 g (64% yield) of product. X-ray quality crystals were grown by slow evaporation of a CH_2Cl_2 solution. ^{1}H NMR (CD_2Cl_2): δ 9.18 (b, 2 H), 8.09 (dd, 4 H, *J* = 1.2, 8.1 Hz), 8.03 (d, 2 H, *J* = 8.1 Hz), 7.96 (s, 2 Hz), 7.55 (m, 6 H), 7.47 (t, 2 H, *J* = 7.2), 7.40 (t, 4 H, *J* = 7.2), 7.29 (t, 2 H, *J* = 7.2), 7.15 (t, 4 H, *J* = 7.2), 6.50 (b, 2 H). HRESIMS (M^+): calcd for $C_{42}H_{30}N_2O_4Ru$, 728.1255; found, 728.1285.

Ru(dpdp)(dbm)$_2$ (5). [Ru(*p*-cym)(dpdp)Cl]Cl (0.0411 g, 0.0669 mmol) and dbm (0.154 g, 0.687 mmol) were dissolved in 95% ethanol (20 mL) and placed under a nitrogen atmosphere. Finely ground K_2CO_3 (0.0944 g, 0.683 mmol) was then added as a solid and the mixture was heated in a water bath to 60–65 °C for 5 h. The brown solution did not change in appearance during the progress of the reaction. The final brown reaction mixture was cooled in the refrigerator overnight and then filtered onto a frit to give a maroon-black solid which was rinsed with water (50 mL) to remove residual base. The solid was dried under vacuum to give 0.0237 g (41% yield) of product. X-ray quality crystals were grown by slow evaporation of a CH_2Cl_2 solution. ^{1}H NMR (CD_2Cl_2): δ 8.92 (broad, 2 H), 8.45 (d, 2 H, *J* = 1.2 Hz), 8.08 (d, 4 H, *J* = 7.5 Hz), 7.79 (dd, 4 H, *J* = 1.5,

8.6 Hz), 7.70 (d, 4 H, J = 7.2 Hz), 7.55 (t, 4 H, J = 7.5), 7.40 (m, 12 H), 7.23 (t, 4 H, J = 7.5 Hz), 6.51 (broad, 2 H). HRESIMS (M^+): calcd for $C_{52}H_{38}N_2O_4Ru$, 856.1884; found, 856.1907.

Ru(dppz)(dbm)$_2$ (6). [Ru(*p*-cym)(dppz)Cl]Cl (0.0508 g, 0.0863 mmol) and dbm (0.195 g, 0.868 mmol) were dissolved in 95% ethanol (25 mL) and placed under a nitrogen atmosphere. Finely ground K_2CO_3 (0.143 g, 1.04 mmol) was then added as a solid and the mixture was heated in a water bath to 60–65 °C for 5 h. After 5 min the color had changed from yellow-orange to a brown which deepened in color as the reaction progressed. The final brown reaction mixture was filtered onto a frit to give a deep purple solid which was rinsed with ethanol and water (50 mL) to remove residual base. The solid was dried under vacuum to give 0.0602 g (84% yield) of product. X-ray quality crystals were grown by slow evaporation of a CH_2Cl_2 solution. ^{1}H NMR (CD_2Cl_2): δ 9.38 (dd, 2 H, J = 1.2, 5.4 Hz), 9.25 (dd, 2 H, J = 1.2, 8.1 Hz), 8.43 (dd, 2 H, J = 3.3, 6.6 Hz), 8.10 (td, 4 H, J = 1.5–2.1, 6.5 Hz), 8.00 (dd, 2 H, J = 3.6, 6.6 Hz), 7.68 (dd, 2 H, J = 5.4, 8.0 Hz), 7.58 (td, 4 H, J = 1.2–2.1, 7.13 Hz), 7.45 (m, 6 H), 7.27 (tt, 2 H, J = 1.2–2.1, 7.3 Hz), 7.16 (tt, 4 H, J = 1.2–1.8, 7.4 Hz), 6.77 (s, 2H). HRESIMS (M^+): calcd for $C_{48}H_{32}N_4O_4Ru$, 830.1475; found, 830.1487.

Single Crystal X-ray Crystallography. Single crystals were attached to glass capillary fibers. **1**, **3**, and **4** were mounted on a Siemens SMART Platform CCD diffractometer while **2** and **6** were mounted on a Bruker SMART Platform CCD diffractometer for data collection at 173(2) K using a graphite monochromator and Mo Kα radiation (λ = 0.71073 Å). An initial set of cell constants was calculated from reflections harvested from three sets of 20 frames such that orthogonal wedges of reciprocal space were

surveyed. Final cell constants were determined from a minimum of 2340 strong reflections from the actual data collection. Data were collected to the extent of 1.5 hemispheres to a resolution of 0.84 Å. Three major sections of frames were collected with 0.30° steps in ω. The intensity data were corrected for absorption and decay using SADABS.[35, 36] Space groups were determined based on systematic absences and intensity statistics. Direct-methods solutions provided the positions of most of the non-hydrogen atoms. Full-matrix least-squares/difference Fourier cycles were performed to locate the remaining non-hydrogen atoms. All non-hydrogen atoms were refined with anisotropic displacement parameters and all hydrogen atoms were placed in idealized positions and refined as riding atoms with relative isotropic displacement parameters. All calculations were performed with the SHELXTL suite of programs.[37] Packing analysis parameters were measured using either PLATON/VOID or PLATON/SQUEEZE.[38, 39] Details of the refinement as well as selected bond lengths are given in Tables 1–3 and 5.

Table 1. Crystallographic data and refinement parameters.

Compound	1	2
empirical formula	$C_{20}H_{10}F_{12}N_2O_4Ru$	$C_{22}H_{10}F_{12}N_2O_4Ru$
crystal color, morphology	purple, plate	red, needle
crystal system	monoclinic	monoclinic
space group	$P2_1/c$	$P2_1/n$
a, Å	6.3809(8)	6.3247(6)
b, Å	31.702(4)	19.6258(18)
c, Å	11.1797(15)	19.4370(18)
α, deg	90	90
β, deg	92.863(3)	96.396(2)
γ, deg	90	90
volume, Å^3	2258.7(5)	2397.6(4)
Z	4	4
formula weight, g mol^{-1}	671.37	695.39
density (calculated), g cm^{-3}	1.974	1.926
temperature, K	273(2)	173(2)
Absorption coefficient, mm^{-1}	0.826	0.782
F(000)	1312	1360
θ range, deg	1.28 to 25.04	1.48 to 25.04
index ranges	$-7 \le h \le 7$	$-7 \le h \le 7$
	$-37 \le k \le 35$	$-21 \le k \le 23$
	$-13 \le l \le 13$	$-23 \le l \le 23$
reflections collected	16560	16925
independent reflections	3995 (R_{int} = 0.0872)	4247 (R_{int} = 0.0877)
weighting factors[a] *a,b*	0.030300, 2.454300	0.048400, 4.098700
max, min transmission	0.980000, 0.838747	0.970000, 0.765117
Data/restraints/parameters	3995/0/352	4247/0/370
R_1, wR_2 [$I > 2\sigma(I)$]	0.0442, 0.0875	0.0486, 0.1065
R_1, wR_2 (all data)	0.0820, 0.0998	0.0870, 0.1233
GOF	1.077	1.061
largest diff. peak, hole, eÅ^{-3}	0.635, -0.669	0.700, -0.728

[a] $w = [\sigma^2(F_o^2) + (aP)^2 + (bP)]^{-1}$, where $P = (F_o^2 + 2F_c^2)/3$.

Table 2. Crystallographic data and refinement parameters.

Compound	3	4
empirical formula	C_{40} H_{30} N_2 O_4 Ru	C_{42} H_{30} N_2 O_4 Ru
crystal color, morphology	green, block	purple, plate
crystal system	orthorhombic	orthorhombic
space group	*Pbcn*	*Pcca*
a, Å	31.708(2)	21.3171(16)
b, Å	9.7834(7)	16.0190(12)
c, Å	21.2507(16)	10.2628(8)
α, deg	90	90
β, deg	90	90
γ, deg	90	90
volume, Å^3	6592.2(8)	3504.5(5)
Z	8	4
formula weight, g mol^{-1}	703.73	727.75
density (calculated), g cm^{-3}	1.418	1.379
temperature, K	173(2)	173(2)
Absorption coefficient, mm^{-1}	0.520	0.492
F(000)	2880	1488
θ range, deg	1.28 to 25.05	1.27 to 25.05
index ranges	$-37 \le h \le 36$	$-25 \le h \le 25$
	$-11 \le k \le 11$	$-17 \le k \le 19$
	$-25 \le l \le 25$	$-12 \le l \le 12$
reflections collected	47415	23193
independent reflections	5834 (R_{int} = 0.0428)	3109 (R_{int} = 0.0470)
weighting factors[a] *a,b*	0.024300, 7.916600	0.024300, 3.500000
max, min transmission	0.940000, 0.831071	0.960000, 0.818911
Data/restraints/parameters	5834/0/424	3109/0/222
R_1, wR_2 [$I > 2\sigma(I)$]	0.0381, 0.0733	0.0337, 0.0677
R_1, wR_2 (all data)	0.0480, 0.0764	0.0408, 0.0704
GOF	1.134	1.095
largest diff. peak, hole, eÅ^{-3}	0.478 and -0.568	0.303, -0.270

[a] $w = [\sigma^2(F_o^2) + (aP)^2 + (bP)]^{-1}$, where $P = (F_o^2 + 2F_c^2)/3$.

Table 3. Crystallographic data and refinement parameters.

Compound	**6**
empirical formula	$C_{49}\ H_{32}\ Cl_2\ D_2\ N_4\ O_4\ Ru$
crystal color, morphology	red, plate
crystal system	orthorhombic
space group	*Pcca*
a, Å	20.228(2)
b, Å	22.722(2)
c, Å	9.1021(9)
α, deg	90
β, deg	90
γ, deg	90
volume, $Å^3$	4183.6(7)
Z	4
formula weight, g mol^{-1}	916.78
density (calculated), g cm^{-3}	1.456
temperature, K	173(2)
Absorption coefficient, mm^{-1}	0.554
F(000)	1864
θ range, deg	0.90 to 25.06
index ranges	$-24 \le h \le 24$
	$-27 \le k \le 27$
	$-10 \le l \le 10$
reflections collected	36885
independent reflections	3717 (R_{int} = 0.0434)
weighting factors[a] *a,b*	0.032600, 5.743000
max, min transmission	0.950000, 0.771817
Data/restraints/parameters	3717/0/279
R_1, wR_2 [$I > 2\sigma(I)$]	0.0321, 0.0764
R_1, wR_2 (all data)	0.0488, 0.0919
GOF	1.150
largest diff. peak, hole, e$Å^{-3}$	0.768, -0.598

[a] $w = [\sigma^2(F_o^2) + (aP)^2 + (bP)]^{-1}$, where $P = (F_o^2 + 2F_c^2)/3$

Results and Discussion.

Synthesis.

Previously our group has shown the ease and utility of displacing the arene rings in the complexes [(Bz)Ru(bpy)Cl]Cl and [(*p*-cym)Ru(bpy)Cl]Cl.[2, 22, 29, 40-42] Arene displacement from these complexes occurs at room temperature with KNO_2 to give $K_2[Ru(bpy)(NO_2)_4]$[40, 42], by photolysis in acetonitrile to give $[Ru(bpy)(CH_3CN)_3Cl]Cl$ [29], by reaction with salicylaldehyde and NaOH in refluxing ethanol to give $Ru(bpy)(sal)_2$[22], and most recently by reaction with $AgNO_2$ followed by refluxing in acetonitrile to give $[Ru(bpy)(CH_3CN)_3(NO_2)]PF_6$.[41] Based on the success of these reactions we considered the use of [(p-cym)Ru(pp)Cl]Cl in the synthesis of neutral Ru(pp)(β-diketonate)$_2$ complexes to be a natural choice of starting material.

The chloro-bridged dimer, $[(p\text{-cym})RuCl_2]_2$, was synthesized according to a literature procedure in which α-phellandrene, a substituted cyclohexadiene, undergoes a dehydrogenation reaction to give η^6-bound *p*-cymene.[27, 28] [(*p*-cym)Ru(bpy)Cl]Cl was also prepared from the chloro-bridged dimer according to literature procedures.[22, 29] The complexes [(*p*-cym)Ru(phen)Cl]Cl, [(*p*-cym)Ru(dpdp)Cl]Cl, and [(*p*-cym)Ru(dppz)Cl]Cl were prepared and isolated in the same way as the bpy analog. Figure 1 shows the ligands used in this study while Scheme 1 shows the synthetic route for the preparation of complexes **1** – **6**. The [(*p*-cym)Ru(pp)Cl]Cl complexes used in this study, as expected, undergo thermal displacement of the *p*-cym ring by substituted-β-diketonate ligands (hfacac and dbm) in the presence of K_2CO_3, to aid in deprotonation, in ethanol at 55–65 °C. The isolated yields range from 60–94%.

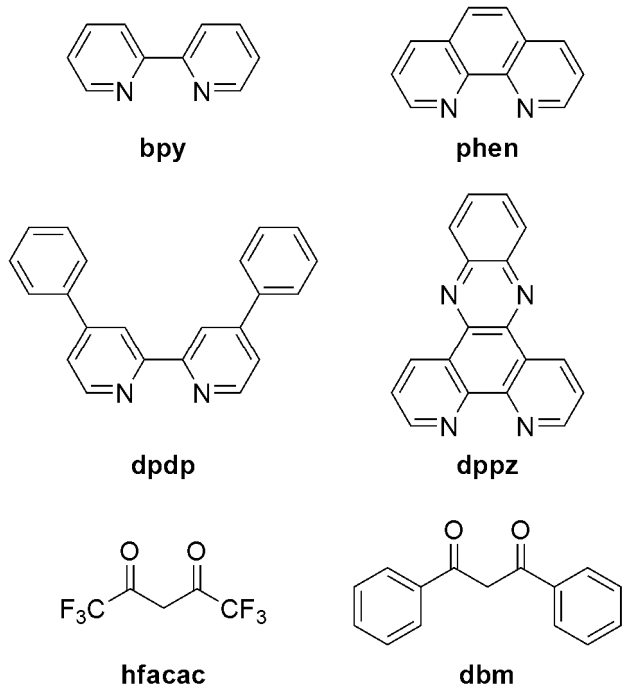

Figure 1. Polypyridyl and substituted β-diketonate ligands used in this study.

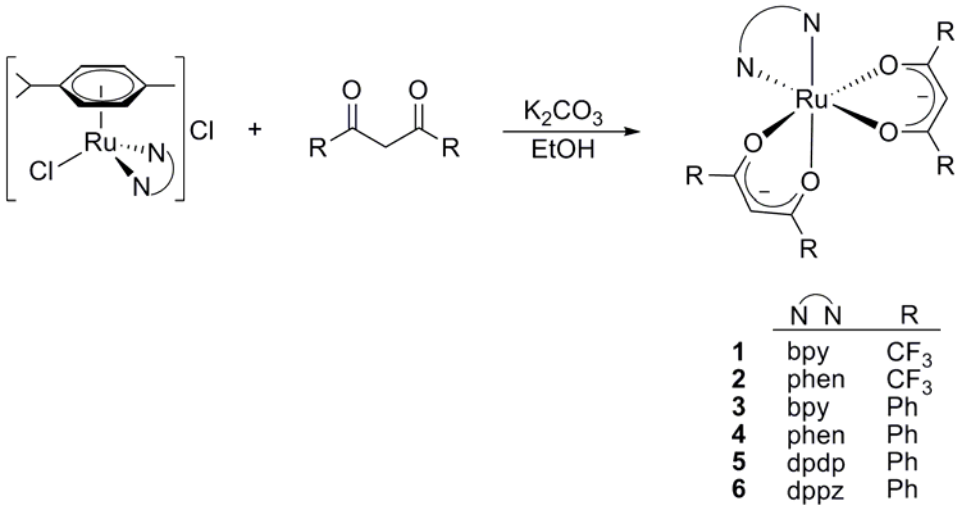

Scheme 1. Synthesis of complexes investigated in this study.

NMR Characterization.

^{1}H NMR spectroscopy confirmed the purity of each sample. The ^{1}H NMR spectra for all the [Ru(pp)(*p*-cym)Cl]Cl starting complexes were uncomplicated. In the case of **1** and **2** ^{1}H NMR characterization was straightforward; each complex has C_2 symmetry with five resonances, four for the respective phen or bpy ligand and one for the β-diketonate α hydrogen atoms. The spectra of the Ru(pp)(dbm)$_2$ complexes showed more complex behavior. An examination of ^{1}H NMR spectra of the dbm derivatives **3**–**6** in dichloromethane revealed some broadening of the protons *ortho*- to the nitrogen of the pp ligand and/or the β-diketonate α hydrogen atoms of the dbm ligands in compounds **3**–**5** but not in compound **6**. We attribute this broadening to very small amounts of Ru(III) impurities. In comparison to dichloromethane less polar solvents like benzene give much sharper signals while all of the signals broaden in more polar solvents such as acetone and methanol for the same solid sample. The resolution of these resonances is also significantly enhanced by passing the compounds down a neutral alumina column to remove the Ru(III) contaminant prior to NMR study. We theorize that the these Ru(III) species are present in such low concentrations that only the protons closest to the metal center are affected. In the case of **6**, no broadening of these resonances is observed, consistent with a higher reduction potential (*vide infra*) that inhibits the aerial oxidation to Ru(III).

Electrochemistry.

As is often the case for other Ru polypyridyl complexes, the redox properties of Ru(pp)(diketonate)$_2$ complexes were easily tuned by systematically changing both the polypyridyl and the β-diketonate ligands. Cyclic voltammetry of CH_2Cl_2 solutions was a

convenient way to study the effect of these ligand changes on the electrochemical behavior of these complexes. The electrochemical data for compounds **1**–**6** as well as data from various related complexes in the literature are compiled in Table 4.

Compounds **1** and **2** exhibit a reversible one-electron oxidation at 0.86 and 0.83 V respectively, and a ligand reduction process at -1.43 V. This oxidation process is assigned to the Ru(III)/Ru(II) couple while the reduction process is assigned as the reduction of the respective bpy or phen ligand. Compared to $Ru(II)(hfacac)_3^-$ (0.358 V)[43], the Ru(III)/Ru(II) oxidations of **1** (0.86 V) and $Ru(bpy)_2(hfacac)^+$ (0.90 V)[44] occur at higher potentials indicative of the π-accepting nature of the bpy ligand which removes electron density from the metal, subsequently making the oxidation from Ru(II) to Ru(III) more difficult. Interestingly, there is very little change in the potential of the Ru(III)/Ru(II) couple going from **1** to $Ru(bpy)_2(hfacac)^+$ in contrast to many complexes of this type which often exhibit well behaved ligand additivity effects in variation of the electrochemical potential.[45, 46]

Compounds **3**–**6** each exhibit two reversible one-electron oxidations near 0 V and 1.7 V which we assign to Ru(III)/Ru(II) and Ru(IV)/Ru(III) processes, respectively. Additionally, **4**–**6** have ligand reduction processes near -1.9 V.[47-50] In the case of **6** a second ligand reduction process is observed at -1.14 V which is ascribed to the reduction of the pyrazine moiety of the dppz ligand.[50] In comparison to $Ru(III)(dbm)_3$ (-0.652 V)[45] and $Ru(II)(bpy)_2(dbm)^+$ (0.702 V)[45], the Ru(III)/Ru(II) oxidation of **3** (0.026 V) is at intermediate potential, as is expected for an increase in number of π-accepting bpy ligands. The ligand additivity to the Ru(III)/Ru(II) potential as described by Lever and again by Xiao et al. is apparent in this series of molecules.[45, 46]

Table 4. Electrochemical and absorbance data.

	E^0 (mV) Ru^{III}/Ru^{II}	E^0 (mV) Ru^{IV}/Ru^{III}	E^0 (mV) ligand reductions	λ_{max} (nm), solution[b]	λ_{max} (nm), film[c]
1[a]	0.86		-1.43	297, 344, 421, 462, 506	422, 471, 516
2[a]	0.83		-1.43	288, 465, 503	463, 511
3[a]	0.026	1.68		329, 485, 618	502, 630
4[a]	-0.019	1.67	-1.91	325, 513, 597	534, 618
5[a]	0.015	1.65	-1.87	328, 485, 641	504, 652
6[a]	0.084	1.75	-1.14, -1.91	335, 512, 570	515, 591
$Ru(bpy)(acac)_2$[d]	-0.05	1.01			
$Ru(phen)(acac)_2$[d]	-0.06	1.01			
$[Ru(bpy)_3](PF_6)_2$[e]	1.29		-1.35, -1.54, -1.79		
$Ru(bpy)_2(hfacac)]PF_6$[f]	0.90		-1.54, -1.73		
$Ru(bpy)(hfacac)_2$[g]	0.51		-1.60		
$K[Ru(hfacac)_3]$[h]	0.358				
$[Ru(bpy)_2(dbm)]ClO_4$[i]	0.702		-1.94, -1.97		
$[Ru(dbm)_3]$[i]	-0.652				

[a]Potentials measured at room temperature with a scan rate of 100 mV/s in 0.1 M (TBA)(PF_6) in dichloromethane. [b]Dichloromethane solutions. [c]Films cast from dichloromethane. [d]Potentials versus SCE in 0.05 M (TBA)(ClO_4) in acetonitrile.[23] [e]Potential measured versus Ag/AgCl in 0.1 M (TBA)(PF_6).[24] [f]Potential versus Ag electrode in 0.1 M (TBA)(PF_6).[44]. [g]Potential versus Ag electrode in 0.1 M (TBA)(PF_6).[51]. [h]Potential versus Ag/($AgClO_4$ in acetonitrile) in (TEA)(ClO_4) in acetonitrile.[43] [i]Potentials versus Ag/$AgClO_4$ in 0.20 M (TEA)(ClO_4) in acetonitrile.[45]

Based on their ligand additivity definitions, Xiao et al. gave a predicted value of -0.024 V versus SCE for the Ru(III)/Ru(II) redox couple of **3** in excellent agreement with our experimental value of 0.026 V.[45]

Changing the β-diketonate substituents has a pronounced effect on the Ru(III)/Ru(II) couples for **1**–**2** (trifluoromethyl substituents) and **3**–**4** (phenyl substituents) compared with Ru(bpy)$(acac)_2$ (-0.05 V)[23] and Ru(phen)$(acac)_2$ (-0.06 V)[23]. The oxidation of Ru(II) to Ru(III) for **1** and **2** occurs near 0.85 V while that of **3** and **4** occurs near 0 V (Figure 2). It is obvious that the change in substitution of the β-diketonate ligand has a large affect on the donating ability and thus the stabilizing power of the ligand. The hfacac ligands, with electron-withdrawing substituents, result in a more electron poor metal center than in the case of acac, stabilizing the Ru(II) state resulting in a more difficult oxidation of Ru(II) to Ru(III). The dbm ligands with electron-rich phenyl rings offer electron density to the metal in a similar manner to acac, resulting in a stabilization of the Ru(III) oxidation state. We speculate that the reduction potentials for the Ru(II) to Ru(III) oxidation in compounds **3**–**5** are sufficiently near 0 V to allow oxidation of a very small amount of the sample to Ru(III). This correlates well with the observed broadening of the above mentioned resonances in the ^{1}H NMR spectra. In the case of **6**, where sharp, clearly resolved NMR spectra are seen, it appears that the reduction potential is sufficiently high (0.084 V) to prevent aerial oxidation to Ru(III).

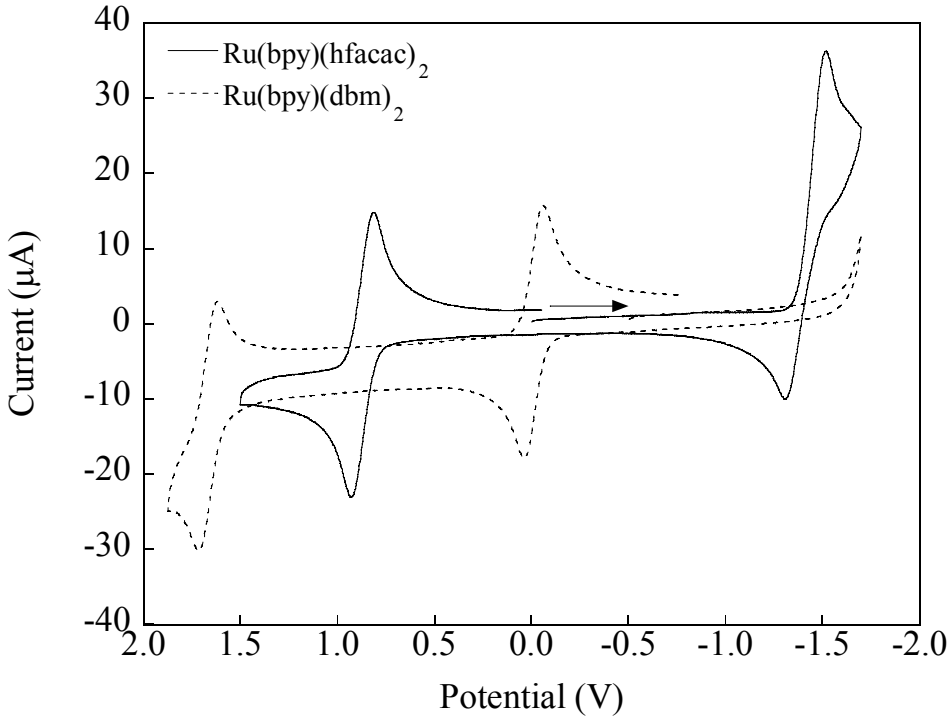

Figure 2. Cyclic voltammograms of **1** (solid line) and **3** (dashed line) in 0.1 M $TBAPF_6/CH_2Cl_2$, ν = 100 mV/s.

UV-Vis Spectroscopy.

Solution UV-Vis spectra for compounds **1**–**6** are shown in Figures 3 and 4, and the results are summarized in Table 3. All compounds contain two broad absorption features, a peak and a high energy shoulder for **1** and **2**, near 465 and 505 nm (Figure 3). These absorptions are shifted to about 500 and 620 nm for **3**–**6** (Figure 4). In all cases both of these absorptions are assigned as MLCT, $d\pi(Ru^{II}) \rightarrow \pi^*(pp)$, bands. In the same way the Ru(III)/Ru(II) couple varies with the β-diketonate ligand, the shift to higher energy for the absorptions observed for the hfacac compounds compared to the dbm compounds may be explained by the enhanced electron withdrawing ability of the $-CF_3$ substituent compared to the –Ph. Additionally, in all complexes, a higher energy, more strongly absorbing feature is also observed, near 290 nm for **1** and **2** and near 330 nm for **3**–**6**, which we tentatively assign to the $\pi \rightarrow \pi^*$ absorption of the respective hfacac or dbm ligand due to the good correlation with the spectral features of the free ligand.[52, 53]

Due to the presence of intermolecular interactions in the crystalline state, solid-state UV-Vis spectra were also taken. Spectra were taken of films of **1**–**6**, cast from dichloromethane solutions onto a cubic zirconia (ZrO_2) ATR crystal, after evaporation of the solvent and after the film was abraded with a cotton swab to observe any spectral change that results from disturbing the ordering of the solid. The spectrum of a film of **3** as cast (Figure 5) exhibits the broadened low energy absorption that is sometimes present in films which are partially crystalline. Abrading the film with a cotton swab improves the contact of the solid with the ZrO_2 substrate, reducing the low energy component that is prominent in the film as cast, resulting in a spectrum very similar to that observed in solution. We ascribe the "abraded spectrum" to a less crystalline state of the solid.

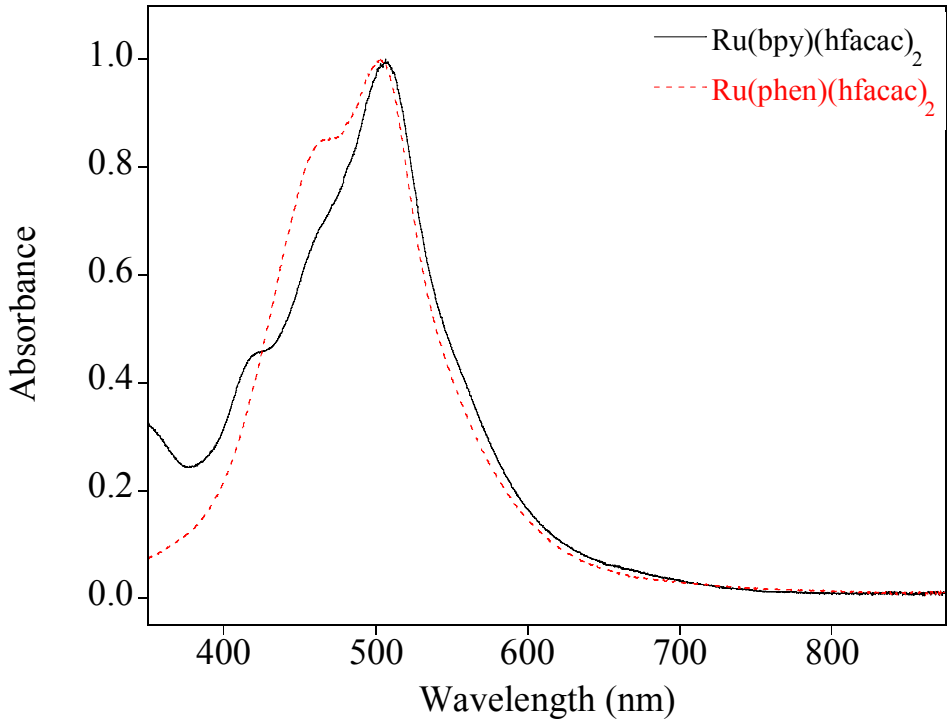

Figure 3. Room temperature UV-Vis solution spectra of **1** (black solid line) and **2** (red dashed line) in CH_2Cl_2.

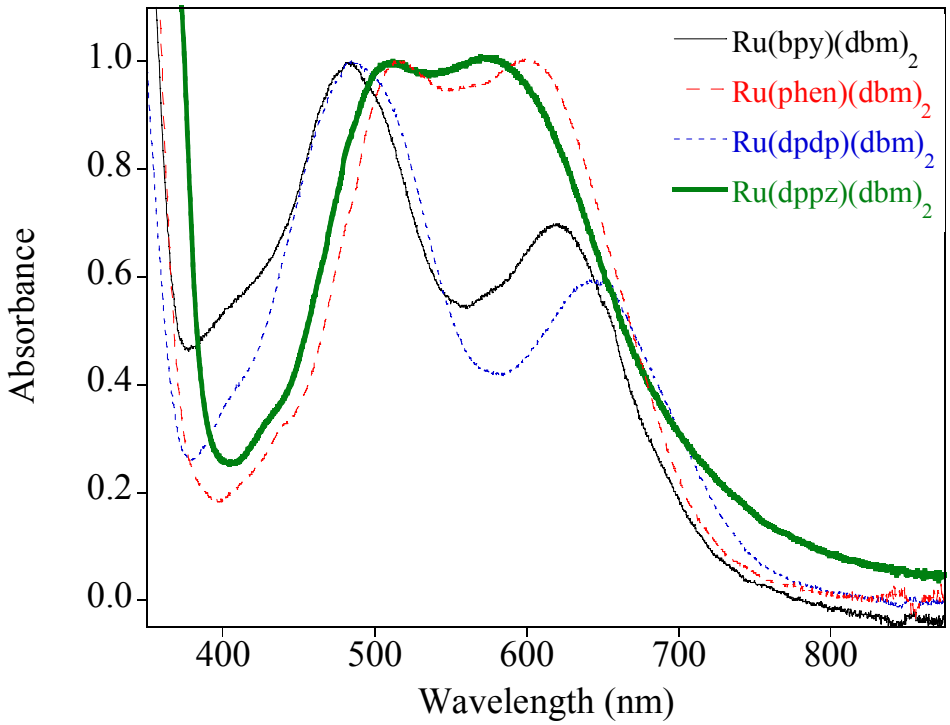

Figure 4. Room temperature UV-Vis solution spectra of **3** (black solid line), **4** (red dashed line), **5** (blue dotted line), **4** (green bold line) in CH_2Cl_2.

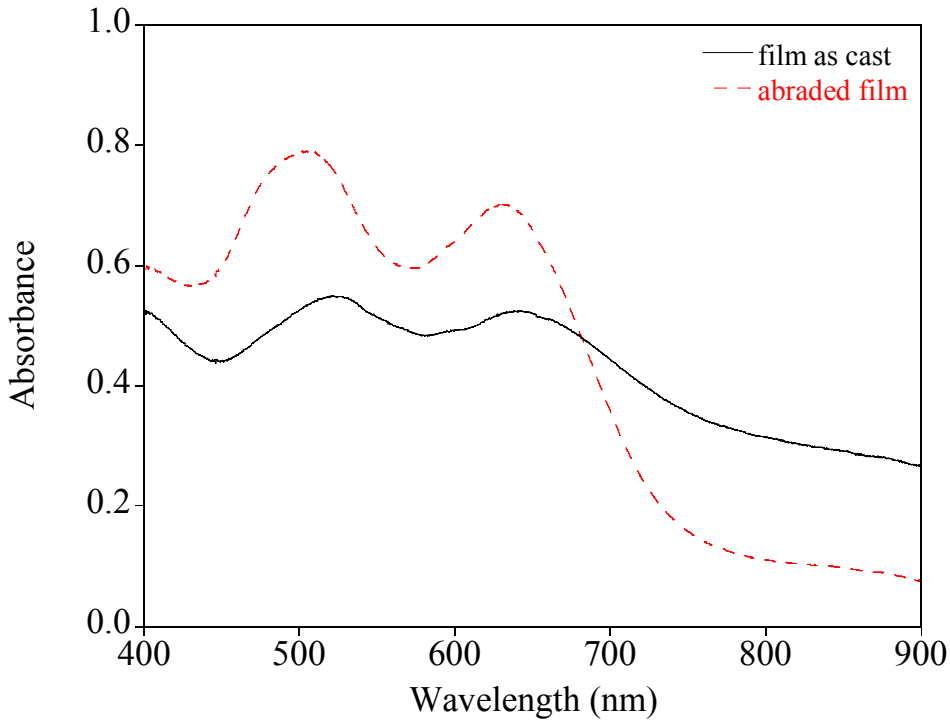

Figure 5. Room temperature UV-Vis solid-state spectra of **3** as a film cast from CH_2Cl_2 (black solid line) and as an abraded film (red dashed line).

X-ray Crystallography.

The molecular structures of **1**, **2**, **3**, **4** , and **6** were determined by X-ray crystallography. Data collected for **5** were of poor quality due to a suspected phase transition at the temperature of collection, however, the connectivity of the atoms was determined to be as expected. Figure 6 shows numbered thermal ellipsoid plots for **1** and **2** while Figure 7 shows labeled thermal ellipsoid plots for **3**, **4** , and **6**. Selected bond lengths and angles are shown in Table 5. A summary of each individual structure will be given followed by comparison of all the structures.

Table 5. Selected bond lengths (Å) for the reported structures.

	1	**2**	**3**	**4**	**6**
Ru–N1	2.023(4)	2.024(5)	2.011(2)	2.020(2)	2.008(2)
Ru–N2	2.024(4)	2.015(5)	2.002(2)	–	–
Ru–O1	2.044(3)	2.045(4)	2.043(2)	2.034(2)	2.026(2)
Ru–O2	2.036(3)	2.039(4)	2.020(2)	2.033(2)	2.028(2)
Ru–O3	2.041(4)	2.039(4)	2.037(2)	–	–
Ru–O4	2.033(3)	2.053(4)	2.035(2)	–	–

Compound **1** crystallizes in the space group $P2_1/c$ with one bpy and two monoanionic hfacac ligands in a pseudo-octahedral arrangement around the metal center. The Ru–N bond lengths are 2.023(4) and 2.024(4) Å respectively for N1 and N2 which correlate well with typical polypyridine-metal bonds. The Ru–O bond distances for O1 and O4 (*trans* to nitrogen) are 2.044(3) and 2.041(3) Å. The Ru–O bond lengths for O2 and O3 are 2.036(3) and 2.033(4) Å. Little difference in the Ru–O bond lengths is observed for those Ru–O bonds trans to N versus those trans to other O atoms which may indicate relatively little back donation occurs to the π-accepting N. Delocalization of the electron density in the β-diketonate ligands is confirmed in all of the structures examined here by virtue of the nearly identical C----O bond lengths in the β-diketonate ligand of

a given complex. These bond lengths are similar to those of $Ru(acac)_3$ as well as other Ru(II) species with two acac and one bidentate nitrogen donor ligand.[54-59] The bipyridine ligand is essentially planar with a mean deviation from a least-squares plane of 0.0398 Å. A short π-stacking distance of 3.3859 Å exists between the bpy ligands which overlap by about ½ of a pyridine ring (Figure 8). The molecules form infinite π-stacks along the a-axis, with alternating pure layers of Δ and Λ enantiomers progressing throughout the crystal. The crystal was face indexed and it was found that the 100 faces are the ends of the long dimension of the plate, thus the a-axis, the direction of π-stacking, is along the largest dimension of the crystal. This shows that the crystal grows such that the largest dimension is in the direction of the strongest intermolecular interactions between molecules.

Compound **2** crystallized in the space group $P2_1/n$ as pseudo-octahedral Ru(II) surrounded by one phen ligand and two hfacac ligands. The Ru–N bond lengths are reasonable for phen bound to Ru, 2.024(5) and 2.015(5) Å. The Ru–O bonds *trans* to the N atoms (Ru–O1, Ru–O4) of the phen ligands are 2.045 and 2.039 Å while the Ru–O2 and Ru–O3 bond lengths are both 2.039 Å. Least-squared planes made from the phen ligands have a mean deviation from planarity of 0.0192 Å. The molecules interact with each other, forming infinite π-stacks, with a stacking distance of 3.3633 Å between least-squares planes formed from the phen ligands and overlap of about ½ of a pyridine ring (Figure 8). As with compound **1**, the molecules form infinite π-stacks along the a-axis, with layers of Δ and Λ enantiomers alternating through the crystal.

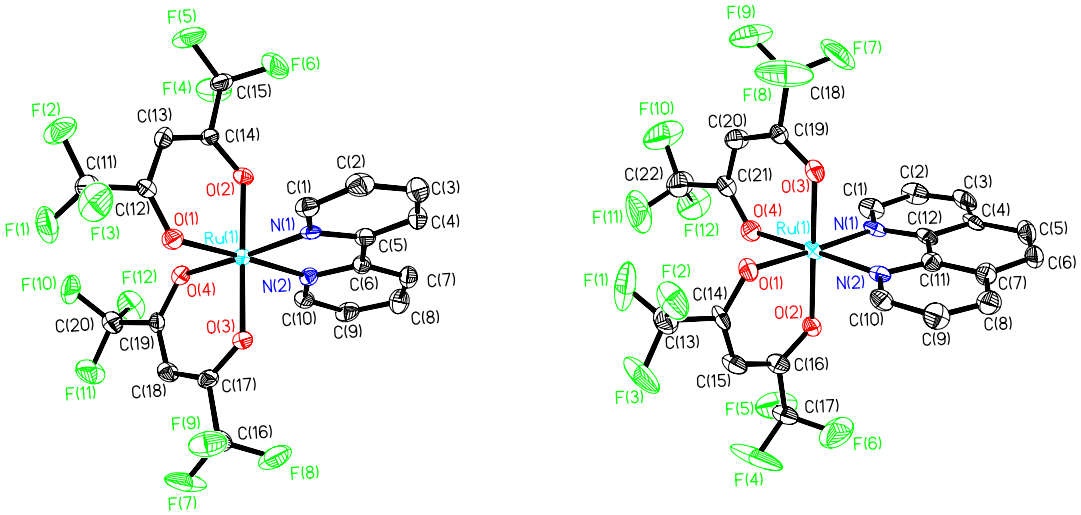

Figure 6. Labeled thermal ellipsoid plots of **1** and **2** with 50% probability surfaces.

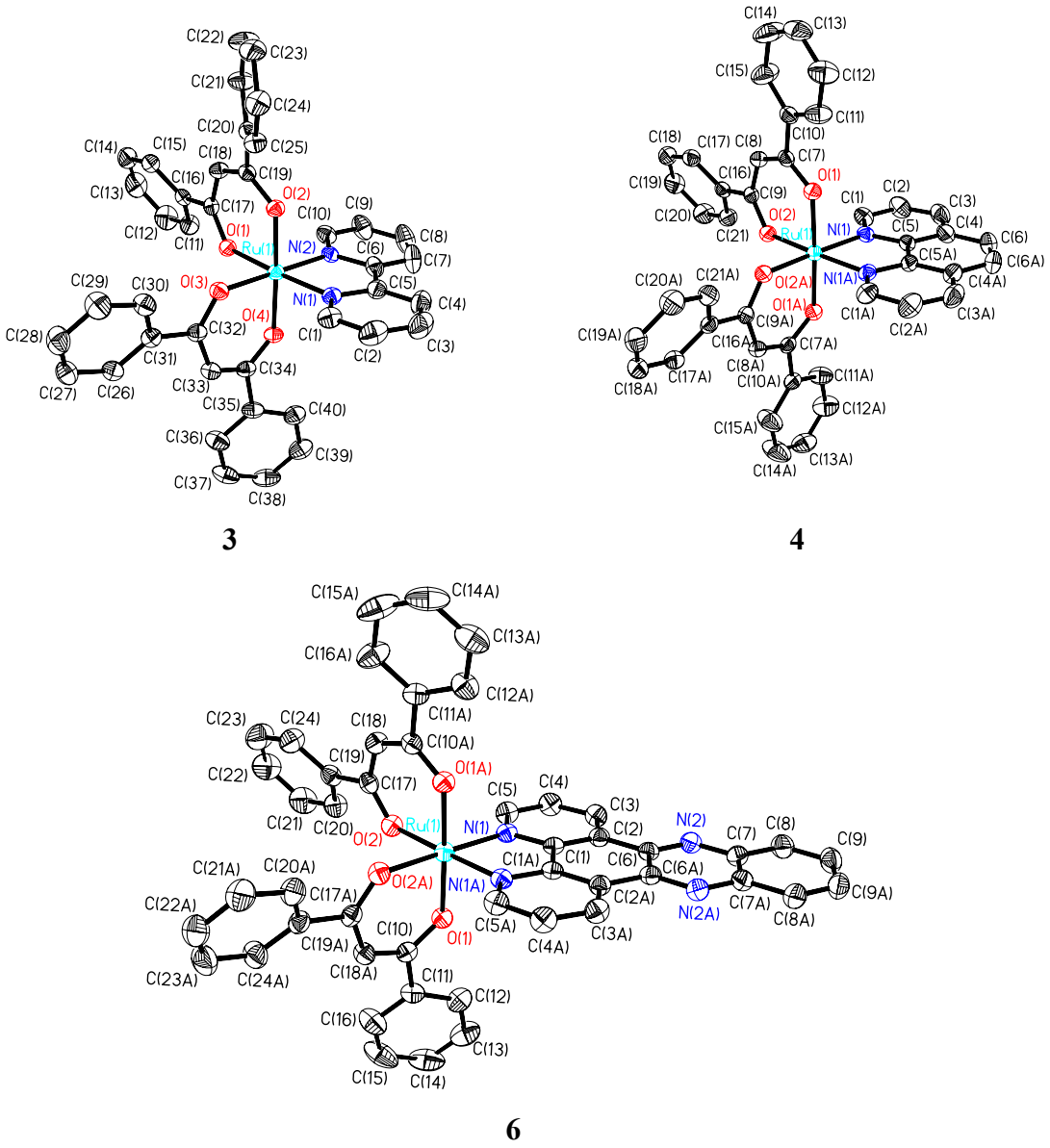

Figure 7. Labeled thermal ellipsoid plots of **3**, **4**, and **6** with 50% probability surfaces.

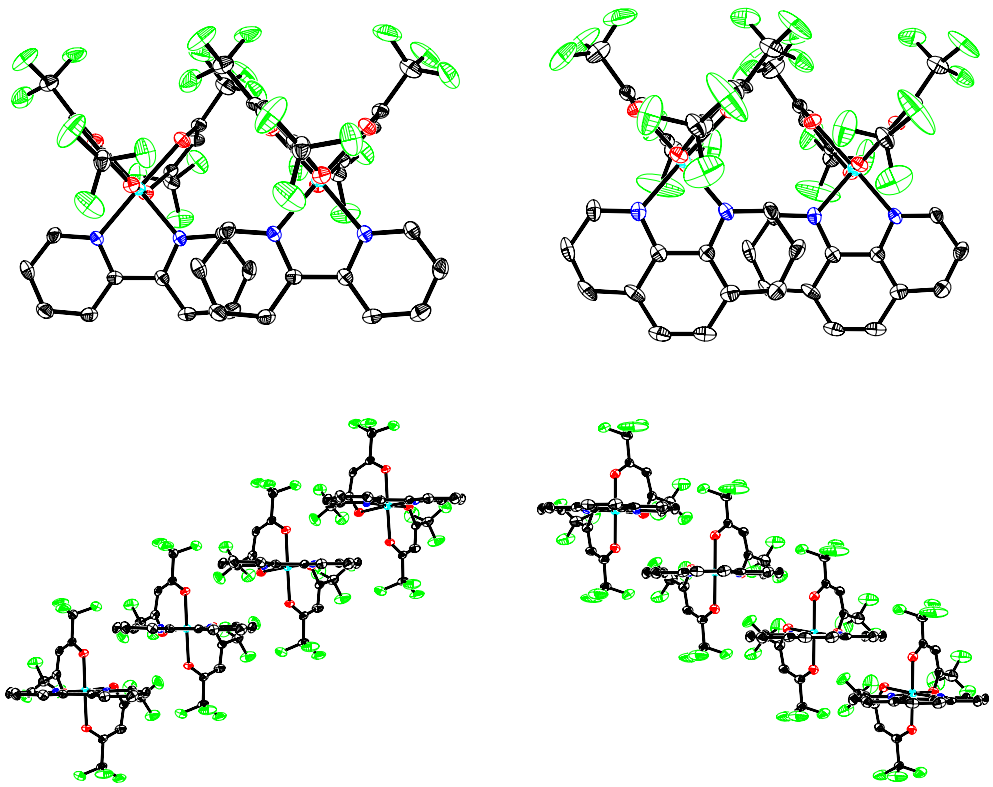

Figure 8. Molecular overlap (top) and π-stacking (bottom) diagrams of Ru(bpy)(hfacac)$_2$ (**1**) (left) and Ru(phen)(hfacac)$_2$ (**2**) (right). **1** has a π-stacking distance of 3.3859 Å while **2** has π-stacking distance of 3.3633 Å.

Compound **3** crystallizes in the space group *Pbcn* as a pseudo-octahedral Ru(II) metal center with one bpy ligand and two dbm ligands completing the coordination sphere. The Ru–N bond lengths to the bpy ligand are 2.011(2) and 2.002(2) Å for Ru–N1 and Ru–N2 respectively. The Ru–O bonds lengths for the oxygens *trans* to N are 2.043(2) and 2.038(2) Å (O1 and O3.) And the Ru–O bond lengths for the oxygens *trans* to oxygen are 2.019(2) and 2.035(2) Å (O2 and O4.) The structure consists of slipped infinite stacks of π-dimers. The dimers have an antiparallel overlap of about ½ of the bpy moiety with an interdimer π-stacking distance of 3.5047 Å (Figure 8). The π-overlap of sets of π-dimers is very minimal with overlap of approximately one carbon and an intradimer stacking distance of 3.4073 Å. A least-squares plane formed from the bpy ligand gave a mean deviation from planarity of 0.0432 Å.

Compound **4** crystallizes in the space group *Pcca* with the Ru(II) lying on a 2-fold rotation axis, thus the asymmetric unit consists of ½ of the molecule. The Ru(II) center is surrounded by one phen ligand and two dbm ligands. The Ru–N bond length is 2.020(2) Å. The Ru–O2 bond, which is *trans* to N, is 2.033(2) Å while the Ru–O3 bond, which is trans to O, is 2.034(2) Å. The very flat phen moiety has a mean deviation from planarity of 0.0069 Å from a least-squares plane formed from this ligand. Infinite π-stacks containing both Δ and Λ enantiomers occur in the structure with an overlap of slightly less than ½ of a phen ligand per interaction. The π-stacking distance between molecules is 3.3523 Å (Figure 9). Adjacent stacks are related to each other by a 2-fold axis. The molecules are in close proximity with contacts less than the van der Waals (VDW) radii between the phen of one complex and the dbm ligands of the molecules with which it is π-stacked.

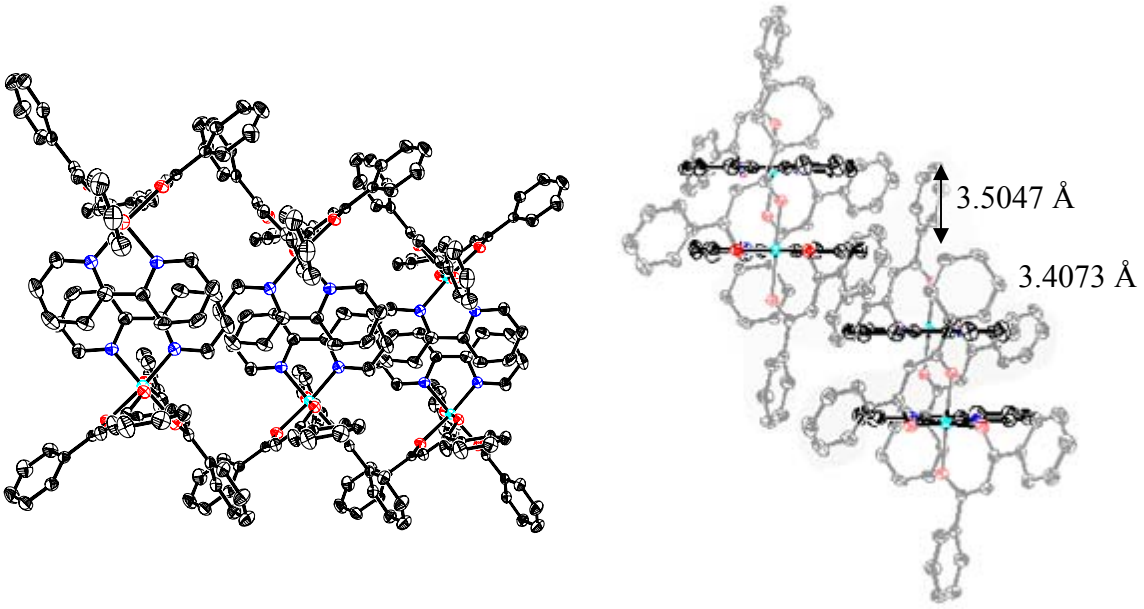

Figure 9. Thermal ellipsoid packing plots showing overlap (left) and π-stacking (right) of $Ru(bpy)(dbm)_2$ (**3**).

Additionally, due to the large degree of π-stacking, the dbm groups also tend to be aggregated in the structure, resulting in several contacts that are less than the VDW radii of the atoms between phenyl groups. The packing in this structure generates accessible void space channels (Figure 10). These channels account for 8.6% (300 $Å^3$) of the space in the structure and are of appropriate dimension to hold small molecules.

Compound **6** crystallizes as a deutero-dichloromethane solvate in the space group *Pcca* and is isostructural to **4**. The Ru(II) metal center lies on 2-fold rotation axis, thus the asymmetric unit consists of ½ of the molecule as well as a dichloromethane molecule. The Ru–N distance is 2.008(2) Å while of the Ru–O distances are 2.026(2) and 2.028(2) Å for O1 and O2 (*trans* to N) respectively. A least-squares plane of the dppz ligand gave a mean deviation from planarity of 0.0143 Å. Infinite π-stacks are observed as in the structure of **4**. Overlap of only half of two rings of the fused dppz ligand occurs, however a very short π-stacking distance of 3.3638 Å is observed between the least-squares planes made from the dppz ligands. As in the structure of **4**, the molecules are in close enough proximity with short contacts from the dppz of one complex to the dbm ligands of the molecules with which it is π-stacked. Also as in **4**, there is aggregation of the dbm groups and resultant short contacts between phenyl groups: both π-π and edge-to-face motifs are observed. Channels occupied by the dichloromethane solvent molecules run through the structure (Figure 10). Upon removal of the solvent and further analysis of the resulting void space it was calculated that these channels account for 14.6% (614 $Å^3$) of the unit cell volume.

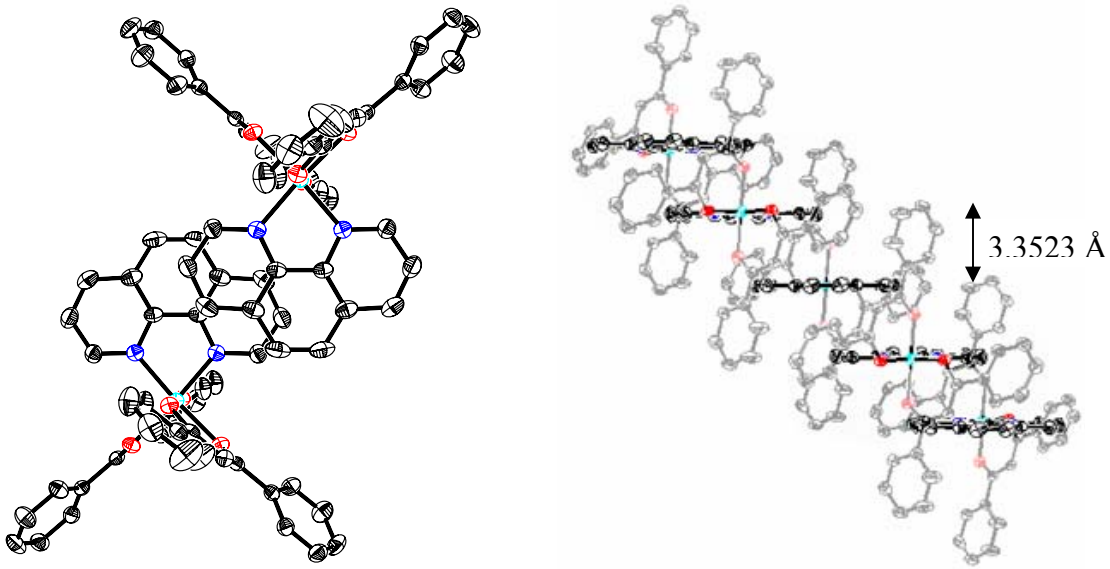

Figure 10. Thermal ellipsoid packing plots showing overlap (left) and π-stacking (right) of Ru(phen)$(dbm)_2$ (**4**).

We were surprised that the variations in the β-diketonate ligands resulted in such dramatic changes in the packing of these Ru molecules. Closer examination of the variations in packing of the above structures offers information about the structural differences observed. Infinite π-stacks occur in the structures of compounds **1** and **2** with π-overlap between the polypyridine ligands within the stacks of about one-half of a pyridine ring. The relatively poor overlap exhibited by these molecules is due to their orientation in the crystal lattice. The metal centers lie adjacent to one another, as shown in Figure 8 (top), allowing less opportunity for π-interaction than if the metals were opposite each other. The expected orientation of the metals opposite of each other has been observed previously in a similar Ru(II) structure with bpy and salicylaldehyde (sal) ligands.[22] Further examination of the molecular packing within these structures shows significant fluorine-fluorine interactions between $-CF_3$ groups on different molecules (Figure 12). Interestingly, these fluorine-fluorine interactions seem to prevent the $-CF_3$ groups from being disordered as is typically observed. The interactions between fluorine atoms appear to take precedence over the tendency to form π-stacks with favorable overlap.

Examination of the $Ru(pp)(dbm)_2$ structures, **3**, **4**, and **6,** revealed the orientation of the molecules with respect to the π-stacking was similar to that of $Ru(bpy)(sal)_2$. With no fluorine interactions the molecules arrange themselves so the metal atoms of opposing chirality are opposite of one another and the π-overlap is improved. The structure of **3** shows overlap of one-half of the full bpy ligand and, due to steric constraints imposed by the dbm, π-dimers are forced to form (Figure 9). X-ray crystallographic data collection of **5** gave a highly disordered structure that may be attributed to a phase change at the

collection temperature of -100 °C. This disordered structure shows π-dimers that have poor overlap. The structures of **4** and **6** reveal infinite π-stacks of slipped molecules with short π-π distances which still give partial, though improved, overlap with respect to **1** and **2** (Figure 10). Additionally, as mentioned above, the strong interaction in one direction of the crystals caused by the infinite π-stacks may lead to the large void space channels that are observed in **4** and **6** (Figure 11).

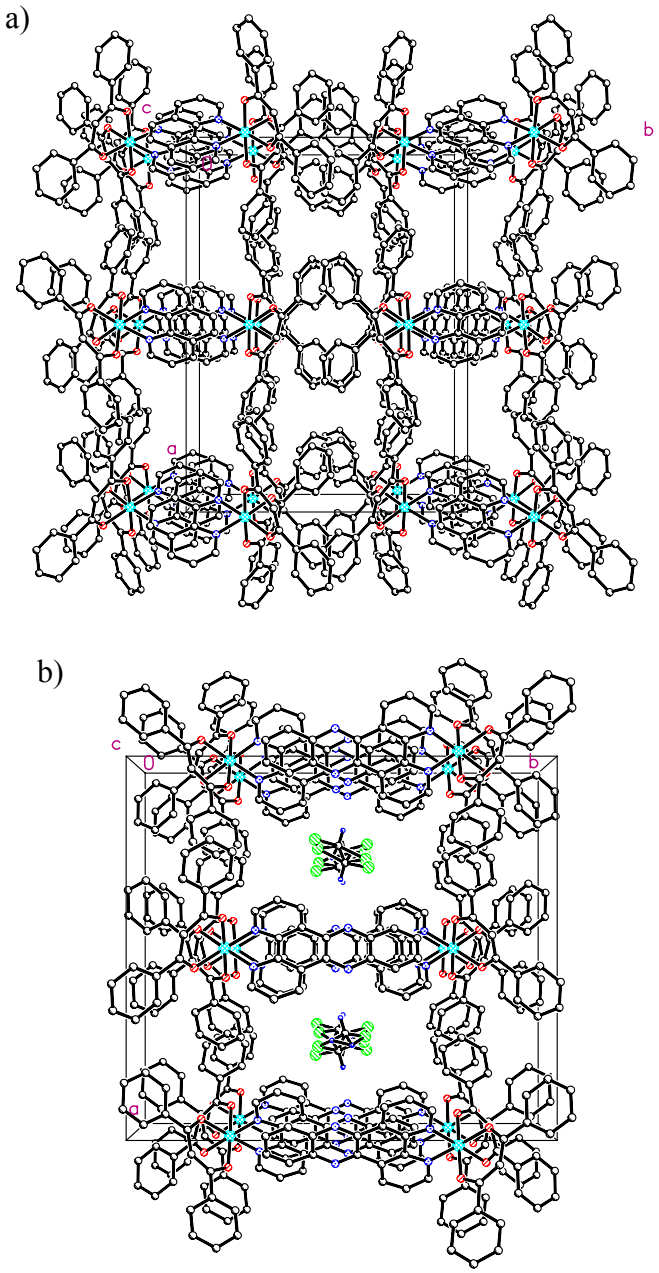

Figure 11. Packing diagrams depicting the large channels migrating through the crystalline solids a) **4**, 8.6% void space/unit cell, and b) **6**, 14.6% void space/unit cell when dichloromethane solvent is removed.

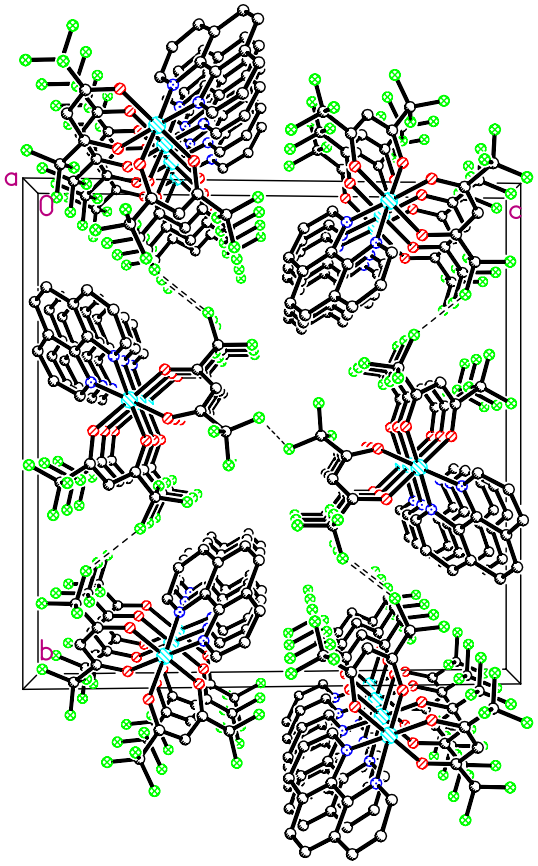

Figure 12. Packing diagram of **2**, fluorine interactions are indicated by dashed lines.

Chlorine Detection.

Due to their potentially porous nature and the Ru(III)/Ru(II) oxidation near 0 V, the sensitivity of **4** and **6** to chlorine was investigated. Chlorine, as a strong oxidant (E^0=1.358)[19], could convert the Ru(II) species to Ru(III) with a resulting large color change. Preliminary testing showed that purple solutions of **4** or **6** were immediately converted to yellow upon exposure to chlorine gas. Further studies showed that in the solid state, exposure of **4** or **6** to chlorine visibly converts the sample from purple to yellow. This color change was studied by monitoring the absorption spectrum of the solid film, when exposed to Cl_2 vapor, by solid-state UV-Vis. An isosbestic change is observed (Figure 13) for the exposure of a film of **4** to chlorine vapor for the conversion of Ru(II)(phen)$(dbm)_2$ to [Ru(III)(phen)$(dbm)_2$]Cl. Although it has been shown with other Ru(II)/Ru(III) systems that an oxidation such as this can be reversed under vacuum, our samples did not exhibit reversible behavior even when heating was applied with the sample under vacuum.[15] A similar isosbestic change was observed for the reaction of solid compound **6** with chlorine (Figure 14).

Somewhat surprisingly, we also observed sensitivity to chlorine for the non-porous crystalline solids, **1–3** and **5** (Figure 15). It appears that porosity in the solid is not necessary for Cl_2 to react, oxidizing Ru(II) to Ru(III) for the very thin layers studied by ATR absorption on the ZrO_2 crystal. It is possible that abrading the film causes a loss in crystallinity that leaves a thin reactive amorphous film. The films used in these studies, by our calculations, are only 20–50 molecules thick for **4–6** and 100–500 molecules thick for **1** and **2**, possibly eliminating the necessity of large channels for Cl_2 to

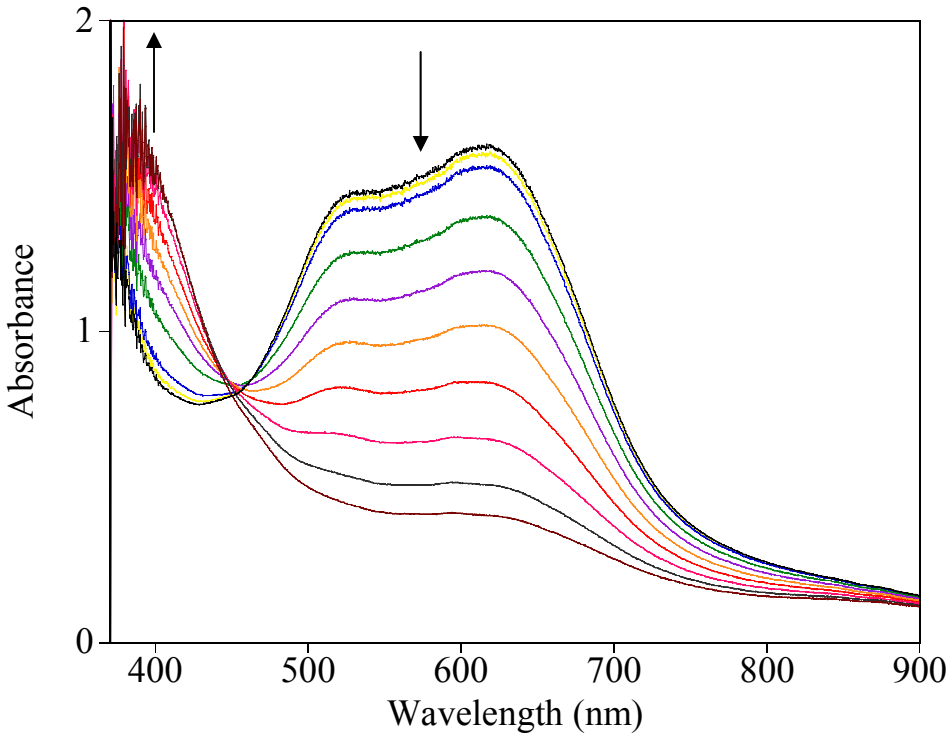

Figure 13. Response of a solid film of Ru(phen)(dbm)$_2$ (**4**) to a large concentration of Cl_2 in nitrogen gas over 1 min.

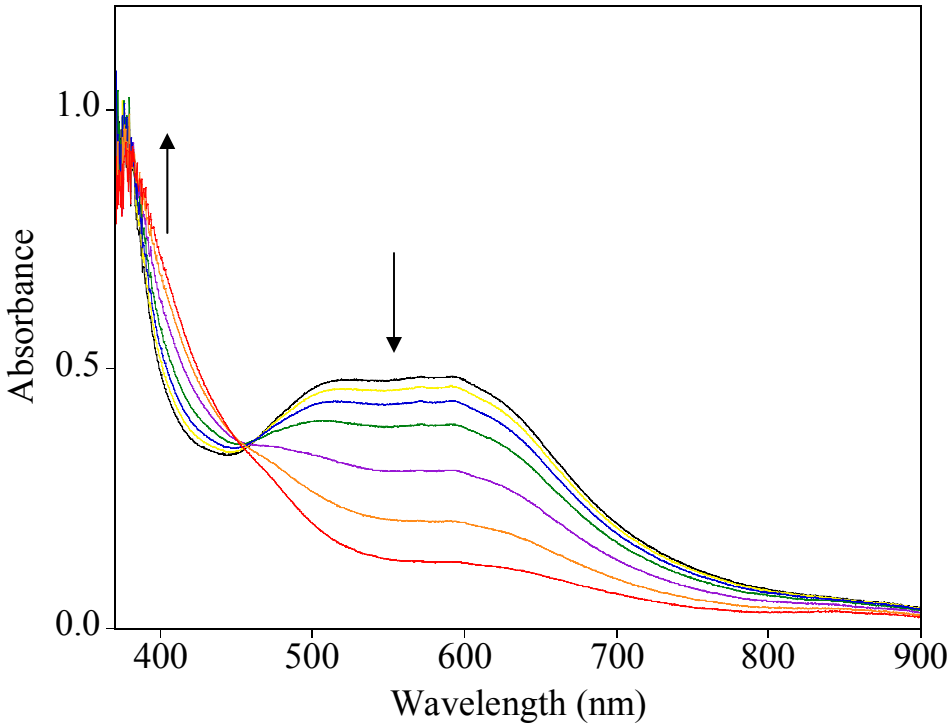

Figure 14. Response of a solid film of Ru(dppz)(dbm)$_2$ (**6**) to a large concentration of Cl_2 in nitrogen gas over 1.5 min.

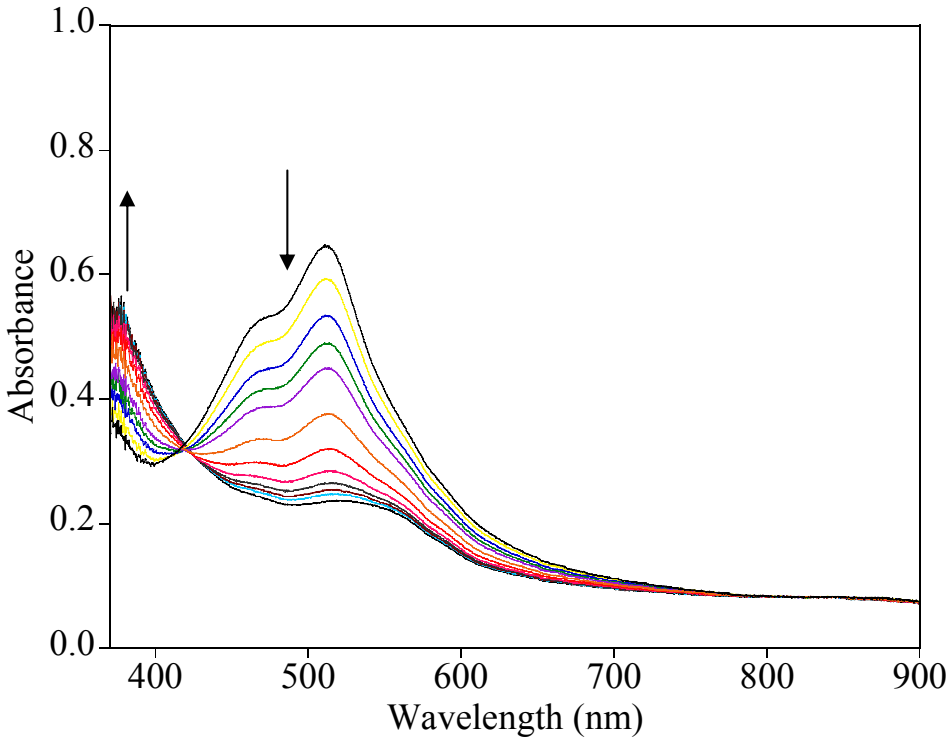

Figure 15. Response of a solid film of Ru(phen)(hfacac)$_2$ (**2**) to a large concentration of Cl_2 in nitrogen gas over 1.5 min.

access all of the Ru sites. We speculate that thicker samples or single crystals of **1–3** and **5** would only undergo oxidation of the surface whereas complexes **4** and **6** would undergo oxidation of a larger portion of the sample. Exposures such as those shown in Figures 12–14 used fairly high concentrations of Cl_2 gas (1–10%, mole percent in nitrogen). For lower concentrations (10–100 ppm) that are closer to the occupational exposure limits, a flow rate of 10 mL/min for 10 min gave an incomplete shift of the absorption band thus limiting the practical utility of these molecules as the sensing medium in a crystalline optical sensor. While these complexes, as pure single crystals, do not efficiently sense ppm concentrations of chlorine, we believe these materials may find use in the colorimetric sensing of Cl_2 when cast in a highly gas permeable polymer matrix as was shown with *o*-tolidine.[ref] Additionally, these compounds could be employed in technology such as Drager tubes where a colorimetric change to a solid or solution is observed upon the uptake of a known amount of Cl_2-contaminated air.[ref] Further studies of the utility of these complexes as sensors of Cl_2 is underway.

Conclusions.

Several Ru(pp)(β-diketonate)$_2$ complexes have been synthesized, characterized, and studied by X-ray crystallography, cyclic voltammetry, and UV-Vis absorption. Not surprisingly, cyclic voltammetric and UV-Vis studies show changes in the electronic properties of these complexes with alteration of the substituents on the β-diketonate ligand. Electron-withdrawing –CF_3 groups (hfacac) result in a more positive Ru(III)/Ru(II) oxidation compared to –Ph groups (dbm) which result in a Ru(III)/Ru(II) standard potential near 0 V. The energy of the MLCT absorption bands are also affected by this change in substituent, with the poorer π-donor, hfacac, resulting in stabilization of the dπ orbitals and a higher energy dπ → π* absorption than is observed in the dbm complexes. X-ray crystallography revealed some form of π-stacking in all of the structures. The hfacac structures exhibit several fluorine-fluorine interactions which appear to greatly affect the organization of the structure, resulting in a different π-stacking regime, with less π-overlap, than in the dbm structures. The dbm structures exhibit more extensive π-stacking in one direction of the crystal, which in two of the structures, **4** and **6**, may aid in the formation of channels. Films of these complexes were found to irreversibly react with chlorine gas which oxidizes Ru(II) to Ru(III) resulting in dramatic color changes from purple/black/red to yellow.

References.

1. Bernhard, S.; Barron, J. A.; Houston, P. L.; Abruna, H. D.; Ruglovksy, J. L.; Gao, X.; Malliaras, G. G., *J. Am. Chem. Soc.* **2002**, *124*, 13624.

2. Evju, J. K.; Mann, K. R., *Chem. Mater.* **1999**, *11*, 1425.

3. Takahashi, Y.; Arakawa, H.; Sugihara, H.; Hara, K.; Islam, A.; Katoh, R.; Tachibana, Y.; Yanagida, M., *Inorg. Chim. Acta* **2000**, *310*, 169.

4. Slinker, J. D.; Rivnay, J.; Moskowitz, J. S.; Parker, J. B.; Bernhard, S.; Abruna, H. D.; Malliaras, G. G., *J. Mater. Chem.* **2007**, *17*, 2976.

5. Chou, P.-T.; Chi, Y., *Chem.--Eur. J.* **2007**, *13*, 380.

6. Vos, J. G.; Kelly, J. M., *Dalton Trans.* **2006**, 4869.

7. Chou, P.-T.; Chi, Y., *Eur. J. Inorg. Chem.* **2006**, 3319.

8. Brook, T. E.; Narayanaswamy, R., *Sens. Actuators, B* **1997**, *B39*, 195.

9. Demas, J. N.; DeGraff, B. A., *Coord. Chem. Rev.* **2001**, *211*, 317.

10. Ghosh, A.; Ganguly, B.; Das, A., *Inorg. Chem.* **2007**, *46*, 9912.

11. Kneas, K. A.; Demas, J. N.; Nguyen, B.; Lockhart, A.; Xu, W.; DeGraff, B. A., *Anal. Chem.* **2002**, *74*, 1111.

12. Kocincova, A. S.; Borisov, S. M.; Krause, C.; Wolfbeis, O. S., *Anal. Chem.* **2007**, *79*, 8486.

13. McGee, K. A.; Veltkamp, D. J.; Marquardt, B. J.; Mann, K. R., *J. Am. Chem. Soc.* **2007**, *129*, 15092.

14. Ralfs, M.; Heinze, J., *Sens. Actuators, B* **1997**, *B44*, 257.

15. Onishi, M.; Ikemoto, K.; Hiraki, K.; Aoki, K., *Chem. Lett.* **1998**, 23.

16. Occupational Safety and Health Guideline for Chlorine. http://www.osha.gov/SLTC/healthguidelines/chlorine/recognition.html (4/28/2008).

17. *Chlorine: Effects on Health and the Environment*; The Chlorine Institute, Inc.: Arlington, 1999; pp 1-8.

18. *Atmospheric Monitoring Equipment for Chlorine*; Pamphlet 73; The Chlorine Institute, Inc.: Arlington, June, 2003; pp 1-23.

19. Schmittinger, P.; Editor, *Chlorine: Principles and Industrial Practice*. **2000**; p 254.

20. *Crystal Engineering: From Molecules and Crystals to Materials*. Kluwer Academic: Dordrecht, **1999**; Vol. 538.

21. *Inclusion Compounds Volume 1*. Academic Press: London, **1984**.

22. Janzen, D. E.; Wang, X.; Carr, P. W.; Mann, K. R., *Inorg. Chim. Acta* **2004**, *357*, 3317.

23. Gupta, A. K.; Poddar, R. K., *Indian J. Chem., Sect A* **1999**, *38A*, 1228.

24. Pappenfus, T. M.; Mann, K. R., *Inorg. Chem.* **2001**, *40*, 6301.

25. Dupureur, C. M.; Barton, J. K., *Inorg. Chem.* **1997**, *36*, 33.

26. Hiort, C.; Lincoln, P.; Norden, B., *J. Am. Chem. Soc.* **1993**, *115*, 3448.

27. Bennett, M. A.; Smith, A. K., *J. Chem. Soc., Dalton Trans.* **1974**, 233.

28. Zelonka, R. A.; Baird, M. C., *Can. J. Chem.* **1972**, *50*, 3063.

29. Freedman, D. A.; Evju, J. K.; Pomije, M. K.; Mann, K. R., *Inorg. Chem.* **2001**, *40*, 5711.

30. Kneas, K. A.; Xu, W.; Demas, J. N.; DeGraff, B. A., *Appl. Spectrosc.* **1997**, *51*, 1346.

31. Demas, J. N.; DeGraff, B. A.; Xu, W., *Anal. Chem.* **1995**, *67*, 1377.

32. Canivet, J.; Karmazin-Brelot, L.; Suess-Fink, G., *J. Organomet. Chem.* **2005**, *690*, 3202.

33. Robertson, D. R.; Robertson, I. W.; Stephenson, T. A., *J. Organomet. Chem.* **1980**, *202*, 309.

34. Compound made by Erica J. Marti.

35. Blessing, R. H., *Acta Crystallogr., Sect. A: Found. Crystallogr.* **1995**, *A51*, 33.

36. Sheldrick, G. *SADABS*, v.2.03; 2002.

37. *SHELXL*, v.6.1; Bruker AXS, Madison, WI, 2001.

38. Spek, A. L., *J. Appl. Crystallogr.* **2003**, *36*, 7.

39. Spek, A. L. *PLATON*, Utrecht University, Utrecht, The Netherlands, 2005.

40. Freedman, D. A.; Janzen, D. E.; Vreeland, J. L.; Tully, H. M.; Mann, K. R., *Inorg. Chem.* **2002**, *41*, 3820.

41. Freedman, D. A.; Kruger, S.; Roosa, C.; Wymer, C., *Inorg. Chem.* **2006**, *45*, 9558.

42. Freedman, D. A.; Janzen, D. E.; Mann, K. R., *Inorg. Chem.* **2001**, *40*, 6009.

43. Hoshino, Y.; Endo, A.; Shimizu, K.; Sato, G. P., *J. Electroanal. Chem.* **1988**, *246*, 225.

44. El-Hendawy, A. M.; Al-Kubaisi, A. H.; Al-Madfa, H. A., *Polyhedron* **1997**, *16*, 3039.

45. Xiao, X.; Sakamoto, J.; Tanabe, M.; Yamazaki, S.; Yamabe, S.; Matsumura-Inoue, T., *J. Electroanal. Chem.* **2002**, *527*, 33.

46. Lever, A. B. P., *Inorg. Chem.* **1990**, *29*, 1271.

47. Al-Anber, M.; Vatsadze, S.; Holze, R.; Lang, H.; Thiel, W. R., *Dalton Trans.* **2005**, 3632.

48. Edelmann, M. J.; Raimundo, J.-M.; Utesch, N. F.; Diederich, F., *Helv. Chim. Acta* **2002**, *85*, 2195.

49. Frank, S. N.; Bard, A. J., *J. Am. Chem. Soc.* **1975**, *97*, 7427.

50. Amouyal, E.; Homsi, A.; Chambron, J. C.; Sauvage, J. P., *J. Chem. Soc., Dalton Trans.* **1990**, 1841.

51. El-Hendawy, A. M.; Alqaradawi, S. Y.; Al-Madfa, H. A., *Transition Met. Chem.* **2000**, *25*, 572.

52. Hemmila, I., *Anal. Chem.* **1985**, *57*, 1676.

53. Jang, H.; Shin, C.-H.; Jung, B.-J.; Kim, D.-h.; Shim, H.-K.; Do, Y., *Eur. J. Inorg. Chem.* **2006**, 718.

54. Boone, S. R.; Pierpont, C. G., *Polyhedron* **1990**, *9*, 2267.

55. Chao, G. K. J.; Sime, R. L.; Sime, R. J., *Acta Crystallogr., Sect. B: Struct. Sci.* **1973**, *29*, 2845.

56. Kar, S.; Chanda, N.; Mobin, S. M.; Urbanos, F. A.; Niemeyer, M.; Puranik, V. G.; Jimenez-Aparicio, R.; Lahiri, G. K., *Inorg. Chem.* **2005**, *44*, 1571.

57. Mitra, K. N.; Choudhury, S.; Castineiras, A.; Goswami, S., *J. Chem. Soc., Dalton Trans.* **1998**, 2901.

58. Nayak, A.; Patra, S.; Sarkar, B.; Ghumaan, S.; Puranik, V. G.; Kaim, W.; Lahiri, G. K., *Polyhedron* **2005**, *24*, 333.

59. Reynolds, P. A.; Cable, J. W.; Sobolev, A. N.; Figgis, B. N., *J. Chem. Soc., Dalton Trans.* **1998**, 559.

Chapter 5

Selective Low-Temperature Syntheses of Facial and Meridional Tris-cyclometalated Iridium(III) Complexes

Abstract

We have developed a selective low-temperature synthesis of *fac* and *mer* tris-cyclometalated Ir(III) complexes. The chloro-bridged dimers $[Ir(C^N)_2Cl]_2$ (C^N = cyclometalating ligand) are cleaved in coordinating solvents like acetonitrile to give neutral $Ir(C^N)_2(NCCH_3)Cl$ species which in turn are reacted with $AgPF_6$ to give hexafluorophosphate salts of the bis-acetonitrile species $[Ir(C^N)_2(NCCH_3)_2]PF_6$ for C^N = 2,2'-thienylpyridine (thpy) and 2-phenylpyridine (ppy). These bis-acetonitrile complexes are excellent starting materials for the synthesis of tris- Ir(III) complexes. The complexes of the general formula *fac*-$Ir(C^N)_3$ were synthesized with the ligands thpy and ppy at 100 ºC in *o*-dichlorobenzene from the corresponding $[Ir(C^N)_2(NCCH_3)_2]PF_6$ complexes. The reaction of $[Ir(C^N)_2(NCCH_3)_2]PF_6$ with thpy at room temperature did not give the expected tris complex but instead gave, $[Ir(thpy)_2(N,S\text{-}thpy)]PF_6$, with the third chelating ligand complexed through the sulfur atom of the thiophene ring. $[Ir(thpy)_2Cl]_2$, $[Ir(ppy)_2Cl]_2$, $Ir(thpy)_2(NCCH_3)Cl$, $[Ir(thpy)_2(NCCH_3)_2]PF_6$, $[Ir(ppy)_2(NCCH_3)_2]PF_6$, and $[Ir(thpy)_2(N,S\text{-}thpy)]PF_6$ were structurally characterized by X-ray crystallography. Additionally, hydroxy-bridged dimers, $[Ir(C^N)_2(OH)]_2$, were synthesized as starting materials for the selective synthesis of *mer*-$Ir(C^N)_3$ complexes at 100 ºC in *o*-dichlorobenzene. A mechanism is proposed that may account for the selectivity observed in the formation of the *mer*-$Ir(C^N)_3$ and *fac*-$Ir(C^N)_3$ isomers in previous studies and the studies presented here.

Introduction

The cyclometalated complexes of metal ions have received a great deal of attention in recent years due in part to their rich photophysical properties. Although d^8 metal ions such as Pt(II),[1-7] Pd(II),[8-11] and Au(III)[12-17] have been examined, the emphasis has been on d^6 tris-cyclometalated complexes. Ir(III) tris-cyclometalated ligand complexes in particular have received increased attention as they are isoelectronic analogues of the highly emissive diimine coordination compounds of Ru(II) and Os(II). Tris-Ir(III) complexes of cyclometalating ligands exhibit long lifetimes and high emission quantum yields, desirable luminescence properties. These photophysical properties have led to the investigation of these molecules for applications such as photocatalysts,[18] singlet oxygen sensitizers,[19] oxygen sensors,[20] and possibly the most widely studied application, organic light emitting diodes (OLEDs).[21-30] These Ir(III) molecules can be incorporated into the layered structure of OLEDs as phosphorescent dopants. The increased spin–orbit coupling provided by Ir(III) promotes mixing of the singlet and triplet excited states and increases the theoretical limit of efficiency beyond the 25% predicted for organic molecules that emit by fluorescence.

Homoleptic cyclometalated complexes of d^6 metal centers like Ir(III) can adopt two configurations, facial (*fac*) or meridional (*mer*). The *fac* and *mer* isomers of cyclometalated Ir(III) complexes have markedly different photophysical properties.[31] Typically, the *fac* isomers have order of magnitude longer lifetimes and quantum efficiencies than the *mer* isomers at room temperature, making them much better for OLEDs and other applications. With this in mind a general, uncomplicated, and selective synthetic route to the *fac* isomers has been an area of interest in the past few years.

Several groups have investigated the synthesis of *fac* isomers of tris-cyclometalated Ir(III) complexes, but in most cases harsh reaction conditions were utilized.[22, 31-37] At the onset of our research, all reported routes to *fac* isomers used the high temperatures (200+ ºC) afforded by refluxing glycerol, or melt reactions employing excess ligand as the solvent.[31-37] The *mer* isomers of these cyclometalated complexes have been reported as kinetic products in glycerol at lower temperatures (120–150 ºC) that inhibit the formation of *fac* isomers.[22, 31] A selective low-temperature route that eliminates the use of glycerol or ligands as solvents and avoids the formation of *mer* isomers could result in the more straightforward isolation of the desired *fac* products. Recently a procedure that utilized silver triflate as a reagent in 2-ethoxyethanol at 95 ºC was reported to give low yields of the *fac* isomer of a heteroleptic complex.[20] Relatively high yields of *mer* isomers have also been reported by treatment of the dimer with a silver salt and triethylamine as a base.[20, 38] Herein we report low-temperature routes for the preparation of *fac*-Ir(thpy)$_3$ and *fac*-Ir(ppy)$_3$ at 100 ºC with improved yields and no evidence of formation of the *mer* isomers of these complexes. Additionally, we report the selective preparation of *mer*-Ir(thpy)$_3$ and *mer*-Ir(ppy)$_3$ at 100 ºC. The mechanistic implications of these synthetic reactions are also discussed.

Experimental

General Considerations. All synthetic procedures involving $IrCl_3 \cdot 3H_2O$ and other Ir(III) species were performed under an inert N_2 atmosphere. NMR spectra were recorded on Varian Unity (300 MHz) or Varian Inova (300 MHz) instruments. High-resolution mass spectrometry was carried out on a Bruker BioTOF II or Bruker microTOF$_Q$ mass spectrometer.

The ligand 2-phenylpyridine (ppy) was purchased from Aldrich Chemical Co., and 2, 2'-thienylpyridine (thpy) was synthesized according to a published procedure utilizing a Grignard coupling.[39] Cyclometalated Ir(III) μ-chloro-bridged dimers, $(C^N)_2Ir(\mu\text{-}Cl)_2Ir(C^N)_2$, (abbreviated as $[Ir(C^N)_2Cl]_2$) were synthesized via a slight modification of the method reported by Nonoyama;[40] $IrCl_3 \cdot 3H_2O$ (Pressure Chemical Co.) was refluxed with 2–2.5 equiv of cyclometalating ligand in a 3:1 mixture of 2-methoxyethanol and water, where 2-methoxyethanol (Aldrich) was used in place of 2-ethoxyethanol. Single crystals of both $[Ir(thpy)_2Cl]_2$ (**1a**) and $[Ir(ppy)_2Cl]_2$ (**1b**) were grown from slow evaporation of dichloromethane solutions. *Mer*-$Ir(ppy)_3$ was prepared by a slight modification of a method previously reported.[20] Compound **1b** was refluxed in acetone with silver triflate (Aldrich); upon filtration, ppy and triethylamine (Aldrich) were added and the solution was again refluxed.

$Ir(thpy)_2(NCCH_3)Cl$ (2a). Compound **1a** was dissolved in acetonitrile; slow evaporation in air gave orange X-ray quality crystals. Examination by ^1H NMR of **1a** in CD_3CN gave evidence for formation of a new asymmetric complex that still contains *trans* nitrogen atoms consistent with the cleavage of the dimer in solution to give **2a**. Subsequent X-ray

crystallography confirmed the structure of **2a** as a bis(2,2'-thienylpyridine) Ir(III) complex with one chloride and one acetonitrile ligand.

$[Ir(thpy)_2(NCCH_3)_2]PF_6$ (3a). Compound **1a** (0.3010 g, 0.2746 mmol) in 150 mL of acetonitrile was heated to dissolve all of the chloro-bridged dimer. A 50 mL acetonitrile solution of $AgPF_6$ (0.1505 g, 0.5953 mmol) was added to the Ir solution. Heating this mixture in the dark to 60–70 ºC for 2 h resulted in a gray precipitate. The reaction mixture was filtered over a Celite pad to separate a yellow solution from the gray AgCl precipitate. The solution was concentrated in vacuo, and diethyl ether was added to give a yellow precipitate that was collected by filtration. A second crop was obtained in a similar manner by removing the solvents from the filtrate then redissolving in a minimal amount of acetonitrile and precipitating with diethyl ether. The solids were dried under vacuum to give 0.3616 g (89% yield) of product. X-ray quality crystals were grown by slow evaporation of a CH_2Cl_2 solution. ^{1}H NMR (CD_2Cl_2): δ 8.85 (dd, 2 H, J = 0.6–0.9, 5.3 Hz), 7.85 (ddd, 2 H, J = 1.2–1.5, 7.7, 7.7 Hz), 7.58 (d, 2 H, J = 7.8 Hz), 7.25 (d, 2 H, J = 4.8 Hz), 7.23 (ddd, 2 H, J = 1.5, 6.0, 7.5 Hz), 6.05 (d, 2 H, J = 4.8), 2.37 (s, 6 H). HRESIMS (M^+): calcd for $C_{22}H_{18}IrN_4S_2$, 593.0573; found, 593.0580.

$[Ir(thpy)_2(OH)]_2$ (4a). Compound **3a** (0.0502 g, 0.0679 mmol) was dissolved in 15 mL of methanol. The addition of solid NaOH (0.0070 g, 0.1750 mmol) resulted in an immediate color change from light orange to dark red-orange and precipitation of a solid. The reaction was allowed to stir for 18 h. The solid was collected by filtration and rinsed with MeOH to remove any residual starting material (2 × 10 mL). The red-orange solid was dried under vacuum to yield 0.0329 g (92% yield) of product. ^{1}H NMR (CD_2Cl_2): δ 8.26 (dd, 4 H, J = 0.6–0.9, 5.7 Hz), 7.52 (m, 8 H), 7.09 (d, 4 H, J = 4.8 Hz), 6.51 (ddd, 4

H, J = 1.2, 6.2, 6.2 Hz), 5.89 (d, 4 H, 4.5 Hz). HRESIMS ($M^+ - OH^-$): calcd for $C_{36}H_{25}Ir_2N_4OS_4$, 1039.0118; found, 1039.0143.

[Ir(thpy)$_2$(N,S-thpy)]PF$_6$ (5a). Compound **3a** (0.0500 g, 0.0676 mmol) was dissolved in 10 mL acetone and purged with N_2 for 20 min. Thpy (0.0129 g, 0.0800 mmol) was added, and the reaction was stirred for 72 h. The acetone was removed by rotary evaporation to give an oily yellow-brown solid. This solid was redissolved in a small amount of acetone and precipitated with diethyl ether to give a yellow-brown solid that was collected by filtration. This procedure was repeated to give two more crops. The solids were dried under vacuum to give a total of 0.0357 g (65% yield) of product. X-ray quality crystals were grown by slow evaporation of an acetone solution. ^{1}H NMR (CD_2Cl_2): δ 8.09 (m, 2 H), 7.95 (ddd, 1 H, J = 0.6–0.9, 1.5, 6.0 Hz), 7.79 (ddd, 1 H, J = 1.5, 7.3–7.5, 8.1 Hz), 7.74 (ddd, 1 H, J = 1.5, 7.2, 8.1 Hz), 7.67 (ddd, 1 H, J = 0.9–1.2, 1.1, 5.7 Hz), 7.62 (ddd, 1 H, J = 0.6–1.1, 1.35–1.5, 8.3 Hz), 7.58 (dd, 1 H, J = 0.9, 3.6), 7.55 (ddd, 1 H, J = 0.6–0.9, 1.5, 8.3 Hz), 7.43 (d, 1 H, J = 4.8 Hz), 7.39 (dd, 1 H, J = 3.3–3.6, 5.1), 7.38 (d, 1 H, J = 5.1 Hz), 7.34 (ddd, 1 H, J = 0.6–0.9, 1.4, 6.0 Hz), 7.31 (ddd, 1 H, J = 2.7, 5.7–6, 6.3 Hz), 7.28 (dd, 1 H, J = 0.9, 5.1 Hz), 7.01 (ddd, 1 H, J = 1.5–1.8, 5.7–5.9, 7.5 Hz), 6.92 (ddd, 1 H, J = 1.2–1.5, 5.9–6.0, 7.4 Hz), 6.21 (d, 1 H, J = 4.8 Hz), 6.11 (d, 1 H, J = 4.8 Hz). HRESIMS (M^+): calcd for $C_{27}H_{19}IrN_3S_3$, 672.0342; found, 672.0314.

***fac*-Ir(thpy)$_3$ (6a).** Compound **3a** (0.0501 g, 0.0677 mmol) and thpy (0.0122 g, 0.0757 mmol) were combined in 5 mL of *o*-dichlorobenzene and heated at ~100 ºC under N_2 for 116 h. The reaction solution was chromatographed on a silica gel column packed with hexanes to first elute *o*-dichlorobenzene with hexanes. Switching to 1:1

dichloromethane/hexanes eluted the product, **6a**, as a bright orange band in 55–65% yield. The ^{1}H NMR spectrum was consistent with previously reported values.[32]

$[Ir(ppy)_2(NCCH_3)_2]PF_6$ (3b). Compound **1b** (0.2006 g, 0.1871 mmol) in 75 mL of acetonitrile was heated to dissolve all of the chloro-bridged dimer. A 50 mL acetonitrile solution of $AgPF_6$ (0.1034 g, 0.4089 mmol) was added to the Ir solution. This mixture was stirred in the dark for 2 h resulting in a gray precipitate. The reaction mixture was filtered over a Celite pad to separate a yellow solution from the gray AgCl precipitate. The solution was concentrated in vacuo and benzene was added. The solution was cooled to freezing in the refrigerator. Upon melting, solid was present and was collected by vacuum filtration. A second crop was obtained in a similar manner by removing the solvents from the filtrate then redissolving in a minimal amount of acetonitrile and precipitating with diethyl ether. The solids were dried under vacuum to give 0.2341 g (86% yield) of the bright yellow solid. X-ray quality crystals were grown from an acetonitrile solution. ^{1}H NMR (CD_2Cl_2): δ 9.00 (ddd, 2 H, J = 1.2, 1.2, 5.9 Hz), 7.97 (m, 4 H), 7.59 (dd, J = 0.9, 7.8 Hz), 7.42 (ddd, 2 H, J = 3.2, 5.8, 5.8 Hz), 6.93 (ddd, 2 H, J = 1.2, 7.5, 7.5 Hz), 6.76 (ddd, 2 H, J = 1.2, 7.5, 7.5 Hz), 6.09 (dd, 2 H, 0.75, 7.7 Hz), 2.32 (s, 6 H). HRESIMS (M^+): calcd for $C_{26}H_{22}IrN_4$, 581.1445; found, 581.1458.

$[Ir(ppy)_2(OH)]_2$ (4b). Compound **3b** was produced in situ by dissolving **1b** (0.0521 g, 0.0486 mmol) in 25 mL of acetonitrile and treating with $AgPF_6$ (0.0350 g, 0.l384 mmol). After being stirred for 1.5 h, the solution was filtered over Celite to remove AgCl and the solvent was removed by rotary evaporation. The remaining solid was dissolved in 20 mL of MeOH, and upon addition of solid NaOH (0.0315 g, 0.7875 mmol) the color changed from yellow to brown and a solid precipitated. After the reaction mixture was stirred an

additional 24 h, the solid was collected by filtration and rinsed with methanol. The orange-brown solid was dried under vacuum to yield 0.0347 g (69% yield). The ^{1}H NMR spectrum in acetone-d_6 was consistent with previously reported values.[41] The spectrum was also taken in dichloromethane-d_2. ^{1}H NMR (CD_2Cl_2): δ 8.48 (dd, 4 H, J = 0.9, 6.0 Hz), 7.87 (dd, 4 H, J = 0.6, 8.4 Hz), 7.64 (ddd, 4 H, J = 1.5, 7.5, 8.1 Hz), 7.55 (dd, 4 H, J = 1.2, 7.8 Hz), 6.75 (ddd, 4 H, J = 0.9–1.2, 7.5, 7.5 Hz), 6.68 (ddd, 4 H, J = 1.2–1.5, 5.9, 7.3 Hz), 6.54 (ddd, 4 H, J = 1.2–1.5, 7.4, 7.4 Hz), 5.87 (dd, 4 H, J = 1.2, 7.5 Hz).

***fac*-Ir(ppy)$_3$ (6b).** Compound **3b** (0.0503 g, 0.0691 mmol) and ppy (0.0110 mL, 0.0770 mmol) were combined in 5 mL of *o*-dichlorobenzene and heated to ~100 ºC under a nitrogen atmosphere for 120 h. The reaction solution was chromatographed on a silica gel column packed with hexanes to first elute *o*-dichlorobenzene with hexanes. Switching to dichloromethane eluted the product, **6b**, as a bright yellow band in 55–65% yield. The ^{1}H NMR spectrum was consistent with previously reported values.[31]

NMR tube reaction of 1a with 4,4'-di-*tert*-butyl-2,2'-bipyridine (bpy*). Compound **1a** (0.0032 g, 0.0029 mmol) and bpy* (0.0015 g, 0.0056 mmol) were combined in an NMR tube in dichloromethane-d_2. After 4 days a mixture of **1a**, bpy*, and predominantly the product $[Ir(thpy)_2(bpy^*)]^+$ were present; examination after 20 days showed complete conversion of the starting materials to $[Ir(thpy)_2(bpy^*)]^+$.

NMR tube reaction of 3a with bpy*. Compound **3a** (0.0051 g, 0.0069 mmol) and bpy* (0.0023 g, 0.0086 mmol) were combined in an NMR tube in acetone-d_6. After 1 h the reaction had gone to completion at room temperature to form $[Ir(thpy)_2(bpy^*)]^+$.

NMR tube reactions of 5a with deuterated solvents. The lability of the N,S-bound ligand was investigated by dissolving compound **5a** in several deuterated solvents. When

5a is dissolved in acetonitrile-d_3, methanol-d_4, or dimethylsulfoxide-d_6, peaks for the free ligand (thpy) and new bis-solvento complexes are present. When dissolved in tetrahydrofuran-d_4, dichloromethane-d_2, tetrachloroethane-d_2, or *o*-dichlorobenzene-d_4 **5a** does not immediately undergo substitution of the N,S-bound ligand.

NMR tube reaction of 4a with thpy in *o*-dichlorobenzene-d_4. Compound **4a** (0.0053 g, 0.0050 mmol) and thpy (0.0017 g, 0.0105 mmol) were combined in an NMR tube with *o*-dichlorobenzene-$d_4$and monitored at room temperature. After 2 days 60% conversion to *mer*-Ir(thpy)$_3$ was observed. After 7 days the conversion to the *mer* isomer was ~70%. After 42 days at room temperature the peaks for *mer*-Ir(thpy)$_3$ were still the only product peaks and the conversion was ~90%. The reaction was driven to completion by heating at 90 ºC. Continued heating of the *mer* product for an additional 12 days resulted in a trace amount (<1%) amount of *fac* isomer.

NMR tube reaction of 5a in *o*-dichlorobenzene-d_4. Compound **5a** was combined with *o*-dichlorobenzene-d_4 in an NMR tube, heated at 90–100 ºC, and monitored by NMR over 6 days. **6a** was formed quickly; a significant amount was present after only 6 h. After 141 h the reaction was essentially complete with the ratio of **6a**/**5a** being 2:1.

NMR tube reaction of 5a in tetrachloroethane-d_2. Compound **5a** was combined with tetrachloroethane-d_2 in an NMR tube, monitored at room temperature for 13 days, and then heated at 60 ºC and later 80 ºC. At room temperature the reaction forms **1a** and upon heating to 60 ºC the production of **1a** is increased and no new products are formed. Increasing the temperature to 80 ºC results in the formation of **6a** after 30 h. The precipitation of **6a** prevented the final quantitative analysis of the reaction by NMR.

Reaction of 3a with thpy. Compound **3a** (0.0250 g, 0.0338 mmol) and thpy (0.00640 g, 0.0397 mmol) were combined with dichloromethane (5 mL) and toluene (35 mL) and heated to reflux under a nitrogen atmosphere for 192 h. **6a** was formed in 36% yield.

NMR tube reaction of 3b with ppy. Compound **3b** (0.005 g, 0.00687 mmol) and ppy (0.001 mL, 0.00700 mmol) were combined in an NMR tube with *o*-dichlorobenzene-d_4 and heated at 80 ºC. **6b** was formed after 1 h with the consumption of **3b** being complete after 66 h. There was no evidence of the *mer* isomer in the reaction.

NMR tube reaction of 3b with ppy in the absence of light. Compound **3b** (0.0060 g, 0.0082 mmol) and ppy (0.0013 mL, 0.0090 mmol) were combined in an NMR tube with *o*-dichlorobenzene-d_4 and heated at 115 ºC. **6b** was formed after 1 h with the consumption of **3b** being complete after 66 h. There was no evidence of the *mer* isomer.

NMR tube reaction of 4b with ppy. Compound **4b** (0.0010 g, 0.0010 mmol) and ppy were combined in an NMR tube with *o*-dichlorobenzene-d_4. After 42 h at room temperature no reaction was observed, due in part to the limited solubility of **4b**. The NMR tube was then heated at 105 ºC, allowing **4b** to dissolve. After 22 h of heat 70% conversion to *mer*-Ir(ppy)$_3$ was observed, and the reaction was complete after 216 h with no evidence of the *fac* isomer **6b**. Additional heating of the *mer* product for 120 h at 105 ºC showed no conversion to the *fac* isomer.

Attempted NMR tube isomerization of *mer*-Ir(ppy)$_3$ to *fac*-Ir(ppy)$_3$. *Mer*-Ir(ppy)$_3$ was combined with *o*-dichlorobenzene-d_4 and monitored at room temperature; after 4 days, no reaction was observed. The tube was then heated at 100 ºC for 10 days; again, no formation of **6b** was detected.

Attempted NMR tube isomerization of *mer*-Ir(ppy)$_3$ to *fac*-Ir(ppy)$_3$ in the absence of light. *Mer*-Ir(ppy)$_3$ was combined with *o*-dichlorobenzene-d_4 and heated at 100–115 ºC for 20 hrs; no reaction was observed. One drop of acetonitrile was added from a Pasteur pipet and the tube was heated at 100 ºC for 10 days; again **6b** was not detected.

Single Crystal X-ray Crystallography. Single crystals were attached to glass capillary fibers. **1a**, **3a**, and **5a** were mounted on a Bruker SMART Platform CCD diffractometer, while **1b**, **2a**, and **3b** were mounted on a Siemens SMART Platform CCD diffractometer for data collection at 173(2) K using a graphite monochromator and Mo Kα radiation (λ = 0.71073 Å). An initial set of cell constants was calculated from reflections harvested from three sets of 20 frames such that orthogonal wedges of reciprocal space were surveyed. Final cell constants were determined from a minimum of 944 strong reflections from the actual data collection. Data were collected to the extent of 1.5 hemispheres to a resolution of 0.84 Å with the exception of **1a**, which was surveyed to a resolution of 0.77 Å. Three major sections of frames were collected with 0.30° steps in ω. The intensity data were corrected for absorption and decay using SADABS.[42, 43] Space groups were determined based on systematic absences and intensity statistics. Direct-methods solutions provided the positions of most of the non-hydrogen atoms. Full-matrix least-squares/difference Fourier cycles were performed to locate the remaining non-hydrogen atoms. All non-hydrogen atoms were refined with anisotropic displacement parameters and all hydrogen atoms were placed in idealized positions and refined as riding atoms with relative isotropic displacement parameters. All calculations were performed with the SHELXTL suite of programs.[44] Details of the refinement as well as selected bond lengths are given in Tables 1, 2, and 3.

Table 1. Crystallographic data and refinement parameters for $[Ir(thpy)_2Cl]_2$ (**1a**), $Ir(thpy)_2(NCCH_3)Cl$ (**2a**), and $[Ir(thpy)_2(NCCH_3)_2]PF_6$ (**3a**).

Compound	1a	2a	3a
empirical formula	$C_{37}H_{26}Cl_4Ir_2N_4S_4$	$C_{20}H_{15}ClIrN_3S_2$	$C_{23}H_{20}Cl_2F_6IrN_4PS_2$
color, morphology	brown/red, block	orange, block	yellow, block
crystal system	Monoclinic	Monoclinic	Triclinic
space group	$C2/c$	$P2_1/n$	$P\bar{1}$
a, Å	15.165(2)	10.4378(19)	8.4639(13)
b, Å	21.011(3)	15.831(3)	13.114(2)
c, Å	11.8879(18)	12.053(2)	13.816(2)
α, deg	90	90	98.724(2)
β, deg	102.626(2)°	102.938(3)	105.480(2)
γ, deg	90	90	102.992(2)
volume, $Å^3$	3696.4(10)	1941.1(6)	1403.1(4)
Z	4	4	2
formula wt, g mol^{-1}	1181.06	589.12	824.62
D_c, g cm^{-3}	2.122	2.016	1.952
temperature, K	173(2)	173(2)	173(2)
μ, mm^{-1}	7.744	7.241	5.216
$F(000)$	2248	1128	796
θ range, deg	1.68 to 25.07	2.16 to 25.04	1.57 to 25.08
index ranges	$-18 \le h \le 18$ $-24 \le k \le 24$ $-14 \le l \le 14$	$-12 \le h \le 12$ $-18 \le k \le 18$ $-14 \le l \le 14$	$-10 \le h \le 10$ $-15 \le k \le 15$ $-16 \le l \le 16$
reflns collected	17995	14146	12046
independent reflns	3288	3438	4952
R_{int}	0.0385	0.0385	0.0417
weighting factors,[a] a,b	0.0242, 22.4128	0.0159, 2.2129	0.0542, 4.7535
max, min transmission	1.000, 0.783	0.630, 0.413	0.354, 0.227
Data/restraints/ parameters	3288/3/239	3438/0/245	4952/0/352
R_1, wR_2 [$I > 2\sigma(I)$]	0.0212, 0.0539	0.0206, 0.0417	0.0374, 0.0975
R_1, wR_2 (all data)	0.0242, 0.0555	0.0257, 0.0430	0.0418, 0.1014
GOF	1.038	1.075	1.056
largest diff. peak, hole, $eÅ^{-3}$	1.317, -1.054	0.660, -0.528	2.402, -1.451

[a] $w = [\sigma^2(F_o^2) + (aP)^2 + (bP)]^{-1}$, *where* $P = (F_o^2 + 2F_c^2)/3$.

Table 2. Crystallographic data and refinement parameters for $[Ir(thpy)_2(N,S\text{-}thpy)]PF_6$ (**5a**), $[Ir(ppy)_2Cl]_2$ (**1b**), and $[Ir(ppy)_2(NCCH_3)_2]PF_6$ (**3b**).

Compound	5a	1b	3b
empirical formula	$C_{27}H_{19}F_6IrN_3PS_3$	$C_{44}H_{32}Cl_2Ir_2N_4$	$C_{26}H_{22}F_6IrN_4P$
color, morphology	orange, block	yellow, plate	yellow, rod
crystal system	hexagonal	monoclinic	triclinic
space group	$R\bar{3}C$	$P2_1/n$	$P\bar{1}$
a, Å	20.8082(18)	9.2872(6)	8.8704(12)
b, Å	20.8082	11.9810(8)	18.131(3)
c, Å	71.402(7)	16.7420(11)	25.655(4)
α, deg	90	90	93.993(2)
β, deg	90	99.6740(10)	96.938(2)
γ, deg	120	90	93.926(2)
volume, $Å^3$	26774(3)	1836.4(2)	4073.6(10)
Z	36	2	6
formula wt, g mol^{-1}	818.80	1072.04	727.65
D_c, g cm^{-3}	1.828	1.939	1.780
temperature, K	173(2)	173(2)	173(2)
μ, mm^{-1}	4.813	7.423	5.039
F(000)	14256	1024	2112
θ range, deg	1.27 to 25.05	2.10 to 25.04	0.80 to 25.08
index ranges	$-24 \le h \le 13$	$-8 \le h \le 11$	$-10 \le h \le 10$
	$-8 \le k \le 24$	$-14 \le k \le 11$	$-21 \le k \le 21$
	$-84 \le l \le 84$	$-19 \le l \le 19$	$-30 \le l \le 30$
reflns collected	27208	10061	40103
independent reflns	5286	3242	14435
R_{int}	0.0771	0.0263	0.0639
weighting factors,[a] *a,b*	0.0519, 107.4903	0.0180, 4.5009	0.0391, 2.5426
max, min transmission	0.790, 0.461	0.500, 0.392	0.830, 0.678
Data/restraints/parameters	5286/95/481	3242/364/386	14435/516/1052
R_1, wR_2 [$I > 2\sigma(I)$]	0.0486, 0.1102	0.0259, 0.0526	0.0503, 0.0922
R_1, wR_2 (all data)	0.0791, 0.1199	0.0325, 0.0548	0.0849, 0.1005
GOF	1.060	1.060	1.027
largest diff. peak, hole, e$Å^{-3}$	1.289, 1.091	0.948, -0.823	1.120, -1.182

[a] $w = [\sigma^2(F_o^2) + (aP)^2 + (bP)]^{-1}$, *where* $P = (F_o^2 + 2F_c^2)/3$.

Table 3. Selected bond lengths (Å) for the reported structures.

	1a	**2a**	**3a**	**5a**	**1b**	**3b**	**$[Ir(tpy)_2Cl]_2$[a]**
Ir-N1	2.043(4)	2.054(3)	2.069(5)	2.072(6)	2.053(12)*	2.052(7)*	2.09(1)
Ir-N2	2.058(4)	2.063(3)	2.071(6)	2.070(7)	2.052(12)*		2.09(1)
Ir-C7	1.976(4)	1.999(4)	2.000(6)	2.030(9)	1.890(12)*	2.004(8)*	2.02(2)
Ir-C16 (C18)[b]	1.984(4)	2.003(4)	2.013(6)	1.991(9)	2.111(12)*		2.03(2)
Ir-Cl1	2.547(9)	2.4730(10)[c]			2.5116(12)*		2.57(1)
Ir-Cl2	2.466(9)						2.50(1)
Ir-N3		2.117(3)	2.102(5)	2.144(22)*[d]		2.131(7)*	
Ir-N4			2.125(5)				
Ir-S3				2.551(7)*			

* Values averaged due to disorder or multiple molecules in asymmetric unit. [a] T=296 K, see ref. 45. [b] C18 analogous carbon in ppy. [c] chloride. [d] pyridine.

Results and Discussion.

Synthesis of *fac*-Ir(C^N)$_3$ and Intermediate Complexes .

Iridium(III) chloride has been shown to react with a variety of cyclometalating ligands to give chloride bridged dimers in refluxing 2-ethoxyethanol.[40] In our hands, replacement of 2-ethoxyethanol with 2-methoxyethanol appears to have no deleterious effect on the formation of **1a** and **1b**; both are formed in 60–80% yields (Scheme 1).

The chloro-bridged dimers **1a** and **1b** are solvated in strongly coordinating solvents such as acetonitrile, dimethylformamide, and dimethylsulfoxide to give mononuclear complexes such as **2a** and **2b** (Scheme 2).[41] This dimeric cleavage and the tendency for solvent molecules such as acetonitrile to occupy open coordination sites were used to synthesize the bis-acetonitrile complexes **3a** and **3b** by reaction with Ag^+ to remove Cl^-. The acetonitrile ligands of complexes **3a** and **3b** are labile; these complexes readily undergo substitution reactions at room temperature to give complexes such as **4a**, **4b**, and **5a** as shown in Scheme 2. Additionally, these bis-acetonitrile complexes undergo cyclometalation reactions at relatively low temperature to make the highly desired *fac* isomers of Ir(thpy)$_3$ and Ir(ppy)$_3$. Complexes **4a** and **4b** also undergo cyclometalation reactions at low temperature but instead give the *mer* isomers of Ir(thpy)$_3$ and Ir(ppy)$_3$. The presence of the basic hydroxide site of **4a** and **4b** provides a convenient route to mer isomers without the addition of an external base. Synthesis of the intermediate bis-acetonitrile complexes **3a** and **3b** eliminates many variables including the harsh reaction conditions involved in previous synthetic reaction schemes to *fac* isomers.

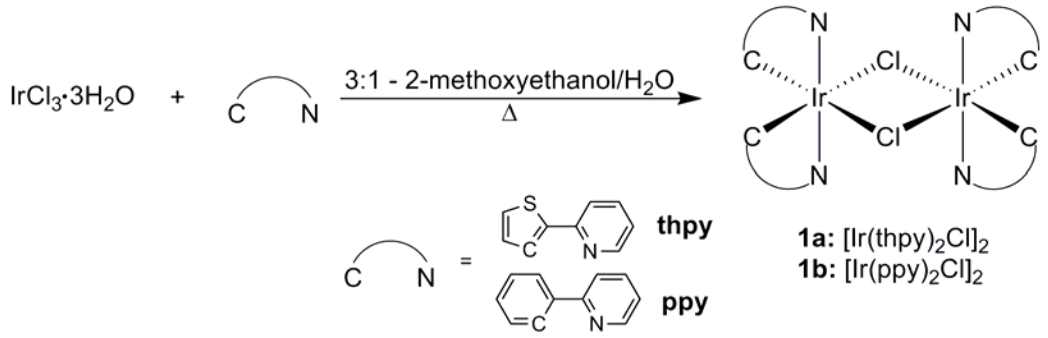

Scheme 1. Synthesis of chloro-bridged dimers.

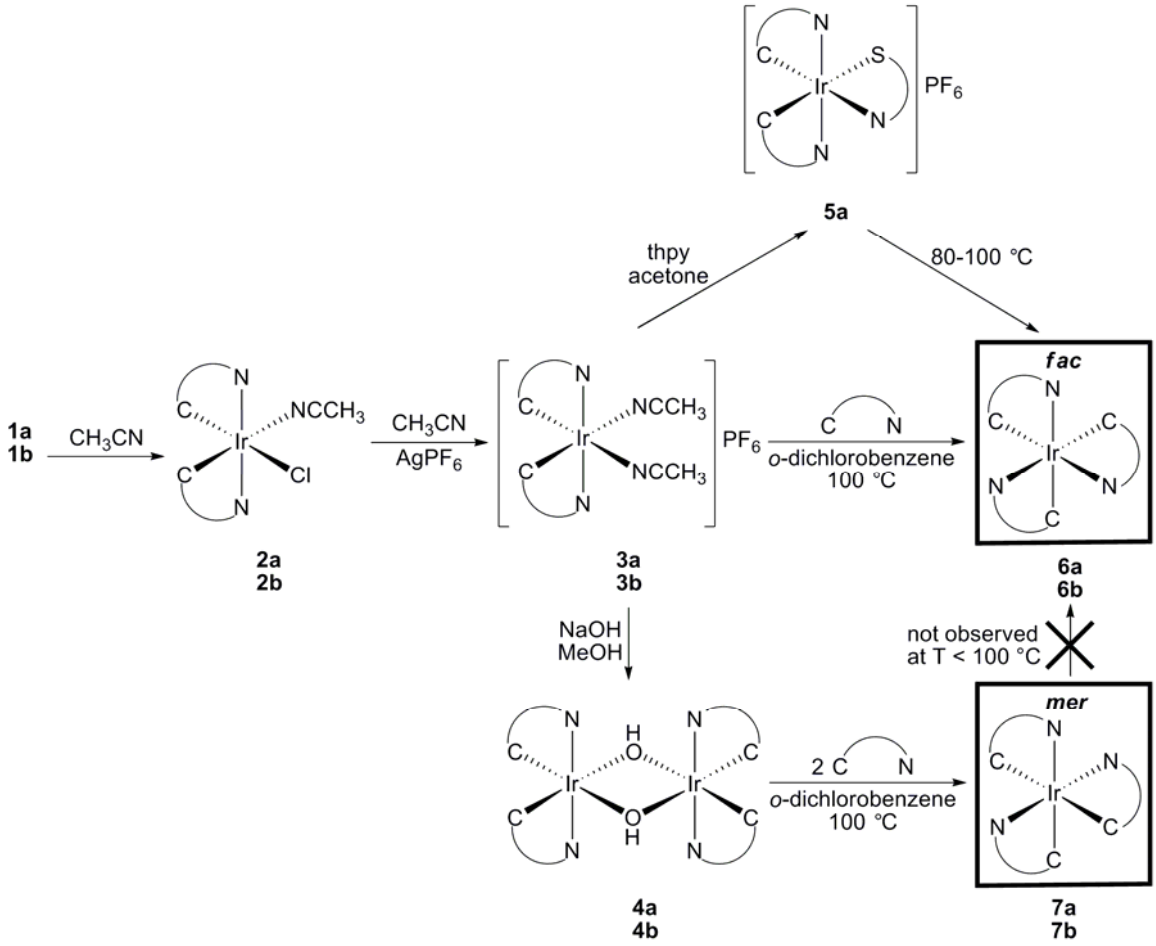

Scheme 2. Low temperature synthetic scheme to *fac*- and *mer*- cyclometalated Ir(III) complexes as well as other intermediate compounds.

NMR Characterization.

The ^{1}H NMR spectra in CD_2Cl_2 solutions of the thpy and ppy dimers, **1a** and **1b** (six and eight resonances, respectively), are consistent with those previously reported. These data are consistent with symmetrical complexes with C_2 symmetry in which both cyclometalated ligands are equivalent; the nitrogen atoms of the pyridyl rings are mutally *trans* as are those in the previously determined structure of $[Ir(tpy)_2Cl]_2$ (tpy = 2-(*p*-tolyl)pyridine).[45] In coordinating solvents such as acetonitrile, the dimeric structure is lost, as is evidenced by the more complicated nature of the ^{1}H NMR spectra of the complexes in these solvents.[41]

Removal of the remaining Cl^- with Ag^+ in acetonitrile gave the cationic bis-acetonitrile complexes (**3a** and **3b**) that were characterized via ^{1}H NMR as well with six and eight peaks in the aromatic region, respectively. The mild reaction conditions preserve the original orientation of the cyclometalating ligands with *trans* nitrogen atoms and *cis* acetonitrile ligands giving complexes of C_2 symmetry. The lowest field resonance in both **3a** (8.85 ppm) and **3b** (9.00 ppm) is assigned to the proton *ortho* to the nitrogen in the pyridyl ring. This proton is positioned over the C≡N of the acetonitrile ligands in a region of deshielded electron density compared to the other ligand protons.[46] Interestingly, the increased shielding effect from the circulation of the electrons of the triple bond in comparison to that of the bridging chlorine atoms in the dimers can be observed by the shift to lower ppm of these *ortho* protons in **3a** and **3b**.

In the case of the reaction of **3a** in acetone with thpy, a non-cyclometalated sulfur-bonded complex **5a** was isolated; **5a** yielded a very complicated ^{1}H NMR spectrum indicative of a molecule with C_1 or C_i symmetry. Integration of the peaks in the

aromatic region indicated a total of 19 protons, indicating that the new product was not *mer*-Ir(thpy)$_3$ which would exhibit 18 aromatic proton resonances. The presence of 19 resonances and the peak patterns observed, suggested that the complex instead consisted of two cyclometalated thpy ligands and one thpy ligand bound through the nitrogen and sulfur atom. Ligation through the sulfur of the thpy ligand gives a complex of C_1 symmetry with an extra proton displayed in the aromatic region as compared to that of *mer*-Ir(thpy)$_3$. Confirmation of **5a** as a cationic species was confirmed by the presence of a peak for a PF_6^- counterion in a ^{31}P NMR spectrum of the compound. Assignment of the ^1H NMR spectrum of **5a** was difficult due to the sheer number of resonances in the aromatic region, some of which were overlapping; however, careful examination of the coupling between peaks and a COSY NMR spectrum determined which protons were associated with a given ring system and allowed the complete simulation[47] and full assignment of the spectrum (Figures 1 - 3).

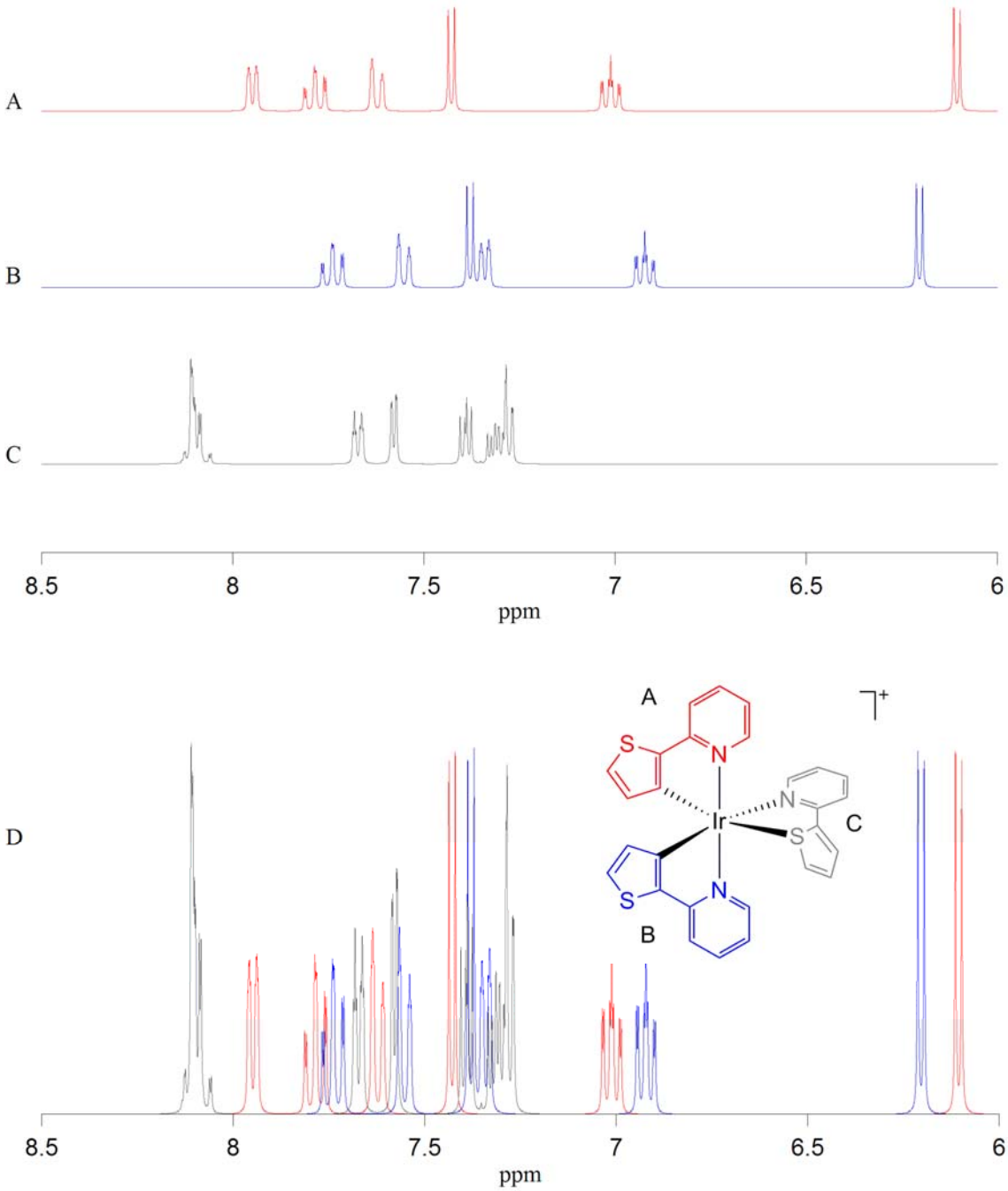

Figure 1. [1]H NMR spectra of **5a** simulated with the program Spinworks[47] showing the individually simulated ligands A, B, and C and the overlay spectrum D. Ligand A is assigned to the red resonances because the proton *ortho* to the nitrogen on the pyridine ring is shifted considerably downfield relative to the analogous proton in ligand B because of the decrease in ring current shielding by the tilted ring of the S-bonded thiophene of ligand C.

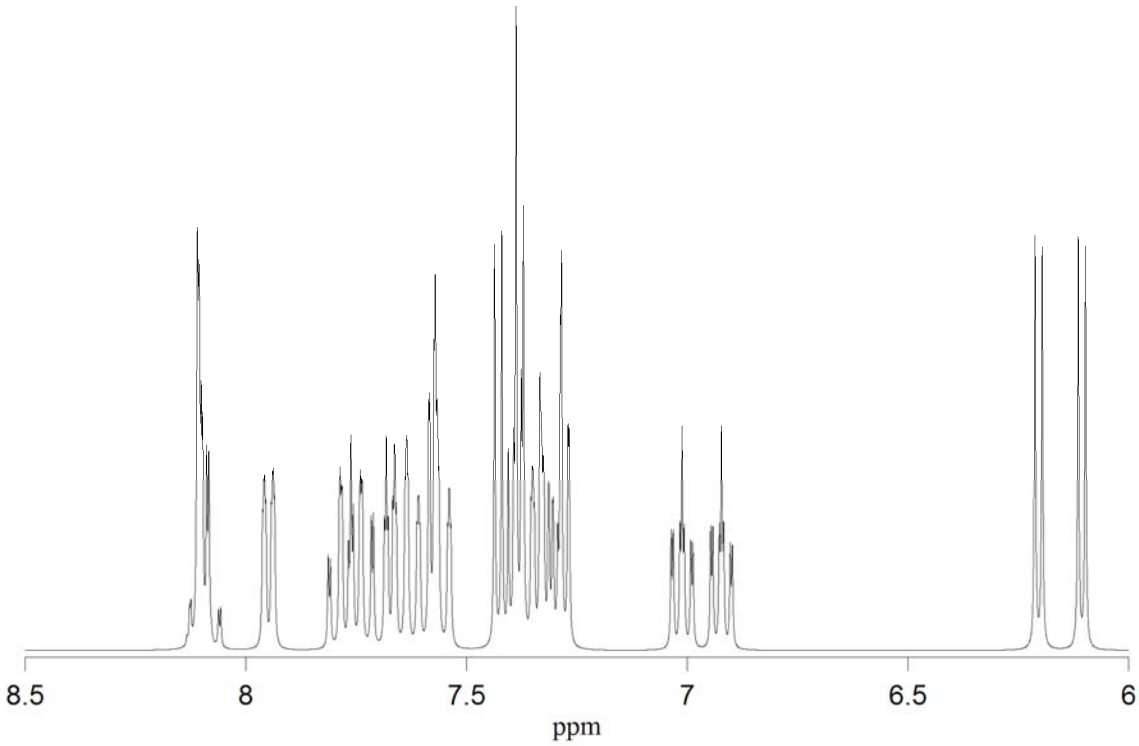

Figure 2. ^{1}H NMR simulated spectrum of **5a**, the additive result of rings A, B, and C.

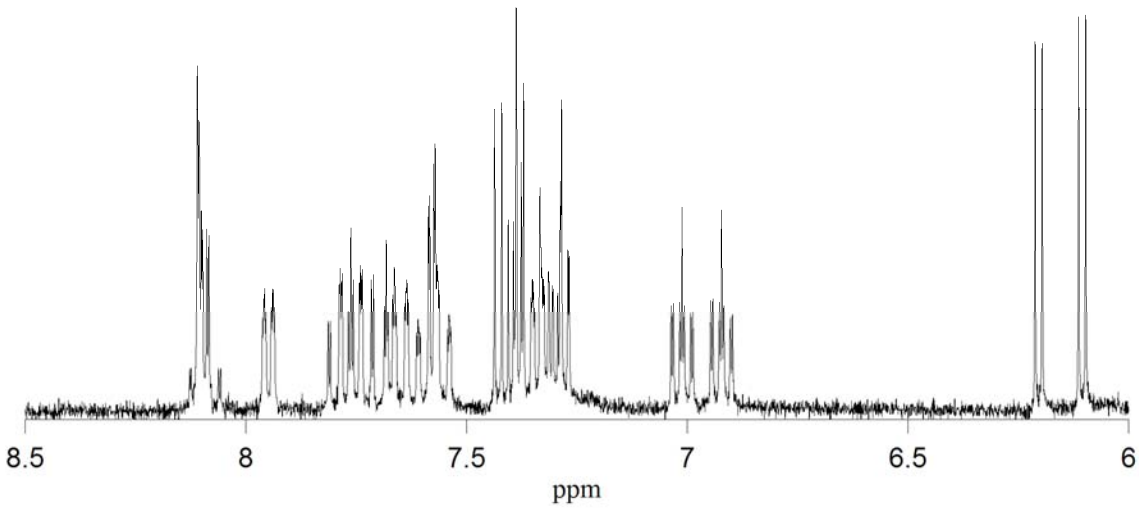

Figure 3. Experimental ^{1}H NMR spectrum of **5a**.

X-ray Crystallography.

Somewhat surprisingly in view of the interest in this area, the X-ray structures of the chloro-bridged starting materials used in this study have not been previously determined. However, $[Ir(tpy)_2Cl]_2$ and two other dimers containing substituted cyclometalating ligands have been characterized by X-ray crystallography. Single crystals of the chloro-bridged dimers, **1a** and **1b**, were grown from dichloromethane, and the resulting structural data are used here for comparison of bond lengths with the newly synthesized complexes. In both **1a** and **1b** the nitrogen atoms were confirmed to be mutually *trans* to each other in the *mer* chelate arrangement; the arrangement of the ligands is such that rearrangement at the metal center must occur for *fac*-$Ir(C^N)_3$ complexes to be formed upon reaction with a third cyclometalating ligand. **1a** crystallized as a dichloromethane solvate in the space group *C2/c* (Figure 4). **1a** crystallized on a 2-fold axis that lies between the chlorine atoms; thus, the asymmetric unit consists of half of the molecule. The co-crystallized dichloromethane molecule also lies on a 2-fold axis and is disordered in a 50:50 ratio over this symmetry element. **1b** crystallized in the space group $P2_1/n$ with the asymmetric unit lying on an inversion center. The ppy rings are also disordered to give both the Λ and Δ orientations in a 50:50 ratio in the asymmetric unit. The absolute structure of the molecule therefore cannot be determined. Dimeric units of ΛΔ and ΔΛ stereochemistry or ΛΛ and ΔΔ stereochemistry could occupy the same space with 50% occupancies; however, we believe that it is more likely an arrangement of ΛΛ and ΔΔ isomers because the structures of **1a** and $[Ir(tpy)_2Cl]_2$ contain discrete molecules of ΛΛ and ΔΔ symmetry which alternate throughout the cell. The Ir–C, Ir–N, and Ir–Cl bond lengths for these complexes are

given in Table 2 along with previously determined values for $[Ir(tpy)_2Cl]_2$.[45] As is the case in $[Ir(tpy)_2Cl]_2$, the Ir–C bonds lengths in **1a** (1.976(4) and 1.984(4) Å) are shorter than the Ir–N bonds (2.043(4) and 2.058(4) Å). The individual bond lengths observed in **1b** vary much more than those of **1a** or $[Ir(tpy)_2Cl]_2$, possibly due to the occupational disorder that is observed in this structure. Average values of the Ir–C (2.000(12) Å) and Ir–N (2.053(12) Å) bond lengths in this structure correlate well with those previously mentioned.

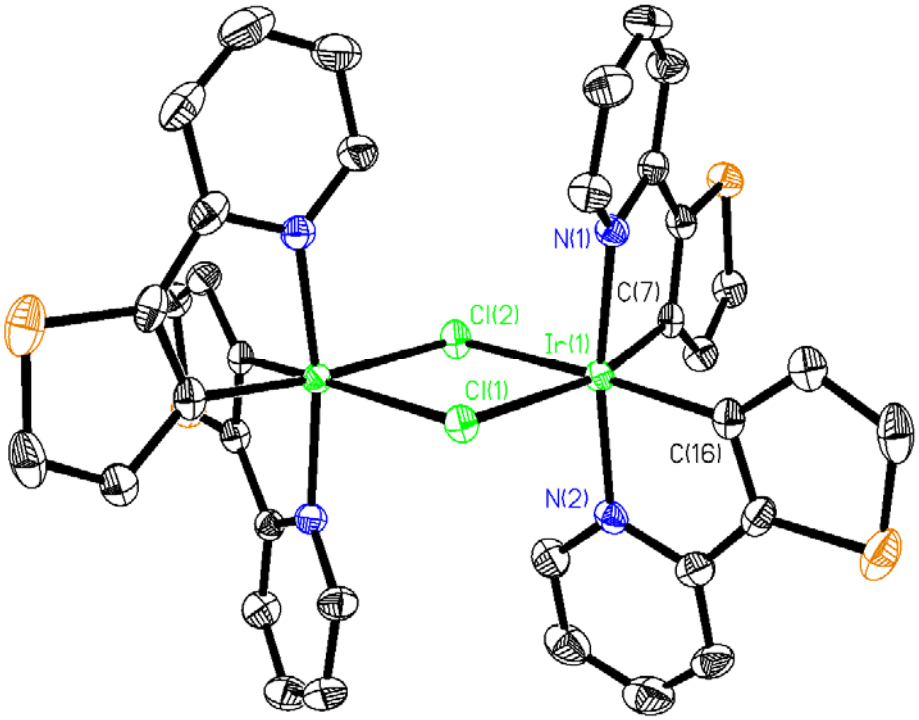

Figure 4. Thermal ellipsoid plot of **1a**. Dichloromethane solvent molecule is removed for clarity.

Thermal ellipsoid plots of the pseudo-octahedral geometry of **2a**, **3a**, and **3b** are shown in Figures 5, 6, and 7. The crystallographic data for these structures, along with those for **1a** and **1b**, are given in Table 2. Discussion of the disorder of these and the following structures, as well as atomic coordinates, bond lengths, and angles for each complex, are available in the supplementary information. The structure of **1** consists of Ir(III) coordinated to two thpy ligands which maintain the *mer* chelate arrangement adopted in the dichloro-bridged dimers with *cis* cyclometalating carbons and *trans* nitrogens. One chloride and one ligating acetonitrile molecule complete the octahedral coordination sphere to give a neutral molecule.

Again observed in the structure of **3a** is the *cis*-C,C and *trans*-N,N chelation geometry of the thpy ligands. Two bound acetonitrile molecules occupy the remaining coordination sites. The Ir–C distances observed for **3a** (2.000(6) and 2.013(6) Å) are slightly longer than those observed for **1a** (1.976(4) and 1.984(4) Å) perhaps due to the better σ-donating and π-accepting nature of the acetonitrile ligands in comparison to Cl^-. Additionally, the *trans* influence of the cyclometalating carbon atoms on the Ir–N acetonitrile bonds is observed by comparing these bond lengths (2.102(5) and 2.125(5) Å) to those in structures of $Ru(bpy)_2(NCCH_3)_2^{2+}$ salts where bpy = 2,2'-bipyridine (2.032 – 2.044 Å).[48, 49] The negatively charged thiophene moiety has a stronger *trans* influence than that of the lone-pair-donating pyridyl group, resulting in lengthening of the *trans* nitrile bonds.

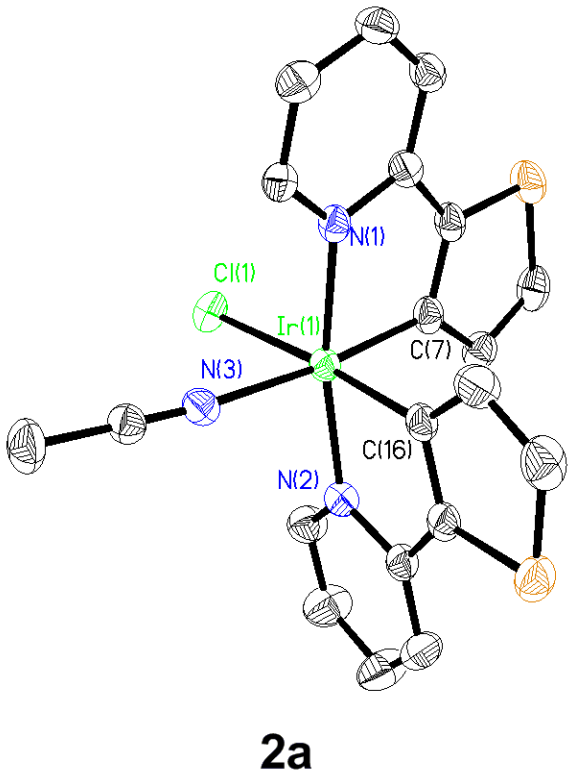

2a

Figure 5. Thermal ellipsoid plot of **2a**. Hydrogen atoms are omitted for clarity.

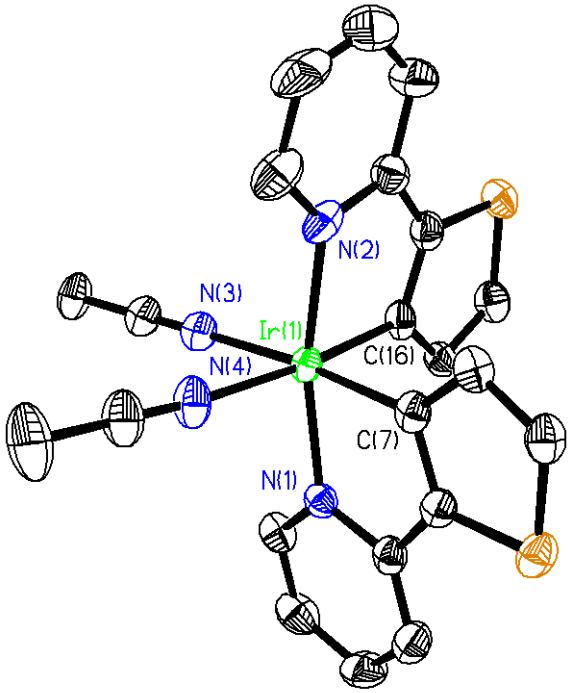

3a

Figure 6. Thermal ellipsoid plot of **3a**. Hydrogen atoms and PF_6 counterions are omitted for clarity.

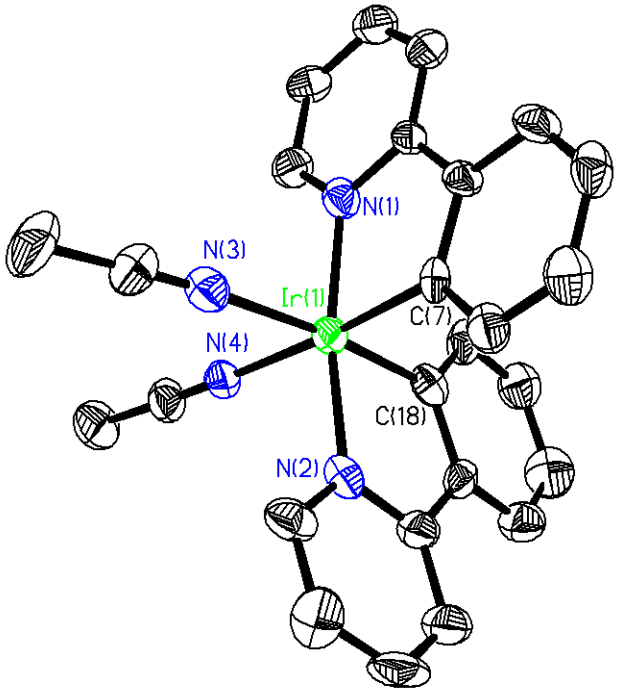

3b

Figure 7. Thermal ellipsoid plot of **3b**. Hydrogen atoms and PF_6 counterions are omitted for clarity.

The structure of **5a** consists of Ir(III) surrounded by two thpy ligands bound in the typical cyclometalating fashion with the *cis*-C,C and *trans*-N,N chelation, as well as a third thpy ligand bound through the N of the pyridyl ring and the S of the thiophene ring. Thiophene has been shown previously to weakly coordinate Ir(III),[50-54] as well as other transition metals,[55-59] through the sulfur atom. The weak nature of the coordination of the sulfur-bound ligand is evident by its facile replacement by solvent molecules when **5a** is in the presence of coordinating solvents such as acetonitrile, methanol, and dimethylsulfoxide. In the crystal structure this third ligand is occupationally disordered by 180º at the Ir atom so that the pyridine ring and thiophene exchange places. The disordered components were resolved to give a 73.3:26.7 ratio of occupancy. The S-bound thpy ligand is not flat, as is typically seen for cyclometalating ligands (Figure 8). The S adopts the sp^3 trigonal pyramidal geometry typically seen for atoms with two bonds and two lone pairs, one of which is coordinated, resulting in the thiophene ring being tilted out of the equatorial plane. The Ir–N distances for the *trans* nitrogen atoms (2.072(6) and 2.070(7) Å) are similar to those previously observed while the Ir–N bond of the S-bound ligand *trans* to the phenyl carbon (2.108(13)/2.180(30) Å) is considerably longer due to the stronger *trans* influence of the thienyl as compared to pyridyl moiety. The Ir–C bond *trans* to the pyridyl group is longer than Ir–C bonds previously observed as pyridine is a better σ-donor than previously examined ligands. The Ir–S bond lengths of the two disorder components are very long (2.430(3) and 2.672(11) Å), as would be expected for a weakly coordinated atom.

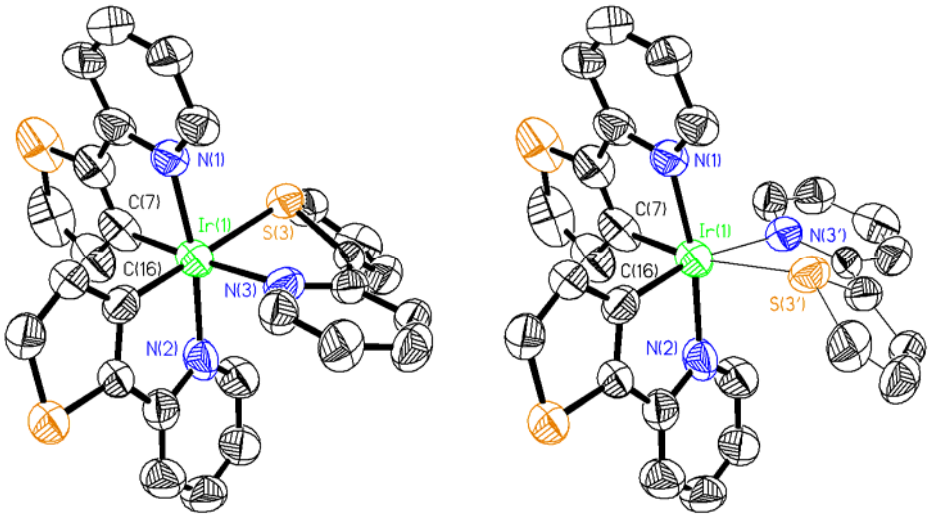

Figure 8. Thermal ellipsoid plots showing the two disorder components of **5a.** Hydrogen atoms and PF_6 counterions are omitted for clarity.

The structure of **3b** contained three crystallographically independent molecules in the asymmetric unit. The Ir–C bond length averaged over each of the three independent molecules (2.004(8) Å) is again shorter than the average Ir–N bond distance (2.052(7) Å). Due to the high estimated standard deviations of the bond distances of the **1b**, no conclusions can be made about the *trans* influence of acetonitrile based on these structures. However, the distances obtained from the structure of **3b** correlate very well with those of **3a**. Not surprisingly the average length of the Ir–N bonds to the acetonitrile ligands (2.131(7) Å) are longer than those of acetonitrile bonds *trans* to pyridyl rings, as previously discussed with **3a**.

Mechanistic Considerations and Discussion.

When we began this work, our goal was to synthesize *fac*-Ir(C^N)$_3$ complexes with high selectivity at low temperatures. In this regard we were successful, although several other groups have been active and published very interesting synthetic studies as well. The traditional syntheses of *fac*-Ir(C^N)$_3$ complexes use high temperature, for example, reactions in refluxing glycerol.[31-37] At lower temperatures (120–150 ºC), otherwise similar reactions give the less emissive *mer* isomers, which are subsequently isomerized to *fac* to avoid low yields and/or contamination.[22, 31] A significant kinetic barrier in these reactions is the breakage of the final Ir–Cl bond as evidenced by (1) the relative ease that the chloro-bridged dimers cleave in polar solvents to give neutral mono-solvento complexes followed by (2) the requirement of Ag^+ ion reactions to induce the second solvent molecule into the Ir(III) coordination sphere. Several reactions that we have carried out attest to the much higher reactivity of these bis-solvento complexes with regard to both ligand substitution and cyclometalation. Among these are the rapid

formation of **5a** from **3a** in acetone and the more rapid reaction of **3a** than **1a** with bpy* in acetone to form the mixed cyclometalating ligand *mer*-Ir(C^N)$_2$(bpy*)PF$_6$ compounds. More recently, a *fac* isomer of a mixed ligand complex has been made at 95 ºC, but in low yield.[20] In all of these cases a consistent mechanistic explanation for the conditions needed for the synthesis and interconversion of the *fac* and *mer* geometry products is absent. Particularly intriguing is the question of how the *mer* geometry in the chloro-bridged starting materials is converted into the tris *fac* products. All of our experiments suggest that the tris *mer* complex is not an intermediate along the "low temperature" reaction path to the tris *fac* product. For example a reaction of *mer*-Ir(ppy)$_3$ at 100 ºC in *o*-dichlorobenzene-d_4 for 10 days gives **no conversion** to **6b**; however, the reaction of **3b** [*mer*-Ir(ppy)$_2$(NCCH$_3$)$_2$]$^+$ with an additional equivalent of ppy at 100 ºC gives exclusively **6b** after 5 days in 60% isolated yield. Another example is the low-temperature rearrangement of the tris- *mer* S-bonded complex **5a** which when heated to only 100 ºC gives *fac*-Ir(thpy)$_3$ and no *mer*-Ir(thpy)$_3$. Clearly, the production of *mer*-Ir(ppy)$_3$ and *mer*-Ir(thpy)$_3$ in these low-temperature reactions without added base is inhibited while the isomerization of one of the C^N ligands of [*mer*-Ir(C^N)$_2$(NCCH$_3$)$_2$]$^+$ and addition of C^N to give the *fac* product is facilitated.

In addition to the observed absence of a low-temperature isomerization reaction of *mer* to *fac*, we have observed that the tris *mer* products can be selectively synthesized at low temperature by the addition of a base to aid in deprotonation of the third ligand. We propose that at low temperature the addition of a base is necessary to obtain the *mer* isomer when starting with the chloro-bridged dimers or bis-acetonitrile complexes; however, when heating hydroxide-bridged dimers **4a** and **4b** in *o*-dichlorobenzene-d_4,

which have a "built-in base" in the hydroxide moiety, to ~100 ºC we observe formation of only tris *mer* species with **no formation** of *fac* isomers. These results, along with the above studies of the synthesis of the *fac* isomers, are consistent with the need for an added base for the production of the *mer* species.

Before I propose a mechanism to rationalize these synthetic results, I would like to address some speculation published after our results were communicated. In particular, the authors disagree with our observations that the bis-acetonitrile complexes, **3a** and **3b**, give only *fac* isomers with no observation of *mer* and that the hydroxide-bridged dimers, **4a** and **4b**, give only *mer* products in *o*-dichlorobenzene. McDonald et al. speculate that the *mer* product was formed initially in both of the above reactions, but in the presence of acetonitrile (a coordinating ligand) and light the *mer* isomer was photochemically converted to the *fac* isomer.[60] In the hydroxo system they believe *fac* isomer formation does not occur because the water formed during the reaction (also a coordinating ligand) phase separates from the *o*-dichlorobenzene. They state: "Previous reports have stated complete photochemical *mer* to *fac* isomerization occurs in NMR tubes, containing pure *mer* compounds, left on the lab bench for a number of days." with no references to support this claim.[60] Our own literature search during the time our experiments were conducted provided the following examples of photochemical conversion of *mer* to *fac* isomers:

(1) Photoisomerization of tris-cyclometalated (phenylpyridine or phenylpyrazolyl ligands with both fluorinated and non-fluorinated substituents) iridum complexes with handheld UV lamps was slower in less coordinating solvents i.e. 72 h in toluene compared with 2 h in DMSO,[31]

(2) Photoisomerization of mixed (difluoro)phenylpyridine/(difluoro)phenylpyrazole tris-cyclometalated iridium complexes occurs after 10 min in acetonitrile using an unfiltered Hg vapor lamp.[38]

(3) Photoisomerization of tris[2-(4',6'-difluorophenyl)pyridine]iridium(III) occurs with a 1 kW Hg lamp or a 150 W Xe lamp in 200 min (3.3 h) in acetonitrile; the rates were faster in methanol and acetonitrile but slow in cyclohexane.[61]

In light of these reports we did not believe that photoisomerization by *room light* on the time scale of our experiments was a valid concern. McDonald et al. also has now reported photoisomerization reactions of mixed ligand tris-cyclometalating Ir(III) complexes in acetonitrile with a medium pressure, 150 W Hg lamp, after photolysis for 4 days.[60] The authors report that *mer* to *fac* isomerism is not observed in *o*-dichlorobenzene in the dark and suggest that our results occur due to unintended photolysis of our reactions by room light in the presence of liberated acetonitrile.[60] We obtained identical results for large scale reactions in our lab that were carried out in flasks wrapped with aluminum foil and the NMR scale reactions which were carried out in room light. Both conditions, the absence and presence room light, resulted in production of the *fac* and *mer* isomers respectively for the bis-acetonitrile and hydroxide-bridged dimer reactions. To further address the concerns of McDonald et al. towards our claims, additional NMR scale experiments were performed *in the dark*. Compound **3b** was combined with ppy in *o*-dichlorobenzene-d_4, protected from room light and heated (100 – 115 $^{\circ}$C); *fac*-Ir(ppy)$_3$, **6b**, was again formed with no trace of the *mer* isomer indicating that light is not required to form the *fac* isomer. In another experiment *mer*-Ir(ppy)$_3$ was dissolved in *o*-dichlorobenzene-d_4 heated in the dark for 20 hrs with no formation of *fac*-

$Ir(ppy)_3$; acetonitrile was then added to test whether the it would aid in the isomerization as suggested by McDonald. Heating for an additional 10 days in the dark did not give any *fac* isomer. Based on the very slow photochemical *mer* to *fac* conversions (~days) that require powerful lamps, and the absence of *mer* to *fac* isomerization at elevated temperatures in the dark or room light in *o*-dichlorobenzene we find it unlikely that *mer* tris complexes are formed but never observed via NMR in the reactions of **3a** and **3b** to make *fac* tris complexes. We also find it highly unlikely that in the reactions of **4a** and **4b** to make *mer* complexes that the small amount of liberated water actually phase separates from the *o*-dichlorobenzene to the extent of inhibiting formation of <u>any</u> *fac* complex. We believe these experiments sufficiently address the concerns of McDonald et al. towards our work.

On the basis of our studies and literature reports, we propose a mechanism that is consistent with the formation of both *mer* and *fac* isomers. The mechanism features common intermediates of the form $Ir(C\hat{}N)_2(-N\hat{}C)L]^+$ where –N^C represents a monodentate cyclometalating ligand attached only through N, and L is either a solvent molecule (e.g., acetonitrile), chloride, or a second ligating atom (other than C) from the entering N^C ligand (such as the S in the case of N^C = thpy). The scheme in Figure 9 drawn for the specific case of L = acetonitrile and N^C = ppy shows the reactions of the $[Ir(C\hat{}N)_2(-N\hat{}C)L]^+$ intermediate which form *mer* and *fac*, respectively.

The proposed mechanism starts with the replacement of one acetonitrile ligand with the nitrogen end of the incoming bidentate ligand to form the intermediate common to both the *mer* and *fac* tris complex mechanisms. In the presence of a sufficient concentration of added base (or in the case of reaction with **4a** and **4b**, the hydroxide

ligand L) the carbon end of the ligand is deprotonated and coordinates with removal of the second acetonitrile. **The determination of the sequence of these steps is beyond the scope of our present studies.** The net result of this path is the fomation of the *mer* tris isomer. If an added base or a basic ligand site is **not** present, the formation of the *fac* isomer is completed by a sequence of steps that includes decomplexation of one of the mutually *trans* nitrogens of the intermediate, proton transfer from the carbon of the incoming ligand, coordination of this carbon to Ir, and then replacement of the remaining acetonitrile by the nitrogen released in the isomerization step. Again, the exact sequence of these steps is not known. Even though the basicity of the carbon is much higher than the nitrogen end of the cyclometalating ligand, the unimolecular nature of the transfer and the presumed exergonic energy balance afforded by the change in coordination geometry at Ir could offer sufficient lowering of the transition-state energies of the overall process. In the traditional high-temperature synthetic scheme, the replacement of acetonitrile in most of the intermediate species by chloride is expected to considerably slow the ligand substitution steps and perhaps make the direct formation of *fac* energetically unfeasible until very high temperatures are available to directly isomerize the *mer* isomer.

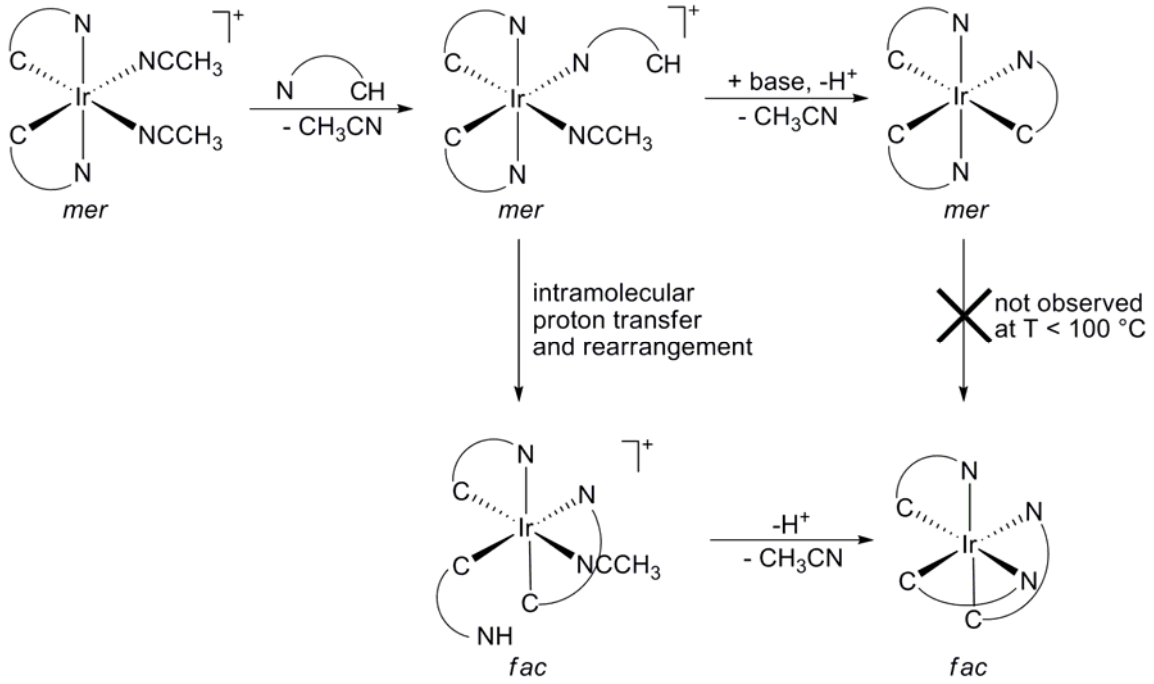

Figure 9. Proposed mechanism for the formation of *mer* and *fac* isomers.

Conclusions.

Selective low-temperature syntheses of *fac* and *mer* tris-cyclometalated Ir(III) complexes have been developed. *Fac* isomers of the cyclometalating ligands thpy and ppy are selectively formed at 100 ºC. The use of bis-acetonitrile complexes as the source of Ir(III) eliminates the activation of Ir–Cl bonds in the rate-limiting step. In *o*-dichlorobenzene and the absence of added base, internal proton transfer and isomerization provides a selective low-temperature route for the preparation of the *fac* isomers after removal of the solvent by flash column chromatography. We suggest that C–H bond activation via proton removal by an added base is the rate-limiting step in the formation of *mer* tris complexes. Our use of hydroxy-bridged dimers provides a "built-in base" that aids deprotonation of the cyclometalating carbon and allows selective formation of the *mer* isomers of thpy and ppy at 100 ºC. We believe that these syntheses will prove to be generally useful for the production of the *fac* and *mer* isomers of other C^N ligands and heteroleptic complexes with two different cyclometalating ligands.

References

1. Vander Donckt, E.; Camerman, B.; Herne, R.; Vandeloise, R., *Sens. Actuators, B* **1996**, *B32*, 121.

2. Brooks, J.; Babayan, Y.; Lamansky, S.; Djurovich, P. I.; Tsyba, I.; Bau, R.; Thompson, M. E., *Inorg. Chem.* **2002**, *41*, 3055.

3. Kawamura, Y.; Brooks, J.; Brown, J. J.; Sasabe, H.; Adachi, C., *Phys. Rev. Lett.* **2006**, *96*, 017404.

4. Chassot, L.; Von Zelewsky, A., *Inorg. Chem.* **1987**, *26*, 2814.

5. Ma, B.; Djurovich, P. I.; Thompson, M. E., *Coord. Chem. Rev.* **2005**, *249*, 1501.

6. Lai, S.-W.; Che, C.-M., *Top. Curr. Chem.* **2004**, *241*, 27.

7. Balashev, K. P.; Puzyk, M. V.; Kotlyar, V. S.; Kulikova, M. V., *Coord. Chem. Rev.* **1997**, *159*, 109.

8. Jolliet, P.; Gianini, M.; von Zelewsky, A.; Bernardinelli, G.; Stoeckli-Evans, H., *Inorg. Chem.* **1996**, *35*, 4883.

9. Maestri, M.; Deuschel-Cornioley, C.; Von Zelewsky, A., *Coord. Chem. Rev.* **1991**, *111*, 117.

10. Craig, C. A.; Watts, R. J., *Inorg. Chem.* **1989**, *28*, 309.

11. Cardenas, D. J.; Echavarren, A. M.; Ramirez de Arellano, M. C., *Organometallics* **1999**, *18*, 3337.

12. Li, C. K.-L.; Sun, R. W.-Y.; Kui, S. C.-F.; Zhu, N.; Che, C.-M., *Chem.--Eur. J.* **2006**, *12*, 5253.

13. Ivanov, M. A.; Puzyk, M. V.; Balashev, K. P., *Opt. Spectrosc.* **2006**, *100*, 382.

14. Wong, K. M.-C.; Zhu, X.; Hung, L.-L.; Zhu, N.; Yam, V. W.-W.; Kwok, H.-S., *Chem. Commun.* **2005**, 2906.

15. Fan, D.; Yang, C.-T.; Ranford, J. D.; Vittal, J. J.; Lee, P. F., *Dalton Trans.* **2003**, 3376.

16. Cinellu, M. A.; Zucca, A.; Stoccoro, S.; Minghetti, G.; Manassero, M.; Sansoni, M., *Dalton Trans.* **1996**, 4217.

17. Constable, E. C.; Leese, T. A., *J. Organomet. Chem.* **1989**, *363*, 419.

18. King, K. A.; Spellane, P. J.; Watts, R. J., *J. Am. Chem. Soc.* **1985**, *107*, 1431.

19. Gao, R.; Ho, D. G.; Hernandez, B.; Selke, M.; Murphy, D.; Djurovich, P. I.; Thompson, M. E., *J. Am. Chem. Soc.* **2002**, *124*, 14828.

20. DeRosa, M. C.; Hodgson, D. J.; Enright, G. D.; Dawson, B.; Evans, C. E. B.; Crutchley, R. J., *J. Am. Chem. Soc.* **2004**, *126*, 7619.

21. Lamansky, S.; Djurovich, P.; Murphy, D.; Abdel-Razzaq, F.; Lee, H.-E.; Adachi, C.; Burrows, P. E.; Forrest, S. R.; Thompson, M. E., *J. Am. Chem. Soc.* **2001**, *123*, 4304.

22. Ragni, R.; Plummer, E. A.; Brunner, K.; Hofstraat, J. W.; Babudri, F.; Farinola, G. M.; Naso, F.; De Cola, L., *J. Mater. Chem.* **2006**, *16*, 1161.

23. Sheraw, C. D.; Zhou, L.; Huang, J. R.; Gundlach, D. J.; Jackson, T. N.; Kane, M. G.; Hill, I. G.; Hammond, M. S.; Campi, J.; Greening, B. K.; Francl, J.; West, J., *Appl. Phys. Lett.* **2002**, *80*, 1088.

24. Kanno, H.; Giebink, N. C.; Sun, Y.; Forrest, S. R., *Appl. Phys. Lett.* **2006**, *89*, 023503/1.

25. Okada, S.; Okinaka, K.; Iwawaki, H.; Furugori, M.; Hashimoto, M.; Mukaide, T.; Kamatani, J.; Igawa, S.; Tsuboyama, A.; Takiguchi, T.; Ueno, K., *Dalton Trans.* **2005**, 1583.

26. D'Andrade, B. W.; Baldo, M. A.; Adachi, C.; Brooks, J.; Thompson, M. E.; Forrest, S. R., *Appl. Phys. Lett.* **2001**, *79*, 1045.

27. Lamansky, S.; Kwong, R. C.; Nugent, M.; Djurovich, P. I.; Thompson, M. E., *Org. Electronics* **2001**, *2*, 53.

28. Watanabe, T.; Nakamura, K.; Kawami, S.; Fukuda, Y.; Tsuji, T.; Wakimoto, T.; Miyaguchi, S.; Yahiro, M.; Yang, M. J.; Tsutsui, T., *Synth. Met.* **2001**, *122*, 203.

29. Meng, H.; Sun, F.; Goldfinger, M. B.; Gao, F.; Londono, D. J.; Marshal, W. J.; Blackman, G. S.; Dobbs, K. D.; Keys, D. E., *J. Am. Chem. Soc.* **2006**, *128*, 9304.

30. Chou, P.-T.; Chi, Y., *Chem.--Eur. J.* **2007**, *13*, 380.

31. Tamayo, A. B.; Alleyne, B. D.; Djurovich, P. I.; Lamansky, S.; Tsyba, I.; Ho, N. N.; Bau, R.; Thompson, M. E., *J. Am. Chem. Soc.* **2003**, *125*, 7377.

32. Colombo, M. G.; Brunold, T. C.; Riedener, T.; Guedel, H. U.; Fortsch, M.; Buergi, H.-B., *Inorg. Chem.* **1994**, *33*, 545.

33. Dedeian, K.; Djurovich, P. I.; Garces, F. O.; Carlson, G.; Watts, R. J., *Inorg. Chem.* **1991**, *30*, 1685.

34. Grushin, V. V.; Herron, N.; LeCloux, D. D.; Marshall, W. J.; Petrov, V. A.; Wang, Y., *Chem. Commun.* **2001**, 1494.

35. Konno, H.; Sasaki, Y., *Chem. Lett.* **2003**, *32*, 252.

36. Ostrowski, J. C.; Robinson, M. R.; Heeger, A. J.; Bazan, G. C., *Chem. Commun.* **2002**, 784.

37. Tsuboyama, A.; Iwawaki, H.; Furugori, M.; Mukaide, T.; Kamatani, J.; Igawa, S.; Moriyama, T.; Miura, S.; Takiguchi, T.; Okada, S.; Hoshino, M.; Ueno, K., *J. Am. Chem. Soc.* **2003**, *125*, 12971.

38. Dedeian, K.; Shi, J.; Shepherd, N.; Forsythe, E.; Morton, D. C., *Inorg. Chem.* **2005**, *44*, 4445.

39. Tamao, K.; Kodama, S.; Nakajima, I.; Kumada, M.; Minato, A.; Suzuki, K., *Tetrahedron* **1982**, *38*, 3347.

40. Nonoyama, M., *Bull. Chem. Soc. Jpn.* **1974**, *47*, 767.

41. Schmid, B.; Garces, F. O.; Watts, R. J., *Inorg. Chem.* **1994**, *33*, 9.

42. Blessing, R. H., *Acta Crystallogr., Sect. A: Found. Crystallogr.* **1995**, *A51*, 33.

43. Sheldrick, G. *SADABS*, v.2.03; 2002.

44. *SHELXL*, v.6.1; Bruker AXS, Madison, WI, 2001.

45. Garces, F. O.; Dedeian, K.; Keder, N. L.; Watts, R. J., *Acta Crystallogr., Sect. C: Cryst. Struct. Commun.* **1993**, *C49*, 1117.

46. Silverstein, R. M.; Webster, F. X., *Spectrometric Identification of Organic Compounds*. 6th ed.; John Wiley & Sons, Inc.: New York, **1998**.

47. Marat, K. *Spinworks*, v.2.3; University of Manitoba, Winnipeg, Manitoba, Canada, 2004.

48. Chattopadhyay, S. K.; Mitra, K.; Biswas, S.; Naskar, S.; Mishra, D.; Adhikary, B.; Harrison, R. G.; Cannon, J. F., *Transition Met. Chem.* **2004**, *29*, 1.

49. Heeg, M. J.; Kroener, R.; Deutsch, E., *Acta Crystallogr., Sect. C: Cryst. Struct. Commun.* **1985**, *C41*, 684.

50. Paneque, M.; Poveda, M. L.; Carmona, E.; Salazar, V., *Dalton Trans.* **2005**, 1422.

51. Paneque, M.; Poveda, M. L.; Rey, L.; Taboada, S.; Carmona, E.; Ruiz, C., *J. Organomet. Chem.* **1995**, *504*, 147.

52. Paneque, M.; Poveda, M. L.; Salazar, V.; Taboada, S.; Carmona, E.; Gutierrez-Puebla, E.; Monge, A.; Ruiz, C., *Organometallics* **1999**, *18*, 139.

53. Rao, K. M.; Day, C. L.; Jacobson, R. A.; Angelici, R. J., *Inorg. Chem.* **1991**, *30*, 5046.

54. Sanchez-Delgado, R. A.; Herrera, V.; Bianchini, C.; Masi, D.; Mealli, C., *Inorg. Chem.* **1993**, *32*, 3766.

55. Amari, C.; Ianelli, S.; Pelizzi, C.; Pelizzi, G.; Predieri, G., *Inorg. Chim. Acta* **1993**, *211*, 89.

56. Bianchini, C.; Gatteschi, D.; Giambastiani, G.; Rios, I. G.; Ienco, A.; Laschi, F.; Mealli, C.; Meli, A.; Sorace, L.; Toti, A.; Vizza, F., *Organometallics* **2007**, *26*, 726.

57. Chelucci, G.; Muroni, D.; Saba, A.; Soccolini, F., *J. Molec. Catal. A* **2003**, *197*, 27.

58. Constable, E. C.; Henney, R. P. G.; Tocher, D. A., *J. Chem. Soc., Dalton Trans.* **1991**, 2335.

59. Constable, E. C.; Henney, R. P. G.; Tocher, D. A., *J. Chem. Soc., Dalton Trans.* **1992**, 2467.

60. McDonald, A. R.; Lutz, M.; von Chrzanowski, L. S.; van Klink, G. P. M.; Spek, A. L.; van Koten, G., *Inorg. Chem.* **2008**, *47*, 6681.

61. Karatsu, T.; Nakamura, T.; Yagai, S.; Kitamura, A.; Yamaguchi, K.; Matsushima, Y.; Iwata, T.; Hori, Y.; Hagiwara, T., *Chem. Lett.* **2003**, *32*, 886.

Bibliography

Chapter 1

1. Demas, J. N.; DeGraff, B. A.; Coleman, P. B., *Anal. Chem.* **1999**, *71*, 793A.

2. Mills, A., *Platinum Met. Rev.* **1997**, *41*, 115.

3. Ando, M., *TrAC, Trends Anal. Chem.* **2006**, *25*, 937.

4. Demas, J. N.; DeGraff, B. A., *Coord. Chem. Rev.* **2001**, *211*, 317.

5. Zhao, Y.; Richman, A.; Storey, C.; Radford, N. B.; Pantano, P., *Anal. Chem.* **1999**, *71*, 3887.

6. Amao, Y.; Okura, I., *Sens. Actuators, B* **2003**, *B88*, 162.

7. Demas, J. N.; DeGraff, B. A.; Xu, W., *Anal. Chem.* **1995**, *67*, 1377.

8. Draxler, S.; Lippitsch, M. E.; Klimant, I.; Kraus, H.; Wolfbeis, O. S., *J. Phys. Chem.* **1995**, *99*, 3162.

9. Ertekin, K.; Kocak, S.; Sabih Ozer, M.; Aycan, S.; Cetinkaya, B., *Talanta* **2003**, *61*, 573.

10. Fuller, Z. J.; Bare, W. D.; Kneas, K. A.; Xu, W. Y.; Demas, J. N.; DeGraff, B. A., *Anal. Chem.* **2003**, *75*, 2670.

11. Garcia-Fresnadillo, D.; Marazuela, M. D.; Moreno-Bondi, M. C.; Orellana, G., *Langmuir* **1999**, *15*, 6451.

12. Hartmann, P.; Leiner, M. J. P.; Lippitsch, M. E., *Anal. Chem.* **1995**, *67*, 88.

13. Huynh, L.; Wang, Z.; Yang, J.; Stoeva, V.; Lough, A.; Manners, I.; Winnik, M. A., *Chem. Mater.* **2005**, *17*, 4765.

14. Kneas, K. A.; Demas, J. N.; Nguyen, B.; Lockhart, A.; Xu, W.; DeGraff, B. A., *Anal. Chem.* **2002**, *74*, 1111.

15. Kneas, K. A.; Xu, W.; Demas, J. N.; DeGraff, B. A., *Appl. Spectrosc.* **1997**, *51*, 1346.

16. McMurray, H. N.; Douglas, P.; Busa, C.; Garley, M. S., *J. Photochem. Photobiol. A* **1994**, *80*, 283.

17. McNamara, K. P.; Li, X.; Stull, A. D.; Rosenzweig, Z., *Anal. Chim. Acta* **1998**, *361*, 73.

18. Mills, A., *Analyst* **1998**, *123*, 1135.

19. Morin, A. M.; Xu, W.; Demas, J. N.; DeGraff, B. A., *J. Fluoresc.* **2000**, *10*, 7.

20. Navarro-Villoslada, F.; Orellana, G.; Moreno-Bondi, M. C.; Vick, T.; Driver, M.; Hildebrand, G.; Liefeith, K., *Anal. Chem.* **2001**, *73*, 5150.

21. Preininger, C.; Klimant, I.; Wolfbeis, O. S., *Anal. Chem.* **1994**, *66*, 1841.

22. Ruffolo, R.; Evans, C. E. B.; Liu, X.-H.; Ni, Y.; Pang, Z.; Park, P.; McWilliams, A. R.; Gu, X.; Lu, X.; Yekta, A.; Winnik, M. A.; Manners, I., *Anal. Chem.* **2000**, *72*, 1894.

23. Wang, Z.; McWilliams, A. R.; Evans, C. E. B.; Lu, X.; Chung, S.; Winnik, M. A.; Manners, I., *Adv. Funct. Mater.* **2002**, *12*, 415.

24. Coutant, M. A.; Payra, P.; Dutta, P. K., *Microporous Mesoporous Mater.* **2003**, *60*, 79.

25. Meier, B.; Werner, T.; Klimant, I.; Wolfbeis, O. S., *Sens. Actuators, B* **1995**, *B29*, 240.

26. Bukowski, R. M.; Ciriminna, R.; Pagliaro, M.; Bright, F. V., *Anal. Chem.* **2005**, *77*, 2670.

27. Bukowski, R. M.; Davenport, M. D.; Titus, A. H.; Bright, F. V., *Appl. Spectrosc.* **2006**, *60*, 951.

28. Leventis, N.; Elder, I. A.; Rolison, D. R.; Anderson, M. L.; Merzbacher, C. I., *Chem. Mater.* **1999**, *11*, 2837.

29. Leventis, N.; Rawashdeh, A.-M. M.; Elder, I. A.; Yang, J.; Dass, A.; Sotiriou-Leventis, C., *Chem. Mater.* **2004**, *16*, 1493.

30. Murtagh, M. T.; Shahriari, M. R.; Krihak, M., *Chem. Mater.* **1998**, *10*, 3862.

31. Cheng, Z.; Aspinwall, C. A., *Analyst* **2006**, *131*, 236.

32. Chu, B. W.-K.; Yam, V. W.-W., *Langmuir* **2006**, *22*, 7437.

33. Jorge, P. A. S.; Mayeh, M.; Benrashid, R.; Caldas, P.; Santos, J. L.; Farahi, F., *Appl. Opt.* **2006**, *45*, 3760.

34. Kocincova, A. S.; Borisov, S. M.; Krause, C.; Wolfbeis, O. S., *Anal. Chem.* **2007**, *79*, 8486.

35. Krenske, D.; Abdo, S.; Van Damme, H.; Cruz, M.; Fripiat, J. J., *J. Phys. Chem.* **1980**, *84*, 2447.

36. Xiong, X.; Xiao, D.; Choi, M. M. F., *Sens. Actuators, B* **2006**, *B117*, 172.

37. FOXY Fiber Optic Oxygen Sensors; OceanOptics: Dunedin, F.

38. Carraway, E. R.; Demas, J. N.; DeGraff, B. A.; Bacon, J. R., *Anal. Chem.* **1991**, *63*, 337.

39. Drew, S. M.; Janzen, D. E.; Mann, K. R., *Anal. Chem.* **2002**, *74*, 2547.

40. Drew, S. M.; Mann, J. E.; Marquardt, B. J.; Mann, K. R., *Sens. Actuators, B* **2004**, *B97*, 307.

41. Grate, J. W.; Moore, L. K.; Janzen, D. E.; Veltkamp, D. J.; Kaganove, S.; Drew, S. M.; Mann, K. R., *Chem. Mater.* **2002**, *14*, 1058.

42. Spek, A. L. PLATON/CALC VOID. http://www.weizmann.ac.il/Chemical_Research Support/xraylab/manuals/Platon/platon/pl000302.html (accessed 03/02/05).

43. *Crystal Engineering: From Molecules and Crystals to Materials*. Kluwer Academic: Dordrecht, **1999**; Vol. 538.

44. *Inclusion Compounds Volume 1*. Academic Press: London, **1984**.

45. Exstrom, C. L.; Britton, D.; Mann, K. R.; Hill, M. G.; Miskowski, V. M.; Schaefer, W. P.; Gray, H. B.; Lamanna, W. M., *Inorg. Chem.* **1996**, *35*, 549.

46. Evans, I. P.; Spencer, A.; Wilkinson, G., *J. Chem. Soc., Dalton Trans.* **1973**, 204.

47. Cooley, L. F.; Headford, C. E. L.; Elliott, C. M.; Kelley, D. F., *J. Am. Chem. Soc.* **1988**, *110*, 6673.

48. Lacour, J.; Goujon-Ginglinger, C.; Troche-Haldimann, S.; Jordry, J. J., *Angew. Chem., Int. Ed.* **2000**, *39*, 3695.

49. Blessing, R. H., *Acta Crystallogr., Sect. A: Found. Crystallogr.* **1995**, *A51*, 33.

50. Sheldrick, G. *SADABS*, v.2.10; 2002.

51. *SHELXTL*, v.6.12; Bruker AXS, Madison, WI, 2001.

52. Spek, A. L., *J. Appl. Crystallogr.* **2003**, *36*, 7.

53. Spek, A. L. *PLATON*, Utrecht University, Utrecht, The Netherlands, 2005.

54. Bruno, I. J.; Cole, J. C.; Edgington, P. R.; Kessler, M.; Macrae, C. F.; McCabe, P.; Pearson, J.; Taylor, R., *Acta Crystallographica, Section B: Structural Science* **2002**, *B58*, 389.

55. Wrighton, M. S.; Ginley, D. S.; Morse, D. L., *J. Phys. Chem.* **1974**, *78*, 2229.

56. Demas, J. N.; Crosby, G. A., *J. Phys. Chem.* **1971**, *75*, 991.

57. Avian Technolgies, 1 Worthington Rd., P.O. Box 822, Wilmington, OH 45177, USA; http://www.aviantechnologies.com/faq.html.

58. Private communication, Paul F. Barbara.

59. LED is ETG-5UV 405-30 from ETG Corporation, 8599 Venice Blvd, Unit K, Los Angeles, CA 90034.

60. The filter is a FF01-406/15-25 from Semrock, 3625 Buffalo Road, Rochester, NY 14624.

61. Araki, T.; Fujisawa, Y.; Hashimoto, M., *Rev. Sci. Instrum.* **1997**, *68*, 1365.

62. Logger Pro software: Vernier Software & Technology, 13979 SW Millikan Way, Beaverton, OR 97005-2886.

63. Marquardt, B. J.; Burgess, L. W. Optical Immersion Probe Incorporating a Spherical Lens. US patent # 6,831,745 B2, 2004.

64. Marquardt, B. J.; Le, T.; Burgess, L. W., *SPIE Proceedings* **2001**, *4469*, 62.

65. Wold, J. P.; Marquardt, B. J.; Dable, B. K.; Robb, D.; Hatlen, B., *Appl. Spectrosc.* **2004**, *58*, 395.

66. Beebe, K. R.; Pell, R. J.; Seasholtz, M. B., *Chemometrics: A Practical Guide*. John Wiley and Sons, Inc.: New York, NY, **1998**; p 278-335.

67. Douglas, P.; Eaton, K., *Sens. Actuators, B* **2002**, *B82*, 200.

68. Gladysz, J. A.; Curran, D. P.; Horvath, I. T.; Editors, *Handbook of Flurorous Chemistry*. **2004**; p 594 pp.

69. Ikeda, N.; Yoshimura, A.; Tsushima, M.; Ohno, T., *J. Phys. Chem. A* **2000**, *104*, 6158.

70. Kalinowski, J.; Fattori, V.; Di Marco, P., *Chem. Phys.* **2001**, *266*, 85.

71. Bowyer, W. J.; Xu, W.; Demas, J. N., *Anal. Chem.* **2004**, *76*, 4374.

Chapter 2

1. Ando, M., *TrAC, Trends Anal. Chem.* **2006**, *25*, 937.

2. Demas, J. N.; DeGraff, B. A., *Coord. Chem. Rev.* **2001**, *211*, 317.

3. Demas, J. N.; DeGraff, B. A.; Coleman, P. B., *Anal. Chem.* **1999**, *71*, 793A.

4. Mills, A., *Platinum Met. Rev.* **1997**, *41*, 115.

5. Zhao, Y.; Richman, A.; Storey, C.; Radford, N. B.; Pantano, P., *Anal. Chem.* **1999**, *71*, 3887.

6. Amao, Y.; Okura, I., *Sens. Actuators, B* **2003**, *B88*, 162.

7. Demas, J. N.; DeGraff, B. A.; Xu, W., *Anal. Chem.* **1995**, *67*, 1377.

8. Draxler, S.; Lippitsch, M. E.; Klimant, I.; Kraus, H.; Wolfbeis, O. S., *J. Phys. Chem.* **1995**, *99*, 3162.

9. Ertekin, K.; Kocak, S.; Sabih Ozer, M.; Aycan, S.; Cetinkaya, B., *Talanta* **2003**, *61*, 573.

10. Fuller, Z. J.; Bare, W. D.; Kneas, K. A.; Xu, W. Y.; Demas, J. N.; DeGraff, B. A., *Anal. Chem.* **2003**, *75*, 2670.

11. Garcia-Fresnadillo, D.; Marazuela, M. D.; Moreno-Bondi, M. C.; Orellana, G., *Langmuir* **1999**, *15*, 6451.

12. Hartmann, P.; Leiner, M. J. P.; Lippitsch, M. E., *Anal. Chem.* **1995**, *67*, 88.

13. Huynh, L.; Wang, Z.; Yang, J.; Stoeva, V.; Lough, A.; Manners, I.; Winnik, M. A., *Chem. Mater.* **2005**, *17*, 4765.

14. Kneas, K. A.; Demas, J. N.; Nguyen, B.; Lockhart, A.; Xu, W.; DeGraff, B. A., *Anal. Chem.* **2002**, *74*, 1111.

15. Kneas, K. A.; Xu, W.; Demas, J. N.; DeGraff, B. A., *Appl. Spectrosc.* **1997**, *51*, 1346.

16. McMurray, H. N.; Douglas, P.; Busa, C.; Garley, M. S., *J. Photochem. Photobiol. A* **1994**, *80*, 283.

17. McNamara, K. P.; Li, X.; Stull, A. D.; Rosenzweig, Z., *Anal. Chim. Acta* **1998**, *361*, 73.

18. Mills, A., *Analyst* **1998**, *123*, 1135.

19. Morin, A. M.; Xu, W.; Demas, J. N.; DeGraff, B. A., *J. Fluoresc.* **2000**, *10*, 7.

20. Navarro-Villoslada, F.; Orellana, G.; Moreno-Bondi, M. C.; Vick, T.; Driver, M.; Hildebrand, G.; Liefeith, K., *Anal. Chem.* **2001**, *73*, 5150.

21. Preininger, C.; Klimant, I.; Wolfbeis, O. S., *Anal. Chem.* **1994**, *66*, 1841.

22. Ruffolo, R.; Evans, C. E. B.; Liu, X.-H.; Ni, Y.; Pang, Z.; Park, P.; McWilliams, A. R.; Gu, X.; Lu, X.; Yekta, A.; Winnik, M. A.; Manners, I., *Anal. Chem.* **2000**, *72*, 1894.

23. Wang, Z.; McWilliams, A. R.; Evans, C. E. B.; Lu, X.; Chung, S.; Winnik, M. A.; Manners, I., *Adv. Funct. Mater.* **2002**, *12*, 415.

24. Coutant, M. A.; Payra, P.; Dutta, P. K., *Microporous Mesoporous Mater.* **2003**, *60*, 79.

25. Meier, B.; Werner, T.; Klimant, I.; Wolfbeis, O. S., *Sens. Actuators, B* **1995**, *B29*, 240.

26. Bukowski, R. M.; Ciriminna, R.; Pagliaro, M.; Bright, F. V., *Anal. Chem.* **2005**, *77*, 2670.

27. Bukowski, R. M.; Davenport, M. D.; Titus, A. H.; Bright, F. V., *Appl. Spectrosc.* **2006**, *60*, 951.

28. Leventis, N.; Elder, I. A.; Rolison, D. R.; Anderson, M. L.; Merzbacher, C. I., *Chem. Mater.* **1999**, *11*, 2837.

29. Leventis, N.; Rawashdeh, A.-M. M.; Elder, I. A.; Yang, J.; Dass, A.; Sotiriou-Leventis, C., *Chem. Mater.* **2004**, *16*, 1493.

30. Murtagh, M. T.; Shahriari, M. R.; Krihak, M., *Chem. Mater.* **1998**, *10*, 3862.

31. Cheng, Z.; Aspinwall, C. A., *Analyst* **2006**, *131*, 236.

32. Chu, B. W.-K.; Yam, V. W.-W., *Langmuir* **2006**, *22*, 7437.

33. Jorge, P. A. S.; Mayeh, M.; Benrashid, R.; Caldas, P.; Santos, J. L.; Farahi, F., *Appl. Opt.* **2006**, *45*, 3760.

34. Kocincova, A. S.; Borisov, S. M.; Krause, C.; Wolfbeis, O. S., *Anal. Chem.* **2007**, *79*, 8486.

35. Krenske, D.; Abdo, S.; Van Damme, H.; Cruz, M.; Fripiat, J. J., *J. Phys. Chem.* **1980**, *84*, 2447.

36. Xiong, X.; Xiao, D.; Choi, M. M. F., *Sens. Actuators, B* **2006**, *B117*, 172.

37. FOXY Fiber Optic Oxygen Sensors; OceanOptics: Dunedin, F.

38. McGee, K. A.; Veltkamp, D. J.; Marquardt, B. J.; Mann, K. R., *J. Am. Chem. Soc.* **2007**, *129*, 15092.

39. Nakamura, A.; Sato, T.; Kuroda, R., *Chem. Commun.* **2004**, 2858.

40. Brock, C. P.; Schweizer, W. B.; Dunitz, J. D., *J. Am. Chem. Soc.* **1991**, *113*, 9811.

41. Herbstein, F. H., Crystalline Molecular Complexes and Compounds. In *IUCr Monographs on Crystallography - 18*, Oxford University Press: Oxford, 2005; Vol. 1, pp 571-574.

42. Lancaster, R. W.; Karamertzanis, P. G.; Hulme, A. T.; Tocher, D. A.; Covey, D. F.; Price, S. L., *Chem. Commun.* **2006**, 4921.

43. Maloney, D. J.; MacDonnell, F. M., *Acta Crystallogr., Sect. C: Cryst. Struct. Commun.* **1997**, *C53*, 705.

44. Blessing, R. H., *Acta Crystallogr., Sect. A: Found. Crystallogr.* **1995**, *A51*, 33.

45. Sheldrick, G. *SADABS*, v.2.03; 2002.

46. *SHELXTL*, v.6.12; Bruker AXS, Madison, WI, 2001.

47. Spek, A. L., *J. Appl. Crystallogr.* **2003**, *36*, 7.

48. Spek, A. L. *PLATON*, Utrecht University, Utrecht, The Netherlands, 2005.

49. Bruno, I. J.; Cole, J. C.; Edgington, P. R.; Kessler, M.; Macrae, C. F.; McCabe, P.; Pearson, J.; Taylor, R., *Acta Crystallographica, Section B: Structural Science* **2002**, *B58*, 389.

50. Breu, J.; Stoll, A. J., *Acta Crystallogr., Sect. C: Cryst. Struct. Commun.* **1996**, *C52*, 1174.

51. Avian Technolgies, 1 Worthington Rd. , P.O. Box 822 , Wilmington, OH 45177, USA; http://www.aviantechnologies.com/faq.html.

52. Carraway, E. R.; Demas, J. N.; DeGraff, B. A., *Anal. Chem.* **1991**, *63*, 332.

53. Carraway, E. R.; Demas, J. N.; DeGraff, B. A.; Bacon, J. R., *Anal. Chem.* **1991**, *63*, 337.

54. Demas, J. N.; DeGraff, B. A., *Sens. Actuators, B* **1993**, *B11*, 35.

55. Klimant, I.; Wolfbeis, O. S., *Anal. Chem.* **1995**, *67*, 3160.

56. Ikeda, N.; Yoshimura, A.; Tsushima, M.; Ohno, T., *J. Phys. Chem. A* **2000**, *104*, 6158.

Chapter 3

1. EPA, *Indoor Air Quality, Sources of Air Pollution - Organic Gases (Volatile Organic Compounds - VOCs)*. updated on October 10, 2008. http://www.epa.gov/iaq/voc.html.

2. EPA, *Technology Transfer Network, Air Toxics Website, Benzene*. updated February 4, 2008. http://www.epa.gov/ttn/atw/hlthef/benzene.html.

3. NIOSH Recommended Exposure Limit (REL): 0.1 ppm (8 h), 1 ppm (15 min), ACGIH Threshold Limit Values (TLV): 0.5 ppm (8 h), 2.5 ppm (15 min), OSHA Permissible Exposure Limits (PEL): 1 ppm (8h), 5 ppm (15 min) from Benzene; CHEMINFO, Canadian Centre for Occupational Health and Safety, http://ccinfoweb2.ccohs.ca (accessed 8/29/08).

4. Dincer, F.; Odabasi, M.; Muezzinoglu, A., *J. Chromatogr., A* **2006**, *1122*, 222.

5. Wu, C.-H.; Feng, C.-T.; Lo, Y.-S.; Lin, T.-Y.; Lo, J.-G., *Chemosphere* **2004**, *56*, 71.

6. Yamada, Y.; Nakamura, T.; Yano, K., *Langmuir* **2008**, *24*, 2779.

7. Endo, T.; Yanagida, Y.; Hatsuzawa, T., *Sens. Actuators, B* **2007**, *B125*, 589.

8. Plante, J. P.; Glass, T. E., *Org. Lett* **2006**, *8*, 2163.

9. Dickinson, T. A.; White, J.; Kauer, J. S.; Walt, D. R., *Nature* **1996**, *382*, 697.

10. White, J.; Kauer, J. S.; Dickinson, T. A.; Walt, D. R., *Anal. Chem.* **1996**, *68*, 2191.

11. Silva, A. M. S.; Pimentel, M. F.; Raimundo, I. M., Jr.; Almeida, Y. M. B., *Vib. Spectrosc.* **2008**, *46*, 39.

12. Ablat, H.; Yimit, A.; Mahmut, M.; Itoh, K., *Anal. Chem.* **2008**, *80*, 7678.

13. Silva, L. I. B.; Rocha-Santos, T. A. P.; Duarte, A. C., *Sens. Actuators, B* **2008**, *B132*, 280.

14. Casalini, R.; Wilde, J. N.; Nagel, J.; Oertel, U.; Petty, M. C., *Sens. Actuators, B* **1999**, *B57*, 28.

15. Ando, M., *TrAC, Trends Anal. Chem.* **2006**, *25*, 937.

16. Borisov, S. M.; Klimant, I., *Anal. Chem.* **2007**, *79*, 7501.

17. Carraway, E. R.; Demas, J. N.; DeGraff, B. A.; Bacon, J. R., *Anal. Chem.* **1991**, *63*, 337.

18. Chu, C.-S.; Lo, Y.-L., *IEEE Photonics Technology Letters* **2008**, *20*, 63.

19. Demas, J. N.; DeGraff, B. A., *Coord. Chem. Rev.* **2001**, *211*, 317.

20. Demas, J. N.; DeGraff, B. A.; Coleman, P. B., *Anal. Chem.* **1999**, *71*, 793A.

21. Demas, J. N.; Harris, E. W.; McBride, R. P., *J. Am. Chem. Soc.* **1977**, *99*, 3547.

22. Draxler, S.; Lippitsch, M. E.; Klimant, I.; Kraus, H.; Wolfbeis, O. S., *J. Phys. Chem.* **1995**, *99*, 3162.

23. Mills, A., *Platinum Met. Rev.* **1997**, *41*, 115.

24. Drew, S. M.; Janzen, D. E.; Mann, K. R., *Anal. Chem.* **2002**, *74*, 2547.

25. Drew, S. M.; Mann, J. E.; Marquardt, B. J.; Mann, K. R., *Sens. Actuators, B* **2004**, *B97*, 307.

26. Grate, J. W.; Moore, L. K.; Janzen, D. E.; Veltkamp, D. J.; Kaganove, S.; Drew, S. M.; Mann, K. R., *Chem. Mater.* **2002**, *14*, 1058.

27. Nagel, C. C. Preparation of thermochromic double-complex salts. 88-300781 277032, 19880129., 1988.

28. Nagel, C. C. Preparation of vapochromic double-complex salts. 88-300782 277033, 19880129., 1988.

29. McGee, K. A.; Veltkamp, D. J.; Marquardt, B. J.; Mann, K. R., *J. Am. Chem. Soc.* **2007**, *129*, 15092.

30. Exstrom, C. L.; Britton, D.; Mann, K. R.; Hill, M. G.; Miskowski, V. M.; Schaefer, W. P.; Gray, H. B.; Lamanna, W. M., *Inorg. Chem.* **1996**, *35*, 549.

31. Evans, I. P.; Spencer, A.; Wilkinson, G., *J. Chem. Soc., Dalton Trans.* **1973**, 204.

32. Cooley, L. F.; Headford, C. E. L.; Elliott, C. M.; Kelley, D. F., *J. Am. Chem. Soc.* **1988**, *110*, 6673.

33. Lacour, J.; Goujon-Ginglinger, C.; Troche-Haldimann, S.; Jordry, J. J., *Angew. Chem., Int. Ed.* **2000**, *39*, 3695.

34. Beebe, K. R.; Pell, R. J.; Seasholtz, M. B., *Chemometrics: A Practical Guide*. John Wiley and Sons, Inc.: New York, NY, **1998**; p 26-182.

35. The authors acknowledge Dr. Victor G Young Jr. and Benjamin E. Kucera at the X-ray Crystallography Laboratory in the Department of Chemistry at the University of Minnesota.

36. Blessing, R. H., *Acta Crystallogr., Sect. A: Found. Crystallogr.* **1995**, *A51*, 33.

37. Sheldrick, G. *SADABS*, v.2.03; 2002.

38. *SHELXTL*, v.6.12; Bruker AXS, Madison, WI, 2001.

39. Spek, A. L., *J. Appl. Crystallogr.* **2003**, *36*, 7.

40. Spek, A. L. *PLATON*, Utrecht University, Utrecht, The Netherlands, 2005.

41. Bruno, I. J.; Cole, J. C.; Edgington, P. R.; Kessler, M.; Macrae, C. F.; McCabe, P.; Pearson, J.; Taylor, R., *Acta Crystallogr., Sect. B: Struct. Sci.* **2002**, *B58*, 389.

42. Oxygen concentration expressed as mole fraction in nitrogen at atmospheric pressure = 0.97 atm.

Chapter 4

1. Bernhard, S.; Barron, J. A.; Houston, P. L.; Abruna, H. D.; Ruglovksy, J. L.; Gao, X.; Malliaras, G. G., *J. Am. Chem. Soc.* **2002**, *124*, 13624.

2. Evju, J. K.; Mann, K. R., *Chem. Mater.* **1999**, *11*, 1425.

3. Takahashi, Y.; Arakawa, H.; Sugihara, H.; Hara, K.; Islam, A.; Katoh, R.; Tachibana, Y.; Yanagida, M., *Inorg. Chim. Acta* **2000**, *310*, 169.

4. Slinker, J. D.; Rivnay, J.; Moskowitz, J. S.; Parker, J. B.; Bernhard, S.; Abruna, H. D.; Malliaras, G. G., *J. Mater. Chem.* **2007**, *17*, 2976.

5. Chou, P.-T.; Chi, Y., *Chem.--Eur. J.* **2007**, *13*, 380.

6. Vos, J. G.; Kelly, J. M., *Dalton Trans.* **2006**, 4869.

7. Chou, P.-T.; Chi, Y., *Eur. J. Inorg. Chem.* **2006**, 3319.

8. Brook, T. E.; Narayanaswamy, R., *Sens. Actuators, B* **1997**, *B39*, 195.

9. Demas, J. N.; DeGraff, B. A., *Coord. Chem. Rev.* **2001**, *211*, 317.

10. Ghosh, A.; Ganguly, B.; Das, A., *Inorg. Chem.* **2007**, *46*, 9912.

11. Kneas, K. A.; Demas, J. N.; Nguyen, B.; Lockhart, A.; Xu, W.; DeGraff, B. A., *Anal. Chem.* **2002**, *74*, 1111.

12. Kocincova, A. S.; Borisov, S. M.; Krause, C.; Wolfbeis, O. S., *Anal. Chem.* **2007**, *79*, 8486.

13. McGee, K. A.; Veltkamp, D. J.; Marquardt, B. J.; Mann, K. R., *J. Am. Chem. Soc.* **2007**, *129*, 15092.

14. Ralfs, M.; Heinze, J., *Sens. Actuators, B* **1997**, *B44*, 257.

15. Onishi, M.; Ikemoto, K.; Hiraki, K.; Aoki, K., *Chem. Lett.* **1998**, 23.

16. Occupational Safety and Health Guideline for Chlorine. http://www.osha.gov/SLTC/healthguidelines/chlorine/recognition.html (4/28/2008).

17. *Chlorine: Effects on Health and the Environment*; The Chlorine Institute, Inc.: Arlington, 1999; pp 1-8.

18. *Atmospheric Monitoring Equipment for Chlorine*; Pamphlet 73; The Chlorine Institute, Inc.: Arlington, June, 2003; pp 1-23.

19. Schmittinger, P.; Editor, *Chlorine: Principles and Industrial Practice*. **2000**; p 254.

20. *Crystal Engineering: From Molecules and Crystals to Materials*. Kluwer Academic: Dordrecht, **1999**; Vol. 538.

21. *Inclusion Compounds Volume 1*. Academic Press: London, **1984**.

22. Janzen, D. E.; Wang, X.; Carr, P. W.; Mann, K. R., *Inorg. Chim. Acta* **2004**, *357*, 3317.

23. Gupta, A. K.; Poddar, R. K., *Indian J. Chem., Sect A* **1999**, *38A*, 1228.

24. Pappenfus, T. M.; Mann, K. R., *Inorg. Chem.* **2001**, *40*, 6301.

25. Dupureur, C. M.; Barton, J. K., *Inorg. Chem.* **1997**, *36*, 33.

26. Hiort, C.; Lincoln, P.; Norden, B., *J. Am. Chem. Soc.* **1993**, *115*, 3448.

27. Bennett, M. A.; Smith, A. K., *J. Chem. Soc., Dalton Trans.* **1974**, 233.

28. Zelonka, R. A.; Baird, M. C., *Can. J. Chem.* **1972**, *50*, 3063.

29. Freedman, D. A.; Evju, J. K.; Pomije, M. K.; Mann, K. R., *Inorg. Chem.* **2001**, *40*, 5711.

30. Kneas, K. A.; Xu, W.; Demas, J. N.; DeGraff, B. A., *Appl. Spectrosc.* **1997**, *51*, 1346.

31. Demas, J. N.; DeGraff, B. A.; Xu, W., *Anal. Chem.* **1995**, *67*, 1377.

32. Canivet, J.; Karmazin-Brelot, L.; Suess-Fink, G., *J. Organomet. Chem.* **2005**, *690*, 3202.

33. Robertson, D. R.; Robertson, I. W.; Stephenson, T. A., *J. Organomet. Chem.* **1980**, *202*, 309.

34. Compound made by Erica J. Marti.

35. Blessing, R. H., *Acta Crystallogr., Sect. A: Found. Crystallogr.* **1995**, *A51*, 33.

36. Sheldrick, G. *SADABS*, v.2.03; 2002.

37. *SHELXL*, v.6.1; Bruker AXS, Madison, WI, 2001.

38. Spek, A. L., *J. Appl. Crystallogr.* **2003**, *36*, 7.

39. Spek, A. L. *PLATON*, Utrecht University, Utrecht, The Netherlands, 2005.

40. Freedman, D. A.; Janzen, D. E.; Vreeland, J. L.; Tully, H. M.; Mann, K. R., *Inorg. Chem.* **2002**, *41*, 3820.

41. Freedman, D. A.; Kruger, S.; Roosa, C.; Wymer, C., *Inorg. Chem.* **2006**, *45*, 9558.

42. Freedman, D. A.; Janzen, D. E.; Mann, K. R., *Inorg. Chem.* **2001**, *40*, 6009.

43. Hoshino, Y.; Endo, A.; Shimizu, K.; Sato, G. P., *J. Electroanal. Chem.* **1988**, *246*, 225.

44. El-Hendawy, A. M.; Al-Kubaisi, A. H.; Al-Madfa, H. A., *Polyhedron* **1997**, *16*, 3039.

45. Xiao, X.; Sakamoto, J.; Tanabe, M.; Yamazaki, S.; Yamabe, S.; Matsumura-Inoue, T., *J. Electroanal. Chem.* **2002**, *527*, 33.

46. Lever, A. B. P., *Inorg. Chem.* **1990**, *29*, 1271.

47. Al-Anber, M.; Vatsadze, S.; Holze, R.; Lang, H.; Thiel, W. R., *Dalton Trans.* **2005**, 3632.

48. Edelmann, M. J.; Raimundo, J.-M.; Utesch, N. F.; Diederich, F., *Helv. Chim. Acta* **2002**, *85*, 2195.

49. Frank, S. N.; Bard, A. J., *J. Am. Chem. Soc.* **1975**, *97*, 7427.

50. Amouyal, E.; Homsi, A.; Chambron, J. C.; Sauvage, J. P., *J. Chem. Soc., Dalton Trans.* **1990**, 1841.

51. El-Hendawy, A. M.; Alqaradawi, S. Y.; Al-Madfa, H. A., *Transition Met. Chem.* **2000**, *25*, 572.

52. Hemmila, I., *Anal. Chem.* **1985**, *57*, 1676.

53. Jang, H.; Shin, C.-H.; Jung, B.-J.; Kim, D.-h.; Shim, H.-K.; Do, Y., *Eur. J. Inorg. Chem.* **2006**, 718.

54. Boone, S. R.; Pierpont, C. G., *Polyhedron* **1990**, *9*, 2267.

55. Chao, G. K. J.; Sime, R. L.; Sime, R. J., *Acta Crystallogr., Sect. B: Struct. Sci.* **1973**, *29*, 2845.

56. Kar, S.; Chanda, N.; Mobin, S. M.; Urbanos, F. A.; Niemeyer, M.; Puranik, V. G.; Jimenez-Aparicio, R.; Lahiri, G. K., *Inorg. Chem.* **2005**, *44*, 1571.

57. Mitra, K. N.; Choudhury, S.; Castineiras, A.; Goswami, S., *J. Chem. Soc., Dalton Trans.* **1998**, 2901.

58. Nayak, A.; Patra, S.; Sarkar, B.; Ghumaan, S.; Puranik, V. G.; Kaim, W.; Lahiri, G. K., *Polyhedron* **2005**, *24*, 333.

59. Reynolds, P. A.; Cable, J. W.; Sobolev, A. N.; Figgis, B. N., *J. Chem. Soc., Dalton Trans.* **1998**, 559.

Chapter 5

1. Vander Donckt, E.; Camerman, B.; Herne, R.; Vandeloise, R., *Sens. Actuators, B* **1996**, *B32*, 121.

2. Brooks, J.; Babayan, Y.; Lamansky, S.; Djurovich, P. I.; Tsyba, I.; Bau, R.; Thompson, M. E., *Inorg. Chem.* **2002**, *41*, 3055.

3. Kawamura, Y.; Brooks, J.; Brown, J. J.; Sasabe, H.; Adachi, C., *Phys. Rev. Lett.* **2006**, *96*, 017404.

4. Chassot, L.; Von Zelewsky, A., *Inorg. Chem.* **1987**, *26*, 2814.

5. Ma, B.; Djurovich, P. I.; Thompson, M. E., *Coord. Chem. Rev.* **2005**, *249*, 1501.

6. Lai, S.-W.; Che, C.-M., *Top. Curr. Chem.* **2004**, *241*, 27.

7. Balashev, K. P.; Puzyk, M. V.; Kotlyar, V. S.; Kulikova, M. V., *Coord. Chem. Rev.* **1997**, *159*, 109.

8. Jolliet, P.; Gianini, M.; von Zelewsky, A.; Bernardinelli, G.; Stoeckli-Evans, H., *Inorg. Chem.* **1996**, *35*, 4883.

9. Maestri, M.; Deuschel-Cornioley, C.; Von Zelewsky, A., *Coord. Chem. Rev.* **1991**, *111*, 117.

10. Craig, C. A.; Watts, R. J., *Inorg. Chem.* **1989**, *28*, 309.

11. Cardenas, D. J.; Echavarren, A. M.; Ramirez de Arellano, M. C., *Organometallics* **1999**, *18*, 3337.

12. Li, C. K.-L.; Sun, R. W.-Y.; Kui, S. C.-F.; Zhu, N.; Che, C.-M., *Chem.--Eur. J.* **2006**, *12*, 5253.

13. Ivanov, M. A.; Puzyk, M. V.; Balashev, K. P., *Opt. Spectrosc.* **2006**, *100*, 382.

14. Wong, K. M.-C.; Zhu, X.; Hung, L.-L.; Zhu, N.; Yam, V. W.-W.; Kwok, H.-S., *Chem. Commun.* **2005**, 2906.

15. Fan, D.; Yang, C.-T.; Ranford, J. D.; Vittal, J. J.; Lee, P. F., *Dalton Trans.* **2003**, 3376.

16. Cinellu, M. A.; Zucca, A.; Stoccoro, S.; Minghetti, G.; Manassero, M.; Sansoni, M., *Dalton Trans.* **1996**, 4217.

17. Constable, E. C.; Leese, T. A., *J. Organomet. Chem.* **1989**, *363*, 419.

18. King, K. A.; Spellane, P. J.; Watts, R. J., *J. Am. Chem. Soc.* **1985**, *107*, 1431.

19. Gao, R.; Ho, D. G.; Hernandez, B.; Selke, M.; Murphy, D.; Djurovich, P. I.; Thompson, M. E., *J. Am. Chem. Soc.* **2002**, *124*, 14828.

20. DeRosa, M. C.; Hodgson, D. J.; Enright, G. D.; Dawson, B.; Evans, C. E. B.; Crutchley, R. J., *J. Am. Chem. Soc.* **2004**, *126*, 7619.

21. Lamansky, S.; Djurovich, P.; Murphy, D.; Abdel-Razzaq, F.; Lee, H.-E.; Adachi, C.; Burrows, P. E.; Forrest, S. R.; Thompson, M. E., *J. Am. Chem. Soc.* **2001**, *123*, 4304.

22. Ragni, R.; Plummer, E. A.; Brunner, K.; Hofstraat, J. W.; Babudri, F.; Farinola, G. M.; Naso, F.; De Cola, L., *J. Mater. Chem.* **2006**, *16*, 1161.

23. Sheraw, C. D.; Zhou, L.; Huang, J. R.; Gundlach, D. J.; Jackson, T. N.; Kane, M. G.; Hill, I. G.; Hammond, M. S.; Campi, J.; Greening, B. K.; Francl, J.; West, J., *Appl. Phys. Lett.* **2002**, *80*, 1088.

24. Kanno, H.; Giebink, N. C.; Sun, Y.; Forrest, S. R., *Appl. Phys. Lett.* **2006**, *89*, 023503/1.

25. Okada, S.; Okinaka, K.; Iwawaki, H.; Furugori, M.; Hashimoto, M.; Mukaide, T.; Kamatani, J.; Igawa, S.; Tsuboyama, A.; Takiguchi, T.; Ueno, K., *Dalton Trans.* **2005**, 1583.

26. D'Andrade, B. W.; Baldo, M. A.; Adachi, C.; Brooks, J.; Thompson, M. E.; Forrest, S. R., *Appl. Phys. Lett.* **2001**, *79*, 1045.

27. Lamansky, S.; Kwong, R. C.; Nugent, M.; Djurovich, P. I.; Thompson, M. E., *Org. Electronics* **2001**, *2*, 53.

28. Watanabe, T.; Nakamura, K.; Kawami, S.; Fukuda, Y.; Tsuji, T.; Wakimoto, T.; Miyaguchi, S.; Yahiro, M.; Yang, M. J.; Tsutsui, T., *Synth. Met.* **2001**, *122*, 203.

29. Meng, H.; Sun, F.; Goldfinger, M. B.; Gao, F.; Londono, D. J.; Marshal, W. J.; Blackman, G. S.; Dobbs, K. D.; Keys, D. E., *J. Am. Chem. Soc.* **2006**, *128*, 9304.

30. Chou, P.-T.; Chi, Y., *Chem.--Eur. J.* **2007**, *13*, 380.

31. Tamayo, A. B.; Alleyne, B. D.; Djurovich, P. I.; Lamansky, S.; Tsyba, I.; Ho, N. N.; Bau, R.; Thompson, M. E., *J. Am. Chem. Soc.* **2003**, *125*, 7377.

32. Colombo, M. G.; Brunold, T. C.; Riedener, T.; Guedel, H. U.; Fortsch, M.; Buergi, H.-B., *Inorg. Chem.* **1994**, *33*, 545.

33. Dedeian, K.; Djurovich, P. I.; Garces, F. O.; Carlson, G.; Watts, R. J., *Inorg. Chem.* **1991**, *30*, 1685.

34. Grushin, V. V.; Herron, N.; LeCloux, D. D.; Marshall, W. J.; Petrov, V. A.; Wang, Y., *Chem. Commun.* **2001**, 1494.

35. Konno, H.; Sasaki, Y., *Chem. Lett.* **2003**, *32*, 252.

36. Ostrowski, J. C.; Robinson, M. R.; Heeger, A. J.; Bazan, G. C., *Chem. Commun.* **2002**, 784.

37. Tsuboyama, A.; Iwawaki, H.; Furugori, M.; Mukaide, T.; Kamatani, J.; Igawa, S.; Moriyama, T.; Miura, S.; Takiguchi, T.; Okada, S.; Hoshino, M.; Ueno, K., *J. Am. Chem. Soc.* **2003**, *125*, 12971.

38. Dedeian, K.; Shi, J.; Shepherd, N.; Forsythe, E.; Morton, D. C., *Inorg. Chem.* **2005**, *44*, 4445.

39. Tamao, K.; Kodama, S.; Nakajima, I.; Kumada, M.; Minato, A.; Suzuki, K., *Tetrahedron* **1982**, *38*, 3347.

40. Nonoyama, M., *Bull. Chem. Soc. Jpn.* **1974**, *47*, 767.

41. Schmid, B.; Garces, F. O.; Watts, R. J., *Inorg. Chem.* **1994**, *33*, 9.

42. Blessing, R. H., *Acta Crystallogr., Sect. A: Found. Crystallogr.* **1995**, *A51*, 33.

43. Sheldrick, G. *SADABS*, v.2.03; 2002.

44. *SHELXL*, v.6.1; Bruker AXS, Madison, WI, 2001.

45. Garces, F. O.; Dedeian, K.; Keder, N. L.; Watts, R. J., *Acta Crystallogr., Sect. C: Cryst. Struct. Commun.* **1993**, *C49*, 1117.

46. Silverstein, R. M.; Webster, F. X., *Spectrometric Identification of Organic Compounds*. 6th ed.; John Wiley & Sons, Inc.: New York, **1998**.

47. Marat, K. *Spinworks*, v.2.3; University of Manitoba, Winnipeg, Manitoba, Canada, 2004.

48. Chattopadhyay, S. K.; Mitra, K.; Biswas, S.; Naskar, S.; Mishra, D.; Adhikary, B.; Harrison, R. G.; Cannon, J. F., *Transition Met. Chem.* **2004**, *29*, 1.

49. Heeg, M. J.; Kroener, R.; Deutsch, E., *Acta Crystallogr., Sect. C: Cryst. Struct. Commun.* **1985**, *C41*, 684.

50. Paneque, M.; Poveda, M. L.; Carmona, E.; Salazar, V., *Dalton Trans.* **2005**, 1422.

51. Paneque, M.; Poveda, M. L.; Rey, L.; Taboada, S.; Carmona, E.; Ruiz, C., *J. Organomet. Chem.* **1995**, *504*, 147.

52. Paneque, M.; Poveda, M. L.; Salazar, V.; Taboada, S.; Carmona, E.; Gutierrez-Puebla, E.; Monge, A.; Ruiz, C., *Organometallics* **1999**, *18*, 139.

53. Rao, K. M.; Day, C. L.; Jacobson, R. A.; Angelici, R. J., *Inorg. Chem.* **1991**, *30*, 5046.

54. Sanchez-Delgado, R. A.; Herrera, V.; Bianchini, C.; Masi, D.; Mealli, C., *Inorg. Chem.* **1993**, *32*, 3766.

55. Amari, C.; Ianelli, S.; Pelizzi, C.; Pelizzi, G.; Predieri, G., *Inorg. Chim. Acta* **1993**, *211*, 89.

56. Bianchini, C.; Gatteschi, D.; Giambastiani, G.; Rios, I. G.; Ienco, A.; Laschi, F.; Mealli, C.; Meli, A.; Sorace, L.; Toti, A.; Vizza, F., *Organometallics* **2007**, *26*, 726.

57. Chelucci, G.; Muroni, D.; Saba, A.; Soccolini, F., *J. Molec. Catal. A* **2003**, *197*, 27.

58. Constable, E. C.; Henney, R. P. G.; Tocher, D. A., *J. Chem. Soc., Dalton Trans.* **1991**, 2335.

59. Constable, E. C.; Henney, R. P. G.; Tocher, D. A., *J. Chem. Soc., Dalton Trans.* **1992**, 2467.

60. McDonald, A. R.; Lutz, M.; von Chrzanowski, L. S.; van Klink, G. P. M.; Spek, A. L.; van Koten, G., *Inorg. Chem.* **2008**, *47*, 6681.

61. Karatsu, T.; Nakamura, T.; Yagai, S.; Kitamura, A.; Yamaguchi, K.; Matsushima, Y.; Iwata, T.; Hori, Y.; Hagiwara, T., *Chem. Lett.* **2003**, *32*, 886.

Appendix A: Calculation of the oxygen diffusion coefficient in $[Ru(phen)_3](tfpb)_2$.

An estimate of the oxygen molecule diffusion coefficient in crystalline $[Ru(phen)_3](tfpb)_2$ was obtained[1] from the equation:

$$D_{O_2} \approx \frac{l^2_{penetration}}{\tau_{diffusion}} \tag{1}$$

where $l_{penetration}$ (the penetration depth of the exciting light) is defined as:

$$l_{penetration} = \frac{1}{\varepsilon C} \tag{2}$$

where C is the concentration of $Ru(phen)_3^{2+}$ calculated from the unit cell dimensions of the $[Ru(phen)_3](tfpb)_2$ crystal and ε is the molar extinction coefficient at the excitation wavelength. The ε values at different excitation wavelengths were estimated from a solid state ATR UV-vis spectrum (Figure A1) of a microcrystalline film of $[Ru(phen)_3](tfpb)_2$ and the aqueous solution spectrum ε_{peak} value (2.5×10^4 M^{-1} cm^{-1}) for $Ru(phen)_3^{2+}$.[2] The value for $\tau_{diffusion}$ (defined as the time required for the oxygen concentration in the film to drop to 1/e of its initial value (or $t_{1/2}/\ln(2)$) was estimated for the three excitation wavelengths shown in Figure 14 as the time required for the corresponding change in the emission response. Because the drop in $[O_2]$ is not exponential, $\tau_{diffusion}$ is not a constant, a potential source of uncertainty in this treatment. The values used for the estimate of D are then: C = 0.6855 M, $\varepsilon_{400nm} = 2.1 \times 10^4$ M^{-1} cm^{-1}, $\varepsilon_{470nm} = 1.8 \times 10^4$ M^{-1} cm^{-1}, $\varepsilon_{518nm} = 4.7 \times 10^3$ M^{-1} cm^{-1}. These values give $l_{penetration}$ values of 7.0×10^{-5} cm, 8.1×10^{-5} cm and 3.1×10^{-4} cm for 400, 470 and 518 nm excitation, respectively.

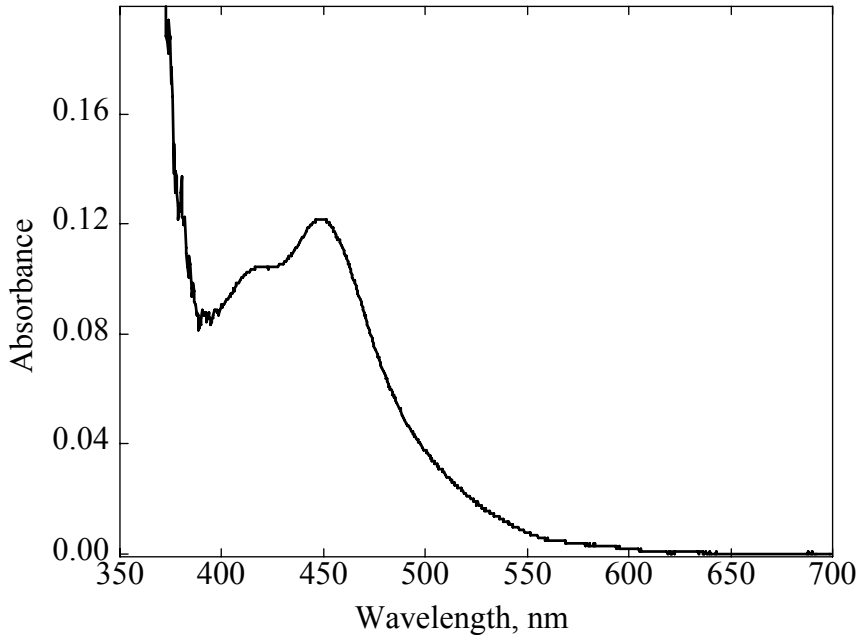

Figure A1. Solid-state UV-vis absorption spectrum of a microcrystalline film of $[Ru(phen)_3](tfpb)_2$ deposited on a cubic zirconia ATR crystal.

These $l_{penetration}$ values combined with the values for $\tau_{diffusion}$ at the respective wavelengths (τ_{400nm} = 29 msec, τ_{470nm} = 173 msec, τ_{518nm} = 3180 msec) give D_{O2} values of 1.6 x 10^{-7} cm^2 s^{-1}, 3.8 x 10^{-8} $cm^2s^{-1}$and 3.0 x 10^{-8} cm^2 s^{-1}, respectively. Even considering the many assumptions made and the nonlinear nature of the differential equation that describes the convolution of the oxygen diffusion with the light penetration, we feel that our order of magnitude estimate of 10^{-7} -10^{-8} cm^2s^{-1} for oxygen diffusion in the film is reasonable. Fitting of the data to an appropriate[3] thin film equation for the front-face illuminated optically dense case here is in progress.

References

1. Kalinowski, J.; Fattori, V.; Di Marco, P., *Chem. Phys.* **2001**, *266*, 85.

2. LED is ETG-5UV 405-30 from ETG Corporation, 8599 Venice Blvd, Unit K, Los Angeles, CA 90034.

3. Bowyer, W. J.; Xu, W.; Demas, J. N., *Anal. Chem.* **2004**, *76*, 4374.

Appendix B: Derivation of lifetime Stern-Volmer equations.

The determination of the Stern-Volmer constant (K_{SV}) from lifetime data is straightforward for the case of a single exponential decay:

$$\frac{\tau_0}{\tau} = \frac{I_{emit0}}{I_{emit}} = 1 + K_{SV}[Q] \tag{1}$$

and is identical to the result obtained for emission intensity data.

The case for two emitting species in a sample has also been treated but two equations have been proposed:

$$\frac{\tau_{M0}}{\tau_M} = 1 + K_{SV}[Q] \tag{2}$$

$$\text{and } \frac{\langle\tau\rangle_0}{\langle\tau\rangle} = 1 + K_{SV}[Q] \tag{3}$$

$$\text{where } \frac{\tau_{M0}}{\tau_M} = \frac{\dfrac{\alpha_{a0}\tau_{a0} + \alpha_{b0}\tau_{b0}}{\alpha_{a0} + \alpha_{b0}}}{\dfrac{\alpha_a\tau_a + \alpha_b\tau_b}{\alpha_a + \alpha_b}} \tag{4}$$

$$\text{and } \frac{\langle\tau\rangle_0}{\langle\tau\rangle} = \frac{\dfrac{\beta_{a0}\tau_{a0}^2 + \beta_{b0}\tau_{b0}^2}{\beta_{a0}\tau_{a0} + \beta_{b0}\tau_{b0}}}{\dfrac{\beta_a\tau_a^2 + \beta_b\tau_b^2}{\beta_a\tau_a + \beta_b\tau_b}} \tag{5}$$

Some confusion has ensued in the literature concerning the use of these equations for the determination of K_{SV}. Empirically, Carraway *et al.* have suggested that the τ_{M0}/τ_M equation gives results consistent with I_0/I results for polymer systems.[1] In this Appendix, I show the relationship between these two equations and the more common steady state I_0/I measurements of the Stern-Volmer constant, K_{SV}.

When a molecule in its ground state, [A], absorbs energy in the form of light (I) sufficient energy excites an electron from the ground state into a higher lying state [A^*]. The energy from this excited state can then decay back to the ground state in two ways, radiatively by emitting light or non-radiatively by emitting heat.

$$A + h\nu \xrightarrow{I_{excite}} A^* \tag{6}$$

$$A^* \xrightarrow{k_r} A + h\nu \tag{7}$$

$$A^* \xrightarrow{k_{nr}} A + \Delta \tag{8}$$

The change in the concentration of the excited state [A^*] is expressed according to the following relationship.

$$\frac{d[A^*]}{dt} = I_{excite} - k[A^*] \tag{9}$$

The above differential equation can be solved to obtain the concentration of the excited state, [A^*], with respect to time.

$$\frac{1}{\frac{I_{excite}}{k} - [A^*]} d[A^*] = k dt \tag{10}$$

$$\int_0^{[A^*]_t} \frac{1}{\frac{I_{excite}}{k} - [A^*]} d[A^*] = k \int_0^{t_{pulse}} dt \tag{11}$$

$$\text{substituting } u = \frac{I_{excite}}{k} - [A^*], \frac{du}{d[A^*]} = -1, du = -d[A^*] \tag{12}$$

$$-\int_{\frac{I_{excite}}{k}}^{\frac{I_{excite}}{k} - [A^*]_t} \frac{1}{u} du = k \int_0^{t_{pulse}} dt \tag{13}$$

$$-\ln\left(\frac{I_{excite}}{k} - [A^*]_t\right) - \ln\left(\frac{I_{excite}}{k}\right) = k t_{pulse} \tag{14}$$

$$\ln\left(\frac{\frac{I_{excite}}{k}-[A^*]_t}{\frac{I_{excite}}{k}}\right)=-kt_{pulse} \tag{15}$$

$$\frac{I_{excite}}{k}-[A^*]_t=\frac{I_{excite}}{k}e^{-kt_{pulse}} \tag{16}$$

$$[A^*]_t=\frac{I_{excite}}{k}(1-e^{-kt_{pulse}}) \tag{17}$$

$$\text{substituting } \tau=\frac{1}{k},\ [A^*]_t=I_{excite}\tau(1-e^{-t_{pulse}/\tau}) \tag{18}$$

Equation 18 shows that the growth of [A^*] is an increasing function that gives a limiting value at $t_{pulse} = \infty$ of $I_{excite}\tau$. Assuming that t_{pulse} is the same for a sample with and without quencher added, the ratio of the emitted light intensity at time = t_{pulse} is:

$$\frac{I_0^{t_{pulse}}}{I^{t_{pulse}}}=\frac{k_r[A^*]_0}{k_r[A^*]_Q}=\frac{k_r I_{excite}\tau_0(1-e^{-t_{pulse}/\tau_0})}{k_r I_{excite}\tau(1-e^{-t_{pulse}/\tau})} \tag{19}$$

For both limiting cases, $t_{pulse} << \tau$ (or τ_0) and $t_{pulse} \rightarrow \infty$ the I_0/I ratio is 1 and τ_0/τ respectively. At early times, the decay step is not important until the excited state grows in thus I_0/I equals 1, and then at the steady state condition ($t_{pulse} \rightarrow \infty$) the familiar result ($I_0/I = \tau_0/\tau$) is obtained.

For a sample that decays biexponentially (i.e. two excited states, A^* and B^*), the situation is more complicated. The total concentration of the excited states can be expanded to contain two terms with the addition of preexponential factors, α, that describe the contribution to the signal at t=0. The preexponential factors depend on many variables including the spectral response of the detector, the concentration, emission, and

absorption characteristics of each component, the spectral transmission properties of the filters, and the spectral distribution of the exciting light.

$$[A^*] = I_{excite}\tau(1 - e^{-t_{pulse}/\tau}) \tag{20}$$

$$[A^*] + [B^*] = I_{excite}\alpha_a\tau_a(1 - e^{-t_{pulse}/\tau_a}) + I_{excite}\alpha_b\tau_b(1 - e^{-t_{pulse}/\tau_b}) \tag{21}$$

The total intensity of the light emitted can be expressed according to the relationship $I_{emit} = k_{r_a}[A^*] + k_{r_b}[B^*]$, therefore we get:

$$I_{emit} = k_{r_a} I_{excite}\alpha_a\tau_a(1 - e^{-t_{pulse}/\tau_a}) + k_{r_b} I_{excite}\alpha_b\tau_b(1 - e^{-t_{pulse}/\tau_b}) \tag{22}$$

Using this expression one can describe the temporal behavior at any time during the grow-in period at constant light intensity according to the Stern-Volmer ratio I_0/I.

$$\frac{I_{emit0}}{I_{emit}} = \frac{I_{excite}[k_{r_a}\alpha_{a0}\tau_{a0}(1 - e^{-t_{pulse}/\tau_{a0}}) + k_{r_b}\alpha_{b0}\tau_{b0}(1 - e^{-t_{pulse}/\tau_{b0}})]}{I_{excite}[k_{r_a}\alpha_a\tau_a(1 - e^{-t_{pulse}/\tau_a}) + k_{r_b}\alpha_b\tau_b(1 - e^{-t_{pulse}/\tau_b})]} \tag{23}$$

replacing k_r by $1/\tau_r$:

$$\frac{I_{emit0}}{I_{emit}} = \frac{\dfrac{\alpha_{a0}\tau_{a0}(1 - e^{-t_{pulse}/\tau_{a0}})}{\tau_{r_a}} + \dfrac{\alpha_{b0}\tau_{b0}(1 - e^{-t_{pulse}/\tau_{b0}})}{\tau_{r_b}}}{\dfrac{\alpha_a\tau_a(1 - e^{-t_{pulse}/\tau_a})}{\tau_{r_a}} + \dfrac{\alpha_b\tau_b(1 - e^{-t_{pulse}/\tau_b})}{\tau_{r_b}}} \tag{24}$$

and finally assuming $\tau_{r_a} = \tau_{r_b}$:

$$\frac{I_{emit0}}{I_{emit}} = \frac{\alpha_{a0}\tau_{a0}(1 - e^{-t_{pulse}/\tau_{a0}}) + \alpha_{b0}\tau_{b0}(1 - e^{-t_{pulse}/\tau_{b0}})}{\alpha_a\tau_a(1 - e^{-t_{pulse}/\tau_a}) + \alpha_b\tau_b(1 - e^{-t_{pulse}/\tau_b})} \tag{25}$$

Equation 25 shows that for biexponential decays, the observed, normalized preexponential factors found from the fitting become:

$$\alpha_a^{obs} = \frac{\alpha_a(1 - e^{-t_{pulse}/\tau_a})}{\alpha_a(1 - e^{-t_{pulse}/\tau_a}) + \alpha_b(1 - e^{-t_{pulse}/\tau_b})} \tag{26}$$

$$\alpha_b^{obs} = \frac{\alpha_b(1-e^{-t_{pulse}/\tau_b})}{\alpha_a(1-e^{-t_{pulse}/\tau_a}) + \alpha_b(1-e^{-t_{pulse}/\tau_b})} \tag{27}$$

When the pulse width, $t_{pulse} >> \tau$, $e^{-t_{pulse}/\tau} \rightarrow 0$ and $\alpha^{obs} = \alpha^{actual}$, giving:

$$\alpha_a^{obs} = \alpha_a \text{ and } \alpha_b^{obs} = \alpha_b \tag{28}$$

and Equation 22 for I_{emit} becomes:

$$I_{emit} = I_{excite}(k_{r_a}\alpha_a\tau_a + k_{r_b}\alpha_b\tau_b) \tag{29}$$

and the equation for I_{emit0}/I_{emit} becomes equivalent to Equation 4, τ_{M0}/τ_M for normalized α's and $k_{r_a} = k_{r_b}$.

$$\frac{I_{emit0}}{I_{emit}} = \frac{\tau_{M0}}{\tau_M} = \frac{\alpha_{a0}\tau_{a0} + \alpha_{b0}\tau_{b0}}{\alpha_a\tau_a + \alpha_b\tau_b} \tag{30}$$

When the pulse width, $t_{pulse} << \tau$, $e^{-t_{pulse}/\tau} \approx 1 - \frac{t_{pulse}}{\tau}$, the preexponential factors we observe from the fitting, α_a^{obs} and α_b^{obs} (and the analogous ones for α_{a0}^{obs} and α_{b0}^{obs}) become:

$$\alpha_a^{obs} = \frac{\frac{\alpha_a}{\tau_a}}{\frac{\alpha_a}{\tau_a} + \frac{\alpha_b}{\tau_b}} \text{ and } \alpha_b^{obs} = \frac{\frac{\alpha_b}{\tau_b}}{\frac{\alpha_a}{\tau_a} + \frac{\alpha_b}{\tau_b}} \tag{31}$$

Solving for α_a and α_b, with $\alpha_a+\alpha_b=1$:

$$\alpha_a = \frac{\alpha_a^{obs}\tau_a}{\alpha_a^{obs}\tau_a + (1-\alpha_a^{obs})\tau_b} = \frac{\alpha_a^{obs}\tau_a}{\alpha_a^{obs}\tau_a + \alpha_b^{obs}\tau_b}$$

$$\alpha_b = \frac{\alpha_b^{obs}\tau_b}{(1-\alpha_b^{obs})\tau_a + \alpha_b^{obs}\tau_b} = \frac{\alpha_b^{obs}\tau_b}{\alpha_a^{obs}\tau_a + \alpha_b^{obs}\tau_b} \tag{32}$$

The equation for I_{emit} becomes:

$$I_{emit} = \frac{\alpha_a^{obs}\tau_a{}^2 + \alpha_b^{obs}\tau_b{}^2}{\alpha_a^{obs}\tau_a + \alpha_b^{obs}\tau_b} \tag{33}$$

The above equation is the true mean lifetime equation, $\langle\tau\rangle$, where $\alpha_a^{obs} = \beta_a, \alpha_b^{obs} = \beta_b$ of equation 5. I_{emit0}/I_{emit} then becomes equivalent to equation 5:

$$\frac{I_{emit0}}{I_{emit}} = \frac{\langle\tau\rangle_0}{\langle\tau\rangle} = \frac{\dfrac{\alpha_{a0}^{obs}\tau_{a0}^2 + \alpha_{b0}^{obs}\tau_{b0}^2}{\alpha_{a0}^{obs}\tau_{a0} + \alpha_{a0}^{obs}\tau_{b0}}}{\dfrac{\alpha_a^{obs}\tau_a^2 + \alpha_b^{obs}\tau_b^2}{\alpha_a^{obs}\tau_a + \alpha_b^{obs}\tau_b}} \tag{34}$$

In summary, in cases when $t_{pulse} << \tau$, Stern-Volmer lifetime data should be treated using Equation 34 instead of Equation 30 which is appropriate for $t_{pulse} >> \tau$. From our examination of these equations with simulated data we have observed that rarely will one be in the short-pulse limit so that Equation 34 can be used directly. If one is unsure which regime in which lifetime data were taken (or if the data were taken with a pulse width intermediate between the extreme cases), the safest route is to use Equation 22 for I_{emit} and Equation 25 for Stern-Volmer data. These equations include the exponential term and t_{pulse} so that the true α values are given in all cases.

References

1. Carraway, E. R.; Demas, J. N.; DeGraff, B. A.; Bacon, J. R., *Anal. Chem.* **1991**, *63*, 337.

Appendix C: Analysis of Stern-Volmer lifetime data for Δ- and Λ-$[Ru(phen)_3][PF_6]_2$.

The appropriate expression for analysis of biexponential emission decay Stern-Volmer lifetime data and comparison to intensity Stern-Volmer data has been explored previously by Carraway *et al.*[1] Carraway came to the empirical conclusion that the preexponential weighted mean lifetime, $\tau_{M,}$ was best-suited to compare intensity and lifetime quenching data where the α's and corresponding τ's are obtained from the fit of the biexponential emission decay.

$$\tau_M = \frac{\alpha_a \tau_a + \alpha_b \tau_b}{\alpha_a + \alpha_b} \tag{1}$$

If the expression in the denominator is equal to one for τ_M and τ_{M0}, the Stern-Volmer relationship becomes:

$$\frac{\tau_{M0}}{\tau_M} = \frac{\alpha_{a0} \tau_{a0} + \alpha_{b0} \tau_{b0}}{\alpha_a \tau_a + \alpha_b \tau_b} \tag{2}$$

They also investigated the use of the true mean lifetime or natural lifetime, ⟨τ⟩, to describe the Stern-Volmer relationship but with unsatisfactory results.

$$\langle \tau \rangle = \frac{\alpha_a \tau_a^2 + \alpha_b \tau_b^2}{\alpha_a \tau_a + \alpha_b \tau_b} \tag{3}$$

$$\frac{\langle \tau \rangle^0}{\langle \tau \rangle} = \frac{\dfrac{\alpha_{a0} \tau_{a0}^2 + \alpha_{b0} \tau_{b0}^2}{\alpha_{a0} \tau_{a0} + \alpha_{b0} \tau_{b0}}}{\dfrac{\alpha_a \tau_a^2 + \alpha_b \tau_b^2}{\alpha_a \tau_a + \alpha_b \tau_b}} \tag{4}$$

We have observed that the effectiveness of the preexponential weighted mean lifetime as a means of portraying the lifetime Stern-Volmer data is dependent on the width of the excitation pulse. We found τ_M to be the appropriate data treatment when the complex was excited with a long pulse to achieve the steady-state. For data we obtained where the pulse was not sufficiently long to reach the steady-state we found τ_M to be inadequate. Instead we suggest the use of the previously derived equation (Appendix B) shown below in which no approximations of the α values are made. The terms in parentheses correct for the insufficient pulse width which overweights the shorter lifetime.

$$\frac{I_{emit0}}{I_{emit}} = \frac{\alpha_{a0}\tau_{a0}(1-e^{-t_{pulse}/\tau_{a0}}) + \alpha_{b0}\tau_{b0}(1-e^{-t_{pulse}/\tau_{b0}})}{\alpha_a\tau_a(1-e^{-t_{pulse}/\tau_a}) + \alpha_b\tau_b(1-e^{-t_{pulse}/\tau_b})} \quad (5)$$

Lifetime data for Δ-$[Ru(phen)_3][PF_6]_2$ and Λ-$[Ru(phen)_3][PF_6]_2$ were fit using equations (2), (4), and (5) and compared to the intensity-based Stern-Volmer plot. The lifetime data collected for Λ-$[Ru(phen)_3][PF_6]_2$ used a pulse width of about 1.005 μsec, sufficiently long to bring the excited state populations to steady state. The lifetime data for Δ-$[Ru(phen)_3][PF_6]_2$ were collected with an intermediate pulse of 0.125 μsec. Plots are shown below of the intensity-based Stern-Volmer as well as the lifetime-based Stern-Volmer plots using the equations above (Figures C1 and C2). For both Δ-$[Ru(phen)_3][PF_6]_2$ and Λ-$[Ru(phen)_3][PF_6]_2$ data are presented using only the two major components, ignoring the small long-lived component (0.5-3%) that is not quenched by oxygen. For Λ-$[Ru(phen)_3][PF_6]_2$ the preexponential weighted mean lifetime (□) (Equation 2) and lifetime calculated without approximations (◆) (Equation 5) both fit the

intensity data quite well because the long pulse condition in Equation 5 collapses to Equation 2 (see Appendix B). The true mean lifetime (◇) (the short-pulse condition estimation) fits reasonably well for Λ-$[Ru(phen)_3][PF_6]_2$ but not nearly as well as the preexponential weighted mean lifetime or lifetime calculated without approximations (Figure C1). Examining the Δ-$[Ru(phen)_3][PF_6]_2$ data in the same way we see the lifetime calculated without approximations (equation 5, ◆) appears to better match the intensity data than the preexponential weighted mean lifetime (△) which is not the approximation for short-pulse conditions. The true mean lifetime (◇) (the short-pulse approximation) also does not fit particularly well to the Δ-$[Ru(phen)_3][PF_6]_2$ lifetime-based Stern-Volmer data (Figure C2). In this case the pulse width is intermediate between the short- and long- pulse limits and is not approximated well by either Equation 2 or 4. In conclusion, while the preexponential weighted mean lifetime and true mean lifetime can approximate Stern-Volmer data for long pulse widths and short pulse widths respectively, calculating the average lifetime without approximations using Equation 5 is the more accurate way of expressing multi-exponential lifetime data, especially for data taken with intermediate to short light pulses relative to the emission decays.

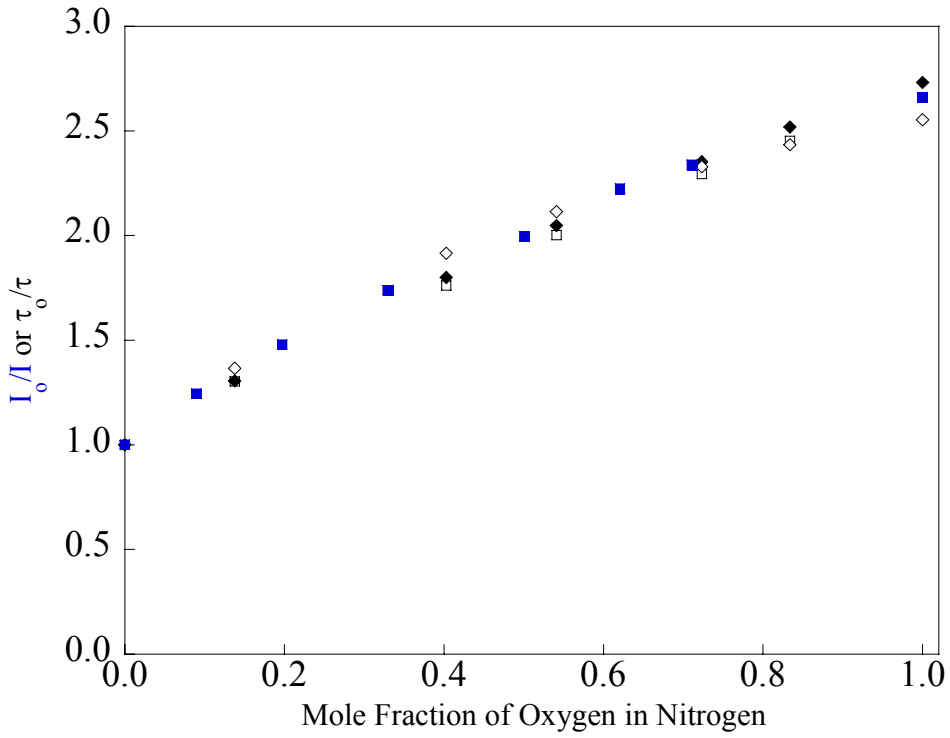

Figure C1. Overlayed plots of intensity (■), preexponential weighted mean lifetime (□) (Equation 2), true mean lifetime (◇) (Equation 4), and lifetime calculated without approximations (◆) (Equation 5) Stern-Volmer data for Λ-$[Ru(phen)_3](PF_6)_2$ utilizing the two major component lifetimes.

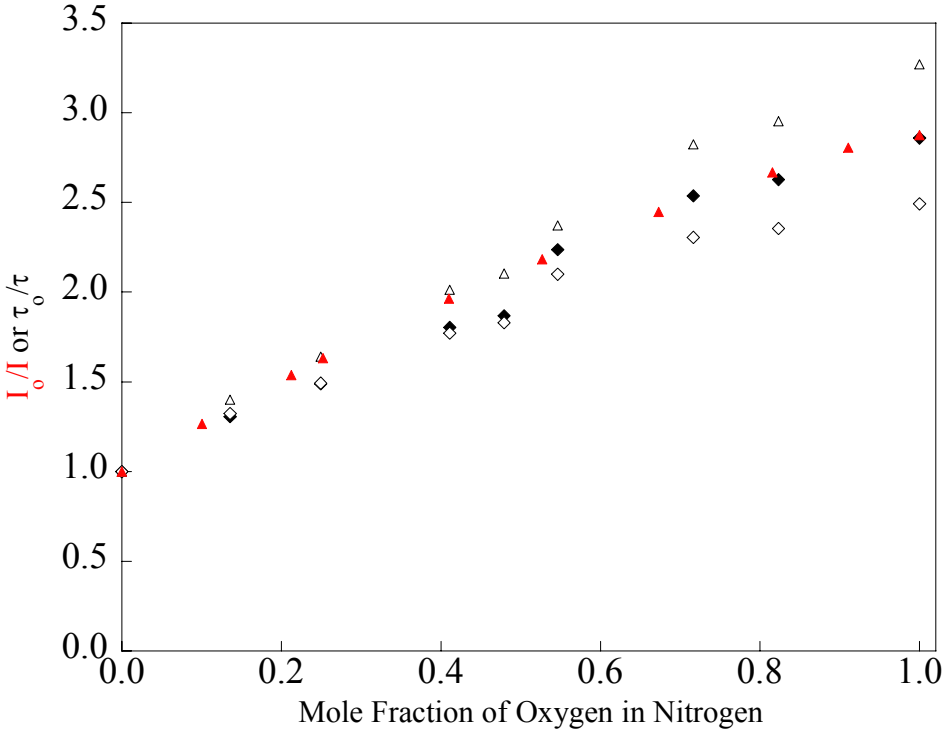

Figure C2. Overlayed plots of intensity (▲), preexponential weighted mean lifetime (△) (Equation 2), true mean lifetime (◇) (Equation 4), and lifetime calculated without approximations (◆) (Equation 5) Stern-Volmer data for Δ-$[Ru(phen)_3](PF_6)_2$ utilizing the two major component lifetimes.

References

1. Carraway, E. R.; Demas, J. N.; DeGraff, B. A., *Anal. Chem.* **1991**, *63*, 332.

Appendix D: Calculation of the thickness of Ru(pp)(β-diketonate)$_2$ films.

For absorption spectra obtained by the ATR method[ref], the thickness of a film can be estimated based upon the penetration depth of the light absorbed by the film as defined according to the equation:

$$l_{penetration} = \frac{1}{\varepsilon C} \tag{1}$$

where C is the concentration of the molecule in the solid state as calculated from the unit cell dimensions from the crystal structure and ε is the molar extinction coefficient at the excitation wavelength. The ε_{peak} values were estimated from solution spectra and were taken as the value at the λ_{max} according to Beer's law:

$$A = \varepsilon l c \tag{2}$$

where A is the absorbance, ε is the molar extinction coefficient, l is the path length, and c is the concentration of the solution. For example Ru(bpy)(dbm)$_2$ gives an absorbance at λ_{max} = 485 nm of 0.337 for a solution of concentration 5.12 x 10^{-4} M with a path length of 0.039 cm. This gives an extinction coefficient of 16,900 L/mol·cm at this wavelength. The concentration of the molecule in the solid state, C, was calculated based on the unit cell contents and volume. The unit cell of the crystal structure of Ru(bpy)(dbm)$_2$ has a Z = 8 (8 molecules in the unit cell). These 8 molecules when converted with Avogadro's number (6.02 x 10^{23}) is 1.329 x 10^{-23} mol of Ru(bpy)(dbm)$_2$ molecules. The volume of the unit cell, 6592.2 Å^3, can be converted to give 6.592 x 10^{-24} L. The concentration of the Ru molecule in the crystal then becomes:

$$C = \frac{1.329 \times 10^{-23}\ \text{mol}}{6.592 \times 10^{-24}\ \text{L}} = 2.016\ \text{M}$$

The penetration depth of the exciting light now becomes:

$$l_{penetration} = \frac{1}{\varepsilon C} = \frac{1}{(16877\ \text{L/mol}\cdot\text{cm})(2.016\ \text{M})} = 2.94\times10^{-5}\ \text{cm}$$

This value of $l_{penetration}$ converts to 2940 Å. The calculation of $l_{penetration}$ from solid-state ATR UV-Vis data in this way requires that the number of internal reflection bounces within the cubic zirconia crystal must be taken into account. Our crystal gives 11 bounces of the light from when the light enters the crystal to when it exits and the penetration depth for each single event is summed to give the total penetration depth of the light into the sample. The total penetration depth calculated above must be divided by 11, giving a depth for penetration into the film for a single event of 267 Å. Conversion of this length to an equivalent number of unit cells can then give the molecular thickness. Using the longest unit cell dimension (a = 31.708 Å) gives a thickness of 8.4 units cell. Multiplying by 4 (for the number of molecules per unit cell in this dimension) this gives a molecular thickness of 34 molecules. A similar calculation using the shortest unit cell dimension (b = 9.7834 Å) gives 27 unit cells thick or 54 molecules thick and a film thickness range of 34-54 molecules for Ru(bpy)(dbm)$_2$. Table 1A below shows film thicknesses calculated for all the molecules used in this study.

Table 1A. Values used for calculating film thickness of Ru(pp)(β-diketonate)$_2$ compounds.

	ε (L/mol·cm)	***C* (M)**	$l_{penetration}$ **(Å)**	**film thickness (molecules)**
Ru(bpy)(hfacac)$_2$	3617	2.940	9400	108-268
Ru(phen)(hfacac)$_2$	2062	2.769	17514	162-503
Ru(bpy)(dbm)$_2$	16877	2.016	2940	34-54
Ru(dppz)(dbm)$_2$	26560	1.588	2370	19-47